

# PENNSSTATE

---



LIDAR SHORT COURSE  
NSF CEDAR MEETING  
BOULDER CO  
17-21 JUNE 1991

Prepared by:  
C. R. Philbrick  
Penn State University

Assisted by:  
D. P. Sipler  
Haystack Observatory  
and  
J. D. Mathews  
Penn State University

CHAPTER 1  
INTRODUCTION TO LIDAR

CHAPTER 2  
OPTICAL SCATTERING

CHAPTER 3  
ATMOSPHERE AND BACKGROUND RADIATION

CHAPTER 4  
LASER TRANSMITTER

CHAPTER 5  
TELESCOPE RECEIVER

CHAPTER 6  
DETECTORS

CHAPTER 7  
DATA SYSTEM

CHAPTER 8  
SAFETY SYSTEM

CHAPTER 9  
EXPERIMENT TECHNIQUE

CHAPTER 10  
DATA FILTERS

CHAPTER 11  
LIDAR SYSTEM PERFORMANCE

CHAPTER 12  
LIDAR MEASUREMENTS

CHAPTER 13  
REFERENCES

# THE MEASUREMENT OF STRATOSPHERIC DENSITY DISTRIBUTION WITH THE SEARCHLIGHT TECHNIQUE

L. ELTERMAN

December 1951

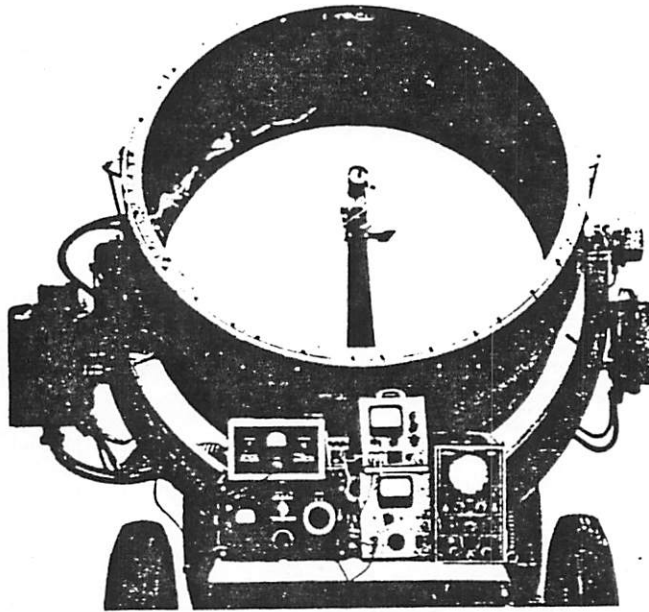


Fig. 7. Receiver with photomultiplier at focus of mirror (impedance matching amplifier and input monitoring scope not included in instrumentation shown).

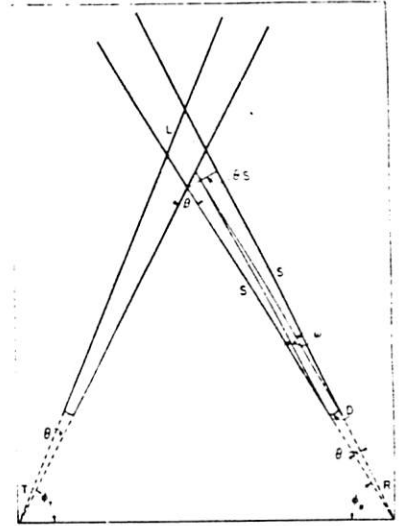
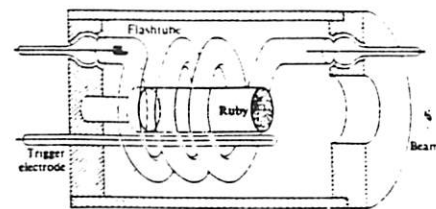
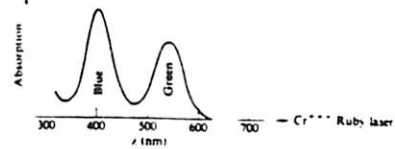


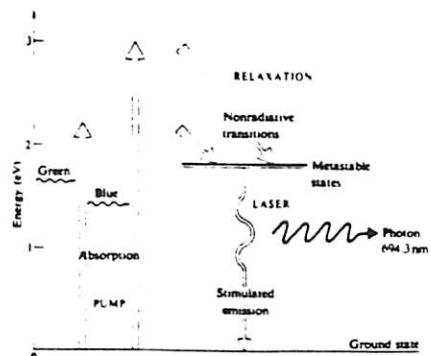
Fig. 1. Searchlight geometry.



The first ruby-laser configuration.

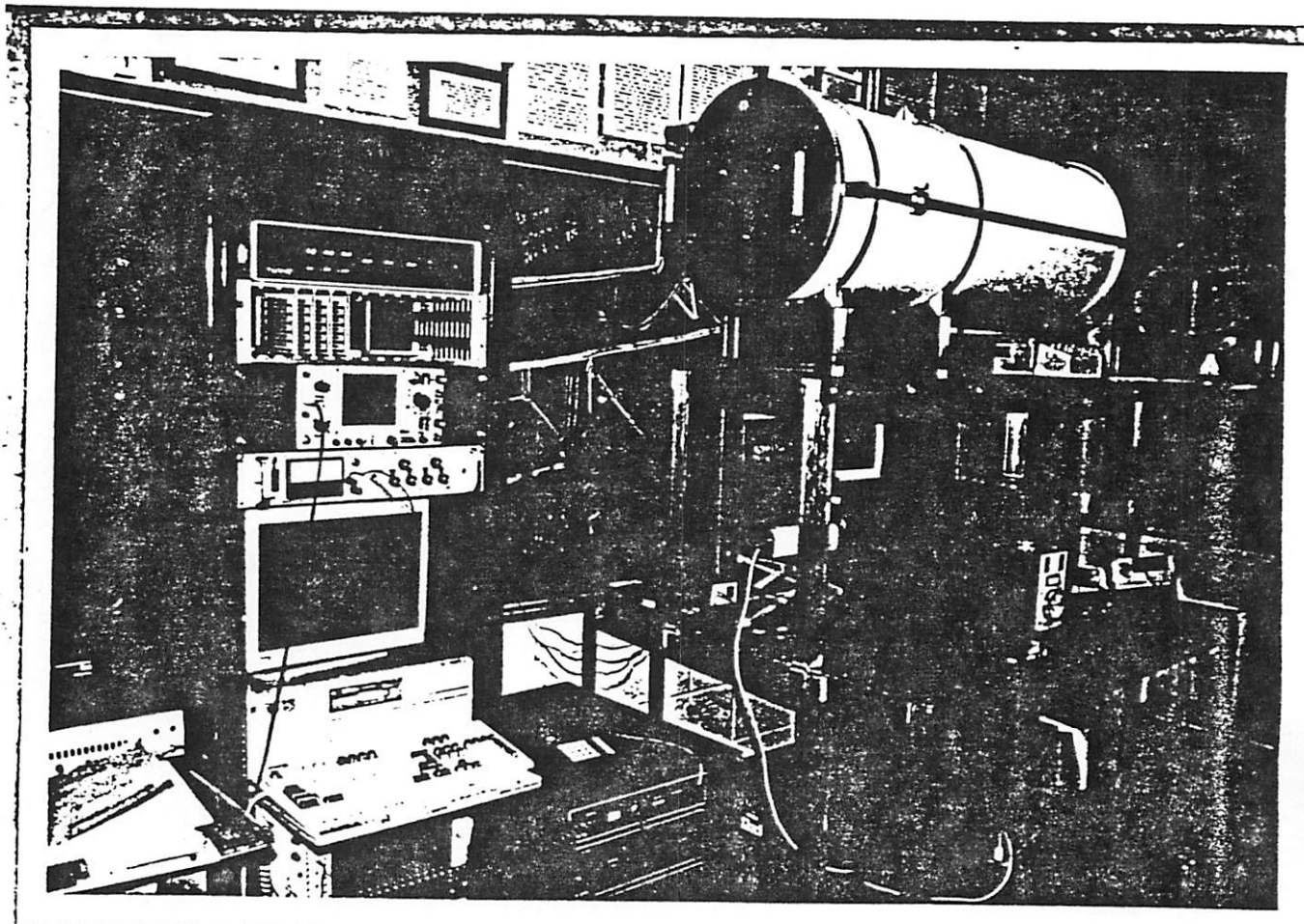
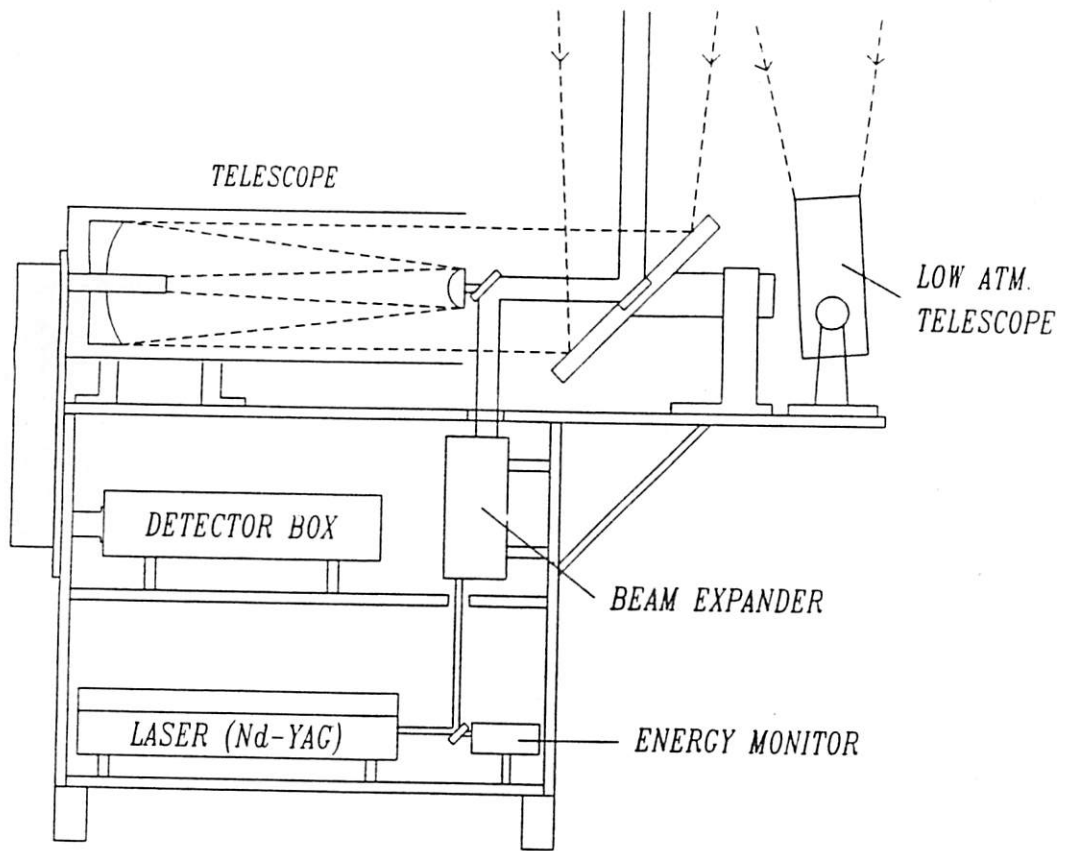


(a)



(b)

Ruby-laser energy levels



Above is a photograph of the Penn State Laser Atmospheric Measurement Program



## MAXWELL'S EQUATIONS

$$\nabla \cdot \mathbf{E} = \frac{q}{\epsilon} \quad (2.1)$$

$$\nabla \cdot \mathbf{H} = 0 \quad (2.2)$$

$$\nabla \times \mathbf{E} = -\mu \frac{\partial \mathbf{H}}{\partial t} \quad (2.3)$$

$$\nabla \times \mathbf{H} = \epsilon \frac{\partial \mathbf{E}}{\partial t} + \mathbf{j} \quad (2.4)$$

### 2.2. WAVE EQUATION AND PLANE-WAVE SOLUTIONS

$$\nabla \times \nabla \times \mathbf{E} = -\mu \frac{\partial(\nabla \times \mathbf{H})}{\partial t} \quad (2.8)$$

$$\nabla \times \nabla \times \mathbf{E} \equiv \nabla(\nabla \cdot \mathbf{E}) - \nabla^2 \mathbf{E}$$

$$\nabla^2 \mathbf{E} = \mu \epsilon \frac{\partial^2 \mathbf{E}}{\partial t^2} \quad (2.9)$$

$$v \equiv (\epsilon \mu)^{-1/2} \quad (2.10)$$

$$c = (\epsilon_0 \mu_0)^{-1/2} = 2.9979 \times 10^8 \text{ m s}^{-1} \quad (2.11)$$

$$r_{\perp} \equiv \left\{ \frac{E_{r0}}{E_{i0}} \right\}_{\perp} = - \frac{\sin(\theta_i - \theta_t)}{\sin(\theta_i + \theta_t)} \quad (2.61)$$

$$t_{\perp} \equiv \left\{ \frac{E_{t0}}{E_{i0}} \right\}_{\perp} = + \frac{2 \sin \theta_i \cos \theta_t}{\sin(\theta_i + \theta_t)} \quad (2.62)$$

$$r_{\parallel} \equiv \left\{ \frac{E_{r0}}{E_{i0}} \right\}_{\parallel} = + \frac{\tan(\theta_i - \theta_t)}{\tan(\theta_i + \theta_t)} \quad (2.63)$$

$$t_{\parallel} \equiv \left\{ \frac{E_{t0}}{E_{i0}} \right\}_{\parallel} = + \frac{2 \sin \theta_i \cos \theta_t}{\sin(\theta_i + \theta_t) \cos(\theta_i - \theta_t)} \quad (2.64)$$

$$R_{\perp} = r_{\perp}^2, \quad R_{\parallel} = r_{\parallel}^2 \quad (2.65)$$

$$T_{\perp} = \left\{ \frac{\tan \theta_t}{\tan \theta_i} \right\} t_{\perp}^2 \quad \text{and} \quad T_{\parallel} = \left\{ \frac{\tan \theta_t}{\tan \theta_i} \right\} t_{\parallel}^2 \quad (2.66)$$

$$R_{\parallel} + T_{\parallel} = 1 \quad \text{and} \quad R_{\perp} + T_{\perp} = 1 \quad (2.67)$$

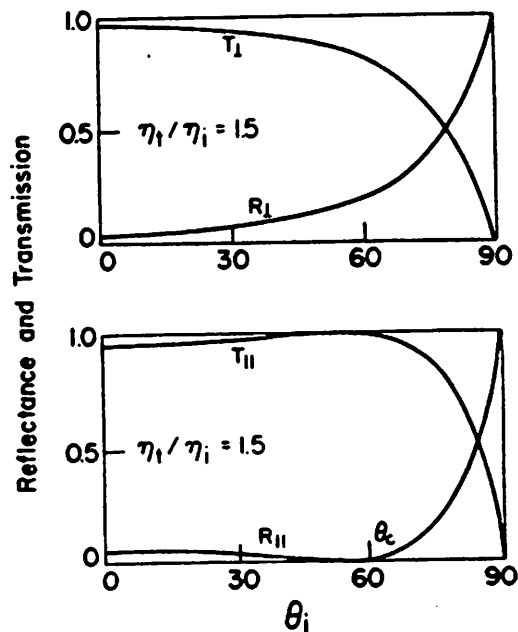


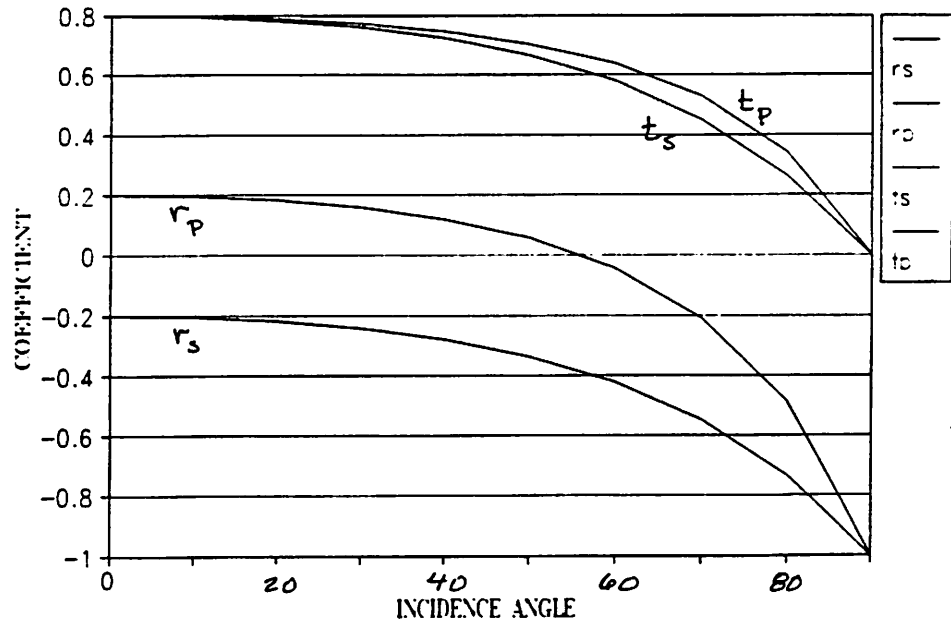
Fig. 29. Reflectance and transmittance versus incident angle for two perpendicular planes of polarization (Hecht and Zajac, 1974).

FRESNEL EQUATIONS

N1	1						
N2	1.5	THE1	THE2	rs	rp	ts	tp
		0.000	0.000	-0.200	0.200	0.800	0.800
		10.000	6.648	-0.204	0.196	0.796	0.797
		20.000	13.180	-0.217	0.183	0.783	0.789
		30.000	19.471	-0.240	0.159	0.760	0.773
		40.000	25.374	-0.278	0.120	0.722	0.746
		50.000	30.710	-0.335	0.057	0.665	0.705
		60.000	35.264	-0.420	-0.042	0.580	0.638
		70.000	38.790	-0.547	-0.206	0.453	0.529
		80.000	41.036	-0.734	-0.487	0.266	0.342
		90.000	41.810	-1.000	-1.000	0.000	0.000

THE1	THE2	Rs	Rp	Ts	Tp	Rs+Ts
0.000	0.000	0.040	0.040	0.960	0.960	1.000
10.000	6.648	0.042	0.038	0.958	0.962	1.000
20.000	13.180	0.047	0.033	0.953	0.967	1.000
30.000	19.471	0.058	0.025	0.942	0.975	1.000
40.000	25.374	0.077	0.014	0.923	0.986	1.000
50.000	30.710	0.112	0.003	0.888	0.997	1.000
60.000	35.264	0.177	0.002	0.823	0.998	1.000
70.000	38.790	0.300	0.042	0.700	0.958	1.000
80.000	41.036	0.539	0.237	0.461	0.763	1.000
90.000	41.810	1.000	1.000	0.000	0.000	1.000

FRESNEL COEFFICIENTS



# ORIEL INTERFERENCE FILTERS : REFLECTANCE

## REFLECTION AT AN INTERFACE

When light strikes a smooth interface between two transparent media as in Fig. 1, some of the light enters the second medium and is refracted, and some is reflected at the interface. The relationship between the angle of incidence,  $i$ , and the angle of refraction is given by Snell's Law:

$$n_1 \sin i = n_2 \sin r \dots\dots(1)$$

Where:

$n_1$  and  $n_2$  are the indices of refraction of the media as shown.

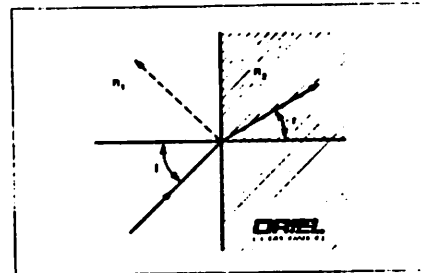


Fig. 1 Refraction at an interface.

Electromagnetic theory provides expressions for the fraction of incident radiation reflected. The reflectance depends on the indices of refraction, the angle of incidence and the polarization of the radiation.

$$R_p = \frac{\tan^2(i - r)}{\tan^2(i + r)} \dots\dots(2)$$

$$R_s = \frac{\sin^2(i - r)}{\sin^2(i + r)} \dots\dots(3)$$

Where:

- $R_p$  = Reflectance for light polarized parallel to the plane of incidence (the plane containing the ray and the surface normal).
- $R_s$  = Reflectance for light polarized perpendicular to the plane of incidence.

Fig. 2 shows the variation of reflectance with angle  $i$  for an air-fused silica interface.

The reflectance at normal incidence ( $i = 0$ ) is given by these equations and Snell's Law:

$$R = R_p = R_s = \left[ \frac{(n_2 - n_1)}{(n_2 + n_1)} \right]^2 \dots\dots(4)$$

For  $n_1 = 1$  and  $n_2 = 1.5$ , typical of an air-glass interface,  $R = 0.04$ . For a glass side the transmittance from two surfaces is  $(1 - 0.4 - (1 - 0.4) 0.04) = 0.9216 = 0.92$ .

Since Fresnel derived equations similar to (4) using his elastic theory of light, the reflection at the interface is sometimes called "e" Fresnel reflection or Fresnel loss.

The reflected wave also undergoes a phase change of  $180^\circ$  at the interface if  $n_2 > n_1$ . This is important in thin film design as discussed later.

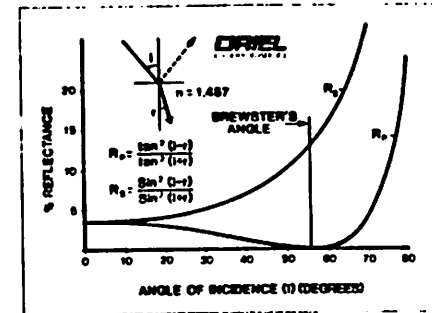


Fig. 2 Reflectance vs. Angle of Incidence for two polarization states.

From (4) you can see that the Fresnel loss becomes high for high index difference,  $n_2 - n_1$ . For a single air-zinc selenide ( $n_2 = 2.4$ ) interface,  $R = 0.17$ .

Interface losses from sequential flat surfaces can be reduced by index matching. Water and many other liquids have refractive indices of about 1.3. If you fill the space between two plane glass surfaces with water you reduce the total Fresnel loss from the two surfaces from 0.08 to 0.01. Index matching fluids are used in some assemblies, but interface loss reduction using thin film optical coatings is usually more practical.

ORIEL FILTERS

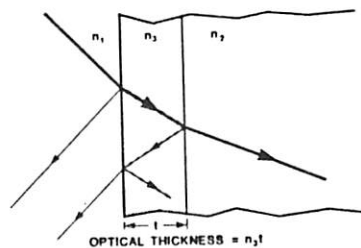
## FILTER THIN FILMS AND COATINGS

### THIN FILMS AND INTERFERENCE

Fig. 3 shows monochromatic light incident on a surface coated with a thin film with index of refraction  $n_2$  and physical thickness  $l$ . Some light is reflected from each surface. You might expect that the total loss is the sum of the Fresnel losses from each surface. However, if  $l$  is small, that is the film is thin, interference takes place between the light reflected from each surface. The light reflected from the "combined surfaces" can in fact be more than or much less than you would expect from the simple Fresnel calculation.

First consider the case where  $n_1 < n_2 < n_3$ , and near normal incidence for simplicity. If the film optical thickness,  $n_2 l$ , is equal to a quarter of the wavelength of the light, then the light reflected from the second interface is completely out of phase with the light reflected from the first. (Remember the phase change mentioned on the previous page.) The two reflected beams interfere destructively to reduce the total reflection. The film is said to be a **quarter wave thick** and acts as an **anti-reflection coating**.

If  $n_1 < n_2 > n_3$ , the double phase change leads to constructive interference between the two reflected beams. The total reflectance is increased, and the thin film makes the surface a **partial reflector**.



3 Thin film coating with an index of refraction  $n_2$  and thickness  $l$ .

### Example

If light travelling through air ( $n_1 = 1$ ) at 550 nm strikes a glass surface ( $n_2 = 1.52$ ) at normal incidence, then about 4% is reflected. If we deposit a layer of magnesium fluoride, ( $n_2 = 1.38$ ) and the layer optical thickness is  $1/4$  wave at 550 nm, the reflectance drops to 1.3%.

If on the other hand, a quarter wave layer of ZnS, ( $n_2 = 2.32$ ) is deposited, the reflectance changes to 31.3%.

### Wavelength Dependence

The reflectance of the coated interface depends on wavelength since the interference effect depends on the wavelength. The film is not exactly a quarter wave thick for any wavelength except the design wavelength. Fig. 4 shows the approximate reflectance against wavelength for the coatings described in the example. Both of these surfaces are simple **interference filters**; their reflectance, and therefore transmittance, depends on wavelength in a manner determined by optical interference.

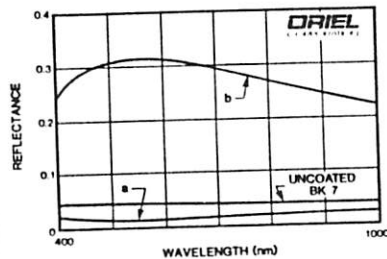


Fig. 4 Reflectance at normal incidence for a glass substrate coated with a quarter wave (@ 550 nm) layer of MgF<sub>2</sub> (a) and ZnS (b).

### Example

If light travelling through air ( $n_1 = 1$ ) at 550 nm strikes a glass surface ( $n_2 = 1.52$ ) at normal incidence, then about 4% is reflected. If we deposit a layer of magnesium fluoride, ( $n_2 = 1.38$ ) and the layer optical thickness is  $1/4$  wave at 550 nm, the reflectance drops to 1.3%.

If on the other hand, a quarter wave layer of ZnS, ( $n_2 = 2.32$ ) is deposited, the reflectance changes to 31.3%.

We describe optical coatings in more detail and list reflective and anti-reflective coatings on pages 10-2 to 10-9.

## FILTER CAVITIES AND TYPES

### FABRY-PEROT ETALON AND FILTER

Interference filters use the basic principles described on the previous page, combining Fresnel reflections and interference in thin layers for strongly wavelength dependent transmittance. It is helpful to understand the filter construction in terms of Fabry-Perot etalons or **cavities**. Fig. 5 shows the basic Fabry-Perot cavity. A thin, accurately parallel, transparent dielectric slice has reflective layers applied to each surface. The dielectric could be air, glass, or one of the thin film dielectrics used for optical coatings.

Internally, there are multiple reflections from the partially reflecting mirror surfaces. When broadband light is incident on the Fabry Perot cavity, constructive and destructive interference leads to transmittance of bands of light with center wavelengths where the cavity optical thickness is  $1/2$  an optical wave thick.

$$nt = k\lambda/2 \dots \dots (5)$$

Where:  
 $nt$  = Optical thickness of the cavity  
 $\lambda$  = Wavelength  
 $k$  = Any integer

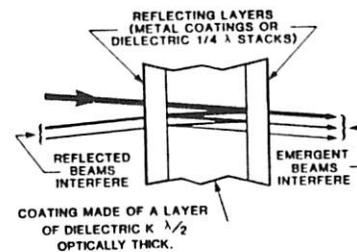


Fig. 5 Single Fabry Perot Cavity.

Multi-layer thin film coatings are used to give better control over the bandshape. The location of the pass bands  $\lambda_1$ ,  $\lambda_2$  and  $\lambda_3$ , etc., depend on the cavity optical thickness.

If the filter is to pass  $\lambda_1$ , and the cavity is made only one half wave thick, (i.e.  $nt = \lambda_1/2$ ) only wavelengths shorter than  $\lambda_1$  can satisfy (5). Wavebands centered around  $\lambda_1/2$  and  $\lambda_1/3$  also pass through. If the cavity thickness is greater than a single half wave, say  $3\lambda_1$ , then longer wavelengths such as  $3\lambda_1$  and  $6\lambda_1$  pass through.

Since most filters are for isolation of a single pass band, the unwanted pass bands must be blocked. Absorbance by the materials of the cavity and partial reflectors often blocks short wavelengths. Absorbing filter glasses may also be used for effective blocking.

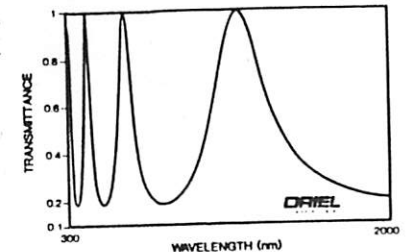


Fig. 6 Transmittance of Ideal Fabry Perot Cavity.

### WHY DO WE KEEP SAYING "THIN"?

We repeatedly use the word "thin" to describe the layers of dielectric. This is because the operation of most of these devices is based on interference. When the light is reflected from the back surface to interfere with light incident on the front surface, there must be a phase relationship between the reflected light and the incoming light, or there will be no interference. Light from any source has a characteristic **coherence length**. If we "look at two points along a light ray" from the source, separated by less than this length, then there is a phase relationship between them. If the points are separated by more than this length there is no phase relationship. This means that the layers we describe must have an optical thickness ( $nt$ ) less than the source coherence length. White light has a coherence length of about  $1 \mu\text{m}$ , so the films must be thinner than this. Light from monochromatic sources (often lasers) has much longer coherence lengths and in principle you could construct "thick thin films". In practice, with these sources interference effects from use of normal optics such as lenses or windows leads to significant, unwanted variations in reflectance.

### TYPES OF FILTERS

#### Multi-cavity Filters

In a Fabry-Perot of given spacing, the bandwidth decreases with increasing reflectance of the reflecting stacks. The reflectance in turn depends on the number of layers in the stack. The result is that the bandwidth is approximately a logarithmic function of the number of layers in the reflector stacks.

Using several Fabry-Perot cavities (i.e. reflector-spacer-reflector) in a single filter adds versatility in bandshaping and allows a better combination of transmittance at the wavelength of interest with improved rejection of other wavelengths.

This type of filter is known as a multi-cavity filter. (Fig. 7 on the following page shows the construction of a multi-cavity filter.) A typical 3 cavity 10 nm bandwidth filter in the mid-visible has approximately 50 individual thin film layers. Multi-cavity filters have characteristic square tops with steeper sides than the simple Fabry-Perot.

Multi-cavity filters still require additional blocking to suppress unwanted harmonics.

## FILTER TYPES AND CHARACTERISTICS

### Induced Transmission Filters

Induced transmission filters use dielectric layers on each side of the metal layers. The metal layer transmittance at the filter wavelength is increased dramatically by the dielectric layers. These filters, which have excellent blocking of long wavelengths, are particularly useful in the ultraviolet.

These filters are sometimes bonded to sharp cut-on colored glass (to absorb the shorter wavelength harmonics), and used as completely blocking broadband filters.

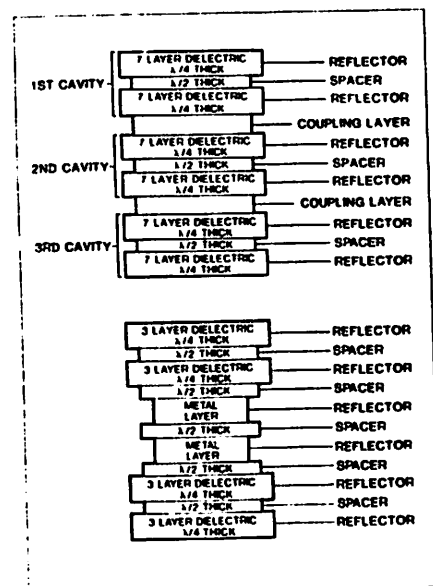


Fig. 7 Construction of Multi-cavity Filter (top) and Induced Transmission Filter (bottom).

### The Finished Filter

A finished filter should have:

- an accurate central wavelength
- good peak transmission
- good band shape
- good rejection on both sides of the pass band

For these, it is necessary to add additional filter devices to an all dielectric filter. The simplest is a colored glass filter. Sometimes, an induced transmission filter is also appropriate. The result is a combination of an all dielectric filter and dielectric/metal filter, and all dielectric and colored glass filter.

In a finished filter, the transmission is the product of the transmissions of each constituent filter component. Table 1 indicates the transmission at the central wavelength and at two wavelengths outside the pass band.

Table 1: Transmittance of a Finished Interference Filter Designed for 550 nm

Wave-length (nm)	All Dielectric Filter	Induced Trans. Filter	Colored Glass Filter	Finished Filter
450	0.05	0.20	0.001	0.00001
550	0.90	0.70	0.92	0.58
700	0.01	0.01	0.92	0.00092

The actual transmission can be up to 10% higher than the values indicated because cementing of the constituent filters with an index matching cement eliminates the reflection losses from some surfaces.

In a finished filter, consisting of an all dielectric filter, an induced transmission filter and a colored glass filter, it is the all dielectric filter which controls the band shape and central wavelength.

### FILTER CHARACTERISTICS

#### Band Shape

As the number of cavities in the all dielectric filter increases, the shape of the band improves, i.e. the transition from maximum transmission to rejection becomes sharper.

Fig. 8 shows the shape of the pass band as a function of the number of cavities.

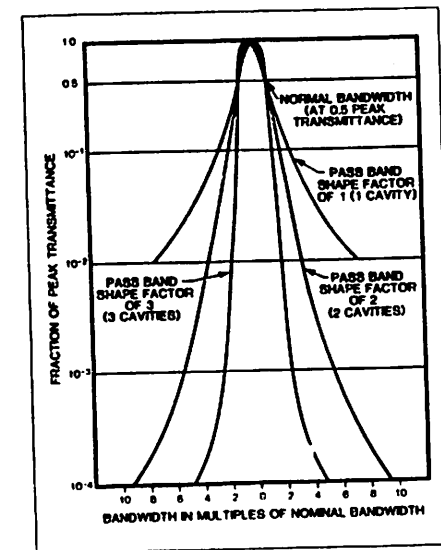


Fig. 8 The shape of the band pass of 1, 2, and 3 cavity filters.

### Environmental Factors

#### Temperature

All Oriol Band Pass Interference Filters are designed to operate from -50 °C to +80 °C; they may be operated intermittently to 100 °C. The rate of temperature change should not exceed 10 °C/minute. At 120 °C or above, permanent changes and possible destruction can occur.

Apart from irreversible changes at high temperatures, the most noticeable temperature effect is the variation of central wavelength. At increased temperature the central wavelength increases. This wavelength change is almost linear between -60 °C and +60 °C with values between 0.01 and 0.03 nm/°C; above 120 °C the change in central wavelength may be irreversible. There are also very slight changes in bandwidth (about 0.001 nm/°C) and peak transmittance (about 0.01%/°C) with increasing temperature.

#### Humidity

All Oriol ultraviolet, visible and near infrared Band Pass Interference Filters are edge sealed as a barrier to environmental moisture. We test our filters to MIL-STD-810C method 507, procedure 1. This test consists of placing the filter in an environmental test chamber and cycling the temperature and humidity over a 24 hour period. Each 24 hour time period is termed a cycle, and the number of cycles tested to is specified for each filter type. After the completion of the test, the filter is inspected for spectral performance and physical damage.

Other Oriol multi-layer filter products such as long and short pass filters comply with the slightly less stringent MIL-C-675A (para. 4, 6 and 9) Temperature and Humidity Specification. This test consists of placing the test sample in an environmental chamber for 24 hours at 95% relative humidity and at 50 °C. Then the filter is inspected for spectral performance and physical damage.

Some infrared interference filters have extremely hard and durable coatings. These coatings are unaffected by ambient humidity and are left exposed to the atmosphere. These coatings also meet the requirements of MIL-STD-810C method 507, procedure 1.

### Filter Orientation

Most band pass interference filters are constructed using some type of auxiliary absorptive blocking filters. Each side of the filter has a distinctively different appearance. One side will be highly mirrored while the other side will be colored (opaque or anywhere from deep violet to deep red).

Always orient the band pass filter so the highly mirrored side is facing the source of radiation. Most of the rejected radiation is reflected and does not heat the internal components of the filter.

### Angle of Incidence

Filter specifications are usually given for collimated radiation incident normal to the filter surface. In many applications, collimated, normal incidence radiation is not practical or even possible. You can, however, estimate the results of using off-normal incident radiation.

Band pass interference filters are composed of a series of layers of precisely controlled thicknesses of dielectrics and metals. Changing the angle of incidence increases the apparent thickness of these layers. However, the phase difference between the interfering waves decreases as angle increases. The effects of off-normal radiation are three fold: there is a decrease in the central wavelength; the transmittance decreases and the bandwidth increases; for off-normal angles less than 25°, the effect on transmittance and bandwidth are minimal. The shift in central wavelength with angle of incidence can be used to precisely "tune" a narrow band filter.

The decrease in central wavelength is a function of the refractive indices of the deposited films and the angle of incidence. The effective refractive index,  $n^*$ , of the filter, is used to simplify the relational formula. For collimated radiation incident at angle  $\theta$ , where  $\theta < 25^\circ$ :

$$\lambda_c = \lambda_0 [1 - (n^*/n^0)^2 \sin^2 \theta] \dots \dots \dots (16)$$

Where:

- $\lambda_c$  = Central wavelength at angle of incidence  $\theta$
- $\lambda_0$  = Central wavelength at normal incidence ( $\theta = 0$ )
- $n_0$  = Refractive index of the medium surrounding the filter
- $n^*$  = Effective refractive index for the filter

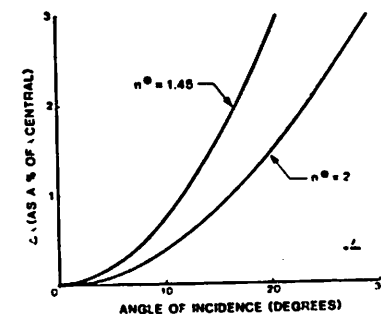


Fig. 9 Approximate wavelength shift with angle of incidence for the  $n^*$  values of our interference filters.

F. FILTERS

## FILTER CHARACTERISTICS

For typical visible and near infrared band pass interference filters (400 - 1100 nm) the experimental values of  $n^*$  have been found to be 2.0 for high index spacer layers, and 1.45 for low index spacer layers.

When the angle of incidence is large,  $> 30^\circ$ , the spectral pass band characteristics of the filter can be so degraded as to yield two distinct peaks and transmittance becomes dependent on polarization.

Table 3 lists multiplying factors for off-normal collimated incident radiation. To find the new central wavelength at an off-normal angle, simply multiply the wavelength at normal incidence by the appropriate factor for that angle.

Table 3: Multiplying Factors for Off-normal Collimated Light

Angle (degrees)	High Index Spacer Layer ( $n^* = 2$ )	Low Index Spacer Layer ( $n^* = 1.45$ )
0.25	1.0	1.0
0.5	1.0	1.0
1.0	1.0	0.9999
2.0	0.9999	0.9997
3.0	0.9997	0.9994
4.0	0.9994	0.9998
5.0	0.9991	0.9982
7.5	0.9979	0.9959
10.0	0.9962	0.9928
15.0	0.9916	0.9839
20.0	0.9853	0.9718
25.0	0.9774	0.9566
30.0	0.9683	0.9387

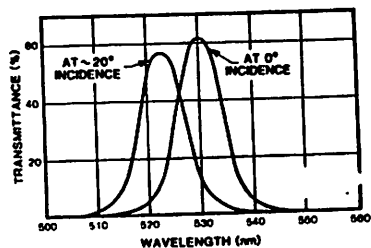


Fig. 10 530 nm center wavelength filter at normal incidence and at  $20^\circ$ .

### Divergent or Convergent Incident Radiation

A diverging or converging beam incident on a filter means a spread of incident angles. The result is a broadening of the apparent band pass and a shift to lower wavelengths. Since the transmittance is angle dependent, the beam which passes the filter will have a slight angular wavelength dependence.

The change in center wavelength can be obtained by using the HALF cone angle in equation (6).

$$\lambda_\theta = \lambda_0 [1 - (n_0 / n^*)^2 \sin^2 \theta]^{1/2} \dots (6)$$

Where:

- $\lambda_\theta$  = Central wavelength at angle of incidence  $\theta$
- $\lambda_0$  = Central wavelength at normal incidence ( $\theta = 0$ )
- $n_0$  = Refractive index of the medium surrounding the filter
- $n^*$  = Effective refractive index for the filter

For solid cone angles to  $20^\circ$ , the change will be about half of that calculated. Band pass interference filters with bandwidths of less than 3.0 nm have negligible center wavelength changes with convergent or divergent beams with up to  $5^\circ$  full cone angle (F/11).

## FILTERS AND MONOCHROMATORS

### A Monochromator or an Interference Filter?

For maximum throughput efficiency with a monochromator, the F/# of the input optics must match that of the monochromator. This puts a fundamental limit on the demagnification of a source to try to get as much light as possible through the slit. An interference filter, on the other hand, has a large acceptance aperture and can have transmission in the range of 50 - 60%. With extended (large) sources an interference filter can have up to 500 times greater throughput than a monochromator.

See our Volume II for an in-depth discussion.

### A Monochromator Used With an Interference Filter

Interference filters are effective in reducing the stray light accompanying the output from a fixed wavelength grating monochromator. If a high intensity continuous source is used, the filter should be placed between the exit slit and the detector to reduce the thermal load on the filter.

## INTERFERENCE FILTERS : BLOCKING

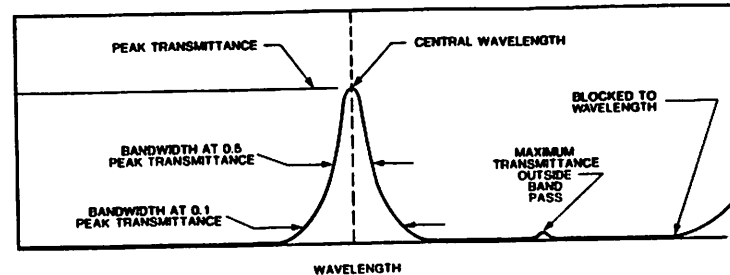


Fig. 11 Typical Interference Filter.

### INTERFERENCE FILTER TRANSMISSION/REJECTION

With an interference filter it is very common to think of the ratio of peak transmission to blocking as a system signal to noise ratio. This assumption can lead to very serious errors. In order to obtain a true system signal to noise ratio the spectral power distribution of the source and response of the detector must be considered as well as the peak transmission, bandwidth, band shape and blocking of the interference filter.

For example, consider the use of an interference filter with a central wavelength of 400 nm, a bandwidth of 10 nm, a peak transmission of 40% and blocking of 0.01% from X-ray to the far infrared in a system which has a tungsten light source and a silicon photodetector. With a typical tungsten source the intensity in the 1000 nm region can be up to 100 times that at 400 nm. Additionally, the silicon photodetector can have 3 - 5 times as much response in the 800 - 1000 nm region as at 400 nm. If the combination of interference filter, light source and detector described above were to be used in a 400 nm absorbance photometer, the result would probably be misleading.

To obtain a good indication of the real signal to noise ratio in such a system, make a signal measurement with the 400 nm interference filter, light source and detector in place. Then place a sharp cut-on colored glass filter (such as Ortel Model 51484) in series with the interference filter and take a measurement. The colored glass filter will absorb the signal at 400 nm leaving most of the "noise" component.

A simple way to improve a system signal to noise ratio is to use two filters in series. The second filter could be a colored glass to eliminate most of the visible and near infrared, or the same type of interference filter.

A near worst case measurement with 53810 Filters (10 nm bandpass at 420 nm), a tungsten halogen source (3200 K) and a silicon detector gave the results below. A 470 nm long pass filter was used to block all the light coming through the filter bandpass to record the leakage signal.

	Relative Signals	
	Single Filter	Two Filters
250 - 1100 <sup>1</sup> nm	100	47.5
Leakage Signal above 480 nm	$3 \times 10^3$	$< 1 \times 10^3$

<sup>1</sup> Most of this signal is in the 400 - 440 nm transmitting region of the filter.

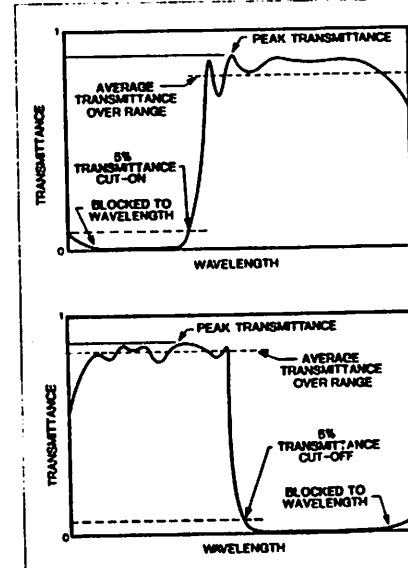
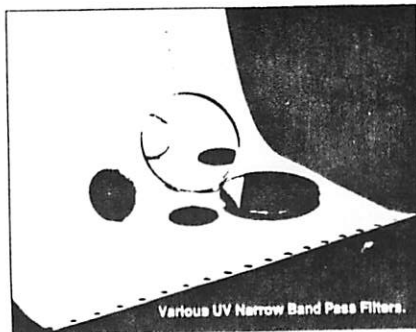


Fig. 12 Typical Long Pass (top) and Short Pass (bottom) filters.

53810 FILTERS

## ULTRAVIOLET INTERFERENCE FILTERS



Various UV Narrow Band Pass Filters.

- Standard wavelength filters available individually or in sets
- Transmittance curves supplied with each filter
- 1 and 2 inch diameter sizes offered

These filters are used to isolate a narrow ultraviolet spectral region while blocking out of band wavelengths from the low UV to the far IR; blocking is better than 0.01%. The filters listed here are available with center wavelengths from 200 nm to 390 nm.

For Laser Line UV Filters see page 2-37; for Analytical Line Filters see page 2-38; for VIS - NIR Interference Filters see page 2-35.

Single and multiple filter holders are listed on pages 2-48 to 2-49.

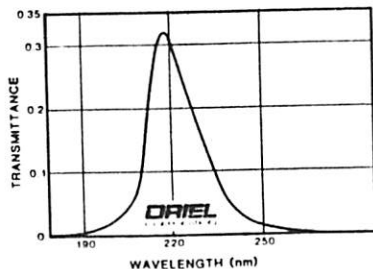


Fig. 1 Transmittance curve of 53320-58560 UV Filters.

### SPECIFICATIONS

Size tolerance:	+ 0 mm; - 0.8 mm
Thickness:	9.5 mm, max
Surface quality:	80 - 50
Useful aperture:	All but a 1.6 mm outer rim
Center wavelength tolerance:	
200 - 240 nm:	± 3.5 nm
250 - 390 nm:	± 2.0 nm
Bandwidth:	
200 - 240 nm:	25 nm
250 - 390 nm:	10 nm
Bandwidth tolerance:	
200 - 240 nm:	± 4.0 nm
250 - 390 nm:	± 2.0 nm
Band shape, # of cavities <sup>†</sup> :	
200 - 340 nm:	2
350 - 390 nm:	3
Wavelength shift factor (n <sup>††</sup> ):	See table
Blocking <sup>†††</sup> :	0.01%
Blocking range:	X-ray to far IR
Max. temperature:	80 °C
Environmental:	Per MIL-STD 810C (method 507, procedure 1) 5 cycles

- <sup>†</sup> See page 2-30 for information on band shape.  
<sup>††</sup> See page 2-31 for discussion on calculating the wavelength shift.  
<sup>†††</sup> See page 2-33 for information on blocking.

### ORDERING INFORMATION

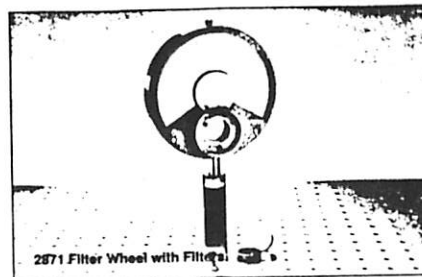
Center Wavelength (nm)	Min. Peak Trans. (%)	Effic. Index (n <sup>†</sup> )	1 Inch (25.4 mm) Diameter		2 Inch (50.8 mm) Diameter	
			Model No.	Price (\$)	Model No.	Price (\$)
200	10	1.72	53310	\$ 235.00	58550	\$ 355.00
220	15	1.72	53320	\$ 235.00	58560	\$ 355.00
240	15	1.72	53330	\$ 235.00	59570	\$ 355.00
250	10	1.90	53340	\$ 235.00	59580	\$ 355.00
260	15	1.90	53350	\$ 235.00	59590	\$ 355.00
270	15	1.90	53355	\$ 235.00	59595	\$ 355.00
280	15	1.90	53360	\$ 235.00	58600	\$ 355.00
290	15	1.90	53365	\$ 235.00	58605	\$ 355.00
300	15	1.90	53370	\$ 235.00	59610	\$ 355.00
310	15	1.90	53375	\$ 235.00	59615	\$ 355.00
320	20	1.90	53380	\$ 235.00	59620	\$ 355.00
330	20	1.57	53385	\$ 235.00	59625	\$ 355.00
340	20	1.57	53390	\$ 235.00	58630	\$ 355.00
350	20	1.57	53400	\$ 235.00	59640	\$ 355.00
360	20	1.57	53410	\$ 235.00	58650	\$ 355.00
370	20	1.57	53415	\$ 235.00	59655	\$ 355.00
380	20	1.57	53420	\$ 235.00	58660	\$ 355.00
390	20	2.00	53425	\$ 235.00	59665	\$ 355.00

### Filter Sets

Each filter set includes a hard shell protective case.

Set Description	1 Inch (25.4 mm) Diameter		2 Inch (50.8 mm) Diameter	
	Model No.	Price (\$)	Model No.	Price (\$)
4 filters, every 50 nm from 200 nm through 350 nm	53280	\$ 940.00	58500	\$ 1420.00
10 filters, every 20 nm from 200 nm through 380 nm	53250	\$ 2350.00	58470	\$ 3550.00
All 18 filters listed above	53255	\$ 4230.00	59477	\$ 6390.00

## VIS-NIR INTERFERENCE FILTERS



2871 Filter Wheel with Filter Holder

- 10 nm bandwidths
- High transmittance at center wavelength
- Center wavelengths from 400 to 1550 nm

These interference filters pass a very narrow spectral band of visible or near infrared radiation and reject out of band wavelengths from the low UV to the far IR.

The bandwidth is 10 nm, and transmittance is 50% minimum for most filters.

Several filters in a filter wheel allow wavelength selection with, in many cases, higher throughput than available from a monochromator. Filters in series give even higher blocking.

See pages 2-48 to 2-49 for filter holders and 2-50 for filter wheels.

### ORDERING INFORMATION

Center Wavelength (nm)	Min. Peak Trans. (%)	Effic. Index (n <sup>†</sup> )	1 Inch (25.4 mm) Diameter		2 Inch (50.8 mm) Diameter	
			Model No.	Price (\$)	Model No.	Price (\$)
400	35	1.45	53800	\$ 72.00	59280	\$ 118.00
410	35	1.45	53805	\$ 72.00	59285	\$ 118.00
420	35	1.45	53810	\$ 72.00	59290	\$ 118.00
430	40	1.45	53815	\$ 72.00	59295	\$ 118.00
440	40	1.45	53820	\$ 72.00	54301	\$ 118.00
450	45	2.0	53830	\$ 72.00	54311	\$ 118.00
460	45	2.0	53840	\$ 72.00	54321	\$ 118.00
470	45	2.0	53845	\$ 72.00	59325	\$ 118.00
480	45	2.0	53850	\$ 72.00	54331	\$ 118.00
490	50	2.0	53855	\$ 72.00	59335	\$ 118.00
500	50	2.0	53860	\$ 72.00	54341	\$ 118.00
510	50	2.0	53865	\$ 72.00	59345	\$ 118.00
520	50	2.0	53870	\$ 72.00	54351	\$ 118.00
530	50	2.0	53875	\$ 72.00	59355	\$ 118.00
540	50	2.0	53880	\$ 72.00	54361	\$ 118.00
550	50	2.0	53890	\$ 72.00	54371	\$ 118.00
560	50	2.0	53900	\$ 72.00	54381	\$ 118.00
570	50	2.0	53905	\$ 72.00	59385	\$ 118.00
580	50	2.0	53910	\$ 72.00	59390	\$ 118.00
590	50	2.0	53915	\$ 72.00	59395	\$ 118.00
600	50	2.0	53920	\$ 72.00	54401	\$ 118.00
610	50	2.0	53925	\$ 72.00	59405	\$ 118.00
620	50	2.0	53930	\$ 72.00	59410	\$ 118.00
630	50	2.0	53935	\$ 72.00	59415	\$ 118.00
640	50	2.0	53940	\$ 72.00	59420	\$ 118.00
650	50	2.0	53950	\$ 72.00	59430	\$ 118.00
660	50	2.0	53960	\$ 72.00	59440	\$ 118.00
670	50	2.0	53965	\$ 72.00	59445	\$ 118.00

### SPECIFICATIONS

Size tolerance:	+ 0 mm; - 0.8 mm
Thickness:	6.4 mm, max.
Surface quality:	80 - 50
Useful aperture:	All but a 1.6 mm outer rim
Center wavelength tolerance:	± 2.0 nm
Bandwidth:	10 nm
Bandwidth tolerance:	± 2.5 nm
Band shape, # of cavities <sup>†</sup> :	3
Wavelength shift factor (n <sup>††</sup> ):	See table
Blocking <sup>†††</sup> :	0.01%
Blocking range:	X-ray to far IR
Max. temperature:	80 °C
Environmental:	Per MIL-STD-810C (method 507, procedure 1) 5 cycles

- <sup>†</sup> See page 2-30 for information on band shape.  
<sup>††</sup> See page 2-31 for discussion on calculating wavelength shift.  
<sup>†††</sup> See page 2-33 for details on blocking.

### FILTER SETS

Set Description	1 Inch (25.4 mm) Diameter		2 Inch (50.8 mm) Diameter	
	Model No.	Price (\$)	Model No.	Price (\$)
7 filters, every 50 nm from 400 nm to 700 nm	53760	\$ 495.00	59250	\$ 798.00
16 filters, every 20 nm from 400 nm to 700 nm	53700	\$ 998.00	54161	\$ 1759.00
10 filters, every 50 nm from 750 nm to 1200 nm	53730	\$ 925.00	54201	\$ 1989.00

Center Wavelength (nm)	Min. Peak Trans. (%)	Effic. Index (n <sup>†</sup> )	1 Inch (25.4 mm) Diameter		2 Inch (50.8 mm) Diameter	
			Model No.	Price (\$)	Model No.	Price (\$)
680	50	2.0	53970	\$ 72.00	58450	\$ 118.00
690	50	2.0	53975	\$ 72.00	59455	\$ 118.00
700	50	2.0	53980	\$ 72.00	58460	\$ 118.00
725	50	2.0	53985	\$ 72.00	59465	\$ 118.00
750	50	2.0	53990	\$ 72.00	54471	\$ 118.00
775	50	2.0	53995	\$ 72.00	59475	\$ 195.00
780	50	2.0	53996	\$ 72.00	59476	\$ 195.00
800	50	2.0	54000	\$ 90.00	58480	\$ 195.00
820	50	2.0	54001	\$ 90.00	59481	\$ 195.00
825	50	2.0	54005	\$ 90.00	59485	\$ 118.00
830	50	2.0	54006	\$ 90.00	59486	\$ 195.00
850	50	2.0	54010	\$ 90.00	58490	\$ 118.00
875	50	2.0	54015	\$ 90.00	59495	\$ 195.00
900	50	2.0	54020	\$ 90.00	54501	\$ 195.00
925	50	2.0	54025	\$ 90.00	59505	\$ 195.00
950	50	2.0	54030	\$ 90.00	58510	\$ 195.00
975	50	2.0	54035	\$ 90.00	59515	\$ 195.00
1000	50	2.0	54040	\$ 90.00	58520	\$ 195.00
1025	50	2.0	54045	\$ 90.00	59525	\$ 195.00
1050	50	2.0	54050	\$ 90.00	58530	\$ 195.00
1075	50	2.0	54055	\$ 90.00	59535	\$ 195.00
1100	50	2.0	54060	\$ 90.00	58540	\$ 195.00
1125	50	2.0	54065	\$ 90.00	58545	\$ 195.00
1150	50	2.0	54070	\$ 90.00	54551	\$ 195.00
1175	50	2.0	54075	\$ 145.00	59555	\$ 195.00
1200	50	2.0	54080	\$ 145.00	54561	\$ 195.00
1300	50	2.0	54081	\$ 145.00	54562	\$ 195.00
1550	50	2.0	54085	\$ 145.00	54565	\$ 195.00



## VIS - NIR LONG AND SHORT PASS FILTERS



Long/Short Pass Filters in 12805 Multiple Filter Holder.

- Visible to near infrared models
- Allow separation of spectral bands
- Excellent monochromator order sorting filters
- High transmittance

Long pass filters transmit (or pass) a wide spectral band of long wavelength radiation while blocking short wavelength radiation. Short pass filters transmit a wide spectral band of short wavelength radiation and block long wave radiation.

Both types are characterized by an extremely sharp transition from the region of maximum transmittance to maximum rejection. See Figs. 1 and 2 for typical curves and definition of parameters.

You can make your own bandpass filter by stacking a long pass and short pass filter. The transmittance of the two filters at any wavelength will be the product of the transmittance of the individual filters at that wavelength.

### REFLECTION AND ABSORPTION

The filters are a combination of absorbing glass and interference thin films. Part of the rejected spectrum is reflected back towards the source and part is attenuated. We tabulate the spectral region blocked by reflection. Filters can handle higher power densities (up to 100 W cm<sup>2</sup>) if the blocked radiation is reflected rather than absorbed.

### TUNING A FILTER

The transmittance of these filters moves to shorter wavelengths when they are tilted so you can purposely shift the cut-on. The change in wavelength can be predicted by using the n<sup>2</sup> factor and the angle shift calculation on page 2-31. For example, tilting the 57889 Long Pass Filter 15 degrees, the recommended maximum, moves the cut-on from 650 nm to 641 nm.

See pages 2-48 to 2-49 for filter holders.

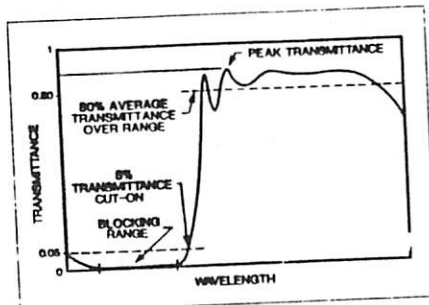


Fig. 1 Typical Long Pass Filter.

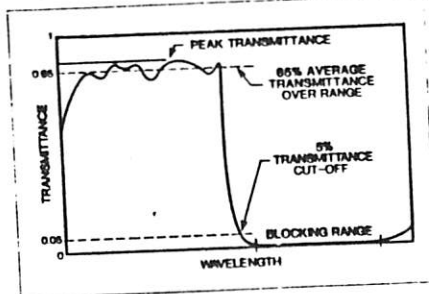


Fig. 2 Typical Short Pass Filter.

### SPECIFICATIONS

Size tolerance:	+ 0 mm; - 0.8 mm
Thickness:	3.0 - 5.0 mm
Surface quality:	80 - 50
Useful aperture:	All but a 1.6 mm outer rim
Wavelength shift factor (n <sup>2</sup> ):	
Long Pass Filters:	1.58
Short Pass Filters:	1.63
Blocking <sup>†</sup> :	0.1%
Slope <sup>††</sup> :	≤ 3%
Max. temperature:	80 °C
Environmental:	Per MIL-STD-81C (method 507, procedure 1) 5 cycles

<sup>†</sup> See page 2-31 for calculation of angle shift.

<sup>††</sup> See page 2-33 for information on blocking.

<sup>†††</sup> Slope is defined as:

$$\% \text{ Slope} = \frac{\lambda (80\% \text{ of Peak}) - \lambda_c}{\lambda_c} \times 100$$

Where:

$\lambda_c$  = Cut-on or cut-off wavelength at 5% of peak transmittance

## IR LONG AND SHORT PASS FILTERS

- Sharp cut-on or cut-off
- Wide bandpass
- Excellent transmittance

These filters are excellent for isolating a wide spectral band in the infrared; they have low absorption so they can withstand incident high power density.

Like the filters on the previous page, they are characterized by a sharp transition between transmittance and blocking. See Figs. 1 and 2 for typical curve shapes and terminology.

You can combine a short and long pass filter to make a custom band pass filter with a "top hat" transmittance profile. The transmittance of the combination at any wavelength will be the product of the transmittances of the individual filters at that wavelength.

### SPECIFICATIONS

Size:	1 inch (25.4 mm) diameter
Size tolerance:	+ 0 mm; - 0.5 mm
Thickness:	3 mm. max.
Surface quality:	80 - 50
Useful aperture:	All but a 1.6 mm outer rim
Transmittance:	
Long Pass Filters:	> 75% avg.
Short Pass Filters:	> 60% avg.
Blocking <sup>†</sup> :	0.1%
Blocking range:	See table
Slope <sup>††</sup> :	0.03 mm
Temperature:	80 °C. max. continuous
Environmental:	MIL-STD-810C (method 507, procedure 1) 7 cycles

<sup>†</sup> See page 2-33 for information on blocking.

<sup>††</sup> Slope is defined as:

$$\% \text{ Slope} = \frac{\lambda (80\% \text{ of Peak}) - \lambda_c}{\lambda_c} \times 100$$

Where:

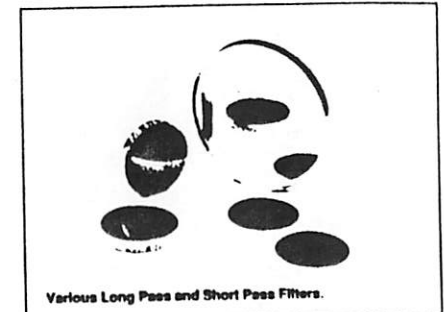
$\lambda_c$  = Cut-on or cut-off wavelength at 5% transmittance

### ORDERING INFORMATION

Cut-on Wavelength <sup>†</sup> (μm)	Tolerance (± nm)	Transmittance To (μm)	Blocking Range	Model No.	Price (\$)
<b>Long Pass Filters</b>					
1.6	30	2.5	X-ray - 1.45 μm	57910	\$ 447.00
2.5	100	5.0	X-ray - 2.10 μm	57925	\$ 447.00
3.5	150	7.0	X-ray - 3.20 μm	57935	\$ 585.00
5.25	150	7.5	X-ray - 4.9 μm	57940	\$ 835.00
8.0	150	14.0	X-ray - 7.7 μm	57955	\$ 932.00
10.0	300	20.0	X-ray - 9.8 μm	57965	\$ 1450.00

Cut-off Wavelength <sup>†</sup> (μm)	Tolerance (± nm)	Transmittance From (μm)	Blocking Range	Model No.	Price (\$)
<b>Short Pass Filters</b>					
2.0	30	1.15	2.15 μm - Far IR	57980	\$ 357.00
3.0	100	1.7	3.25 μm - Far IR	57990	\$ 357.00
4.1	150	2.1	3.80 μm - Far IR	57995	\$ 357.00
6.0	200	3.0	6.40 μm - Far IR	58020	\$ 357.00

<sup>†</sup> Cut on and cut off wavelengths are defined as 5% transmittance. See Figs. 1 and 2.



Various Long Pass and Short Pass Filters.

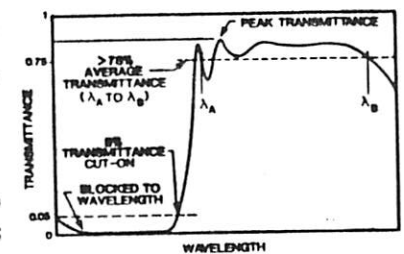


Fig. 1 Typical Long Pass Filter.

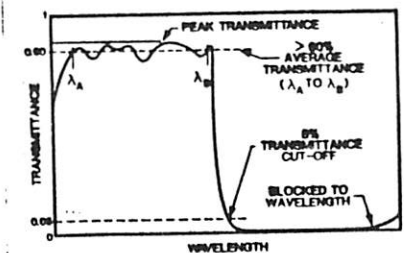
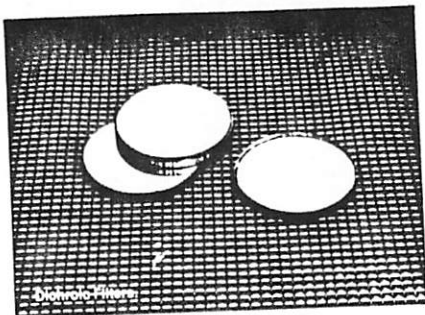


Fig. 2 Typical Short Pass Filter.

## DICHROIC FILTERS



### ULTRAVIOLET REFLECTING LONG PASS FILTERS

- Used at 45° or 0° angle of incidence
- Three spectral ranges available

These UV mirrors are used primarily for UV irradiation. Applications include photolithography, UV curing, material aging studies and photobiology. They have an average of  $\geq 90\%$  reflectance over the specified wavelength range. See Figs. 1 and 2 for curves.

#### SPECIFICATIONS

Size tolerance:	+ 0 mm; - 0.5 mm
Thickness:	6.4 mm, max.
Material:	Optical quality crown glass
Surface quality:	80 - 50
Useful aperture:	All but a 2.6 mm outer rim
Temperature:	80 °C, max. continuous
Environmental:	Per MIL-C-675A
Abrasion:	Per MIL-M-13508C

### HEAT CONTROL FILTERS (HOT AND COLD MIRRORS)

- Thermal borosilicate glass substrates withstand high temperature
- Non-absorbing coating minimizes heat build-up
- May be used in high intensity applications

The following heat control mirrors act as long and short pass filters. They transmit one spectral region and reflect another.

#### 0° Heat Reflecting Filter (Hot Mirror)

Hot mirrors transmit the visible while reflecting much of the infrared. They are typically used at normal (0°) incidence to the source of radiation. In this position, the visible radiation is allowed to pass undeviated while the infrared (heat) is reflected back towards the light source.

When used at 45°, the transmittance/reflectance curve is shifted towards the shorter wavelengths. For higher rejection of infrared, use an infrared absorbing filter (page 2-5) after the hot mirror. The visible transmittance is the product of the visible transmittance of both filters.

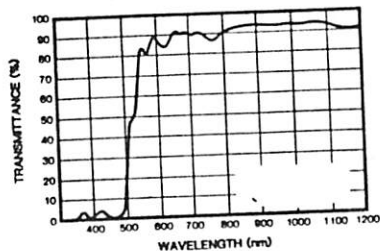


Fig. 1 Typical transmittance of 59451 UV Long Pass Filter. The unwanted radiation above 500 nm is transmitted through the filter while the ultraviolet is efficiently reflected.

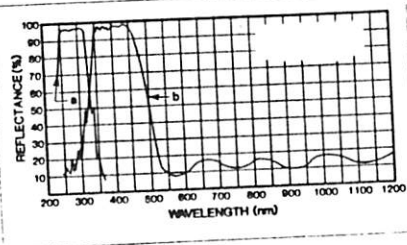


Fig. 2 Reflectance of our 260 - 320 nm (a) UV Reflecting Filters, and 350 - 450 nm (b) UV Reflecting Filters used at 45°. At normal incidence the curves shift to longer wavelength (by - 20 nm) for the UV and 40 nm for the 350 - 450 nm filter.

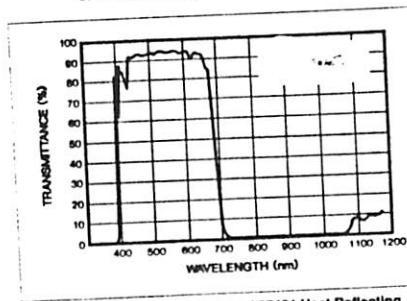


Fig. 3 Typical transmittance of 57401 Heat Reflecting Filter.

### 45° Heat Transmitting Filters (Cold Mirrors)

Cold mirrors are typically used at 45° to a beam of radiation from a source. In this configuration, the infrared is transmitted undeviated, while the visible is reflected at 90°. For many sources this is better than reflecting the infrared back towards the source.

At normal (0°) incidence the reflectance/transmittance curve is shifted towards longer wavelengths. We offer circular and rectangular cold mirrors. The rectangular sizes are large enough for 1.5 inch (38 mm) 2 inch (51 mm) and 3 inch (76 mm) diameter beams incident at 45°.

#### SPECIFICATIONS

Size tolerance:	+ 0 mm; - 0.5 mm
Thickness:	6.4 mm, max.
Substrate material:	Polished thermal borosilicate glass
Surface quality:	80 - 50
Useful aperture:	All but a 2.6 mm outer rim
Max. temperature:	190 °C
Environmental:	Per MIL-C-675A
Abrasion:	Per MIL-M13508C

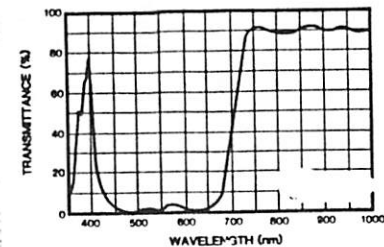


Fig. 4 Typical transmittance of Heat Transmitting Filters.

#### ORDERING INFORMATION

Size In. (mm)	Average Reflectance (%)	Reflectance Range (nm)	Average Transmittance (%)	Transmittance Range (nm)	Model No.	Price (\$)
<b>Ultraviolet Long Pass Filters</b>						
2.0 (50.8)	90	325 - 475	85	600 - 1200	59451	\$ 179.00
1.64 x 2.4 (41.7 x 61.0)	95	260 - 320	85	350 - 1200	66217	\$ 145.00
	95	350 - 450	85	550 - 1200	66218	\$ 125.00
2.2 x 3.0 (55.9 x 76.2)	95	260 - 320	85	350 - 1200	66227	\$ 195.00
	95	350 - 450	85	550 - 1200	66228	\$ 175.00
3.2 x 4.5 (81.3 x 114.3)	95	260 - 320	85	350 - 1200	66237	\$ 288.00
	95	350 - 450	85	550 - 1200	66238	\$ 268.00
<b>Heat Reflecting Filter (Hot Mirror)</b>						
2.0 (50.8)	90	750 - 1200	85	450 - 675	57401	\$ 219.00
<b>Heat Transmitting Filters (Cold Mirrors)</b>						
2.0 (50.8)	90	420 - 630	85	750 - 1200	57431	\$ 219.00
1.64 x 2.4 (41.7 x 61.0)	90	420 - 630	85	750 - 1200	66219	\$ 98.00
2.2 x 3.0 (55.9 x 76.2)	90	420 - 630	85	750 - 1200	66229	\$ 125.00
3.2 x 4.5 (81.3 x 114.3)	90	420 - 630	85	750 - 1200	66239	\$ 198.00

The rectangular models are used at the output of our light source condensers to filter the UV or VIS. See Volume II, page 150 for more information, and holders.

# POLARIZING OPTICS TECHNICAL DISCUSSION

Light travels as transverse electro-magnetic waves. The electric and magnetic fields are perpendicular to the direction of propagation and each other (Fig. 1). Defining the direction of a ray and its electric field specifies the three vector directions: propagation, electric field and magnetic field. Most incoherent light sources consist of a large number of atomic or molecular emitters. The rays emitted from such sources have electric fields with no preferred orientation; these rays are unpolarized.

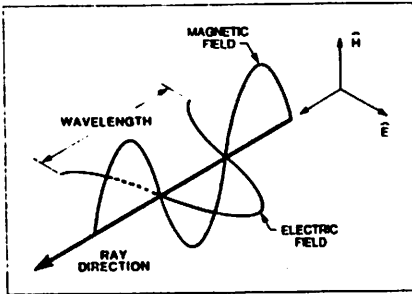


Fig. 1 Electro-magnetic wave.

## LINEARLY POLARIZED LIGHT

The direction of the electric field vector is used to describe the polarization. If a light beam is made up of rays where the electric field vectors are oriented in the same direction, the beam is said to be linearly polarized. If the E field vector (E vector) is vertical, the light is vertically polarized. Fig. 2 shows some symbols used to designate linear polarization.

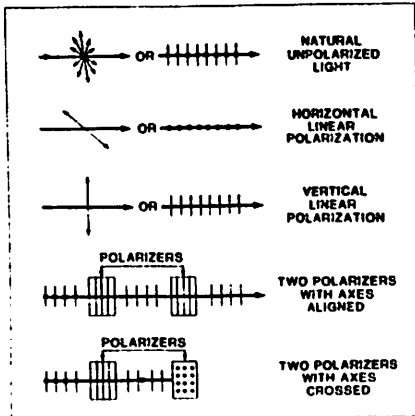


Fig. 2 Polarization Symbols.

## S and P Polarizations

The terms "s" and "p" polarization are convenient when linearly polarized light is incident on an optic. If the direction of polarization is parallel to the plane of incidence the ray is said to be "p" polarized. If the direction of polarization is perpendicular to the plane of incidence, the ray is "s" polarized. (The plane of incidence is the plane containing the ray, and the normal to the surface.)

## Using vector resolution simplifies analysis

The polarization direction of a plane polarized light beam may not be parallel to the "X" or "Y" axes of an optical system. Analysis of what happens to a light beam, polarized or unpolarized, in going through an optical system is simplified if the beam is broken into two components, one polarized along each axis. The system modifies the amplitude and phase of each component beam and the emergent "beams" are then recombined to give the intensity and polarization state of the output beam.

Any ray that is linearly polarized can be resolved into its components polarized along any arbitrary orthogonal axes by normal vector sum rules.

In Fig. 3, ray Z-Z is linearly polarized with the vibration direction making the angle  $\theta$  with the X axis. The length of ray Z-Z represents the amplitude of the electric field. Ray Z-Z can be resolved into two rays: the horizontal polarized component with an amplitude of  $E \cos \theta$ , and the vertical polarized component with an amplitude of  $E \sin \theta$ .

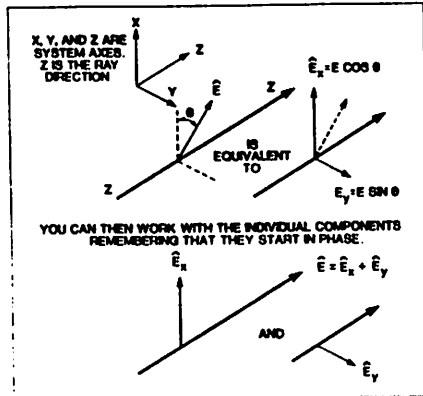


Fig. 3 Resolution of polarized ray into two orthogonally polarized components.

## CIRCULARLY AND ELLIPTICALLY POLARIZED LIGHT

The electric field (E vector) of linearly polarized light has a fixed direction perpendicular to the direction of propagation. The E vector of a circularly polarized light beam has constant amplitude and rotates about the direction of propagation at the frequency of the light.

If the E vector rotates clockwise as viewed by an observer receiving the beam, the circularly polarized light is said to be right-handed.

Many materials have different refractive indices for light polarized in orthogonal directions. Two equal rays passing through such a medium travel at different speeds and become out of phase. If the phase difference as they leave the medium is an odd multiple of  $\pi/2$ , the two rays combine to give circularly polarized light. Our quarter wave retarders on page 3-30 convert linearly polarized light to circularly polarized or circularly polarized to linear.

If the E vector rotates at the frequency of the radiation but varies in amplitude then the light is elliptically polarized. This is the most general form of polarized light; linear and circular polarizations are special versions of elliptical polarization.

## PRODUCTION OF POLARIZED LIGHT

Light from natural and incoherent artificial sources is often slightly polarized; i.e. the degree of polarization is small, usually small enough to be negligible. Many lasers, on the other hand, emit polarized radiation.

We follow with a discussion of some of the ways to produce polarized light from unpolarized. Some of these are used deliberately, others are unavoidable and can cause serious error in radiometric measurements.

## Polarization by Reflection

If an unpolarized beam of light is incident at an off-normal angle onto an optical surface, the reflected and transmitted beams become polarized to some degree. This is because the reflectance differs for s and p polarized light. Any unpolarized beam is equivalent to equal s and p linearly polarized components. This effect is important for selection of beam splitters and in polarization sensitive radiometry.

Fig. 4 shows the reflectance for s and p polarized light against angle of incidence for a light incident from air onto a fused silica interface ( $n = 1.457$ ). P polarized light incident at Brewster's angle ( $55.5^\circ$ ) is completely transmitted by the surface. None is reflected. Only 86.5% of s polarized light incident at Brewster's angle is transmitted. The remainder (13.5%) is reflected. This means that for an unpolarized beam incident at Brewster's angle, the reflected beam is linearly polarized (s) and the transmitted beam partly polarized.

Brewster's angle is given by:

$$i_b = \tan^{-1} \frac{n_1}{n_0}$$

Where:

- $n_0$  = Refractive index of air
- $n_1$  = Refractive index of the optical material
- $i_b$  = Brewster's angle

For air ( $n_0 = 1.0$ ) and glass ( $n_1 = 1.5$ ), Brewster's Angle =  $56.3^\circ$ .

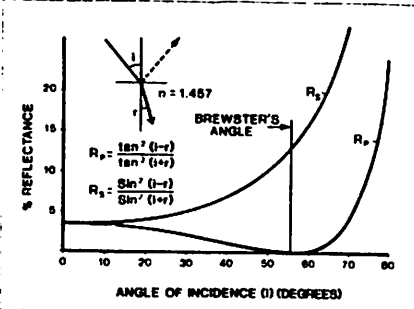


Fig. 4 Reflectance for s and p polarized light.

After an unpolarized beam (50% s and 50% p) passes through a stack of 20 fused silica plates at Brewster's angle, the transmitted beam has 99.7% p polarized light and 0.3% s polarized.

Instead of 20 stacked plates it is more practical to use a single surface with a multi-layer dielectric coating to produce highly polarized light. "Thin film polarizers" of this type are on pages 3-12 to 3-14.

The reflectance of light from metallic surfaces is also angle of incidence and polarization dependent. P polarized light goes through a reflectance minimum at an angle called the "principal angle".

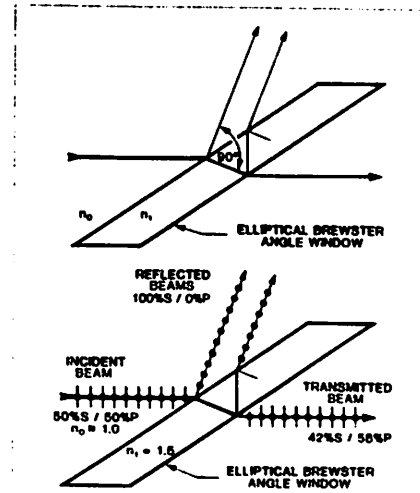


Fig. 5 At Brewster's Angle, the refracted and reflected rays of an incident beam are perpendicular. The transmitted beam is 42% s/58% p polarized for  $n = 1.5$ .

## POLARIZING OPTICS: TECHNICAL DISCUSSION

### Polarization by Scattering

Light scattered at 90° by charged particles is polarized perpendicular to the plane of incidence (s polarization). In the atmosphere, light from the sun is scattered by charged particles and molecules. The intensity of scatter increases with increased frequency (decreasing wavelength) which accounts for the blue appearance of the sky. Without a scattering atmosphere, as in space, there is no blue sky.

### Polarization by Wire Grids

A series of fine parallel metal wires can function as a polarizer (Fig. 6). The component of the incident radiation which has its E vector parallel to the wire grids is absorbed and reflected so the transmitted component is largely polarized. The electric field along the grid drives the conduction electrons leading to Joule heating and re-radiation. For efficiency, the space between the wires must be small, compared to the wavelength, so these polarizers are more easily constructed for infrared radiation.

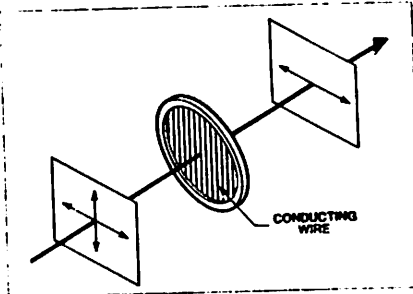


Fig. 6 Wire Grid Polarizer.

### Polarization by Dichroism

Some materials absorb light polarized in one direction more strongly than light of the orthogonal polarization. Sheet polarizers such as those on page 3-12 exhibit this property called dichroism.

The sheet polarizers are made from long chain polyvinyl alcohols. The sheets are stretched to orient and align the molecules. The stretched sheets are treated with iodine. Electrons can then move easily along the chain. This is equivalent to a fine grid polarizer. Light with the E vector in a plane perpendicular to the chain is transmitted; light with the E vector parallel to the chain is absorbed.

Dichroic sheet polarizers for the ultraviolet, visible and near infrared are moderately efficient and inexpensive. They do not withstand ultraviolet or high power beams and so are not recommended for use with intense sources. Dichroic sheet polarizers are relatively insensitive to angle of incidence, and are available in large sizes.

### Polarization by Double Refraction (Birefringence)

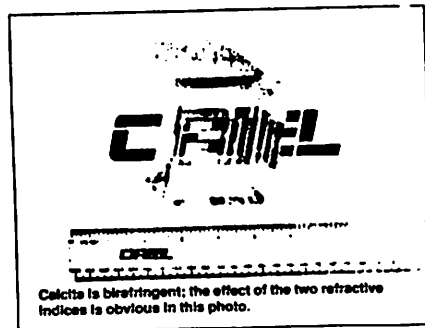
Some transparent materials such as crystal quartz, sapphire, mica and calcite, do not have a single value for refractive index. This is due to structural anisotropy. These materials are crystals and many of their physical properties vary with crystal lattice orientation. The refractive index for a ray passing through these materials depends on the direction of the ray with respect to the crystalline structure, and on the direction of the E vector. Material characterized by two refractive indices are birefringent.

We use calcite for our polarizers because the difference in the two refractive indices is large. Light traveling parallel to the optic axis exhibits no double refraction. Light traveling perpendicular to the optic axis has one index of refraction value ( $n_o$ ) for light polarized in the plane of the optic axis (called the extraordinary or e-ray), and a different index of refraction value ( $n_e$ ) for light polarized perpendicular to the optic axis (called the ordinary or o-ray).

At 550 nm, calcite has a refractive index of 1.66 for the o-ray which is independent of the direction of travel. For the e-rays, the refractive indices are 1.66 for rays traveling parallel to the optic axis, and 1.49 for rays traveling perpendicular to the optic axis.

To follow the propagation of light rays through the calcite crystal, we resolve the rays into components parallel to the optic axis (e-rays), and perpendicular to the optic axis (o-rays). There are three possible conditions for light traveling through the calcite crystal:

1. If the rays travel parallel to the optic axis, then rays of any polarization have the same refractive index.
2. If the rays travel perpendicular to the optic axis, then the e-ray travels faster than the o-ray. Because of the lower index of refraction of the e-ray, it will be bent or refracted less than the o-ray on leaving the crystal at an angled interface.
3. The rays travel at some angle between 0° and 90° from the optic axis. The o-ray travels undeviated and is refracted according to Snell's Law. As it enters the crystal at an angle, the e-ray deviates from the o-ray due to the variation of refractive index with direction; the direction of deviation will be away from the optic axis and generally out of the plane of incidence.



Calcite is birefringent; the effect of the two refractive indices is obvious in this photo.

Fig. 7 shows an unpolarized beam incident on a calcite rhomb. The unpolarized ray is split into its o-ray and e-ray components at the entrance face and then both rays travel through the crystal at different speeds. They exit the crystal at different points and so are separated. The degree of separation is a function of the difference in index of refraction between the o-ray and e-ray and the thickness of the crystal.

It is often more convenient to split a beam into orthogonally polarized beams by exploiting the large difference in  $n_o$  and  $n_e$  in calcite through total internal reflection. The birefringent crystal is cut so as the o and e rays leave the calcite crystal the o ray is totally internally reflected. Most of the e-ray passes through the interface, and by use of a compensating prism continues parallel to its original direction (Fig. 8). This is the basis of operation of our Glan-Taylor polarizing prisms listed on page 3-18.

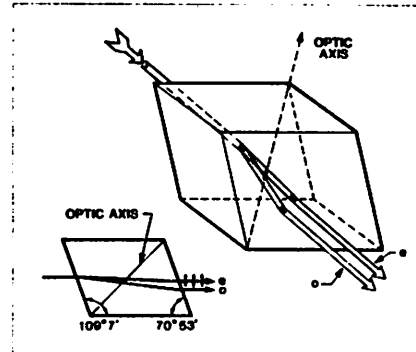


Fig. 7 A light beam traveling through a cleaved calcite rhomb is split into two orthogonally polarized beams. The e and o components emerge separated.

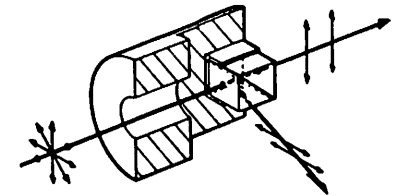


Fig. 8 With our Glan-Taylor Polarizers the e-ray exits parallel to its original direction.

### EXTINCTION RATIOS OF POLARIZERS

When unpolarized light passes through a polarizer the light which emerges is largely polarized with the E vector parallel to the transmission axis of the polarizer.

When a linearly polarized beam is incident on a polarizer and the polarizer rotated for maximum transmission, then  $k_1$ , the major principal transmittance is the ratio of transmitted to incident intensities,  $k_2$ , the minor principal transmittance, is the ratio when the polarizer is rotated for minimum transmittance. The extinction ratio is equal to  $k_1/k_2$ .

This ratio is typically  $10^3$  for sheet polarizers,  $10^4$  for thin film polarizers, and  $< 10^5$  for Oriol Crystal Polarizers.

As the polarizer is rotated in a polarized beam the transmittance,  $k$ , varies as:

$$k = (k_1 - k_2) \cos^2 \theta + k_2 \dots \dots \dots (1)$$

Where:

$\theta$  = Angle between the E vector of the light and the transmission axis of the polarizer

### Two Polarizers in Series

For unpolarized light passing through a pair of identical polarizers, the ratio of the intensity with the polarizers crossed, i.e. at extinction, to the intensity with the polarizers aligned is:

$$\frac{2k_1 k_2}{k_1^2 + k_2^2} = 2k_2 / k_1 \dots \dots \dots (2)$$

Where:

$k_1 \gg k_2$

Note that from (2) the ratio of minimum and maximum intensity with two polarizers in unpolarized light is approximately twice the extinction ratio.

## POLARIZING MATERIALS

### BIREFRINGENT POLARIZING MATERIALS

The polarization behavior of a crystal is determined by the crystal structure and electron bonding. Isotropic crystals have a single index of refraction and therefore are not birefringent. Calcite, crystalline quartz, sapphire and magnesium fluoride are birefringent with one optic axis. These uniaxial crystals have two principal refractive indices,  $n_o$  and  $n_e$ . Still other materials such as mica have two optic axes and three principal refractive indices.

Calcite is widely used as a polarizing material because of its excellent transmission and large difference in the two index of refraction values. The large difference simplifies the separation of the two different polarizations. Table 1 lists the index of refraction values at 589 nm for the ordinary ( $n_o$ ) and extraordinary ( $n_e$ ) rays of several materials. Table 2 lists the variation of  $n_e - n_o$  with wavelength.

Table 1 Refractive Indices at 589 nm

	$n_o$	$n_e$	$n_e - n_o$
Calcite	1.658	1.486	-0.172
Crystal Quartz	1.544	1.553	0.009
Mica*	1.598	1.593	-0.005
Sapphire ( $Al_2O_3$ )	1.768	1.760	-0.008

Table 2 Variation of  $n_e - n_o$  with Wavelength

Wavelength ( $\mu m$ )	Crystalline			
	Calcite	Quartz	Mica*	Sapphire
0.2	-0.326	0.0130		-0.0117
0.3	-0.206	0.0103		-0.0091
0.4	-0.184	0.0091		0.0085
0.5	-0.176	0.0093	-0.0047	-0.0082
0.6	-0.172	0.0091	-0.0048	-0.0081
0.7	-0.169	0.0090	-0.0048	-0.0080
0.8	-0.167	0.0089		-0.0079
0.9	-0.165	0.0088		-0.0079
1.0	-0.164	0.0088		-0.0079

\* As used in Oriel waveplates.

## POLARIZER OVERVIEW

The next three pages briefly summarize our family of Polarizing Optics. They are discussed in complete detail at the end of this section.

We offer the following types of Polarizing Optics:

Dichroic Polarizers	3-12
Crystal Polarizing Prisms	3-18
Polarizing Beam Splitting Cubes	3-24

### DICHROIC POLARIZERS

- High acceptance angle
- Large apertures

We offer three types:

Sheet Polarizers	3-12
Surface Film Polarizer	3-14
Silver in Glass Polarizers	3-15

### Surface Film Polarizer

We offer one polarizer of this type; the 27320. It is made by depositing a proprietary coating on a specially prepared fused silica substrate. This polarizer is notable for its wide effective range; 230 - 770 nm, very large acceptance angle, and durability. It withstands prolonged exposure to ultraviolet and visible radiation much better than the sheet polarizers.

### Silver in Glass Polarizers

Our new silver in glass polarizers have very high transmittance, acceptance angles to 60° and higher power handling capability than our other dichroic polarizers. They are made by embedding tiny elongated silver particles in a borosilicate glass. The particles are aligned so the material works like a tiny wire grid, absorbing light with its E vector parallel to the long, conducting silver particles. The spectral range of these polarizers is limited, but we offer models for most popular near infrared regions.

### Sheet Polarizers

These polarizers are available for the ultraviolet to visible, visible, and near infrared. The low cost, wide acceptance angle, and large apertures make these the polarizers of choice for many applications. You should only select these polarizers for low power applications since they operate by absorbing the unwanted polarization and are easily bleached, particularly by ultraviolet light.

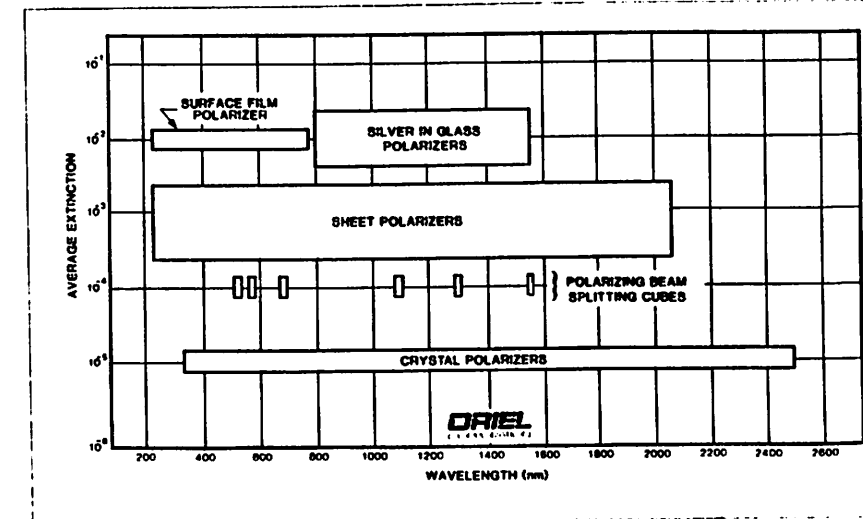


Fig. 1 Average Extinction vs. wavelength range for our family of polarizers. Lower extinction is better. The chart does not highlight advantages such as power handling, transmittances, and local extinction. These make the Surface Film Polarizer and the Silver in Glass Polarizers much more attractive.

## POLARIZER OVERVIEW

### CRYSTAL POLARIZING PRISMS

- Broad usable wavelength range
- High power handling capability
- Highest Extinction Ratio

Our polarizing prisms are made from select laser quality calcite to provide the purest polarized light available. These prisms have smaller apertures and acceptance angles than our dichroic polarizers. They are ideal for use with lasers, and for applications such as ellipsometry where high extinction is crucial.

We offer four types of crystal polarizers:

Glan-Thompson Polarizers.....	3-20
Glan-Taylor Polarizers.....	3-18
Low Loss Prism Polarizers.....	3-23
Wollaston Polarizers.....	3-22

### Glan-Thompson and Glan-Taylor Polarizers

These similar polarizers operate by separating the two polarizations at an angled interface. The interface angle is such that the o-ray strikes it at more than the critical angle and is totally reflected. It is either absorbed at the exit face, or emerges from the models with exit windows. The e-ray passes through the angled interface, with some reflection loss, and exits the prism slightly displaced laterally, but parallel to the input beam. If the input beam satisfies the acceptance angle conditions, then the transmitted beam has a high degree of polarization.

The transmitted e-ray contains typically less than  $10^{-5}$  to  $10^{-6}$  parts of the unwanted polarization. The beam that exits the side of the prism is mainly o-ray, contaminated with some of the e-ray component which was reflected from the angled interface. In the reflected beam the o-ray and the e-ray are not co-linear, and therefore they can be easily separated.

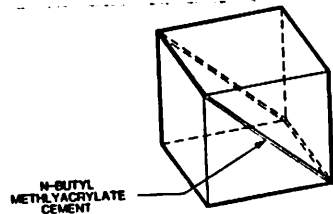


Fig. 2 Ortel Glan-Thompson Polarizer

In our Glan-Thompson polarizers, the interface between the two prisms is filled with n-butyl methacrylate optical cement (Fig. 2). The visible to infrared transmittance is excellent and the acceptance angle is  $15^\circ$  (F/3.8). You can use these polarizers with our monochromators without beam collimation.

The Glan-Taylor Polarizers use an optimized Foucault design with an air space between the calcite prisms. Using an air space extends the transmittance into the ultraviolet and allows transmission of higher power beams. The acceptance angle and visible to near infrared transmittance are lower than those of the Glan-Thompson polarizer.

### Low Loss Prism Polarizers

Like our other crystal polarizers, these split an unpolarized beam into two widely separated polarized components. Because of the Brewster's angle input and output, and close to Brewster's angle internal faces, the e-ray has a transmittance of 98% at 632.8 nm.

These polarizers are usable with visible collimated beams up to 15 mm in diameter. The output beam is displaced from the input by 6 mm.

### Wollaston Polarizers

Our Wollaston Polarizers split an unpolarized beam into two orthogonally polarized components which exit the polarizer with high angular separation ( $\sim 20^\circ$  at 633 nm.) The two orthogonally polarized rays travel co-linearly with different refractive indices through the first prism. At the interface the crystal orientation switches, so the o-ray beam is refracted away from the normal and the e-ray is refracted towards the normal. The rays are further separated on exiting the polarizer. The output rays are almost symmetrical about the input direction.

### POLARIZING BEAM SPLITTING CUBES

- Excellent extinction ratio
- High transmittance

When light strikes an angled interface between two dielectric media, the reflectance depends on the polarization state of the light. We describe this on page 3-3. These polarizers exploit this effect with thin film coatings designed for high reflectance for one polarization and high transmittance for the other.

The beam transmitted through our polarizing beam splitting cubes is almost pure p polarized (with respect to the cube reflecting face). The extinction ratio of  $10^3$  is unmatched for this type of polarizer. The beam reflected at  $90^\circ$  to the incident beam is mostly s polarized. The cubes are usually designed for a specific wavelength, but sophisticated coating design has allowed us to offer broadband models with excellent transmitted beam extinction.

Polarizing beam splitters offer the convenience of orthogonal beam splitting. They are available in apertures up to 1 inch, have limited acceptance angles (typically a few degrees) and the power handling capability is limited by the construction.

## RETARDERS: TECHNICAL DISCUSSION

Retarders change the state of polarization. They resolve an incident beam of light into two orthogonally polarized components and retard the phase of one component relative to the other. The emergent beam usually has a different polarization state from the incident beam.

The most common type of retarder is a slice of birefringent material in which the o-ray and e-ray travel at different velocities. Two rays which start in phase get out of phase with each other. For light of wavelength  $\lambda$  the phase difference,  $\phi$ , is given by:

$$\phi = \pm 2 \pi d (n_e - n_o) / \lambda \quad \dots\dots (1)$$

and the path difference by:

$$k \lambda = \pm d (n_e - n_o) \quad \dots\dots (2)$$

Where:

- d = Thickness of the plate
- $n_e$  = Refractive index for the extraordinary ray
- $n_o$  = Refractive index for the ordinary ray

k allows us to express the path difference in terms of  $\lambda$ , the wavelength.

When  $k = m/4$  where m is any odd integer, the path difference is effectively a quarter wave, so the plate is called a quarter wave plate. When the path difference is a half wave, the retarder is called a half wave plate.

Fig. 1 shows the operation of a half wave plate on a linearly polarized beam. The  $\vec{E}$  vector of the input beam is at  $\theta$  to the optic axis. The input beam is effectively resolved into two orthogonally polarized component beams (page 3-28), one with the  $\vec{E}$  vector parallel and the other with the  $\vec{E}$  vector perpendicular to the optic axis.

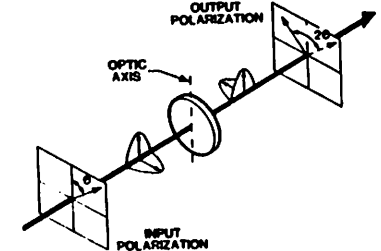
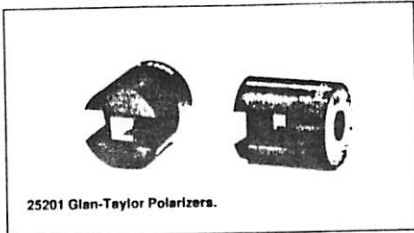


Fig. 1 Rotation of polarization by a Half Wave Retarder.

The retarder delays one of these beams with respect to the other. After passing through the retarder, the phase of one vector component is delayed by  $\pi$  ( $180^\circ$ ) with respect to the other; a path difference of one half wavelength. The sum of the two emergent beams is a beam with linear polarization but rotated by  $2\theta$  from the original input beam.

The action of this half wave plate is to rotate the  $\vec{E}$  vector of the light through  $2\theta$ , twice the angle between the  $\vec{E}$  vector of the incident beam, and the optic axis.

## GLAN-TAYLOR POLARIZERS



25201 Glan-Taylor Polarizers.

- High power handling capacity
- Transmittance from 400 to 2500 nm

These high extinction polarizers are specifically designed for use with high power lasers. They are extensively used for pulse extraction and feedback elimination. Because they use an air gap rather than optical cement, they also have advantages over Glan-Thompson or Wollaston polarizers for any ultraviolet applications.

Two types are available:

- Standard models (without exit window). This type is intended to remove unwanted polarization from a substantially polarized beam.
- With exit window. The rejected beam exits the polarizer, so this type should be used in pulse extraction or any application where there is significant rejected power. They can also be used for beam combination.

### POLARIZER DESIGN

Our Glan-Taylor polarizers are made from grade "A" natural calcite ( $\text{CaCO}_3$ ). The material is carefully selected, optically oriented and then cleaved to size. The two calcite prisms are mechanically coupled at the hypotenuse. The hypotenuse faces are aligned parallel and separated by an air gap. The air gap is so small that beam displacement is negligible.

The entrance and exit faces are normal to the mechanical axis. The hypotenuse faces are near the Brewster angle so there is minimal reflection loss for the transmitted component. The entrance and exit faces of the prism can be anti-reflection coated to increase the transmittance. See pages 10-6 to 10-7 for coatings. The polarizers come mounted in a black anodized aluminum housing.

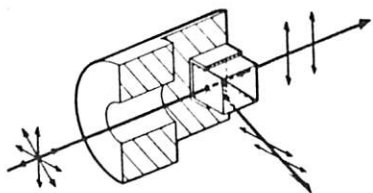


Fig. 1 Oriel Glan-Taylor Polarizer with exit window.

### STANDARD MODELS

The rejected beam is absorbed at the face of the crystal. This limits the application of these models to cases where the rejected component has low average or peak power.

### MODELS WITH EXIT WINDOWS

The reflected beam escapes through two polished side windows and out through one of the two holes in the mount. See Fig. 1. Having two escape windows allows the polarizer to be used with high power cw or pulsed lasers travelling in either direction through the polarizer. This is important in intra-cavity gain switching applications. Be sure to terminate the rejected beam safely if it is not to be used. Our 14041 Beam Stop is a convenient beam terminator.

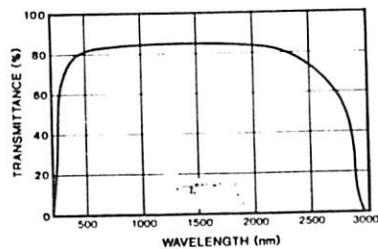


Fig. 2 Transmittance ( $k_1$ ) of Oriel Standard Glan-Taylor Polarizers for polarized light.

### SPECIFICATIONS

Dimension tolerance:	+ 0 mm; - 0.25 mm
Material:	Select grade calcite ( $\text{CaCO}_3$ )
Wavelength range:	400 - 2500 nm
e ray transmittance:	> 88%
Extinction ratio <sup>*</sup> :	< $10^{-5}$
Field angle @ 632.8 nm:	8 (0.14 rad)
Beam deviation:	3 (0.9 mrad)
Wavefront distortion @ 632.8 nm:	< $1/8 \lambda$
Surface quality:	10 - 5
Maximum transmitted power <sup>**</sup> :	
Standard models:	10 $\text{W/cm}^2$ CW 20 $\text{MW/cm}^2$ in 10 ns pulses 100 $\text{W/cm}^2$ CW
Models with exit windows:	200 $\text{mW/cm}^2$ in 10 ns pulses
Face coating:	None. Faces may be AR coated to increase transmission. See pages 10-6 to 10-7 for coatings.

\* The extinction ratio is somewhat dependent on beam collimation. The stated specification is for an input beam collimated to at least one half of the acceptance angle.

\*\* For lasers with wavelengths above 450 nm. Damage thresholds drop with wavelength.

### MOUNTING

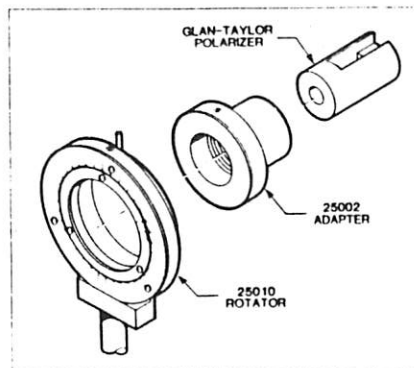
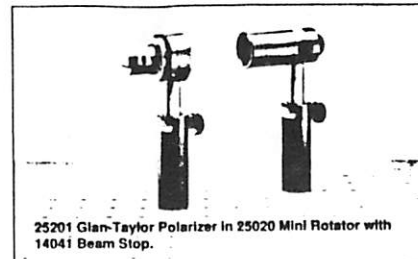


Fig. 3 You can mount any 1.0 inch Glan-Taylor Polarizer in the 25010 Rotator using the 25001 or 25002 Adapter.

See pages 3-35 to 3-36 for manual rotators and Volume I for a full listing of manual and motorized rotators.

Any polarizer in a 1.0 inch (25.4 mm) O.D. mount fits in our new 25020 Mini Rotator. You can mount polarizers with 1, 1.25, or 1.5 inch (25.4, 31.8, or 38.1 mm) O.D. mounts into the 25010 or other 2 inch Rotator using adapters. These adapters have a 2 inch (50.8 mm) O.D.



25201 Glan-Taylor Polarizer in 25020 Mini Rotator with 14041 Beam Stop.

### ORDERING INFORMATION

Clear Aperture (mm)	Mount Length (mm)	Mount O.D. In. (mm)	Model No.	Price (\$)
<b>Standard Models (without exit window)</b>				
7	26	1.0 (25.4)	25201	\$ 529.00
10	29	1.0 (25.4)	25202	\$ 639.00
12	31	1.0 (25.4)	25203	\$ 917.00
15	34	1.25 (31.8)	25204	\$ 1335.00
20	43	1.5 (38.1)	25205	\$ 1850.00
<b>Models With Exit Window</b>				
10	29	1.0 (25.4)	25601	\$ 748.00
12	31	1.0 (25.4)	25602	\$ 825.00
15	34	1.25 (31.8)	25603	\$ 1730.00
20	43	1.5 (38.1)	25614	\$ 2128.00

14041	Beam Stop	\$ 74.00
25001	Adapter to mount 1.0 inch OD Standard Model Polarizers in 2.0 inch Rotator	\$ 33.00
25002	Adapter to mount 1.0 inch OD Polarizers with Exit Window in 2.0 inch Rotator	\$ 52.00
25003	Adapter to mount 1.25 inch OD Polarizers in 2.0 inch Rotator	\$ 52.00
25007	Adapter to mount 1.5 inch OD Polarizers in 2.0 inch Rotator	\$ 58.00

\* The 25001 holds any polarizer with a 1" OD mount. If you have a polarizer with a side exit window the 25001 allows you to use the side exit beam.

\*\* Use the 25002 if your polarizer has a side exit window and you want to terminate the side exit beam.



## MIRRORS: TECHNICAL DISCUSSION

Every surface reflects light. The reflected light is both diffuse and **regular** (or **specular**) and sometimes comes both from the surface and the bulk material. (Fig. 1) Regular and specular reflection are defined as "reflection in accordance with the laws of geometrical optics, without diffusion". (Fig. 2). The **reflectance** of any surface is the ratio of the reflected radiant flux to the incident flux.

**Reflectivity** is the reflectance of a layer of material of such a thickness that there is no change in reflectance with increase in thickness.

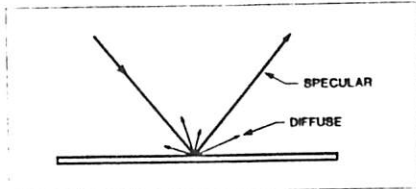


Fig. 1 Diffuse and specular reflectivity. Only specular reflections will be important for any surface which is smooth (on the scale of a fraction of a wavelength).

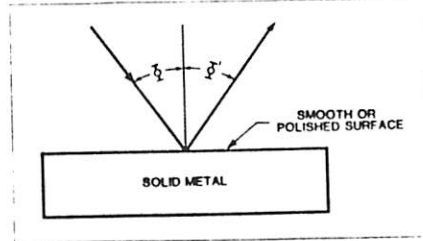


Fig. 2 With specular reflection, the angle of the reflected component is equal to the angle of the incident beam with respect to the normal.

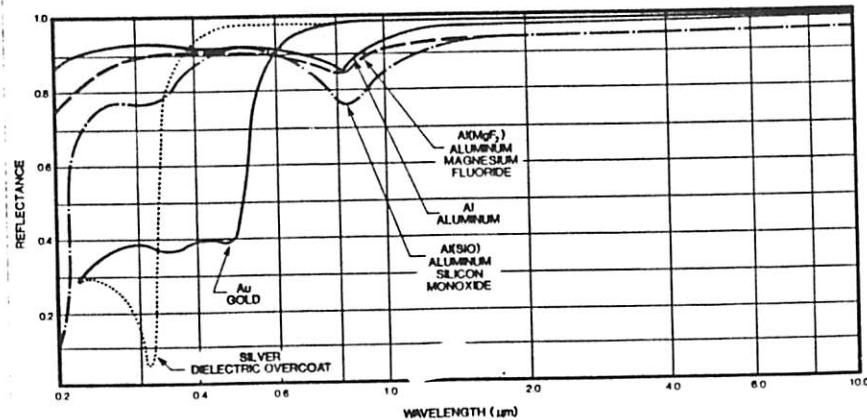


Fig. 3 Typical near normal reflectance of our metal reflector coatings. They are described on pages 10-8 to 10-9.

### BARE SUBSTRATES

- The reflectivity of any uncoated surface depends on:
- The refractive index of the material which varies with the wavelength of the incident light
  - The angle of incidence
  - The polarization state of the incident light
  - The smoothness or polish of the surface

For transmissive optics, the single surface reflectances range from 3% for calcium fluoride to 17% for zinc selenide, a high index material

### SUBSTRATES WITH DIELECTRIC COATINGS

The reflectance of a surface with a dielectric coating depends on the optical properties of both the substrate and the coating. Coatings can be designed for very high reflectance or as partial reflectors. The useful wavelength range of any dielectric reflector is limited. (See page 10-5.)

### METALLIC REFLECTORS

Highly polished metal surfaces are good broadband specular reflectors. The best metallic reflectors are made by vacuum depositing a thin coating of the metal on a polished substrate. Aluminum adheres directly to glass but a chrome intermediary layer must be used for gold. A typical coating is less than 100 nm thick; thicker coatings have higher scatter from surface roughness. A freshly deposited aluminum coating has a reflectance of more than 0.8 from 200 nm to beyond 40,000 nm. Fig. 4 shows the reflectance of freshly deposited metallic reflector coatings.

Unfortunately the freshly deposited metals tarnish very quickly with the formation of oxides or other compounds. The reflectance drops dramatically. To prevent significant loss of reflectance we overcoat the metal films with thin dielectric films. See the following page.

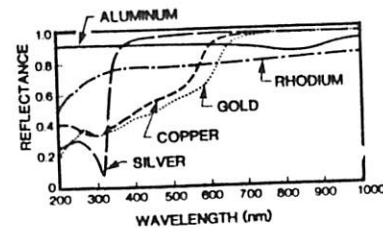


Fig. 4 Reflectance of freshly deposited metallic coatings.

### METALLIC OR DIELECTRIC REFLECTOR FOR HIGH REFLECTANCE?

Dielectric coatings are more durable, and can be designed for a desired reflectance, including reflectances higher than available from a metal coating. Any high reflectance dielectric coating however, is effective only over a narrow range of wavelengths. Most dielectric coatings are more sensitive to angle of incidence and polarization than metallic coatings. (Our maximum reflection mirrors on page 5-8 are exceptionally broadband and insensitive to polarization or angle of incidence to 45°.)

### CALCULATING REFLECTANCE

#### Bare Substrate

If light hits a nominally transparent substrate surface, the **Fresnel reflectance** from a single surface, for normal incidence,  $\rho$ , is given by:

$$\rho = \left[ \frac{n_1 - n_0}{n_1 + n_0} \right]^2$$

$$\text{as } n_1 > n_0$$

Where:

$n_0$  = Refractive index of air (1.0)

$n_1$  = Refractive index of the substrate

For an air ( $n_0 = 1.0$ ) - glass

( $n_1 = 1.5$ ) system,  $\rho \approx 4\%$  per surface.

(The **spectral Fresnel reflectance**,  $\rho(\lambda)$ , includes the wavelength dependence of  $\rho$  as the refractive indices vary with  $\lambda$ .)

We list some bare substrates as "Beam splitters" on pages 7-6 to 7-8. On page 12-2 we describe the dependence of the reflectance on angle of incidence and polarization

### METALLIC COATINGS

Metals are conductive and since optical radiation is electromagnetic in nature the conductivity leads to loss of energy through Joule heating. Metals are highly absorbing for EM radiation which "enters the metal", but this absorption is accompanied by high reflectance. Conductivity, and therefore absorbance and reflectance, are wavelength dependent. The reflectivity from a metal surface is given by:

$$\rho = \frac{n(1 + i\kappa) - 1}{n(1 + i\kappa) + 1}$$

$$= \frac{n^2(1 + \kappa^2) + 1 - 2n}{n^2(1 + \kappa^2) + 1 + 2n}$$

Where:

$n(1 + i\kappa)$  = Complex refractive index

$\kappa$  = Extinction coefficient

The complex refractive index includes the conductivity of the metal. The energy not reflected is absorbed in the metal.

For aluminum at 594 nm,  $n = 1.44$ , and  $\kappa = 5.23$ . From these values  $\rho = 0.83$ . Strong absorbance (high values of  $\kappa$ ) is accompanied by high reflectance. The slow variation of the complex refractive index with wavelength leads to excellent broadband reflectance.



## MIRRORS: TECHNICAL DISCUSSION

### Angle of Incidence Effects

Unlike dielectric reflectors, metal reflectors are effective over a wide range of angles of incidence. There is a phase change on reflection and this differs for s and p polarized radiation (Fig. 5). A nearly polarized ray incident at high angle will be reflected partially elliptically polarized.

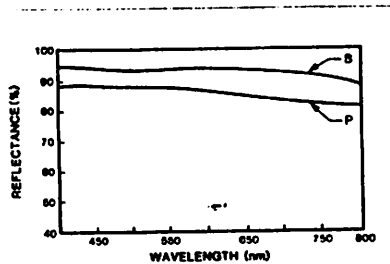


Fig. 5 Reflectance for s and p polarized light incident at 45° on a freshly deposited aluminum surface. An unpolarized beam incident at 45° will reflect as an elliptically polarized beam due to the phase change and reflectance differences for the s and p components.

### Overcoating Metal Reflectors

Aluminum or silver quickly tarnish and the reflectivity drops. We overcoat our metal reflectors with silicon monoxide or magnesium fluoride for protection. Fig. 3 on page 5-2 shows the reflectance of Al(MgF<sub>2</sub>) and Al(SiO<sub>2</sub>).

MgF<sub>2</sub> is better in the ultraviolet but is more delicate than the SiO<sub>2</sub> coating.

Any such coating must be a half wave thick or the reflectance will be reduced. This is feasible for ultraviolet or visible wavelengths, but not for the infrared as the layer stresses increase with thickness. The half wave coating keeps the reflectance close to that of the bare metal over a spectral range of several hundred nm. We can also enhance the reflectance over a narrower spectral range by applying a multi-layer dielectric coating.

We list our metal and overcoated metal coatings on pages 10-8 to 10-9.

### DIELECTRIC COATINGS ON TRANSPARENT SUBSTRATES

Dielectric coatings can be optimized for a single wavelength or a narrow (typically 250 nm) spectral range. The simplest coating is a single thin layer coating (page 10-8). To increase the reflectance from that of the bare substrate the refractive index of the coating must be higher than that of the substrate.

The reflectance of a mirror with a single layer high index coating is shown in Fig. 6.

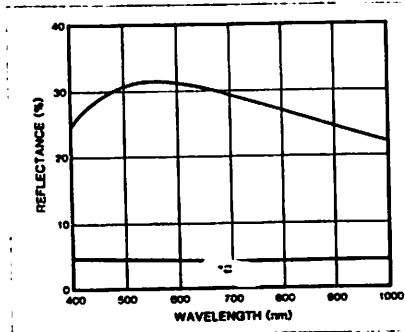


Fig. 6 The reflectance from an uncoated BK 7 substrate and the same substrate coated with a 1/4 wave (at 550 nm) dielectric layer of refractive index 2.32.

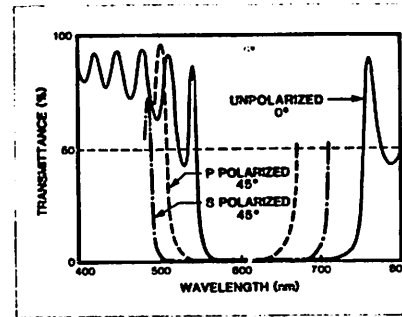


Fig. 7 Typical multi-layer dielectric reflective coating designed for maximum reflectance at normal incidence and at 630 nm.

### Multi-layer Dielectrics

Fig. 6 showed the reflectance with a single 1/4 wave dielectric layer on a transparent surface. If additional layers of alternating high (2.2) and low (1.35) index of refraction dielectrics which are 1/4 wave thick at  $\lambda_0$  are deposited on this nominally transparent substrate, the reflectivity increases substantially. A 13 layer coating of this type has a reflectance of > 99.5% at  $\lambda_0$ . Usually such coatings have high reflectance only over a very narrow wavelength range and the reflectance is very dependent on angle of incidence (Fig. 7). There are ways to improve things. The coating on our Maximum Reflection Mirrors (> 0.99) uses slight controlled departures from 1/4 wave thicknesses for maximum bandwidth (several 100 nm) and insensitivity to angle of incidence.

Multi-layer dielectric coatings can be designed for narrowband reflectors with very high reflectances (> 0.995), very broadband reflectors (our Maximum Reflection Mirrors on page 5-8) or partial reflectors. Multi-layer dielectric techniques are also used to produce polarizers (page 3-12), interference filters (page 2-34), and cold mirrors (page 2-46)

For a detailed listing of our standard reflector coatings see pages 10-8 to 10-9.

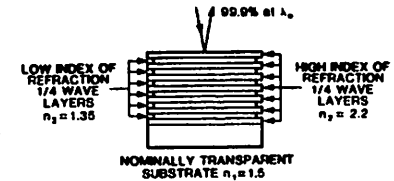


Fig. 8 13 layer Dielectric reflective coating.

### Angle of Incidence and Polarization

The reflectance curve of dielectric reflectors shifts slightly to shorter wavelengths as the angle of incidence increases from 0° (normal incidence). Additionally, the reflectance for s polarized light becomes different to that of p polarized (as for an uncoated substrate) (Fig. 7). For incidence above several degrees, the effective bandwidth for s polarized light is noticeably greater than that of p polarized. We exploit this difference to make our dielectric polarizers, but for reflectors it can be restrictive.

## FIBER OPTICS TECHNICAL DISCUSSION

All optical fibers operate by "total internal reflection". If a ray of light in a medium of refractive index  $n_1$  strikes the interface with another medium of refractive index  $n_2$  ( $n_2 < n_1$ ), at an angle  $\theta$ , and  $\theta$  is greater than  $\theta_c$ , the ray is totally reflected back into the first medium.  $\theta_c = \sin^{-1}(n_2/n_1)$  and is called the critical angle. See Fig. 1

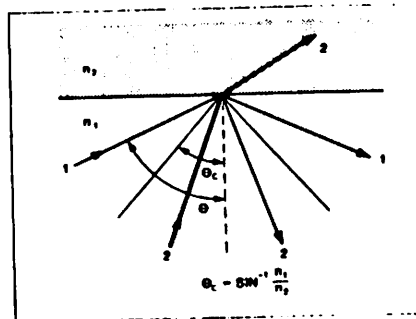


Fig. 1 Ray 1 is incident at an angle  $> \theta_c$  (41.8° for glass) and is totally reflected. Ray 2, incident at an angle  $< \theta_c$ , is partially refracted into the glass and partially reflected.

An optical fiber exploits total internal reflection by having an inner region of low refractive index and a cladding of higher index. Light is confined by repeated reflections. Single strands of transparent material such as glass or fused silica can pipe trapped light over long distances with very low loss.

Figs. 2 and 3 show the simplest type of fiber, a cylindrical core of transparent material with an outer layer of lower index material. (The same effect can be obtained by grading the index from high in the center to lower values at the periphery.) Light entering the fiber within the acceptance cone is totally reflected at the core-cladding interface.

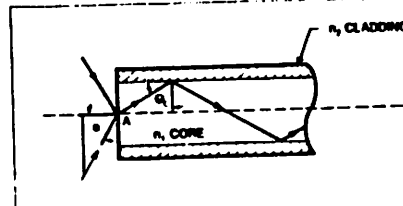


Fig. 2 A single fiber accepts and guides light incident within the acceptance cone. Oriol Fiber Bundles are comprised of a large number of fibers, each with a core and thin outer layer of cladding.

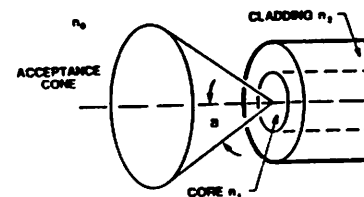


Fig. 3 The light entering the fiber within the acceptance cone is totally reflected at the core-cladding interface.

The acceptance angle,  $a$ , depends on the refractive indices of the core and cladding:

$$\sin a = \frac{1}{n_0} \sqrt{n_1^2 - n_2^2}$$

Note that the acceptance cone angle is  $2a$ , and  $n_0$  is usually  $= 1$ .

Fiber input and output behavior is usually described in terms of numerical aperture (NA). If  $n_0 = 1$ :

$$NA = \sin a = \sqrt{n_1^2 - n_2^2}$$

This relates  $F/\#$  through

$$F/\# = \frac{1}{2 \sin a} = \frac{1}{2 NA}$$

(This is sometimes written as  $1/(2 \tan a)$ . We use  $\sin a$  here because at high values of  $a$ ,  $\sin a$  is more appropriate. At low values of  $a$ ,  $\sin a \approx \tan a \approx a$ .)

NAs and  $F/\#$ s for Oriol Fibers are tabulated below (in all cases a range of NAs are available for material combinations such as glass-glass where the indices are determined by the particular glass used.)

Table 1 NAs and  $F/\#$ s for Oriol Fibers

Core	Cladding	NA	$F/\#$	Acceptance Cone Angle $2a$ deg (rad)
Silica	Plastic	0.27	1.9	31 (0.55)
Silica	Silica	0.22	2.3	25 (0.44)
Liquid	Plastic	0.47	1.1	56 (0.98)
Glass	Glass	0.56	0.9	68 (1.2)

## FIBER OPTICS: TECHNICAL DISCUSSION

Because of the small cross section required for flexibility, typically much less than a millimeter, single fibers are not efficient in collection of energy from larger incoherent (non laser) sources. Fibers packed in a bundle provide both the flexibility and large aperture. We supply bundles for illumination or energy transfer only. In these, the individual fibers are haphazardly located in the input and output of the bundle.

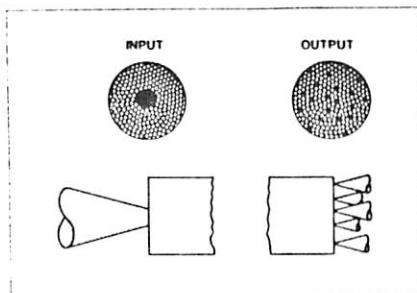


Fig. 4 All Oriol Fiber Optic Bundles are for energy transfer. Any correlation of the position of an individual fiber in the output face to its position in the input face is an unintended result of the comb technique of preparing the bundles.

### WHAT'S IN A FIBER BUNDLE?

Our standard Fused Silica Bundles are made of fibers with relatively large (to 250  $\mu\text{m}$ ) cores. Our Glass and High Grade Fused Silica Bundles use smaller (~ 100  $\mu\text{m}$ ) fibers. A thin (9  $\mu\text{m}$ ) cladding confines the light. The bundle may have 50 to 500 fibers depending on type and diameter. The fibers are held in a flexible stainless steel protective sheath. The fibers at each end of the bundles are bonded in a stainless steel ferrule. The ends are cut and polished flush with the ferrule.

The input apertures of our bundles are 0.063 inch (1.6 mm) or 0.125 inch (3.2 mm) in diameter. The entire aperture does not collect light since the fiber bundle is made up of small cylindrical fibers packed together. The ratio of useful area to the full aperture area is called the **packing fraction**. We maximize this in our bundles.

### TRANSMITTANCE

The transmittance of a single fiber, fiber bundle or liquid light guide varies with test conditions. A ray which passes down the axis travels a much shorter distance than a ray which enters at the limiting acceptance angle. The reflectance at the core-cladding interface is close to, but not exactly 1. A ray which enters at a high angle can have many thousands of reflections in going through a fiber and so experience more loss than an axial ray or one with few reflections. When a fiber is bent sharply, light leaks out and the transmittance drops.

We show transmittance data for practical conditions of a large launch cone for a specified length of fiber which is loosely coiled. The transmittance is derived by rationing the radiation through the fiber bundle to that through an aperture of the same size. This eliminates any loss from overfilling a fiber bundle. The data includes packing loss.

Light is reflected from the input and output faces, and absorbed or scattered as it passes through the fiber. The absorption and scattering losses depend on the wavelength of the radiation.

Transmittance decreases with length. For light of one wavelength, the transmittance - length relationship for constant operating conditions is approximately:

$$T = P(1 - R)^2 e^{-\alpha L}$$

Where:

- P = Packing fraction
- R = Reflection loss
- $\alpha$  = Absorption coefficient
- L = Length of the average light path through the fiber.

R is typically 0.04 for Oriol Fibers. P varies from 0.8 to 0.92 for fiber bundles and is 1 for single fibers and liquid light guides.

### Glass and Fused Silica Bundles

We offer Glass Bundles and two grades of Fused Silica bundles. The economical Glass Bundles transmit visible light and near infrared radiation (see Fig. 5). They have a very large acceptance angle (68°), and are therefore excellent for illumination of large areas or capture of radiation emitted from large sources.

Our Standard Grade Fused Silica Bundles use silica fibers with polymer cladding. They have excellent transmittance from the UV to 1200 nm and from 1500 - 1900 nm. Our High Grade Fused Silica Bundles use smaller silica fibers with a doped silica cladding. These have better overall transmittance and significantly better low UV transmittance than the Standard Grade. Fig. 6 shows the transmittance for the standard grade. We list both grades on page 8-12.

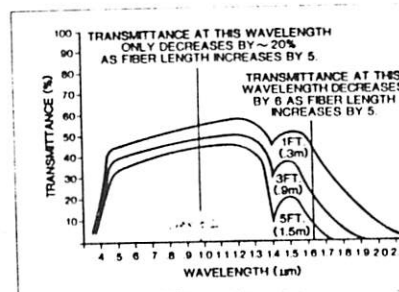


Fig. 5 How much the transmittance decreases as the fiber bundle length is increased depends on the wavelength. These curves are for glass fiber bundles.

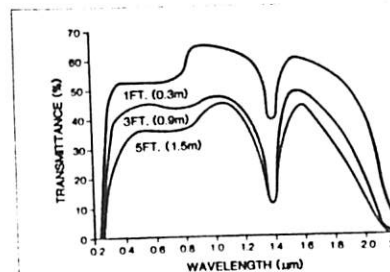


Fig. 6 Transmittance of Standard Grade Fused Silica Bundles.

### Single Fibers

We carry two types of single fibers in core sizes from 200  $\mu\text{m}$  to 1 mm. Both have a single cylindrical core with a cladding and protective jacket.

All our single fibers are **multimode**, as the smallest core size is 200  $\mu\text{m}$ . **Single mode** fibers with cores of about 5 to 10  $\mu\text{m}$  are used for long haul communication.

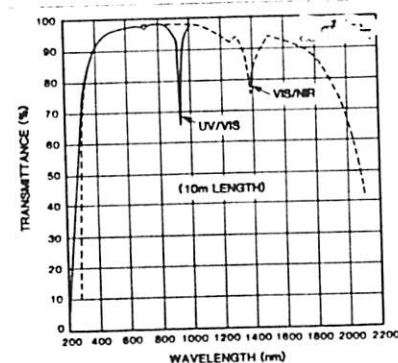


Fig. 7 Transmittance of Oriol UV-VIS and VIS-NIR Single Fibers

### Liquid Light Guides

Our Liquid Light Guides consist of a clear, non-toxic anaerobic liquid in a flexible tube with polished silica windows on each end. They are available in 3 and 5 mm diameters, and have high transmittance from 270 to 750 nm (Fig. 8). They have no packing fraction loss and a large acceptance angle which makes them the most efficient type of large aperture flexible light guide in the 270 - 400 nm range.

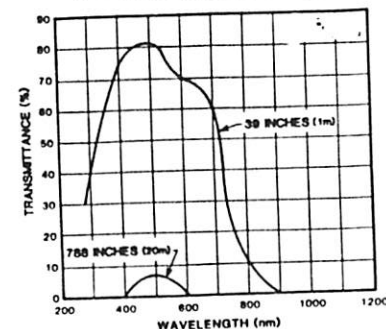


Fig. 8 Transmittance of Oriol Liquid Light Guides.

## FIBER OPTICS: TECHNICAL DISCUSSION

### CHOOSING THE FIBER OPTIC

The important considerations include:

- Spectral distribution of the light to be transmitted
- Size of the source and angular distribution of source radiation: size and acceptance angle of output target
- Cost

### Spectral Considerations

See the transmittance curves on the previous page for the transmittance of the various fiber types. The curves have extended flat portions and sloping portions as shown in Fig. 5.

The transmittance of light with a wavelength which lies on the flat portion of the curve will decrease gradually as the fiber length is increased. The transmittance for light on the sloping portions of the curve will decrease rapidly with fiber length.

### Throughput/Collection Considerations

A large NA and bundle diameter are best for collection of radiation from large sources. Collection from a large area source varies as the square of the NA and the square of the diameter. If the light from the bundle is for illumination of a large target, or is to be measured using an Integrating Sphere, then the larger the bundle and the higher the NA the better.

For a small intense source and a small target with a restricted acceptance angle at the output of the fiber, it may be important to conserve "brightness". When using a laser (effectively a point source) or other small source, you might do better with a low NA and small diameter fiber system.

### Cost and Availability

We provide both standard and custom fiber bundles and liquid light guides. Standard products are most economical, followed by longer guides with standard apertures.

Fused silica fiber bundles cost more than glass bundles. Our higher grade silica bundles use high performance silica-silica fibers. Because of the small diameter of these fibers, a high grade bundle requires many more fibers than a standard grade bundle. The increased performance is often worth the higher cost.

The liquid light guides have best transmittance from 300 to 700 nm, so you should consider these if the wavelengths you work with are in this range. Liquid light guides are more expensive than glass or standard grade fused silica bundles, but significantly less expensive than higher grade fused silica bundles.

If you need a very long length of fiber, then consider using one or more single fibers. You can select the length of single fiber you need. The VIS-NIR fiber is more economical than the UV-VIS fiber, and has excellent transmission in the visible

### NA AND WAVELENGTH

The index of refraction of fused silica varies rapidly with wavelength in the UV. Therefore the acceptance and output cones change with wavelength. Fig. 9 shows the significance of this for our standard grade fiber bundles. The higher grade silica bundles do not show this effect. The 254 and 546 nm scans are almost identical for the higher grade bundles.

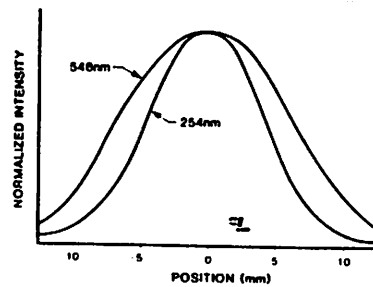


Fig. 9 Normalized linear scans across the output cones from the 77561 24 inch (610 mm) long, standard grade fused silica fiber bundle for two input wavelengths (254 and 546 nm). The input conditions were identical; slightly asymmetrical from a concave mirror at F/3.

### EMERGENT CONE

The light cone pattern which emerges from the fiber will be determined by the input illumination, the fiber properties, and the lay of the fiber bundle.

For long fibers, the fiber properties dominate, while for short fibers (< 1.2 m) the launch (or input) conditions dominate. Fig. 11 shows the outputs for various input conditions for the 77578, 36 inch (914 mm) long, 3 mm diameter high grade fused silica bundle. The same broadband source was used. The bundle was loosely coiled and turned through 90°.

Our glass and standard grade fused silica bundles show similar effects. The output from our liquid light guides is a little less sensitive to input conditions, but more sensitive to bending of the guide.

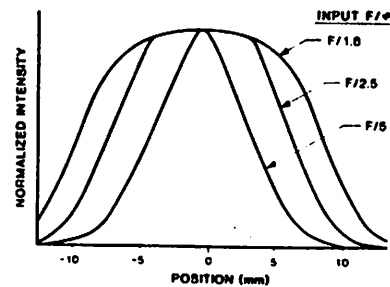


Fig. 10 Linear scan across the output pattern from the 77578 Fiber Bundle for different input conditions. The curves have been normalized for clarity. The F/1.0 cone corresponds to just overfilling the fiber acceptance angle. For a short fiber bundle, the lower the input angle, the smaller the divergence of the output cone.

## LASER TO FIBER COUPLING

We offer UV to NIR single fibers for use with lasers. With such small fiber core diameters, coupling becomes an important consideration. We offer fiber couplers on page 8-25.

### COUPLING LASER BEAMS INTO FIBERS

#### Numerical Aperture and Spot Size

The numerical aperture of a fiber is a measure of the acceptance angle. For acceptance by the fiber, light must strike the fiber at an angle smaller than  $\alpha$ , where  $\alpha$  is given by:

$$n_0 \sin \alpha = (n_1^2 - n_2^2)^{1/2}$$

Where:

- $n_0$  = Index of refraction of the incident medium
- $n_1$  = Index of refraction of the fiber core
- $n_2$  = Index of refraction of the fiber cladding.

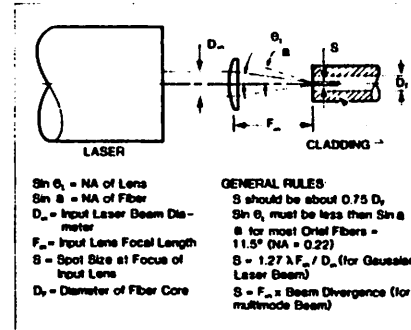


Fig. 1 General rules for coupling laser beams into fiber bundles.

The incident medium is usually air for which  $n_0$  is 1. Often the angle is not calculated but the NA for the beam matched to that of the fiber.

The numerical aperture (NA) of the fiber is defined as  $\sin \alpha$ . It is just like the NA for a microscope objective, and related to the familiar F/# for a lens through:

$$F/\# = 1/2 \sin \alpha$$

There are two simple conditions for efficient coupling:

- The beam NA should be lower than that of the fiber so that all the beam can enter the fiber. See Fig. 1
- The focused beam at the fiber face must be smaller than the fiber core.

### Practical Guidelines For Multimode Fibers

All the fibers we list on pages 8-18 to 8-19 are multimode fibers. Laser to fiber coupling can be optimized using straight-forward geometrical optics

- The focused laser spot should be smaller than the core, and the NA of the focused beam less than that of the fiber.

To calculate the spot size use:

For Gaussian beams:

$$S = 1.27 \lambda F_m / D_m$$

For multimode lasers:

$$S = F_m \theta$$

Where:

- $\theta$  = Full angle beam divergence
- $F_m$  = Focal length of the lens used
- $D_m$  = 1/e<sup>2</sup> diameter of the Gaussian beam at the focusing lens
- $\lambda$  = Laser wavelength

Beam divergence and  $D_m$  can be changed with one of the Beam Expanders listed on pages 1-61 to 1-63.

- A smaller spot eases alignment tolerances, but increases the power density on the vulnerable fiber face. We recommend a spot size of 0.75 times the core diameter for high power operation. For Gaussian beams the spot size (1/e<sup>2</sup>) should be less than 0.65 times the core diameter.
- Use as small an NA for the laser beam as possible to minimize bending losses. Since the spot size and the NA of the beam are linked, it is often possible to trade these parameters to optimize the launch conditions. The NA for the beam is given by:

$$NA = 1/2 (D_m / F_m)$$

When  $D_m$  is increased (or a lens of shorter focal length is chosen) to make the spot size smaller, the NA (beam angle) goes up.

## LASER TO FIBER COUPLING

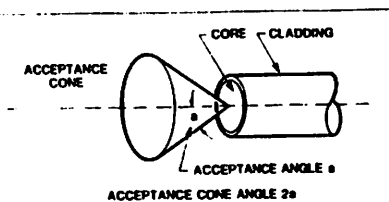


Fig. 2 Acceptance cone angle of a fiber.

Our multimode fibers have NAs of about 0.22. The acceptance angle is 12.5°. The acceptance cone angle is 25°.

- The laser beam should be centered in the lens. Spot size and launch angles change if the laser is off center.
- Donut or ring pattern outputs usually indicate off-axis launch. A sharp reduction in the size of the output beam when the fiber position is adjusted usually indicates correct fiber positioning.
- Our microscope objectives produce very small spots from low power beams. For high power beams use the plano convex lenses listed on page 1-18. The curved side should face the incoming laser beam.

### Example

Select a lens to couple the 79262 2.0 mW HeNe to a 50  $\mu\text{m}$  core fiber with 0.22 NA.

The beam diameter is about 0.7 mm at the laser output.

$$\text{Since } S = 1.27 \lambda F_n / D_n,$$

$$S = 1.27 \times 0.633 \frac{F_n}{0.7} = 1.15 F_n$$

Where:

S is in  $\mu\text{m}$  and  $F_n$  is in mm.

For a spot size ( $1/e^2$ ) of less than  $0.65 \times 50 = 32.5 \mu\text{m}$ , the lens focal length must be less than 28 mm. The 13570 Microscope Objective has a focal length of 25.5 mm, and is well corrected so the spot size will be close to that calculated. The beam NA with this lens will be about 0.006, which is much less than the 0.22 of the fiber.

### Example

Couple a 100 W multimode cw ND:YAG into a 77571 Fiber. The beam diameter for the laser is 6 mm and beam divergence is 11 mrad.

The fiber, listed on page 8-18 has a 400  $\mu\text{m}$  core and NA of 0.22.  $S = F_n \theta$ . If  $\theta$  is in mrad,  $F_n$  in mm, then S will be in  $\mu\text{m}$ .

The spot size is  $11 \times F_n$  microns. Our 25 mm focal length lens (41220) gives a 275  $\mu\text{m}$  spot size but the beam NA is then 0.12, which matches well with the fiber NA of 0.22.

### Single Mode Fibers

The number of modes which a fiber can guide drops as the fiber core diameter or NA is reduced. At small enough values of either, only one fiber mode exists. The fiber is then called single mode or monomode. Most single mode fibers have core diameters of 4 - 8  $\mu\text{m}$  and NAs of about 0.2.

Optimizing the coupling of a laser into a monomode fiber requires mode matching theory. The focused laser spot should match the fiber mode diameter. This is in the range of 1 - 1.5 times the fiber core diameter. The converging beam must also be within the acceptance angle determined by the fiber NA.

The key to getting the maximum light through a fiber optic is to use a bright (high radiance) source of appropriate size, and optimize the source to fiber coupling. Lamp brightness is sometimes described by color temperature. Our short arc lamps have color temperatures of more than 5000K while our tungsten halogen lamps have color temperatures as high as 3400K. Our Volume II catalog comprehensively describes the widest range of laboratory light sources available. It also discusses source to fiber coupling and has specific performance data. Here we give some general guidance.

1. Short arc lamps provide the maximum ultraviolet and visible light for fiber optic irradiation. Our xenon arc lamps have intense output from 250 nm to beyond 1000 nm. Our mercury arc lamps have more UV output and strong line outputs at 550 and 580 nm. See the spectra and source sizes in Volume II.

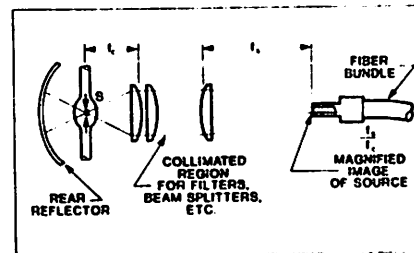


Fig. 1 Collecting the light from a source and re-focusing it on the fiber. The refocused cone should have an  $F/\#$  equal to or greater than the fiber acceptance cone. The refocused image of the source is magnified by the ratio of the focal lengths of the focusing lens to the condenser lens. A typical efficient system for a fused silica fiber collects at  $F/1$  and refocuses at  $F/2$ .

2. Use the dimensions of the fiber to select the size of the light source, arc or filament. Re-imaging optics will magnify the source by  $\sim 1$  for glass bundles and  $\sim 2$  for fused silica bundles. These numbers are based on collecting light at  $F/1$  and refocusing at the fiber  $F/\#$ .

Using a larger size source eases alignment, but produces a lot of unwanted power which may have to be removed. A 50-100 watt arc lamp will give as much power through a single fiber of a 600  $\mu\text{m}$  core as a kW arc lamp since these lamps have similar brightness. The ideal source has a very bright arc about the size of the fiber or fiber bundle.

## FIBER OPTICS AND CONVENTIONAL LIGHT SOURCES

3. Non imaging optics, such as those in our PhotoMax™, the reflectors which are an integral part of the tungsten halogen lamps on page 48 of Volume II, or the conical reflectors described on page 5-10 of this catalog are useful particularly with fiber bundles and Liquid Light Guides. We offer an  $F/2$  reflector for PhotoMax™ to match the acceptance cone of fused silica fibers. With these broadband reflectors you do not need additional focusing optics, but you do need spectral filtering to reduce the power density on the fiber input.

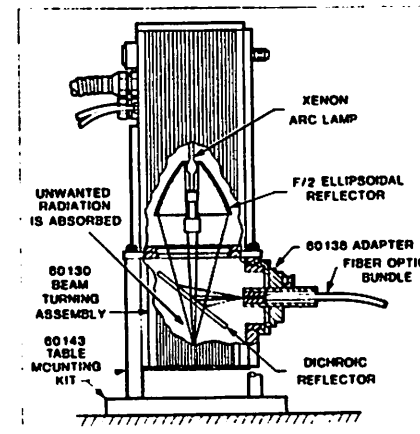
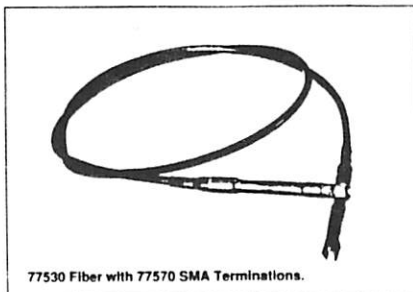


Fig. 2 Using the efficient PhotoMax™ source with an  $F/2$  reflector to focus the output of a 150 watt arc lamp into a fused silica fiber bundle. The dichroic reflector removes unwanted radiation, reducing the power load on the fiber input.

## LARGE CORE OPTICAL FIBERS for UV to NIR



77530 Fiber with 77570 SMA Terminations.

- Transmit from 200 nm to 2 μm
- Core diameters from 200 to 1000 μm
- Available with SMA connectors
- Flexible nylon jacket protects fiber
- Ideal for laser or small bright sources

Single fibers are an economical and convenient method of transferring energy for long distance applications. They can be used for remote sensing or processing with high power lasers. We provide optional SMA connectors to simplify optical coupling to a sample, laser, or detector.

We offer two types of fiber: UV-VIS and VIS-NIR.

### CONSTRUCTION

Our single fibers are available with core diameters from 200 to 1000 μm. They consist of a fiber core with cladding, and a nylon jacket for protection. They may be ordered with bare ends or with SMA terminations.

### ADVANTAGES OVER FIBER BUNDLES

Single fibers have several advantages over fiber bundles. These include:

- Lower transmission losses
- Higher damage threshold
- More economical in long lengths
- Require much smaller apertures and conduits

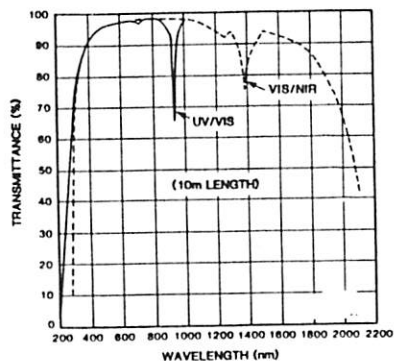


Fig. 1 Transmittance of Oriol UV-VIS and VIS-NIR Single Fibers.

### LIGHT COLLECTION

You cannot use a single fiber for efficient capture and transmission of radiation from large sources. The optical extent of the fibers is too small. Single fibers have major advantages for small sources including high transmittance over long lengths, flexibility, compactness and they are economical. You can mechanically hold several single fibers together for efficient capture of the output of a large arc source. This gives you the advantages of these fibers and efficient light transfer. Pages 8-9 to 8-10 discuss fiber to laser coupling. Page 8-25 describes our single fiber couplers.

### OPTICAL CHARACTERISTICS

Available core sizes range from 200 to 1000 μm (1 mm). Transmittance for both fiber types is shown in Fig. 1. The numerical aperture is 0.22.

### UV-VIS FIBER

This fiber has a high purity UV grade silica core and silica glass cladding. It is usable from 300 to 2000 nm (see Fig. 1 for transmittance curve), and suitable for high power laser beams. The damage threshold for a clean input surface is more than 10 J cm<sup>-2</sup> or 100 W cm<sup>-2</sup> cw for wavelengths above 360 nm.

### VIS-NIR FIBER

This fiber has a water free silica core to reduce absorption in the IR, and depending on the size, is clad with silica or silicone. (See Fig. 1 for transmittance curve.) This is an economical alternative to the UV-VIS Fiber for any application where UV transmittance is not required.

### FIBER OUTPUT

For short straight lengths (< 1 m) of fiber, the output retains many of the characteristics of the beam launched into the fiber. The spectral-spatial distribution may change due to the attenuation of rays launched at an angle. These travel longer distances in the fiber.

For very long lengths of fiber, particularly where the fiber is coiled or bent, the output is determined by the fiber NA. The launch conditions are "forgotten." A central cone, determined by the fiber NA, may be surrounded by a lower intensity high angle output. Fiber bend conditions also have an impact. Fig. 2 shows a scan of the output from the 77512 Fiber coupled to a mercury arc lamp. Fiber length was 5 m.

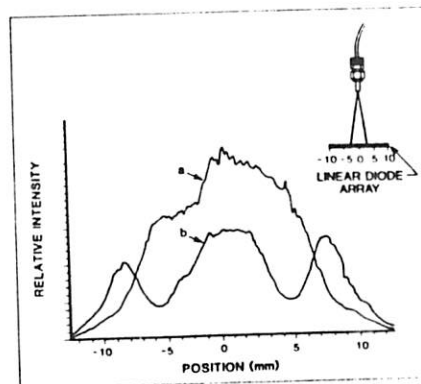


Fig. 2 Linear scan of output patterns from a coiled 5 m length of 77512 UV-VIS Fiber with 77572 SMA connectors. The arc of a 100 W Hg lamp was reimaged on the fiber input. (a) shows the pattern with the arc focused at the fiber input; (b) shows the pattern with the fiber moved 0.5 mm from focus.



SMA terminated single fiber with 6058 Holder for Spectral Calibration Lamps. (See Volume II for 6058.)

### SPECIFICATIONS

Numerical Aperture	0.22 ± 0.02
Refractive Index of Core	1.452 at 850 nm
Refractive Index of Cladding	1.438 at 850 nm
Outer Jacket:	Black Nylon

### ORDERING INFORMATION

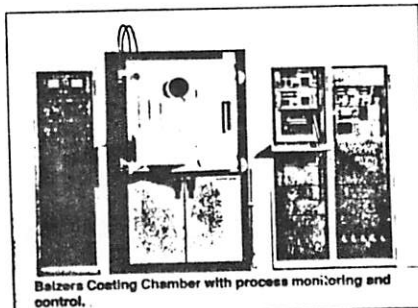
Core Diameter (μm)	Cladding Diameter (μm)	Jacket Diameter (mm)	Minimum Bend Radius (mm)	Maximum Length (m)	Fiber only, without connectors		Price for Terminating Fiber			
					UV-VIS Fiber	VIS-NIR Fiber	2 SMA Connectors	with 2 SMA Connectors**		
Model No.	Price/Meter* (\$)	Model No.	Price/Meter* (\$)	77570	77571	77572	77573	77574		
200	250	1.0	50	500	77530	\$ 15.00	77515	\$ 15.00	77570	\$ 131.00
400	500	1.3	100	200	77511	\$ 45.00	77516	\$ 45.00	77571	\$ 147.00
600	750	1.7	150	50	77512	\$ 92.00	77517	\$ 92.00	77572	\$ 163.00
800	1000	2.0	200	20	77513	\$ 155.00	77518	\$ 148.00	77573	\$ 173.00
1000	1250	2.25	250	20	77514	\$ 298.00	77519	\$ 257.00	77574	\$ 189.00

- \* Multiply length of fiber in meters by price/meter to get the price for fiber with bare unpolished ends. Minimum length is 1 meter.
  - \*\* Find the price for the fiber and add this price to get the total price for fiber terminated with two SMA connectors.  
E.g. To buy 5 meters of 600 μm UV-VIS Fiber terminated with 2 SMA connectors:  
Order 5 meters of 77512 fiber at \$ 92.00/meter, and a 77572 Set of 2 SMA connectors at \$ 163.00, for a total cost of \$ 623.00.
- See page 8-25 for Fiber Holders.

## OPTICAL COATINGS: TECHNICAL DISCUSSION

### OPTICAL COATING TECHNOLOGY

Optical coatings are used to alter the reflectance, transmittance, absorbance, or polarization properties of optical components. The optic being coated is usually called the **substrate**. The coating is deposited in high vacuum ( $< 10^{-6}$  Torr) using the process of evaporation. Coating materials include metals, dielectrics or semiconductors. Oxides, fluorides and sulfides are the most common dielectric materials. Tellurides and selenides are used for specialized applications.



Balzers Coating Chamber with process monitoring and control.

### Evaporation

The coating material must be converted from a solid into a vapor, and then condensed on to the optic surface. The most common methods of vaporization are Thermal Vaporization and Electron Beam Ion Bombardment.

### Thermal Vaporization

In this process the coating material is resistance heated in a tungsten, molybdenum or platinum "boat" for metals and high temperature dielectrics. For some low temperature dielectrics, indirect heating with a refractory filament suffices.

### Electron Beam Ion Bombardment

In this process the coating material is heated by direct electron bombardment. A variable voltage and current (5 - 15 kV at up to several amps) electron beam is concentrated in a very small movable spot in a multi-pocket water cooled copper crucible; different evaporation materials can be contained in the multi-pockets. This method of evaporation is versatile and reduces contamination resulting from interaction between the coating material and the crucible. The heating is localized and temperatures can be high enough to evaporate refractory materials.

### Sputtering

Sputtering is another technique used for thin film deposition. It is particularly useful for large area substrates. The substrate and a target of the material to be deposited are held close together in a plasma chamber. The substrate is cooled. Heavy ions from the plasma bombard the target and knock out small particles of target material. These "condense" on the cooled substrate. Sputtering can quickly produce uniform coatings over large areas, and uses the deposition material more efficiently than evaporation techniques.

### Thickness Control

The control of layer thickness is crucial in optical coating; there are two principal methods used to control layer thickness: interference monitoring, and measuring the resonance of a crystal oscillator.

### Interference Monitoring

Interference thickness monitoring is useful for deposition materials with a well defined refractive index. The technique is useful with dielectrics and some semiconductor materials. Either the transmitted or reflected beams can be monitored. In transmission mode, monochromatic light passes through the substrate being coated and the transmittance is monitored. The transmittance changes as the layer thickness builds up. If the indices of the dielectric are higher than that of the substrate, the transmission gradually decreases. When the optical thickness reaches 1/4 of the monitoring wavelength, the change in transmission momentarily stops.

If evaporation is continued beyond the 1/4 wave thickness, the transmittance increases to the original value and then, again, momentarily stops at the 1/2 wave monitoring thickness. This process could be continued, observing minimum transmissions at 1/4 wave multiples and maximum transmissions at 1/2 wave multiples of the monitoring wavelength.

This evaporation process can be repeated many times using layers of different indices. As the number of layers increases each additional layer produces a smaller change in transmittance or reflectance.

Measurements become more difficult and eventually monitoring is limited by the signal to noise and stability of the monitoring instrument.

In a typical vacuum deposition system, light from a continuous source, a deuterium lamp, tungsten halogen lamp or infrared element, is mechanically chopped, collimated and passed into the vacuum chamber. In the vacuum chamber, the collimated beam is transmitted through a monitoring test plate mounted on a rotating planetary which is on the same plane as the substrates to be coated. The transmitted beam then exits the vacuum chamber and is focused into a monochromator and on to a photodetector. A lock-in amplifier selects the chopped signal from background. The lock-in output is used to observe the transmission minima and maxima.

- Recent trends in thickness monitoring include the use of Oriel's InstaSpec™ Diode Array System and MultiSpec™ Spectrograph for simultaneous monitoring of many wavelengths.
- The Oriel 7340 Dual Source Lamp Housing is widely used for this purpose. It simplifies source interchange.
- The Oriel 77250 Monochromator is incorporated in many vacuum deposition systems.

### Crystal Deposition Rate Monitors

Quartz crystal oscillator monitoring is very often used to control the thickness of metal layers and for dielectric coatings with a few layers. A quartz crystal plate is placed on the same plane as the substrates to be coated. The resonant frequency of the crystal depends on its mass. Monitoring the resonant frequency allows determination of the deposited film thickness. As layers accumulate on the crystal the sensitivity to increasing thickness diminishes and film stresses complicate the relationship between resonant frequency and layer thickness. Because of this, the quartz crystal oscillator type of monitoring is usually limited to several layers.

### HOW OPTICAL COATINGS WORK

#### Reflection From Uncoated Optics

When light is incident to a smooth surface between two transparent media as in Fig. 1, some of the light enters the second media and is refracted, and some is reflected at the interface. The relationship between the angle of incidence (i), and the angle of refraction (r) is given by Snell's law:

$$n_1 \sin i = n_2 \sin r \dots\dots\dots (1)$$

Where:

$n_1$  and  $n_2$  = Indices of refraction of the media as shown

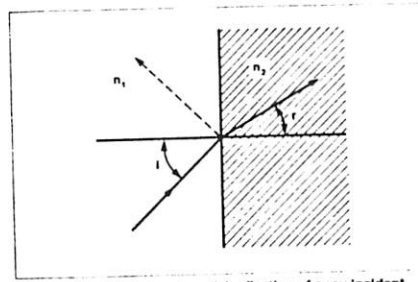


Fig. 1 Refraction and partial reflection of a ray incident at angle i in an interface between two media, one of refractive index  $n_1$  and the other  $n_2$ .  $r$  is the angle of refraction.

Reflectance depends on the indices of refraction of the materials involved, and the angle of incidence and polarization of the incident light:

$$R_p = \frac{\tan^2(i - r)}{\tan^2(i + r)} \dots\dots\dots (2)$$

$$R_s = \frac{\sin^2(i - r)}{\sin^2(i + r)} \dots\dots\dots (3)$$

Where:

- $R_p$  = Reflectance of light polarized parallel to the plane of incidence (p polarized)
- $R_s$  = Reflectance of light polarized perpendicular to the plane of incidence (s polarized)

At normal incidence, these equations reduce to:

$$R = R_p = R_s = \left[ \frac{n_2 - n_1}{n_2 + n_1} \right]^2 \dots\dots\dots (4)$$

At normal incidence for an air-glass system where  $n_1 = 1.0$  and  $n_2 = 1.5$ ,  $R = 0.04$  for each surface or  $\sim 0.08$  for the two surfaces. In an optical system with 8 glass ( $n_2 = 1.5$ ) optical elements there will be a reflection loss of  $1 - (.96)^8$  or 47.9%, and possible ghost images. Anti-reflection coatings will reduce both the loss and the ghosts.

From (4) we can also see that for a surface in air, ( $n_1 = 1$ ), the reflectance increases as  $n_2$  increases.

Note that the reflected wave undergoes a phase change of  $180^\circ$  if  $n_1 > n_2$ . This phase change upon reflection is important in optical coating.

#### Single Layer Anti-reflection Coatings

Fig. 2 shows a 1/4 wave optical thickness of a transparent dielectric material deposited on the surface of glass. At normal incidence there will be reflection from the air-dielectric and dielectric-glass boundaries. If the dielectric material has an index lower than the glass, the two reflections will be from a medium having an index greater than the one in which the light was traveling. Because of the 1/4 wave optical thickness of the dielectric layer, the two reflections will be  $180^\circ$  out of phase with each other, causing destructive interference. As shown in Fig. 3, the 1/4 wave optical thickness of dielectric reduces the total reflectance.

If the optical thickness of the layer is not an odd multiple of 1/4 wave, then the two reflections are not  $180^\circ$  out of phase and the interference is not totally destructive. The reflectance will be greater than the minimum (Fig. 3). For an optical thickness of a half wave, the phase change is  $360^\circ$ . This is equivalent to not having any layer, so the reflectance is the same as that of the bare substrate.

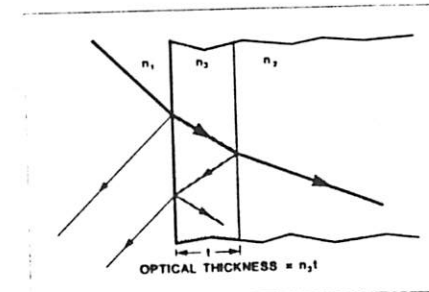


Fig. 2 Transparent thin film coating showing reflection from the air-dielectric-glass interfaces.

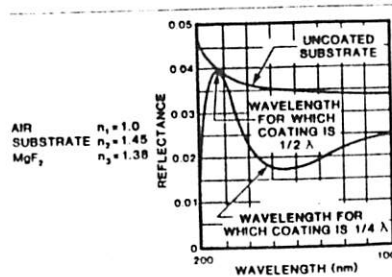


Fig. 3 1/4 wave thick AR coating of magnesium fluoride on a fused silica substrate reduces the reflection from 4% to  $< 2.0\%$  at the design wavelength.



## OPTICAL COATINGS: TECHNICAL DISCUSSION

### How much is the reflectance reduced?

The positions of the minima and maxima in Fig. 3 depend on the film optical thickness; i.e. thickness times refractive index. The reflectance, at normal incidence, for any 1/4 wave thick coating on a non absorbing substrate is given by:

$$R = \frac{(n_1 n_2 - n_3^2)^2}{(n_1 n_2 + n_3^2)^2} \dots \dots \dots (5)$$

This is 0 for  $n_3^2 = n_1 n_2 \dots \dots (6)$

For air ( $n_1 = 1.0$ ), and glass ( $n_2 = 1.5$ ) the ideal value for  $n_3$  would be 1.22. Unfortunately, a dielectric material having an index of refraction of 1.22 with desirable mechanical, environmental and optical properties does not exist.  $MgF_2$  with an index of 1.38 is a good compromise as a relatively hard and durable anti-reflection coating.

For BK7/A, ( $n_2 = 1.5167$ ) and magnesium fluoride ( $n_3 = 1.38$ ), R is about 0.0128. A 1/4 wave coating of magnesium fluoride on a flint glass of index  $n_2 = 1.7$  reduces the reflectance from 0.067 to 0.003.

Further reduction in reflectance is possible by using a multi-layer V coat such as those on page 10-7.

### Wavelength dependence

Since the optical thickness can only be 1/4 wave for one wavelength, the reflectance depends on the wavelength of the incident light. Fig. 3 shows the computed wavelength dependence at normal incidence for a 1/4 wave coating. Reflectance is reduced over a large part of the visible by designing the coating for a wavelength of 550 nm. The reflectance increases in the red and blue, giving the surface a slight purple tinge when viewed in white light. This resembles the bloom on ripe plums and so application of this type of coating is sometimes called **blooming**.

### Angle of incidence

The change in reflectance which occurs with the application of a thin film coating is not only wavelength dependent, it is also angle of incidence dependent. At off-normal incident angles the expressions for calculating reflectance become more complicated and also differ for s and p polarized incident light. Angles of incidence of up to about 25° shift the reflectance curve to slightly shorter wavelengths. A single 1/4 wave thick (at 550 nm) layer of  $MgF_2$  will provide an average of less than 2% reflection from 400 to 700 nm for angles of incidence up to 25° for unpolarized light.

### Multi-layer Anti-reflection Coatings

There are several ways of improving the efficiency and wavelength range of anti-reflection coatings. Most of these techniques involve the use of multi-layer coatings. One of the simplest is the double quarter layer. Two quarter wave layers of different materials are used. The reflectance from a two layer AR system at normal incidence is given by:

$$R_{min} = \frac{(n_1^2 n_2 - n_3^2)^2}{(n_1^2 n_2 + n_3^2)^2} \dots \dots \dots (7)$$

where the layer indices are shown in Fig. 4

This has a minimum at  $n_3 = n_1 n_2 / n_2 \dots \dots (8)$

Since  $n_1$  is usually  $\approx 1$ ,  $n_3 > n_2$  to satisfy (8).



Fig. 4 Layer indices of a multi-layer coating.

This double AR coating on glass is often designated by gHLA. (glass, high index, low index, air). Materials such as zirconium dioxide ( $n = 2.1$ ) zinc sulfide ( $n = 2.32$ ), or titanium dioxide ( $n = 2.4$ ), are used as H layers while magnesium fluoride ( $n = 1.38$ ) or cerium fluoride ( $n = 1.63$ ) may be used as L layers.

An alternate method of multi-layer anti-reflection coating involves the use of a single dielectric with layers having different thicknesses (Fig. 5). In a typical example of this type of coating the first layer is 1/4 wave thick  $MgF_2$  at 450 nm. The second layer is a so called "absentee" layer which returns the index of refraction back to that of the substrate. The third layer is 1/4 wave thick of  $MgF_2$  at 900 nm. This third layer is not only 1/4 wave thick at 900 nm, it is also 1/2 wave thick at 450 nm. The result is a coating which has two minimum reflection wavelengths: 450 and 900 nm and lower (than a single 1/4 wave coating) reflection at intermediate wavelengths.

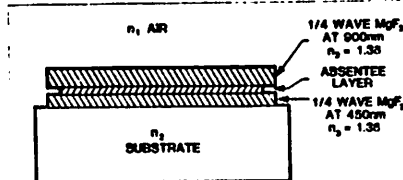


Fig. 5 Multi-layer AR Coating using a single dielectric with different thickness layers, and an absentee layer in between.

The ideal anti-reflection coating would be completely effective, reducing surface loss to zero, wavelength independent, angle of incidence independent, polarization state independent, able to tolerate high power densities, and inert. Unfortunately, such a coating does not exist. There is however always a "best coating" for your application. This may be anything from a simple and inexpensive quarter-layer coating to a computer optimized multi-layer with tens of layers. Computer modeling the many variables in optical coating, and knowledge of the film properties, adherence, stresses, durability, etc., allows the coater to design the coating for the application. There are many multi-layer anti-reflection coating designs already available, each of which tends to optimize a particular parameter.

### DIELECTRIC REFLECTOR COATINGS

Equation 5 gives the reflectance at normal incidence for a 1/4 wave layer on a substrate. If the dielectric layer has a refractive index ( $n_3 = 2.32$ ) higher than that of the glass substrate, the reflectance of the quarter wave layer is 0.314, much higher than the 0.042 from the bare substrate.

If now a second layer having an index lower than the first layer is deposited, this second layer acts as an anti-reflection coating for the first layer, decreasing the reflectance. If a third layer is added with a material having an index higher than the second layer, this last layer acts as a reflector layer to the second layer, increasing total reflectance. In this way the reflectance can be built up from the 0.042 from the glass surface to close to 1.

In the air - glass system, 13 layers of alternating high index material ( $n_3 = 2.2$ ) and low index material ( $n_4 = 1.35$ ) produces a 0.999 reflectance at the wavelength where the layers are 1/4 wave optically thick (Fig. 6). This reflector is now substantially wavelength dependent; at wavelengths above and below the 1/4 wavelength the reflectance decreases.

In the alternating high and low index refraction stacks, manipulation of the number of layers, layer thickness and materials can produce: long pass filters, short pass filters, cold and hot mirrors, maximum and partial reflectors and beam splitters.

As a custom service we can coat substrates with Dielectric Reflector Coatings. Contact us for a quote.

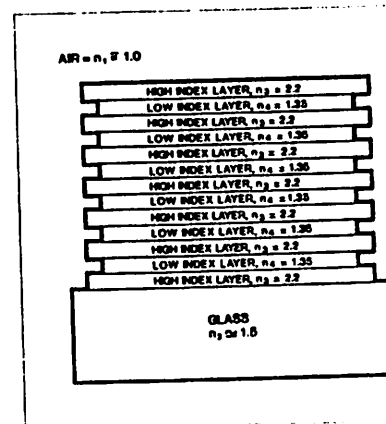


Fig. 6 13 layer multi-layer dielectric coating. This coating has a 99.9% reflectance at the design wavelength.

Fig. 7 shows the reflectance of a typical multi-layer reflector. Maximum reflector coatings at different wavelengths can be superimposed to increase the range of high reflectance. Other variants include making one or more stacks a different odd multiple times 1/4 wave thick to block a specific order, and slightly varying the layer thickness from 1/4 wave in a controlled fashion to increase the high reflectance bandwidth. We use this technique for our broadband reflectors on page 5-8.

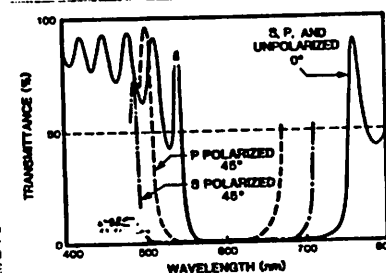


Fig. 7 Typical transmittance of a multi-layer dielectric reflector coating at 0 and 45° incidence.

### METAL REFLECTOR COATINGS

In metal reflector coatings the main considerations are: reflectance, durability, hardness, adherence, uniformity and long term stability. Metal reflector coatings are deposited under stringently clean high vacuum conditions. The optic to be coated is first cleaned in a series of ultrasonic baths (detergent, de-ionized distilled water, and reagent grade organic solvents). Then the optic is air dried in a dust-free environment. In the vacuum chamber, the optic is heated and further cleaned by ion bombardment glow discharge.

We offer the following metal coatings:

- Bare aluminum
- Aluminum with  $SiO_2$  overcoat
- Aluminum with  $MnF_2$  overcoat
- Graded Chrome - Gold
- Silver with overcoat

See pages 10-8 to 10-9.

### BEAM SPLITTER COATINGS

These coatings are offered only for flat optics such as windows, flats etc. The following coatings are offered:

- Inconel metal in a thickness which gives a spectrally neutral coating with a 32/32 beam splitting ratio from 400 - 700 nm. (Absorption  $\approx 0.36$ )
- All dielectric beam splitter coatings for 425 - 700 nm. Four R/T ratio coatings are available: 20/80, 30/70, 50/50 and 70/30.

See page 10-10 for a detailed listing.



## ANTI-REFLECTION COATINGS

### SINGLE LAYER BROADBAND AR COATING FOR GLASS AND FUSED SILICA

Magnesium fluoride is an excellent, inexpensive anti-reflection coating for windows, lenses, and beam splitters. A layer of  $MgF_2$  on a glass or fused silica substrate reduces surface reflectance to less than 1.5% per surface over a wide spectral band. See Fig. 1.

We offer single layer  $MgF_2$  anti-reflection coatings to cover five spectral ranges from the ultraviolet to the near infrared.

The thickness of the  $MgF_2$  layer is 1/4 wave at the mid point of the wavelength range, e.g. the 400 to 700 nm, 79710 Coating is 1/4 wave thick at 550 nm.

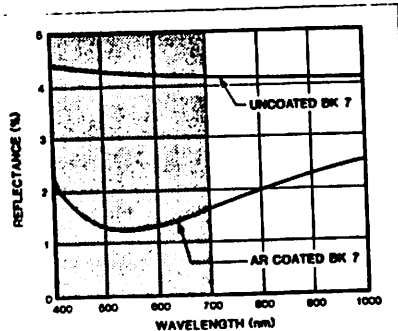


Fig. 1 Reflectance of a BK 7 surface coated with 1/4 wave thick layer of  $MgF_2$  centered at 550 nm.

#### SPECIFICATIONS

**Material:**  $MgF_2$   
**Refractive index:** 1.377 @ 589 nm  
**Reflectance:** Depends on the refractive index of the coated material. The curve on page 10-3 shows the data for fused silica with 1/4 wave coating at 550 nm.  
**Mil spec compliance:** Meets or exceeds Abrasion, Mil-C-675A Adhesion, Mil-M-13508C Hardness, Mil-M-13508C  
**Incident angle:** 0° to 20°

#### ORDERING INFORMATION

Wavelength Range (nm)	Model No.	Prices	
		Run Charge*	Piece Price**
250 to 400	79700	\$150.00	\$15.00
400 to 700	79710	\$150.00	\$15.00
700 to 1100	79715	\$150.00	\$15.00
1100 to 1700	79718	\$150.00	\$15.00
1700 to 2500	79719	\$150.00	\$15.00

\* Cost for coating each surface.  
 \*\* Cost for coating each optic.

These prices are for up to 2.0 inch (50.8 mm) diameter optics. For larger sizes contact OriTel for a quote.

### SINGLE LAYER BROADBAND AR COATING FOR ZINC SELENIDE AND ZINC SULFIDE

Because of their high index of refraction, zinc selenide and zinc sulfide have high surface reflection losses. ZnSe has an index of refraction of 2.4 at 10.6  $\mu m$ ; reflection losses are = 17% per surface. ZnS has an index of refraction of 2.2 at 10.6  $\mu m$ , and reflection losses of = 14% per surface.

A single 1/4 wave layer of Barium Fluoride can reduce the reflection loss to  $\leq 2\%$  per surface for ZnSe and for ZnS. See Fig. 2.

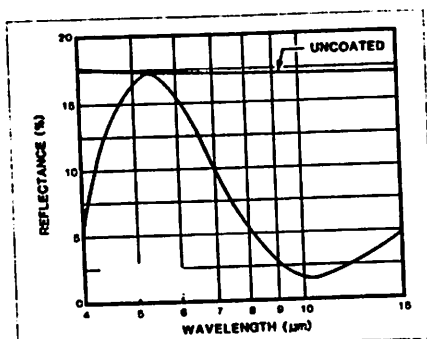


Fig. 2 Single surface reflectance from ZnSe coated with 1/4 wave of  $BaF_2$  at 10.6  $\mu m$ .

#### SPECIFICATIONS

**Material:**  $BaF_2$   
**Refractive Index:** 1.4 @ 10.6  $\mu m$   
**Reflectance:** ZnSe:  $< 1.5\%$  @ 10.6  $\mu m$   
 ZnS:  $< 0.5\%$  @ 10.6  $\mu m$   
**Mil spec compliance:** Meets or exceeds Abrasion, Mil-C-675A Adhesion, Mil-M-13508C Hardness, Mil-M-13508C  
**Incident angle:** 0° to 20°

#### ORDERING INFORMATION

Wavelength Range (nm)	For Materials	Model No.	Prices	
			Run Charge*	Piece Price**
9.5 to 12	ZnSe	79750	\$775.00	\$25.00
9 to 13	ZnS	79755	\$775.00	\$25.00

\* Cost for coating each surface.  
 \*\* Cost for coating each optic.

### ELECTRON BEAM BROADBAND MULTI-LAYER ANTI-REFLECTION COATINGS

These electron beam deposited multi-layer dielectric coatings are designed for minimum reflectance. Reflection losses are reduced to  $\leq 0.5\%$  per surface for the specified wavelength range. These coatings are extremely durable and withstand up to  $2J/cm^2$  in 10 ns pulses.

Because of the high number of layers, these coatings are more sensitive to incident angle than the single layer anti-reflection coatings. We offer these coatings for normal and 45° incidence.

These coatings are for fused silica substrates and lenses.

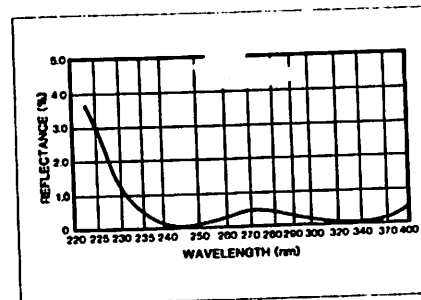


Fig. 3 Transmittance of 79700 Coating on a fused silica surface.

#### SPECIFICATIONS

**Material:** Multi-layer dielectrics  
**Reflectance:**  $\leq 0.5\%$  surface avg over the wavelength range specified  
**Mil spec compliance:** Meets or exceeds Abrasion, Mil-C-675A Adhesion, Mil-M-13508C Hardness, Mil-M-13508C  
**Incident angle:** 0°,  $\pm 10^\circ$  or 45°,  $\pm 10^\circ$

#### ORDERING INFORMATION

Wavelength Range (nm)	Angle of Incidence (degrees)	Model No.	Prices
250 to 400	0	79700	Contact OriTel
400 to 700	0	79710	
700 to 850	0	79711	
250 to 400	45	79712	
400 to 700	45	79713	
700 to 850	45	79714	

### ELECTRON BEAM NARROW BAND MULTI-LAYER ANTI-REFLECTION COATINGS ("V" COATINGS)

These multi-layer dielectric coatings reduce surface reflections to  $\leq 0.25\%$  for a single wavelength. We offer them for 632.8 nm; other wavelengths are available on special request. Like the broadband multi-layer coatings, these are sensitive to angle of incidence. We offer a 0° and 45° coating. For "V" Coatings at other wavelengths contact us.

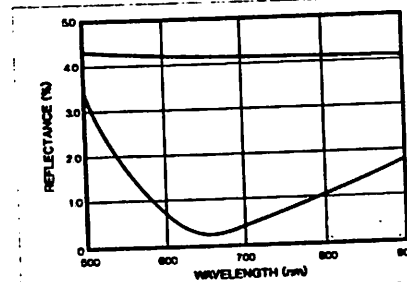


Fig. 4 Transmittance of 79655 Coating on a fused silica surface.

#### SPECIFICATIONS

**Material:** Multi-layer dielectrics  
**Reflectance:**  $\leq 0.25\%$  surface max.  
**Mil spec compliance:** Meets or exceeds Abrasion, Mil-C-675A Adhesion, Mil-M-13508C Hardness, Mil-M-13508C  
**Incident angle:** 0°,  $\pm 5^\circ$  or 45°,  $\pm 5^\circ$

#### ORDERING INFORMATION

Wavelength (nm)	Angle of Incidence (degrees)	Model No.	Price	
			Run Charge*	Piece Price**
632.8	0	79650	\$ 275.00	\$ 15.00
632.8	45	79655	\$ 275.00	\$ 15.00

\* Cost for coating each surface.  
 \*\* Cost for coating each optic.

These prices are for up to 2.0 inch (50.8 mm) diameter optics. For larger sizes contact OriTel for a quote.

## METALLIC REFLECTOR COATINGS

Vacuum deposited thin films of several different metals make excellent reflectors. It is difficult to polish metal substrates to the smoothness required for specular reflectance in the visible and ultraviolet, so most metallic reflectors are made by applying a thin metal film to a highly polished glass substrate. We call these coatings metallic reflector coatings to distinguish them from dielectric reflector coatings.

Metallic reflector coatings are inexpensive, cover a broad spectral range, and have good reflectance (there is some loss due to absorption). Some metal coatings, such as aluminum and silver, tarnish rapidly, and reflectance drops significantly. If the optic is to be used as a first surface reflector a protective overcoat is strongly recommended. Fig. 1 shows a first surface and second surface reflector.

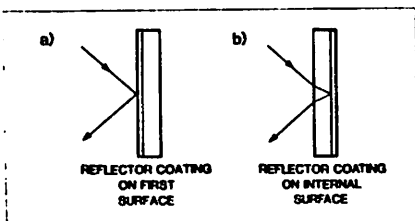


Fig. 1 First surface reflector (a), and second surface reflector (b).

### BARE ALUMINUM COATING

Freshly deposited aluminum has an average of 90% reflectivity between 200 and 1000 nm, with an absorption band (85% R) at 820 nm. From 1.0 to 30  $\mu\text{m}$ , reflectivity is 94% to 99%.

A thin oxide coating forms quickly on aluminum exposed to air. UV reflectance falls due to the oxide coating, and deterioration of overall reflectance results from continued exposure to chemicals in the atmosphere. We recommend a bare aluminum coating only for second surface reflectors.

### SPECIFICATIONS

Material: Bare aluminum  
 Reflectance: See curve (Fig. 2)  
 Meets or exceeds  
 Mi spec compliance: Abrasion, MI-C-675A  
 Adhesion, MI-M-13508C  
 Hardness, MI-M-13508C  
 Incident angle: 0 to 45

79950 Bare Aluminum Coating.....	\$ 90.00 Run Charge*
	\$ 19.00 Piece Price**

- \* Cost for coating each surface.
- \*\* Cost for coating each optic.

These prices are for up to 2.0 inch (50.8 mm) diameter optics. For larger sizes contact Oriel for a quote.

### ALUMINUM WITH PROTECTIVE SiO OVERCOAT

Overcoating aluminum with silicon monoxide (SiO) produces an excellent general purpose, broadband reflector for the visible and infrared. The reflectivity of this coating is between 85 and 90% from 400 nm to 20  $\mu\text{m}$  with a dip to ~75% at around 825 nm. This coating is much more durable than bare aluminum, but can still be easily scratched; care must be used in handling. The coated optic may be cleaned using a soft optical cloth. We list cleaning supplies on pages 11-1 to 11-3.

### SPECIFICATIONS

Material: Aluminum with SiO overcoat  
 Reflectance: See curve (Fig. 2)  
 Meets or exceeds  
 Mi spec compliance: Abrasion, MI-C-675A  
 Adhesion, MI-M-13508C  
 Hardness, MI-M-13508C  
 Incident angle: 0 to 45

79990 Aluminum with Silicon Monoxide Overcoat.....	\$ 120.00 Run Charge*
	\$ 19.00 Piece Price**

- \* Cost for coating each surface.
- \*\* Cost for coating each optic.

### UV ALUMINUM COATING

This aluminum coating has a protective layer of magnesium fluoride. The MgF<sub>2</sub> overcoat prevents oxidation and ensures high reflectance from the UV to the infrared.

This coating is easily scratched, and must be cleaned carefully. See pages 11-1 to 11-3 for cleaning supplies.

### SPECIFICATIONS

Material: Aluminum with MgF<sub>2</sub> overcoat  
 Reflectance: See curve (Fig. 2)  
 Meets or exceeds  
 Mi spec compliance: Abrasion, MI-C-675A  
 Adhesion, MI-M-13508C  
 Hardness, MI-M-13508C  
 Incident angle: 0 to 45

79920 Aluminum with Magnesium Fluoride Overcoat.....	\$ 145.00 Run Charge*
	\$ 22.00 Piece Price**

- \* Cost for coating each surface.
- \*\* Cost for coating each optic.

### GRADED CHROME - GOLD COATING

Gold is an excellent reflector from the near IR (800 nm) to the far IR (30  $\mu\text{m}$ ); in this region reflectivity exceeds 98%. Beyond 1.5  $\mu\text{m}$ , reflectance is greater than 99%. Unlike aluminum, gold is resistant to surface oxidation, but it is extremely soft and care should be used in handling and cleaning. Clean a gold coated optic using a non-contact flow of water, organic solvent and clean dry air.

Gold adheres poorly to most types of glasses. An intermediate layer of chromium, which adheres strongly to glass optics, is required. We apply a thin layer of chromium to the optic, and then deposit the gold. The result is a coating that is pure chrome, chrome with gold, and pure gold.

### SPECIFICATIONS

Material: Graded Chromium - Gold  
 Reflectance: See curve  
 Meets or exceeds  
 Mi spec compliance: Abrasion, MI-C-675A  
 Adhesion, MI-M-13508C  
 Hardness, MI-M-13508C  
 Incident angle: 0 to 45

79930 Graded Chromium Gold Coating.....	\$ 675.00 Run Charge*
	\$ 60.00 Piece Price**

- \* Cost for coating each surface.
- \*\* Cost for coating each optic.

### SILVER WITH DIELECTRIC OVERCOAT

As bare silver tarnishes rapidly in air and the reflectance falls quickly, we only recommend bare silver for internal or second surface reflectors. We offer an efficient dielectric protected silver coating as a first surface reflector. A layer of magnesium fluoride protects the silver from degradation.

The 79938 has high visible and infrared reflectance and is durable. You can clean it with our 49122 Metallic Reflector Cleaning Fluid described on page 11-1.

On special order we can coat your transparent optics with an internal silver reflector coating. The silver is deposited on the surface and overcoated with a protective black paint. You should consider an anti-reflection coating on the entrance surface of any internal reflector.

### SPECIFICATIONS

Material: Ag (MgF<sub>2</sub>)  
 Reflectance: See curve  
 Meets or exceeds  
 Mi spec compliance: Abrasion, MI-C-675A  
 Adhesion, MI-M-13508C  
 Hardness, MI-M-13508C  
 Incident angle: 0 to 45

79938 Silver with Dielectric Overcoat.....	\$ 195.00 Run Charge*
	\$ 40.00 Piece Price**

- \* Cost for coating each surface.
- \*\* Cost for coating each optic.

These prices are for up to 2.0 inch (50.8 mm) diameter optics. For larger sizes contact Oriel for a quote.

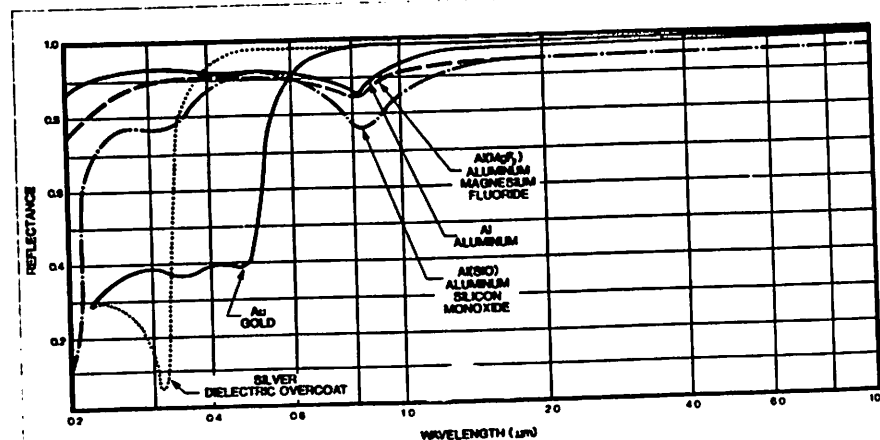


Fig. 2 Typical near normal incidence reflectance of our metallic reflector coatings. The reflectance of the aluminum coating falls rapidly in the ultraviolet when it is exposed to air.

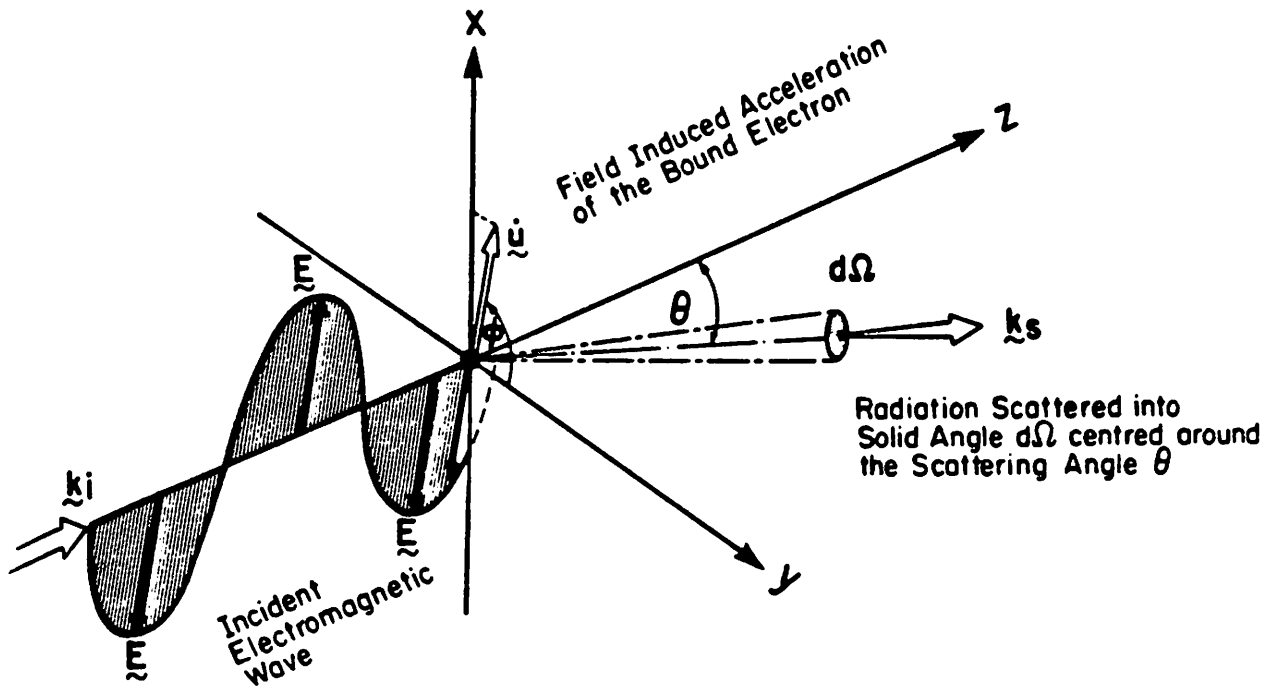


Fig. 2.15. Angular configuration for scattering of electromagnetic radiation from a bound electron.

$$\sigma_R(\lambda) = \frac{8\pi}{3} \left[ \frac{\pi^2(n^2 - 1)^2}{N^2\lambda^4} \right] \quad (2.132)$$

$$\sigma_\pi^R \equiv \frac{d\sigma_R(\theta = \pi)}{d\Omega} = \frac{\pi^2(n^2 - 1)^2}{N^2\lambda^4} \quad (2.133)$$

$$\sigma_\pi^R(\lambda) = 5.45 \left[ \frac{550}{\lambda(\text{nm})} \right]^4 \times 10^{-28} \text{ cm}^2 \text{ sr}^{-1} \quad (2.134)$$

$$\beta_\pi^R(\lambda) \equiv N\sigma_\pi^R(\lambda) = 1.39 \left[ \frac{550}{\lambda(\text{nm})} \right]^4 \times 10^{-8} \text{ cm}^{-1} \text{ sr}^{-1} \quad (2.135)$$

TABLE 2.3. RAYLEIGH BACKSCATTERING CROSS SECTION  $\sigma_{\pi}^R$  AT 694.3 nm

Gas	Formula	$\sigma_{\pi}^R$ ( $10^{-28} \text{ cm}^2 \text{ sr}^{-1}$ )	Ref.
Hydrogen	H <sub>2</sub>	0.44	<i>a, b</i>
Deuterium	D <sub>2</sub>	0.43	<i>a</i>
Helium	He	0.03	<i>a, b</i>
Oxygen	O <sub>2</sub>	1.80	<i>b</i>
Nitrogen	N <sub>2</sub>	2.14	<i>a, b</i>
Carbon dioxide	CO <sub>2</sub>	6.36	<i>b</i>
Methane	CH <sub>4</sub>	4.60	<i>a, b</i>
Nitrous oxide	N <sub>2</sub> O	6.40	<i>a</i>
Neon	Ne	0.09	<i>b</i>
Argon	Ar	2.00	<i>a, b</i>
Xenon	Xe	11.60	<i>a</i>
Freons—important to stratospheric studies:			
Freon-12	CCl <sub>2</sub> F <sub>2</sub>	36.08	<i>b</i>
Freon-13B1	CBrF <sub>3</sub>	24.87	<i>b</i>
Freon-14	CB <sub>4</sub>	4.91	<i>b</i>
Freon-22	CHClF <sub>2</sub>	21.90	<i>b</i>

<sup>a</sup>Rudder and Bach (1968).<sup>b</sup>Shardanand and Prasad Rao (1977).

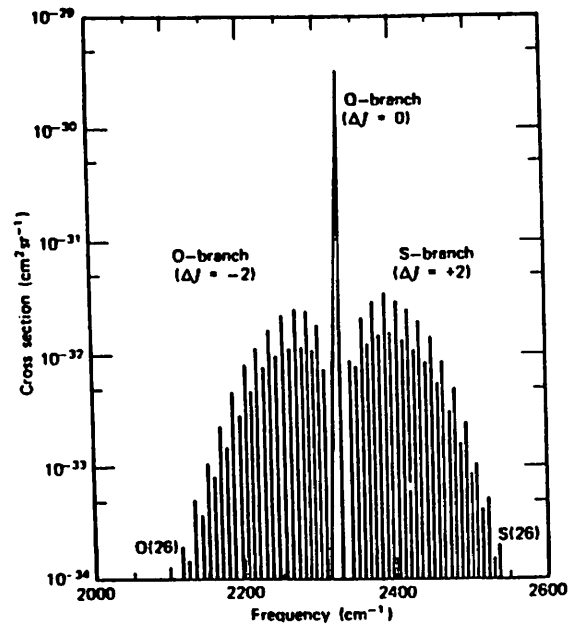


Fig. 3.21. Theoretical distribution of vibrational-rotational Raman spectrum ( $\nu = 0 \rightarrow 1$  vibrational transition) at 300 K, showing the O-, Q-, and S-branch structures and the differential Raman-scattering cross section for  $N_2$  molecules (Inaba and Kobayasi, 1972).

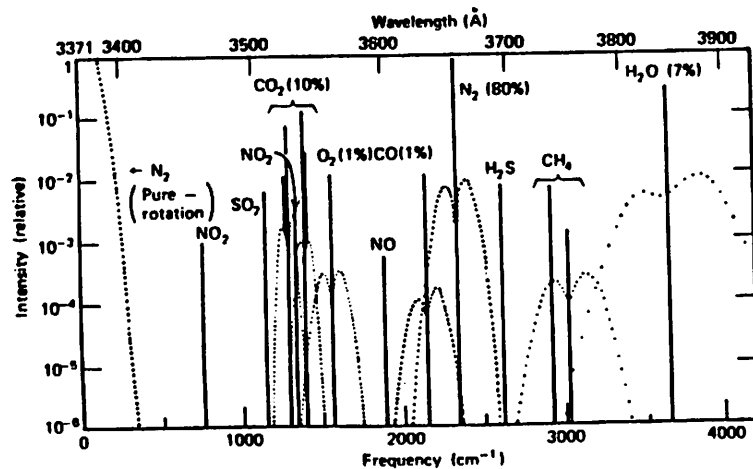


Fig. 3.22. Theoretical distribution of Raman volume backscattering coefficient due to a molecular mixture contained in a typical oil smoke as a function of Raman-shifted frequency (Inaba and Kobayasi, 1972).

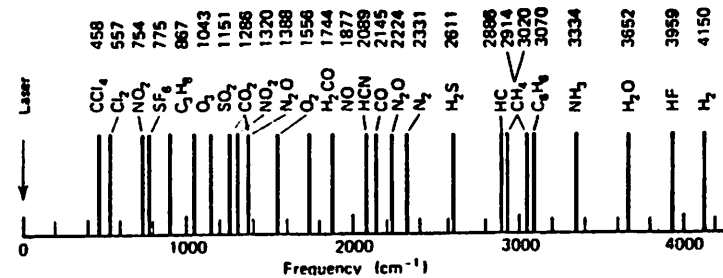


Fig. 3.23. Frequency shifts of the Q-branch of vibrational-rotational Raman spectra of typical molecular species present in polluted as well as ordinary atmosphere relative to the exciting laser frequency (Inaba and Kobayasi, 1972).

TABLE 3.3. RAMAN (Q, O + S BRANCHES, AND TOTAL), PURE-ROTATION RAMAN, AND RAYLEIGH BACKSCATTERING CROSS SECTIONS\*

Molecule	Raman Shift $\omega_j/2\pi c$ ( $cm^{-1}$ )	$d\sigma/d\Omega$ ( $cm^2 sr^{-1}$ )					
		Q-branch	O + S Branches	Total	Rayleigh	Pure Rotation	Total
$N_2$	2329.66	$2.9 \times 10^{-30}$	$5.5 \times 10^{-31}$	$3.5 \times 10^{-30}$	$3.9 \times 10^{-27}$	$1.1 \times 10^{-28}$	$4.0 \times 10^{-27}$
$O_2$	1556.26	$3.3 \times 10^{-30}$	$1.3 \times 10^{-30}$	$4.6 \times 10^{-30}$	$3.3 \times 10^{-27}$	$2.0 \times 10^{-28}$	$3.5 \times 10^{-27}$
$CO_2(\nu_1)$	1388.15	$3.4 \times 10^{-30}$	$7.3 \times 10^{-31}$	$4.2 \times 10^{-30}$	$9.0 \times 10^{-27}$	$8.3 \times 10^{-28}$	$9.9 \times 10^{-27}$
$CH_4(\nu_1)$	2914.2	$2.1 \times 10^{-29}$	0	$2.1 \times 10^{-29}$	$8.6 \times 10^{-27}$	0	$8.6 \times 10^{-27}$

\*Based on the polarizability tensor theory of Placzek (1934); reproduced from Inaba (1976).

TABLE 3.4. RAMAN WAVE-NUMBER SHIFTS AND MEASURED DIFFERENTIAL RAMAN BACKSCATTERING CROSS SECTIONS APPROPRIATE FOR 337.1-nm EXCITATION\*

Molecule	Raman Shift (cm <sup>-1</sup> )	Raman-Shifted Wavelength (nm)	Raman Differential Cross Section (10 <sup>-30</sup> cm <sup>2</sup> sr <sup>-1</sup> )	Cross Section Relative to Q-branch of N <sub>2</sub>	Ref. <sup>b</sup>
Freon 114 <sup>c</sup>	442	342.2	4.2(P)	1.49(P)	1
CCl <sub>4</sub>	459	342.4	26.0	9.3	2
Freon C-318 <sup>d</sup>	699	345.2	7.8(P)	2.77(P)	1
NO <sub>2</sub> (ν <sub>2</sub> )	754	345.7	24.0	8.6	3
SF <sub>6</sub>	775	346.1	12.0	4.3	2
Freon 116 <sup>e</sup>	807	346.5	7.3(P)	2.6(P)	1
Freon 114 <sup>f</sup>	908	347.7	5.3(P)	1.9(P)	1
C <sub>6</sub> H <sub>6</sub> (ν <sub>2</sub> )	991	348.7	44.0	15.7	2,3
O <sub>3</sub>	1103.3	350.2	6.4	2.3	4
SO <sub>2</sub>	1151.5	350.8	17.0	6.1	3,5
CO <sub>2</sub> (2ν <sub>2</sub> )	1285	352.5	3.1	1.1	2,3
NO <sub>2</sub> (ν <sub>1</sub> )	1320	352.8	51.0	18.2	3
CO <sub>2</sub> (ν <sub>1</sub> )	1388	353.7	4.2	1.5	2,3
O <sub>2</sub>	1556	355.9	4.6	1.6	2,3
			3.3(Q)	1.2(Q)	2,3
C <sub>2</sub> H <sub>4</sub> (ν <sub>2</sub> )	1623	356.6	5.4(Q)	1.9(Q)	2
NO	1877	360.0	1.5	0.54	3,5
CO	2145	363.5	3.6	1.3	2,3
N <sub>2</sub>	2330.7	365.9	3.5	1.3	2,6
			2.8(Q)	1.0(Q)	2,6
H <sub>2</sub> S	2611	369.7	19.0	6.8	2,5
CH <sub>3</sub> OH (ν <sub>2</sub> )	2846	372.8	14.0	5.0	2,3
C <sub>3</sub> H <sub>12</sub>	2885	373.4	124.0(C)	44.3(C)	1
C <sub>3</sub> H <sub>8</sub>	2886	373.4	81.8(C)	29.2(C)	1
C <sub>4</sub> H <sub>14</sub>	2886	373.4	134.0(C)	48.0(C)	1
C <sub>4</sub> H <sub>10</sub>	2890	373.5	93.5(C)	33.4(C)	1
CH <sub>4</sub>	2914	373.8	32.2(C)	11.5(C)	1
—(ν <sub>1</sub> )			21.0	7.5	2,3,6
C <sub>3</sub> H <sub>10</sub>	2941	374.2	102.5(C)	36.6(C)	1
C <sub>3</sub> H <sub>6</sub>	2942	374.2	63.6	22.7	1
C <sub>2</sub> H <sub>5</sub> OH	2943	374.2	19.0	6.8	2,3
CH <sub>3</sub> OH (2ν <sub>6</sub> )	2955	374.4	7.5	2.7	2,3
C <sub>4</sub> H <sub>8</sub>	3010	375.2	89.6(C)	32.0	2
CH <sub>4</sub> (ν <sub>3</sub> )	3017	375.3	14.0	5.0	2,3
C <sub>2</sub> H <sub>4</sub>	3020	375.3	28.6	10.2	1
—(ν <sub>1</sub> )			16(Q)	5.7(Q)	2
C <sub>4</sub> H <sub>10</sub>	3064	375.9	87.9(C)	31.4(C)	1
C <sub>6</sub> H <sub>6</sub> (ν <sub>1</sub> )	3070	376.0	30.0	10.7	2,3
C <sub>6</sub> H <sub>6</sub>	3072	376.0	65.2	23.3	1
NH <sub>3</sub>	3334	379.8	11.0	3.9	2
C <sub>2</sub> H <sub>2</sub>	3372	380.3	3.36	1.2	1
H <sub>2</sub> O	3651.7	384.4	7.8(Q)	2.8(Q)	2,6
H <sub>2</sub>	4160.2	392.2	8.7	3.1	2,3

\*Q indicates the value of the Q-branch vibrational Raman backscattering cross section; C indicates a broad multi-peaked structure associated with the C—H stretch mode; P indicates a cross section based on a ratio of peak intensities rather than spectrally integrated signals.

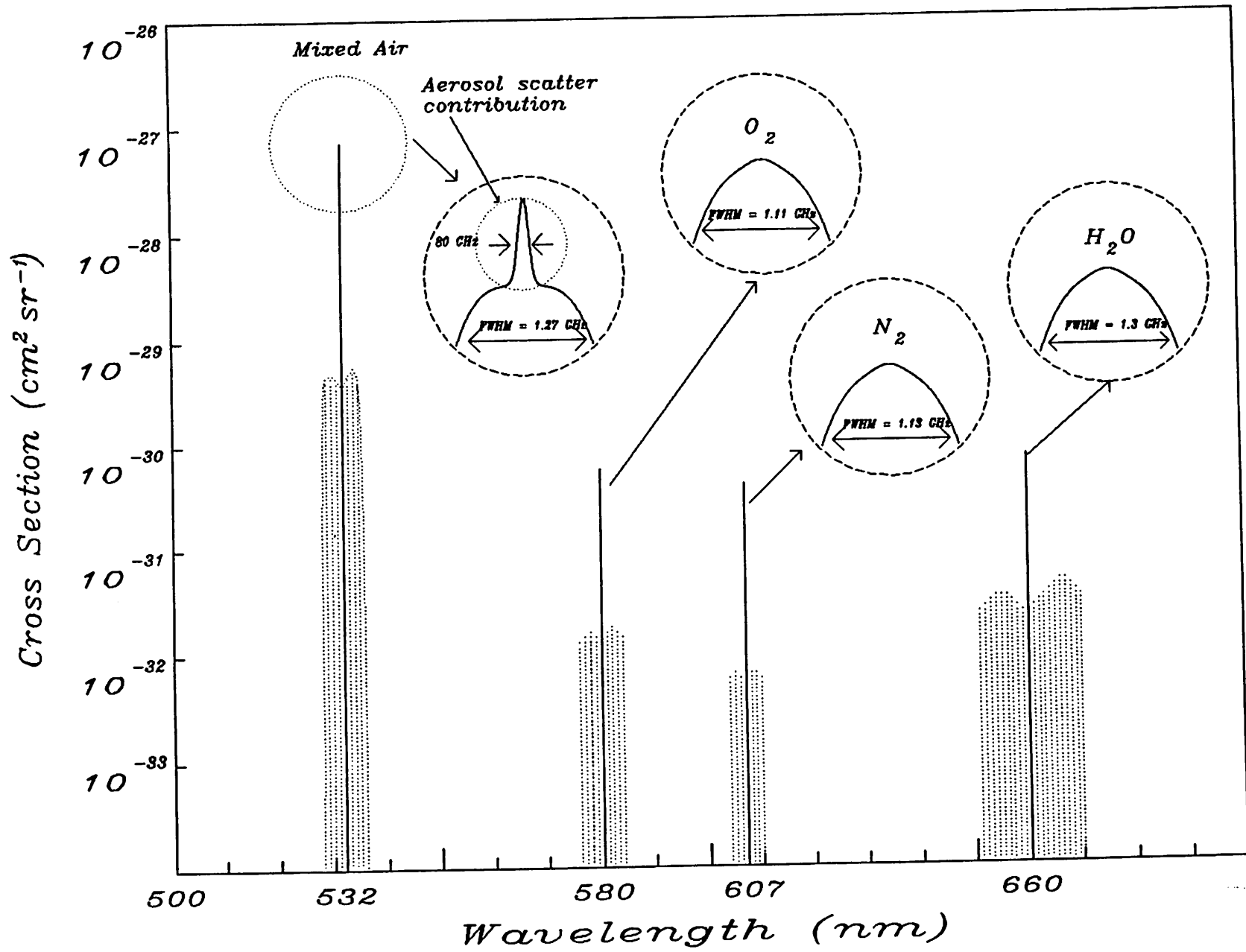
<sup>b</sup>References: 1. Stephenson (1974); 2. Murphy et al. (1969); 3. Inaba and Kobayasi (1972); 4. Schwiesow and Abshire (1973); 5. Fouche and Chang (1971); 6. Penney et al. (1974).

<sup>c</sup>1,2-Dichlorotetrafluoroethane.

<sup>d</sup>Octafluorocyclobutane.

<sup>e</sup>Hexafluoroethane.

<sup>f</sup>Tetrafluoromethane.



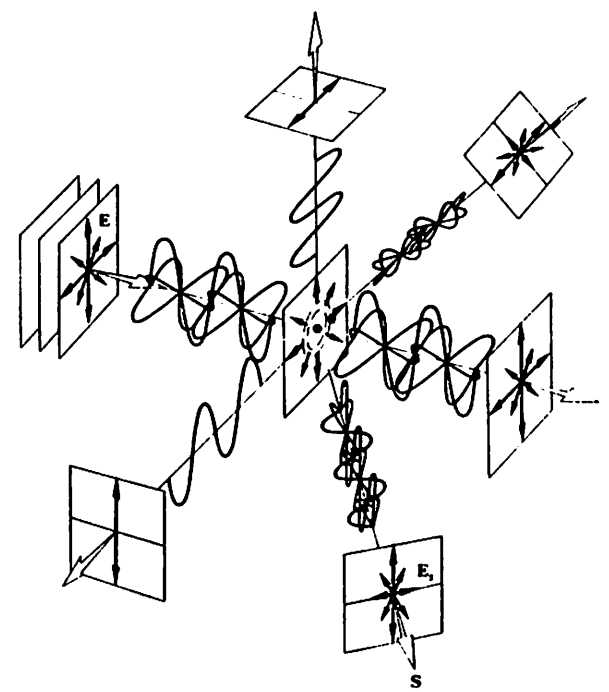
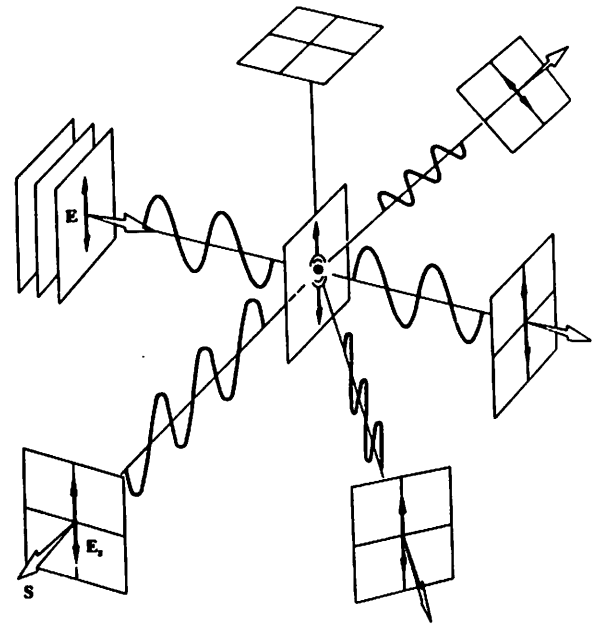
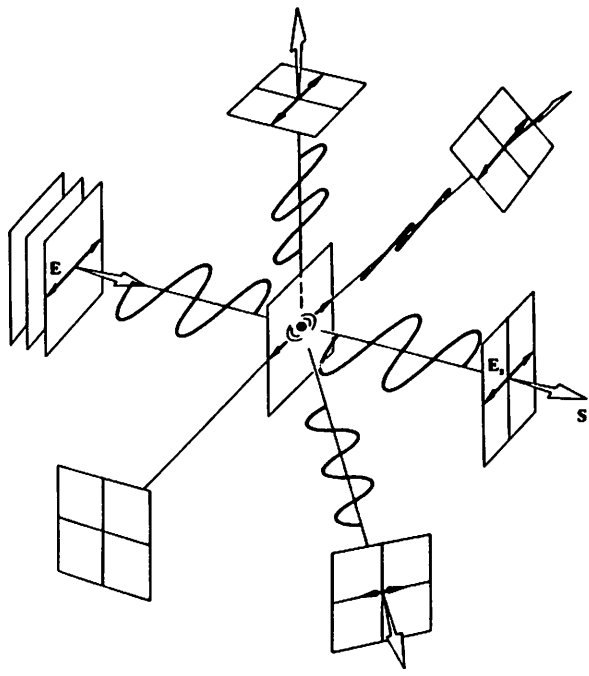

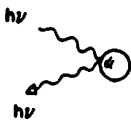
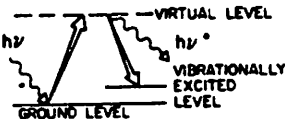
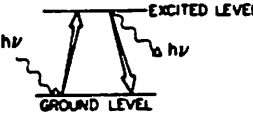
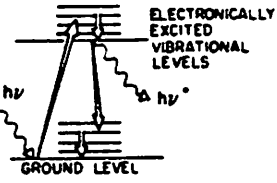

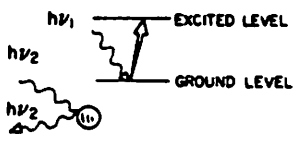




TABLE 6.1. OPTICAL INTERACTIONS OF RELEVANCE TO LASER ENVIRONMENTAL SENSING

Technique	Physical description
Rayleigh scattering	laser radiation elastically scattered from atoms or molecules is observed with no change of frequency 
Mie scattering	laser radiation elastically scattered from small particulates or aerosols (of size comparable to wavelength of radiation) is observed with no change in frequency 
Raman scattering	laser radiation inelastically scattered from molecules is observed with a frequency shift characteristic of the molecule ( $h\nu - h\nu^* = E$ ) 
Resonance scattering	laser radiation matched in frequency to that of a specific atomic transition is scattered by a large cross section and observed with no change in frequency 
Fluorescence	laser radiation matched to a specific electronic transition of atom or molecule suffers absorption and subsequent emission at lower frequency; collision quenching can reduce effective cross section of this process; broadband emission is observed with molecules 
Absorption	observe attenuation of laser beam when frequency matched to the absorption band of given molecule 
Differential absorption and scattering (DAS)	the differential attenuation of two laser beams is evaluated from their backscattered signals when the frequency of one beam is closely matched to a given molecular transition while the other's frequency is somewhat detuned from the transition 

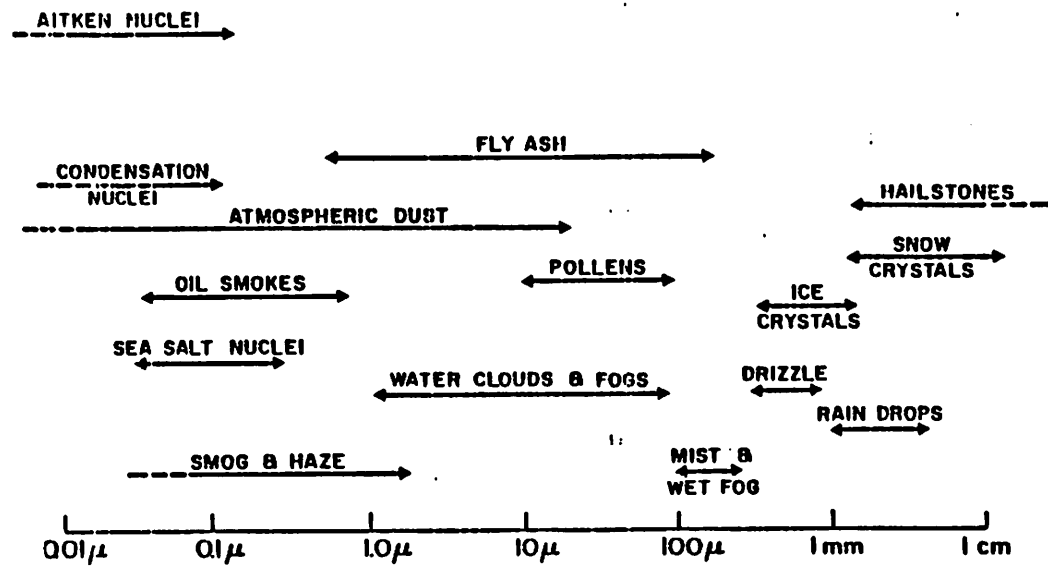


Fig. 2.19. Representative diameters of common atmospheric particles (Johnson, 1969).

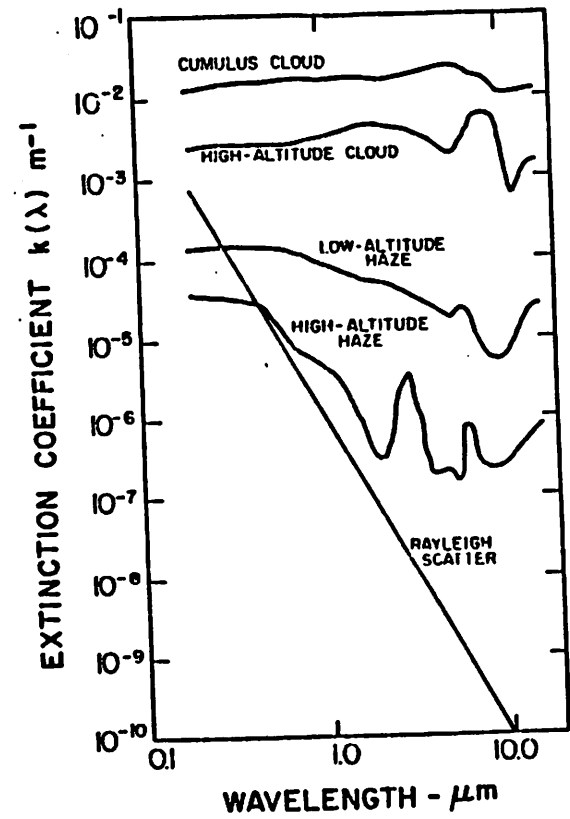
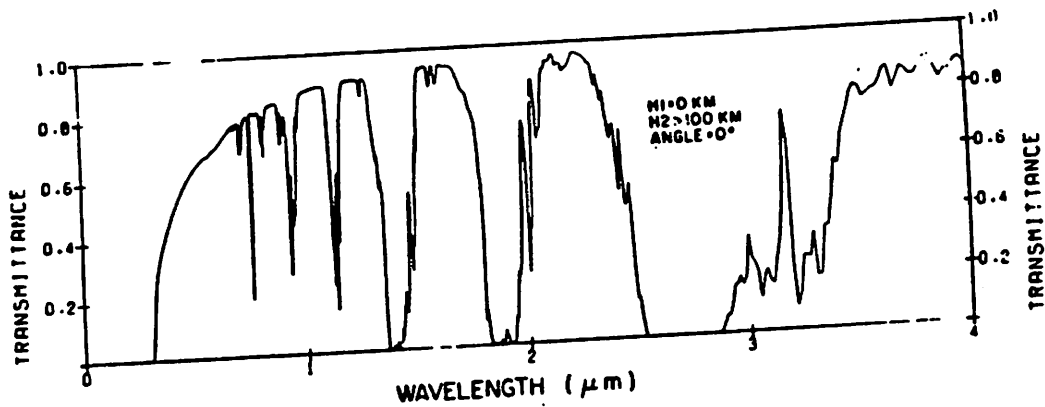


Fig. 2.27. Aerosol extinction coefficient as a function of wavelength (Wright et al, 1977).



Transmittance spectra for a vertical path from ground to space from 0.25 to 4  $\mu$ , using the rural aerosol model, 23-km VIS and the U.S. Standard Model Atmosphere.

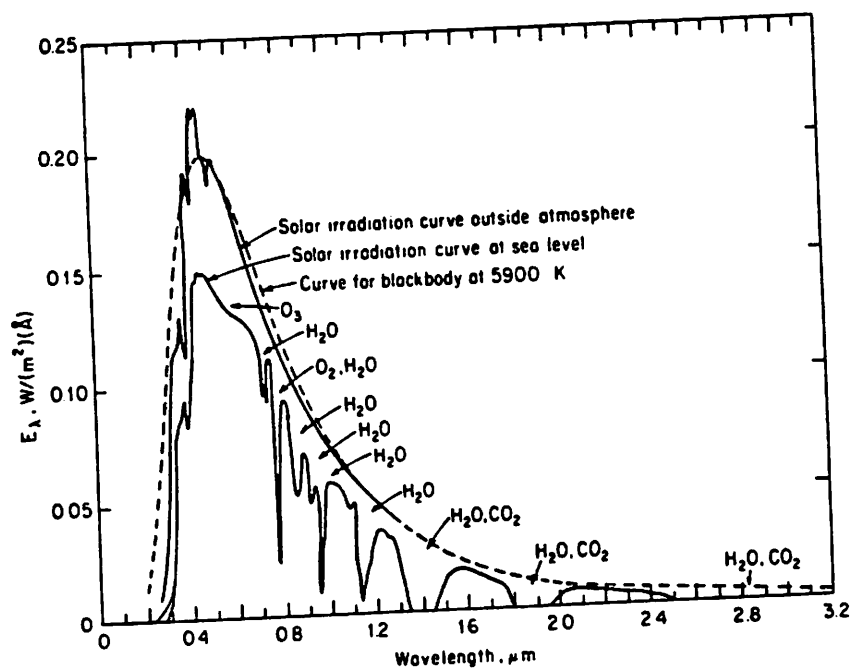


Fig. 51 Spectral distribution curves related to the sun; shaded areas indicate absorption at sea level due to the atmospheric constituents shown. [Valley (1965).]

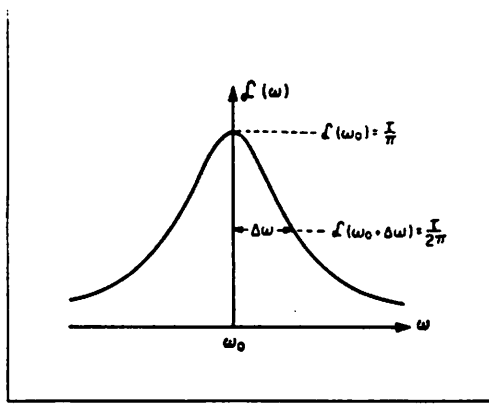


Fig. 3.15. Lorentz dispersion line profile function.

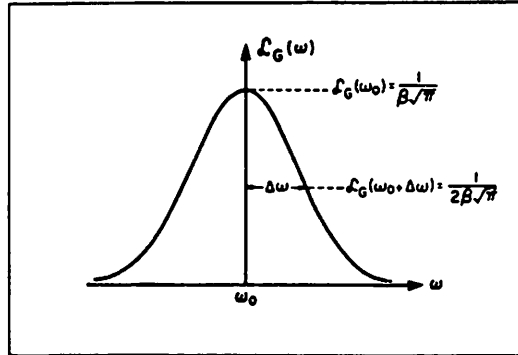


Fig. 3.17. Doppler-broadened Gaussian line profile function.

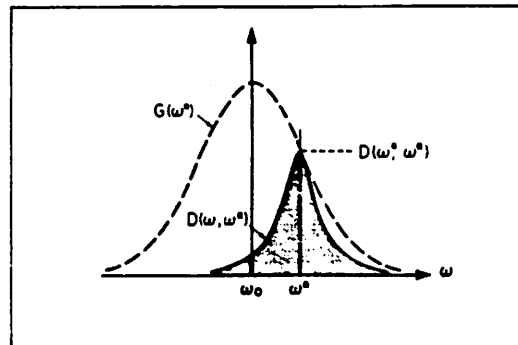
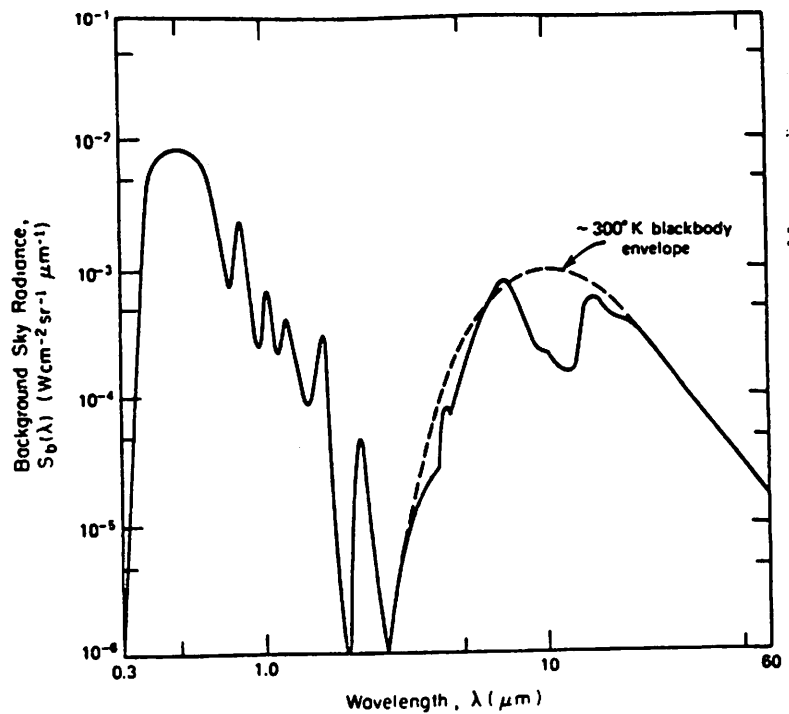


Fig. 3.18. Convolution of Gaussian and dispersive profiles.

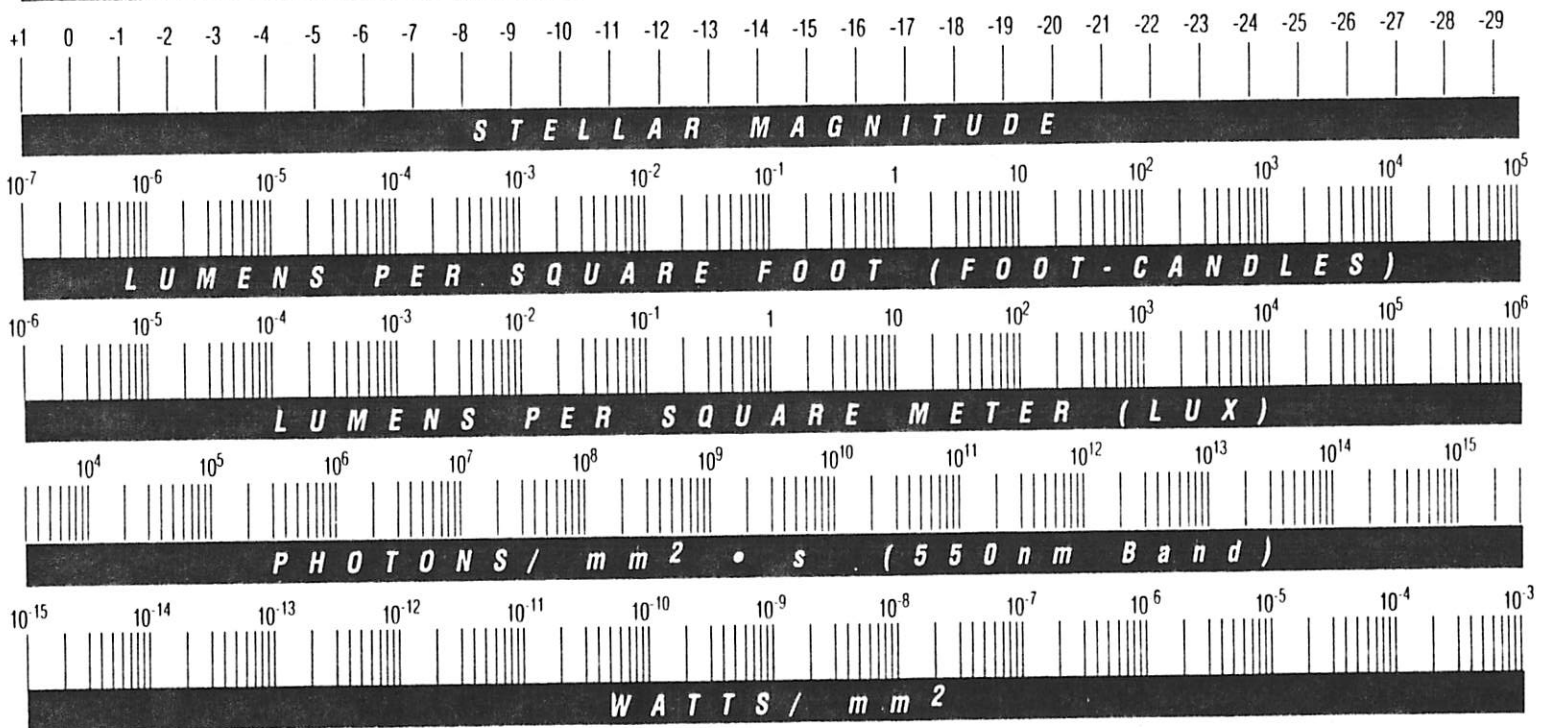




# LIGHT INTENSITY CONVERSION CHART

**SCOTOPIC VISION**

**PHOTOPIC VISION**



OVERCAST  
NIGHT SKY

CLEAR  
NIGHT SKY

QUARTER  
MOON

FULL  
MOON

TWILIGHT

SUNRISE  
SUNSET

HEAVILY  
OVERCAST

UNOBSCURED  
SUNLIGHT

**INTENSIFIER**

**... plus AUTO-IRIS**

**... plus AUTO-GATING**

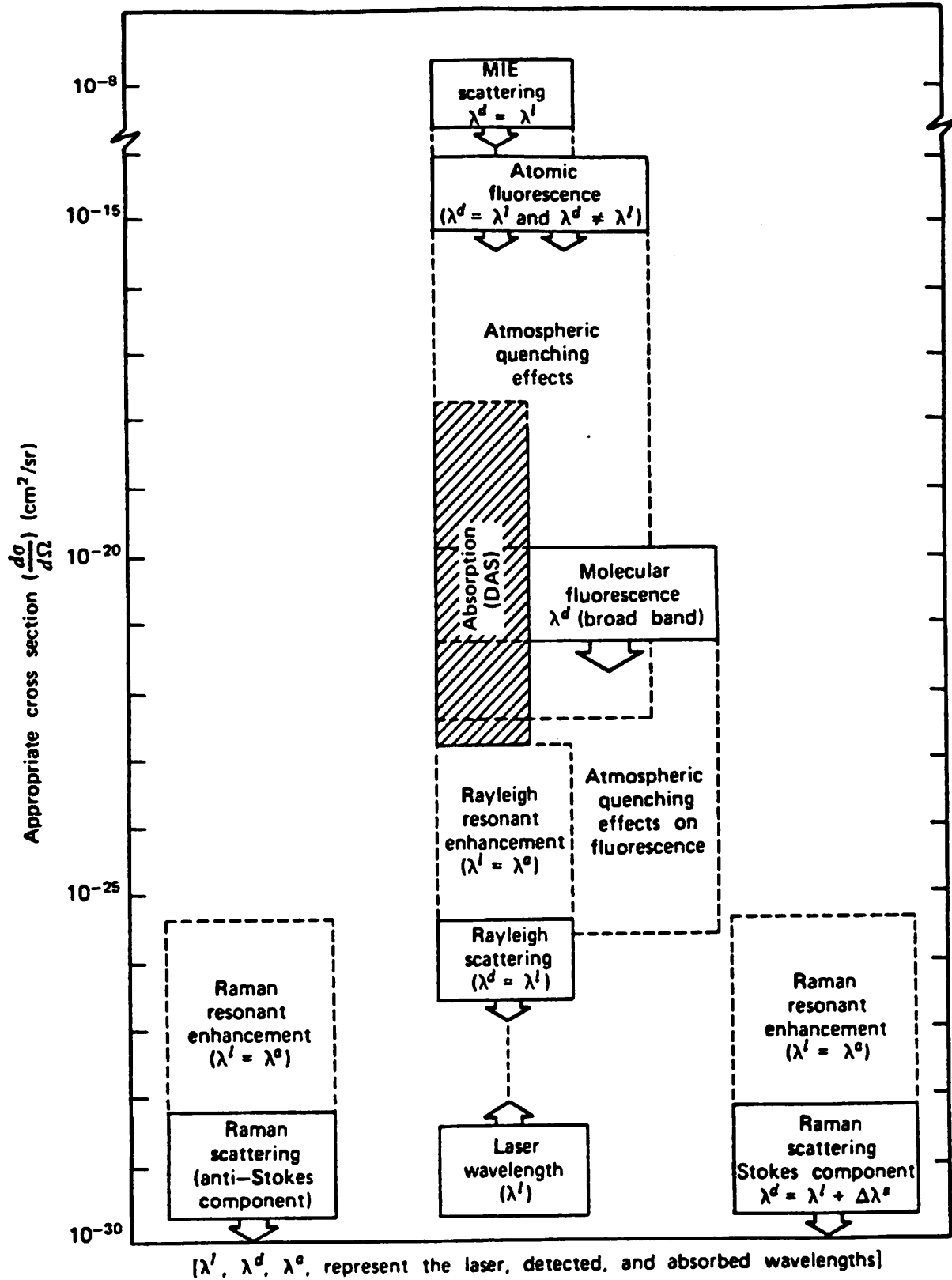
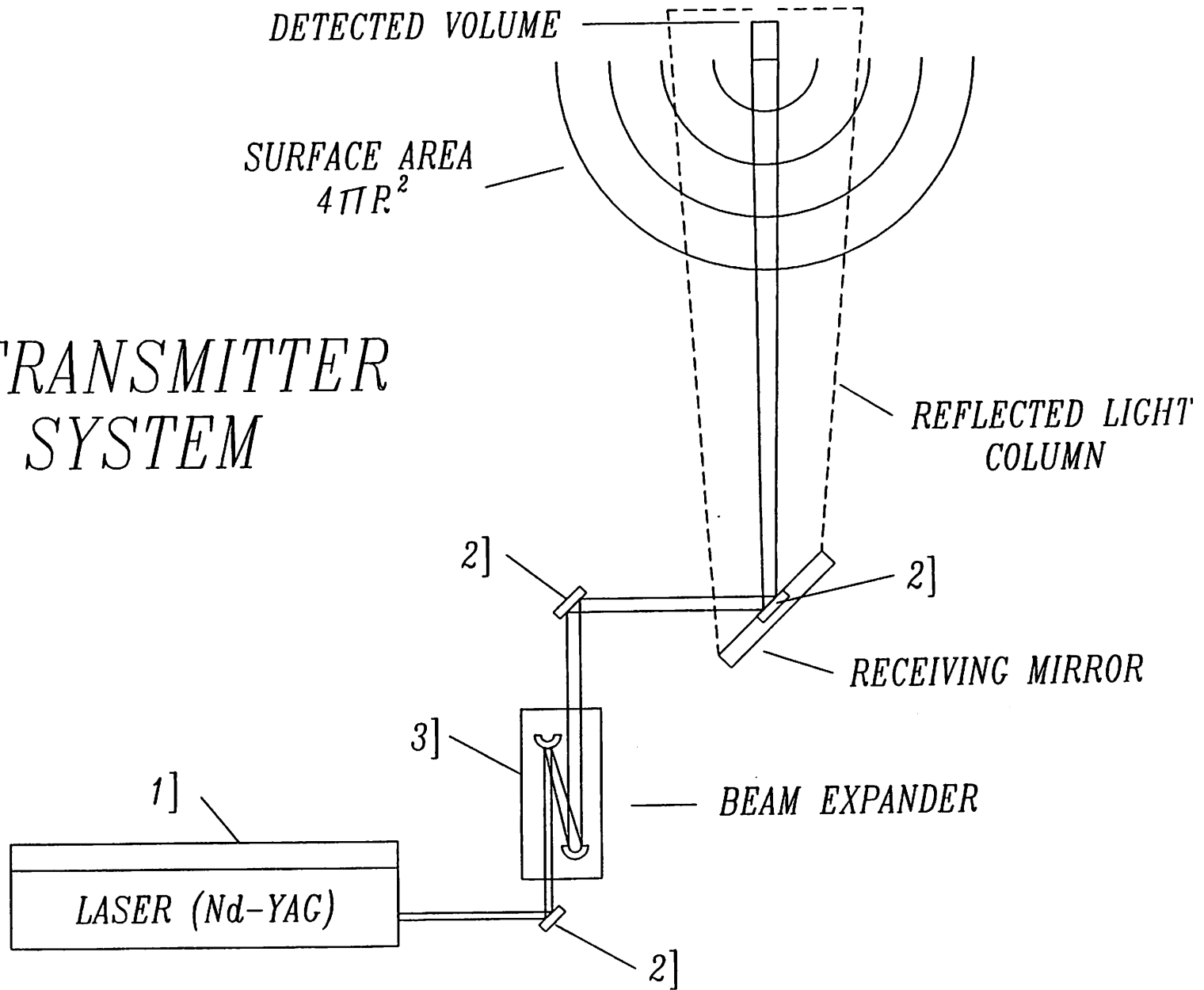
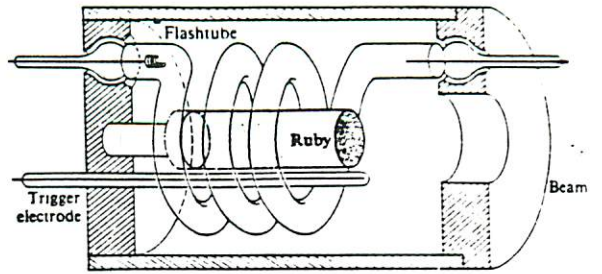


Fig. 6.1. Optical interactions of relevance to laser environmental sensing.

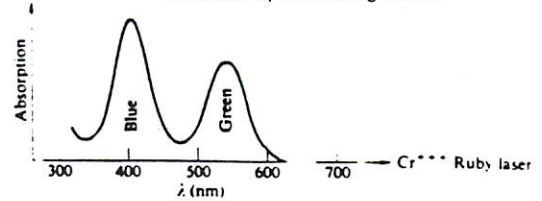
# TRANSMITTER SYSTEM



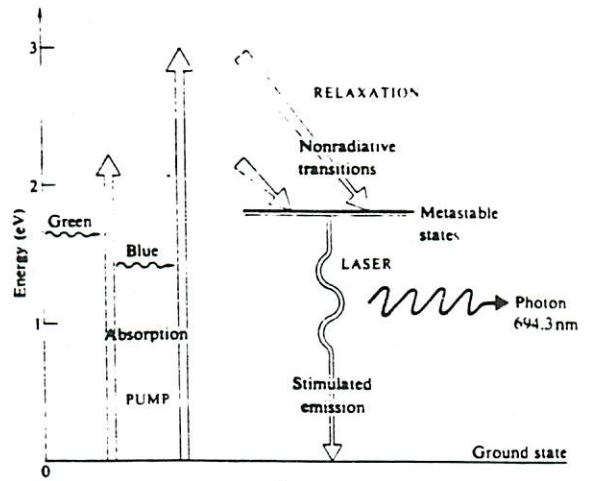




The first ruby-laser configuration.

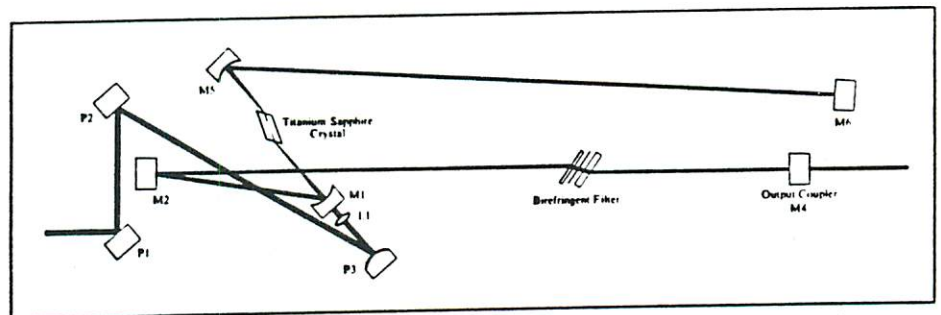


(a)

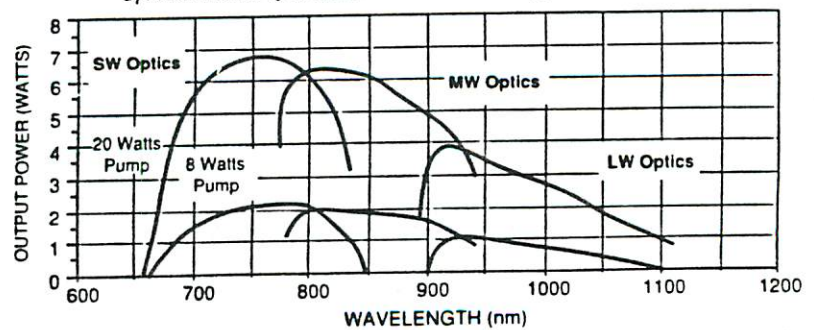


(b)

Ruby-laser energy levels.



Optical Schematic of the Model 899-LC Titanium:Sapphire Laser



Typical Tuning Curve of the Model 899-LC Titanium:Sapphire Laser

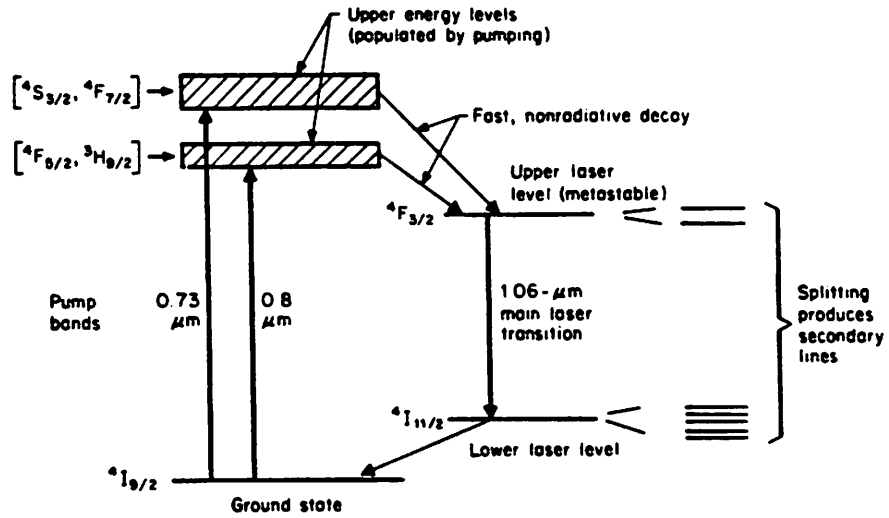


Figure 20-2 Energy levels in Nd-YAG (simplified).

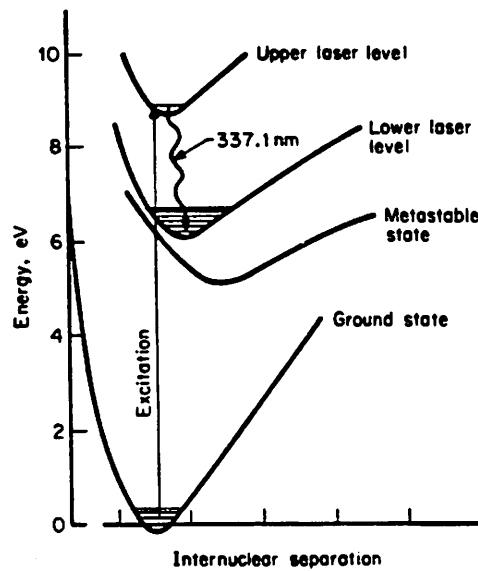


Figure 14-1 Energy levels in neutral nitrogen molecules involved in 337.1-nm laser transition. The broad curves represent electronic energy levels, with the lines within the potential wells representing vibrational energy levels for molecules in those electronic states. The laser transition is a vibronic one in which both electronic and vibrational energy states change.

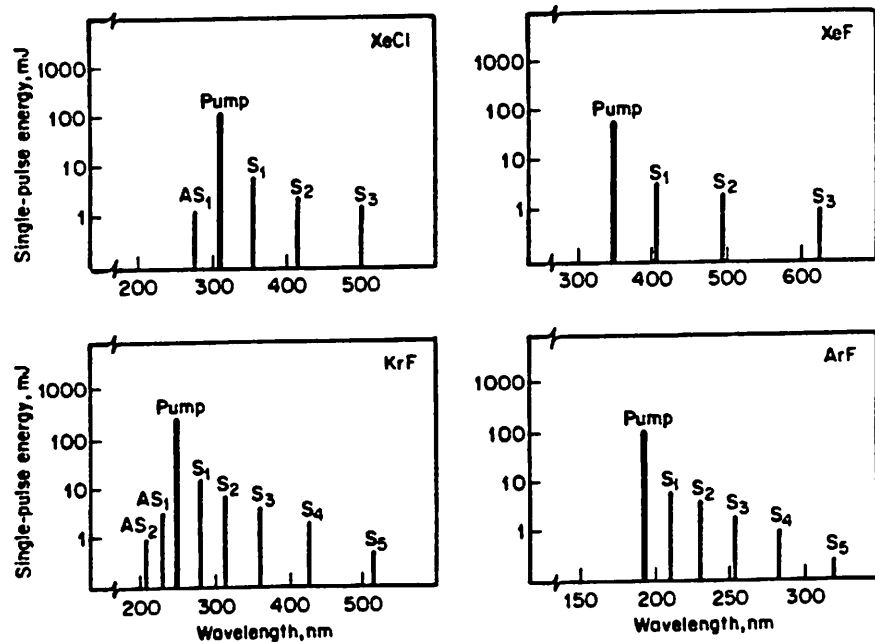
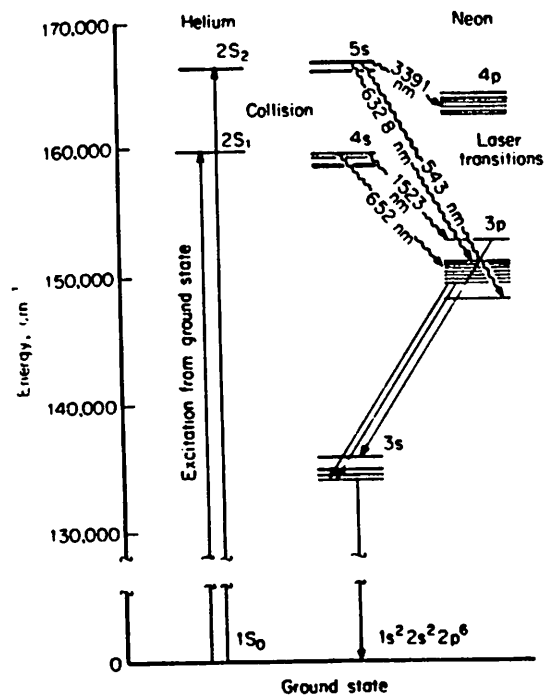
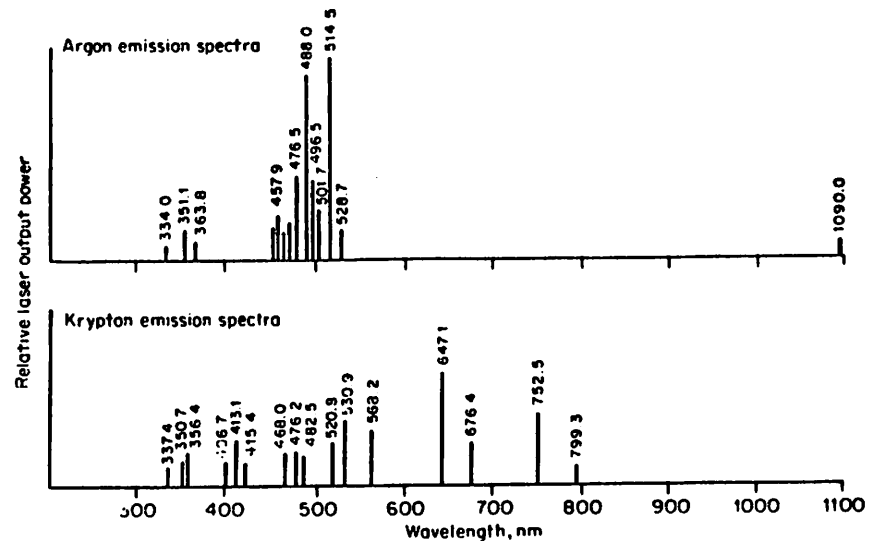


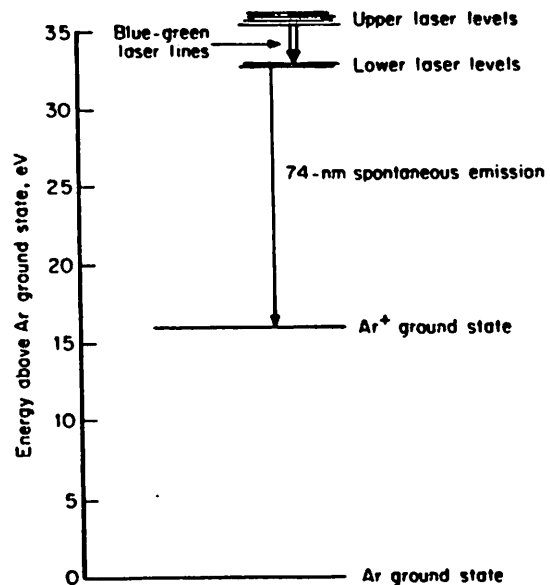
Figure 13-4 Typical output characteristics of a Raman-shifting cell for operation at 1-Hz repetition rate and optimum hydrogen pressure.  $S_n$  indicates Stokes-shifted line  $n$ ;  $AS_n$  indicates anti-Stokes-shifted line  $n$ . The pumping laser is identified in the upper right corner of each small graph. (Courtesy of Lambda Physik.)



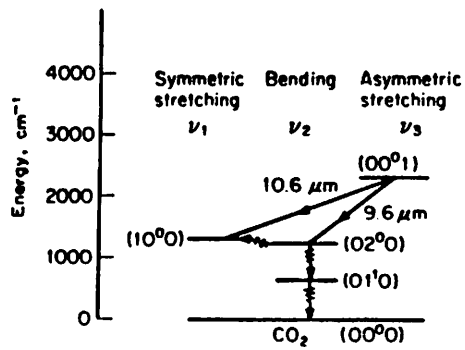
**Figure 7-1** Energy levels in a helium-neon laser, with major laser transitions indicated. Collisions transfer energy from helium atoms to neon atoms, which drop through laser transitions on their way to the ground state. (Courtesy of Melles Griot.)



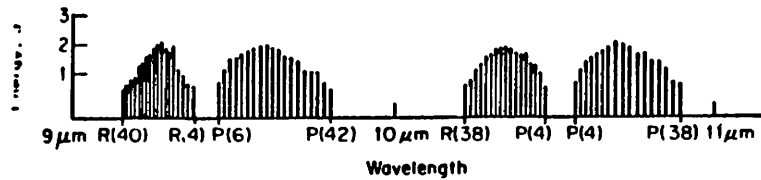
**Figure 8-1** Relative intensities of major lines of argon and krypton for one laser model. Strengths of various lines may differ somewhat between models. (Courtesy of Spectra-Physics Inc.)



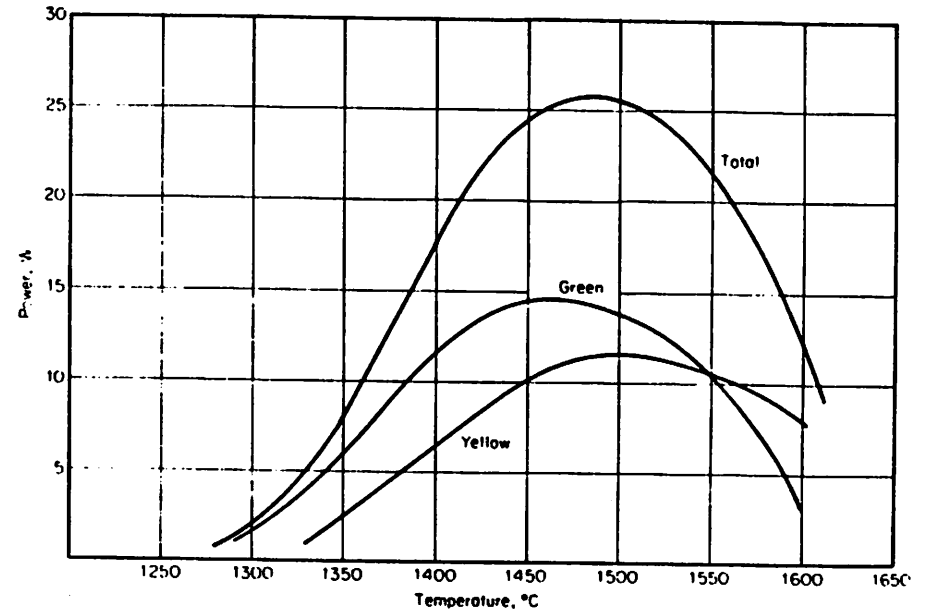
**Figure 8-2** Energy levels of singly ionized argon, showing only the blue-green laser lines. Actual energy-level structure is considerably more complex, as indicated by the many possible emission lines.



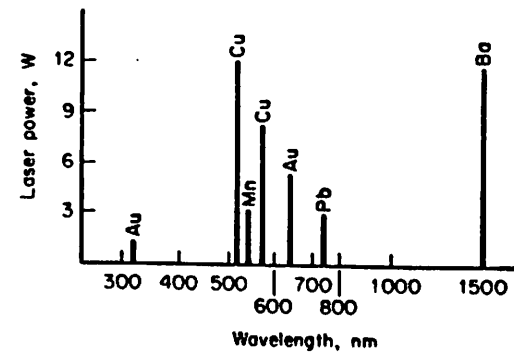
**Figure 10-1** Energy-level structure in the CO<sub>2</sub> laser, showing the relevant vibrational modes of the CO<sub>2</sub> molecule. Numbers in parentheses indicate the excitation levels of the symmetric stretching, bending, and asymmetric stretching vibrational modes, respectively, of the molecule.



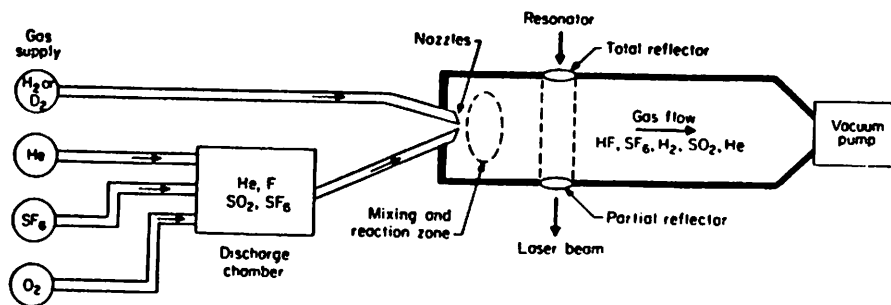
**Figure 10-5** Spectrum of wavelengths produced by a transversely excited atmospheric pressure CO<sub>2</sub> laser, showing pulse energy emitted at each line in single-line operation by a commercial laser. *R* and *P* denote rotational sublevels for each of the two main vibrational transitions of the carbon dioxide laser. (Courtesy of Lumonics Inc.)



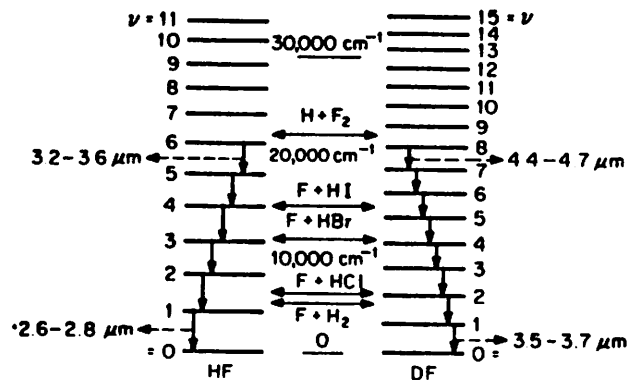
**Figure 12-2** Relative strengths of copper vapor lines as a function of temperature. (Courtesy of Oxford Lasers Ltd.)



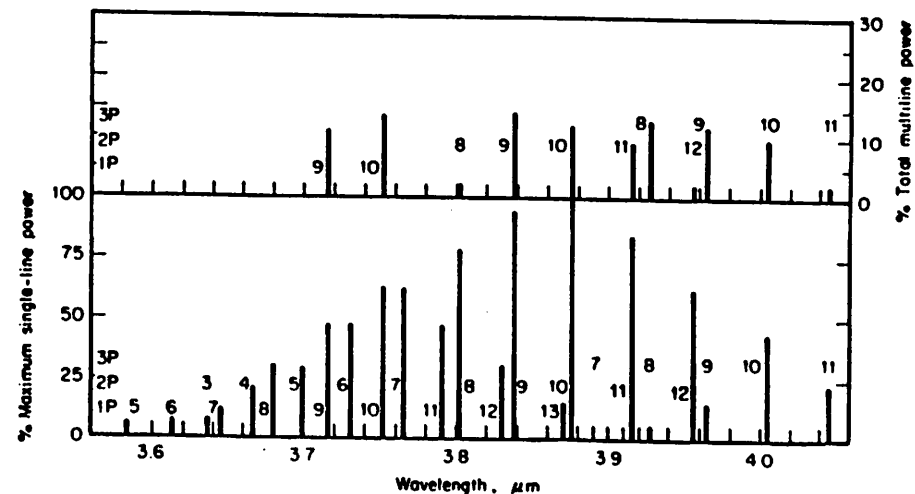
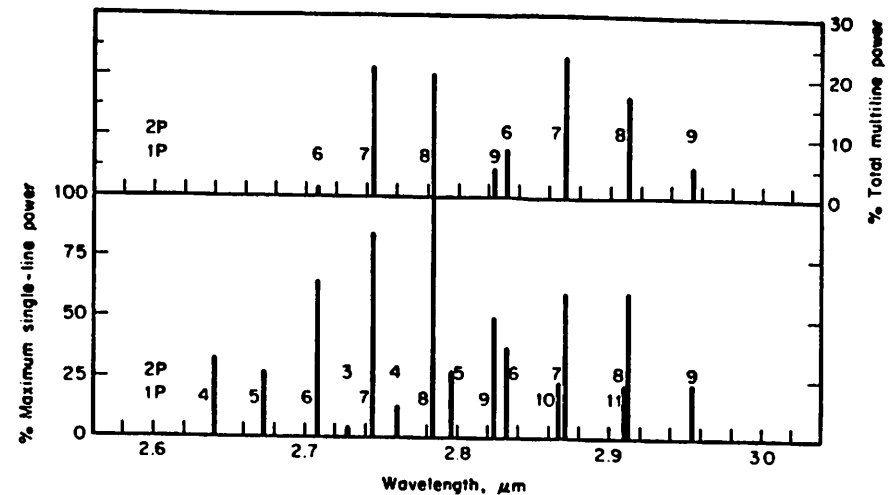
**Figure 12-3** Wavelengths and relative intensities of some major neutral metal vapor laser lines. (Courtesy of Quenron Optics Pty. Ltd.)



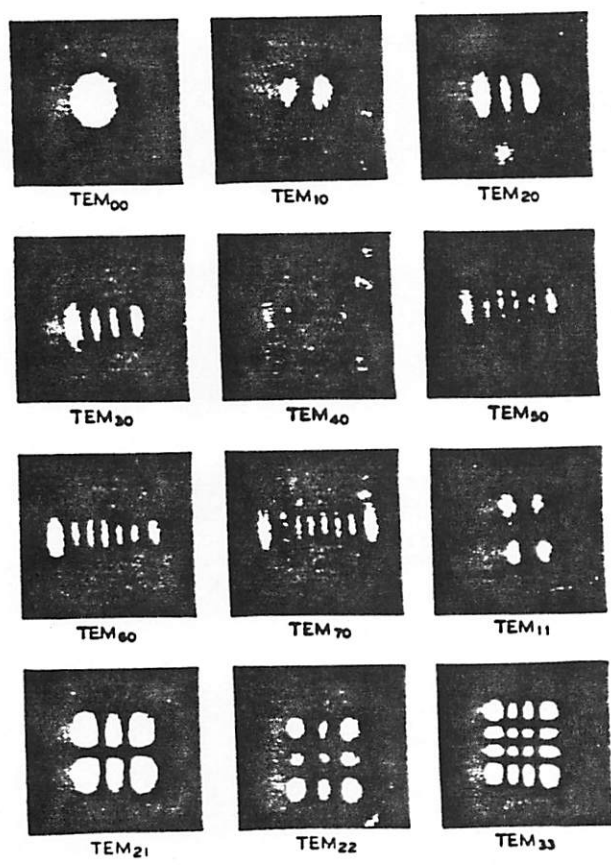
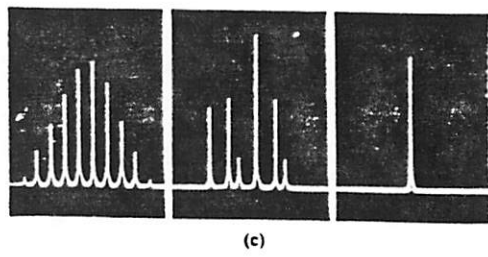
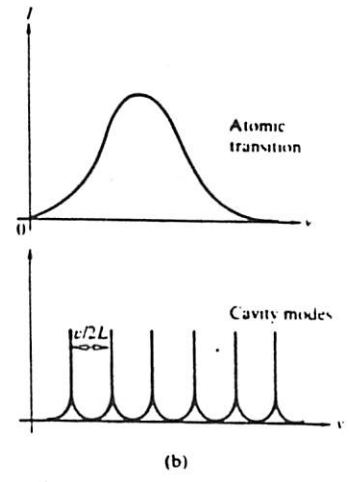
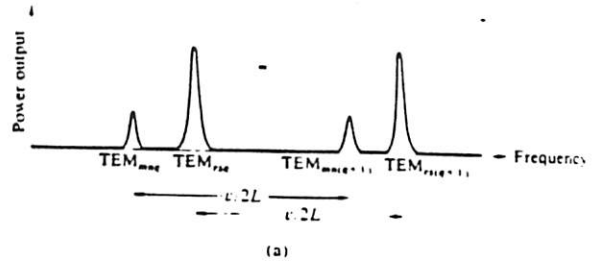
**Figure 11-2** Basic elements of a commercial continuous-wave chemical laser include a gas supply, a discharge chamber that produces free fluorine, nozzles which mix the reactants, a mixing region, a laser resonator, and a vacuum pump to collect spent gas. Gas flow is from left to right; the laser beam is perpendicular to the gas flow.



**Figure 11-3** Vibrational energy levels of HF and DF, shown with the energies remaining with the HF or DF molecules after certain reactions. (From Chester, 1976.)



**Figure 11-4** (a) HF and (b) DF emission lines from a continuous-wave chemical laser. (Courtesy of Helios Inc.)



**Figure 14.27 Laser modes:** (a) illustrates the nomenclature; (b) compares the broad atomic emission with the narrow cavity modes; (c) depicts three operation configurations for a c-w gas laser, first showing several longitudinal modes under a roughly Gaussian envelope, then several longitudinal and transverse modes, and finally a single longitudinal mode.

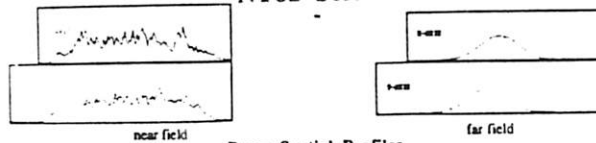
**Figure 14.28 Mode patterns** (without the faint interference fringes this is what the beam looks like in cross section). (Photos courtesy Bell Telephone Laboratories.)

NY82 Series		NY82-10	NY82-20
Repetition Rate		10	20
Energy (mJ)		1400	1200
1064nm		750	600
532nm (Type II doubling)		350	275
355nm (Type I doubling)		120	85
266nm			
Pulsewidth <sup>1</sup> (ns)		6-9	6-9
1064nm		5-8	5-8
532nm		5-8	5-8
355nm		4-7	4-7
266nm			
Linewidth <sup>2</sup> (cm <sup>-1</sup> )		1.0	1.0
no options		0.1	0.1
Line Narrowing Etalon (LINE) <sup>3</sup>		0.0045	0.0045
Injection Seeded SLM (S1500)		0.45	0.45
Divergence <sup>4</sup> (mrad)		9.5	9.5
Rod diameter (mm)		250	250
Beam pointing stability (urads)		0.5	0.5
Jitter <sup>5</sup> (tns)			
Energy stability <sup>6</sup> (%)		2.5	2.5
1064nm		3.5	3.5
532nm		4.0	4.0
355nm		10	10
266nm			
Power drift <sup>7</sup> (%)		3.0	3.0
1064nm		6.0	7.0
532nm		6.0	6.0
355nm			
Beam Spatial Profile (fit to Gaussian) <sup>8</sup>		0.70	0.70
Near Field (<1m)		0.95	0.90
Far Field (∞)			
Max. deviation from fitted Gaussian <sup>9</sup> (±%)		30	35
Near Field (<1m)			
Service Requirements		16A	20A
Power 220V, single φ			18A/φ
208V, 3φ			
Water			3-4GPM at 40-60PSI

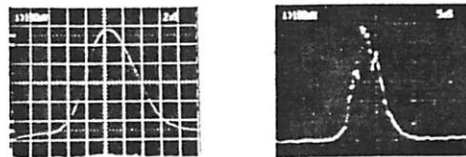
(All specifications at 1064nm unless otherwise noted)

- 1 Full Width Half Maximum.
- 2 Full Width Half Maximum (1cm<sup>-1</sup> = 30GHz).
- 3 10% energy reduction.
- 4 Full angle for 86% energy.
- 5 With respect to external trigger; ±1ns with S1500.
- 6 shot-to-shot for 99.9% of pulses from average for 8 hours.
- 7 from average for 8 hours.
- 8 A least squares fit to a Gaussian profile. A perfect fit would have a coefficient of 1.
- 9 At beam center.

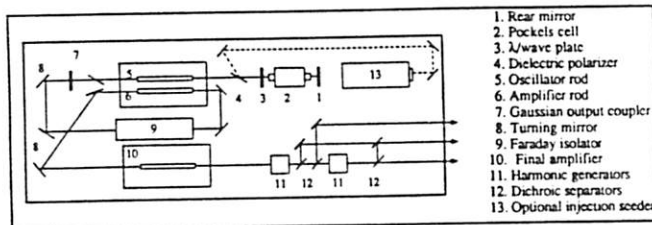
### NY82 Series



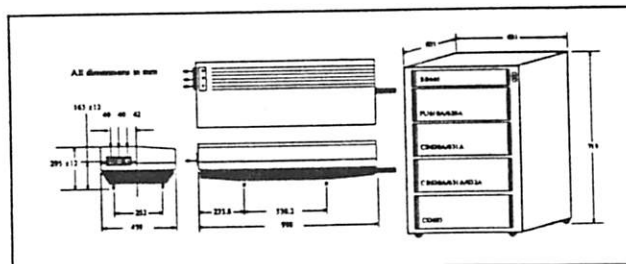
Beam Spatial Profiles



Beam Temporal Profiles

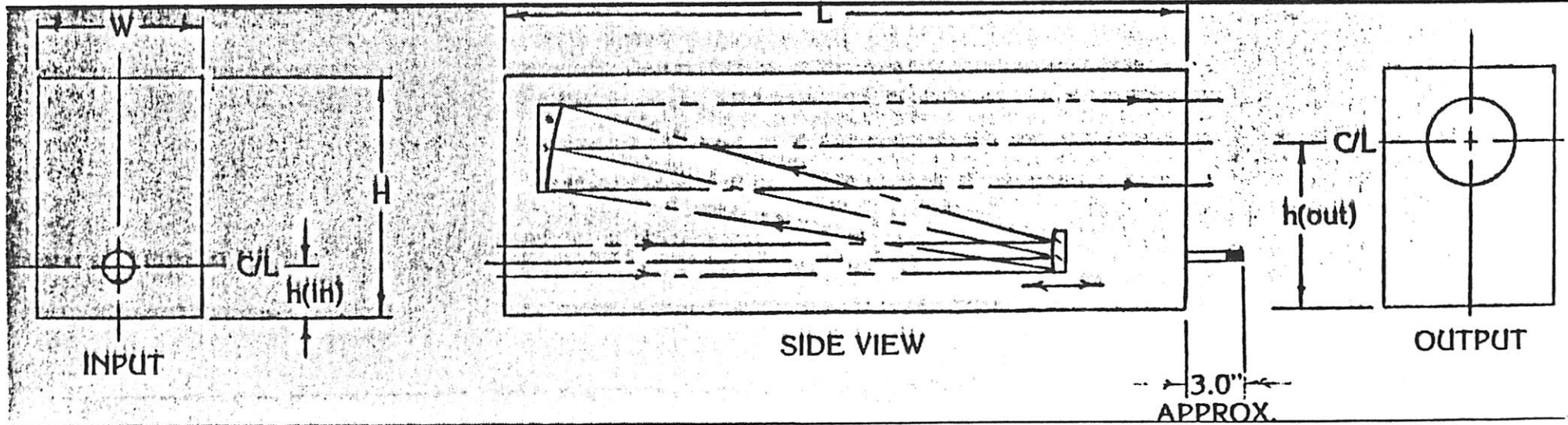
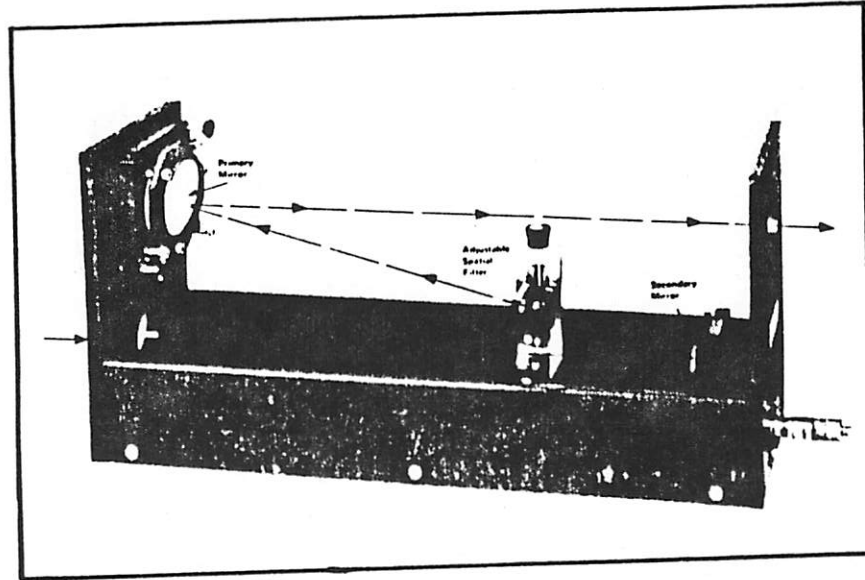
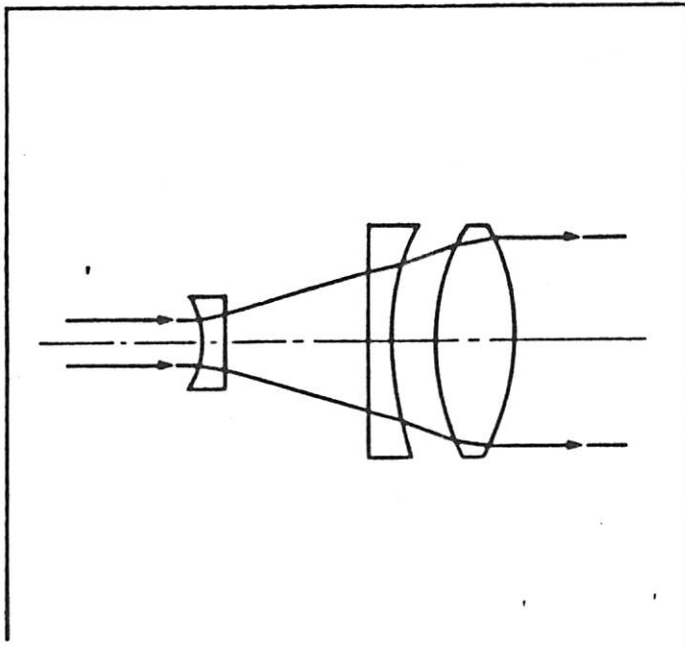


Optical Layout NY82



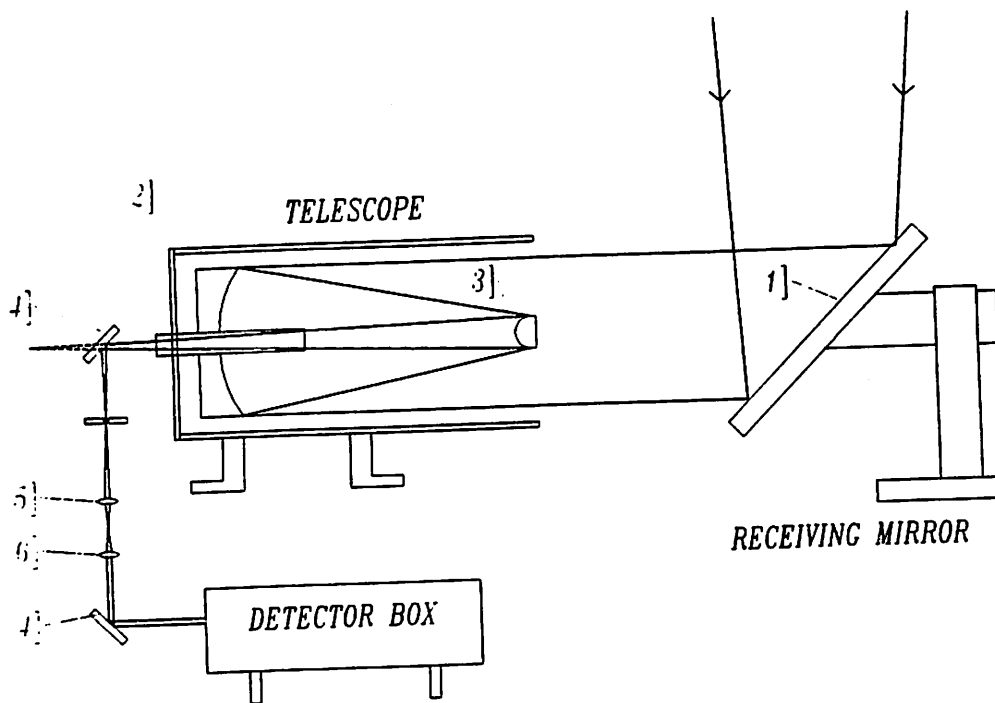
Physical Layout NY82

# Beam Expanders





# RECEIVER SYSTEM

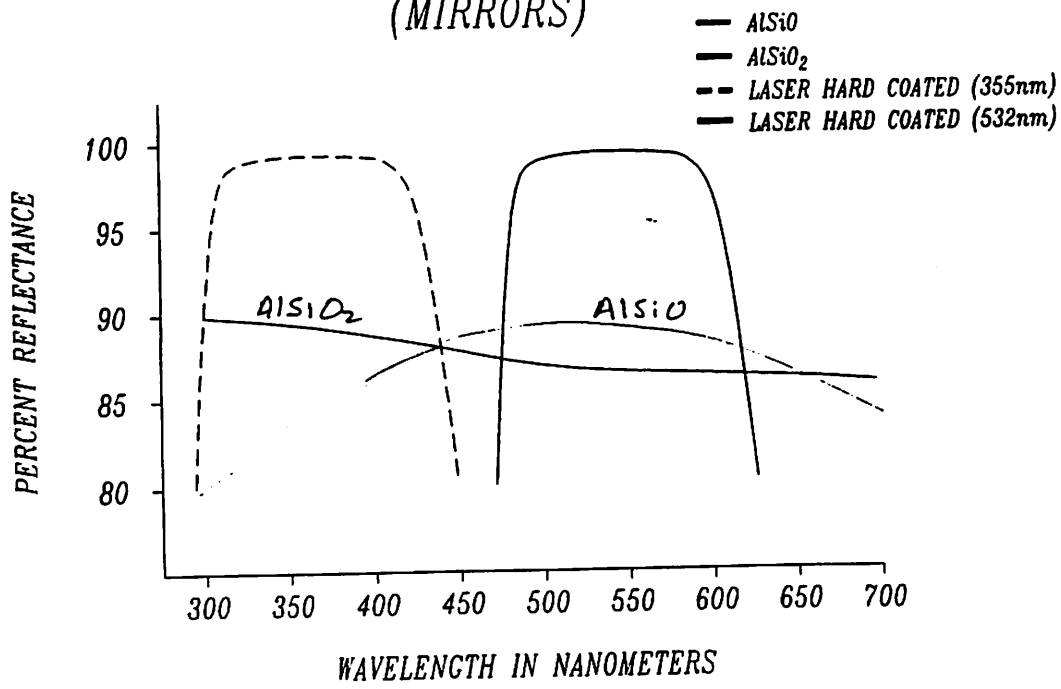


## RECEIVER

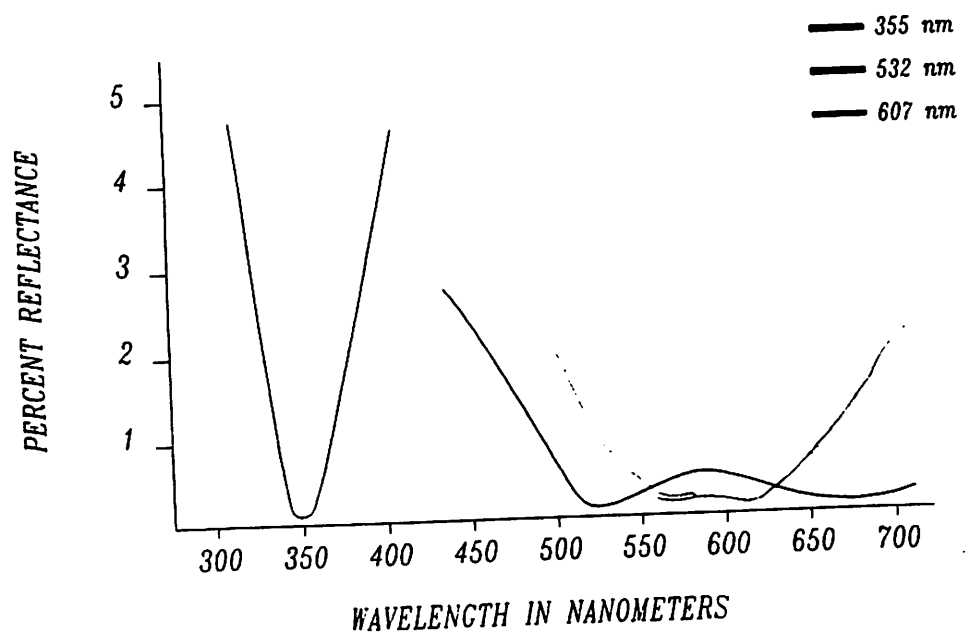
- 1) 24" optical flat: Reflectivity 90% @ 532nm  
 coating: AlSiO 84% @ 355nm  
 88% @ 607nm
- 2) Cassagrain telescope primary mirror:  
 Reflectivity 87% @ 532nm  
 coating: AlSiO<sub>2</sub> 89.5% @ 355nm  
 87% @ 607nm
- 3) Secondary mirror: Reflectivity 87% @ 532nm  
 89.5% @ 355nm  
 87% @ 607nm
- 4) 2", high reflective low power mirror:  
 Reflectivity 99.8% @ 532,355,and 607nm.
- 5) 1" fabry lens: Reflectivity .3% @  
 AR coated 532,355,607nm
- 6) 1" collimating lens: Reflectivity .3% @  
 AR coated 532,355,607nm

$$R_{eff} = \begin{array}{l} 67.4\% @ 532nm \\ 66.8\% @ 355nm \\ 66.1\% @ 607nm \end{array}$$

# REFLECTIVE SURFACES (MIRRORS)

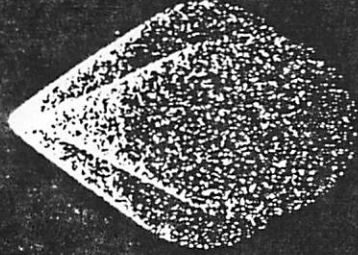


# ANTI-REFLECTIVE SURFACES (LENSES)



# TELESCOPE OPTICS

Evaluation and Design  
by Harrie Rutten and Martin van Venrooij



A Comprehensive Manual  
for Amateur Astronomers.

Published by:

**Willmann-Bell, Inc.**  
P.O. Box 35025  
Richmond, Virginia 23235 ☎ (804)  
United States of America 320-7016

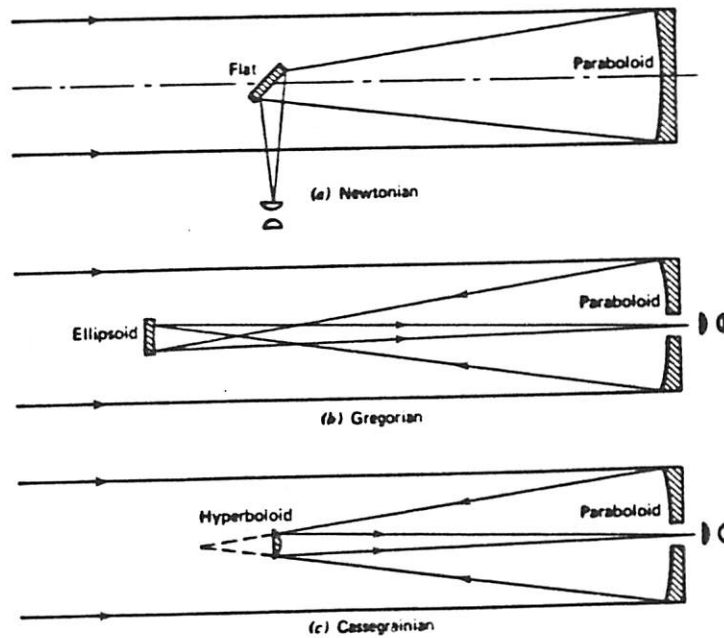


Fig. 6.4. Telescope configurations: (a) Newtonian; (b) Gregorian; (c) Cassegrainian (Ross, 1966).

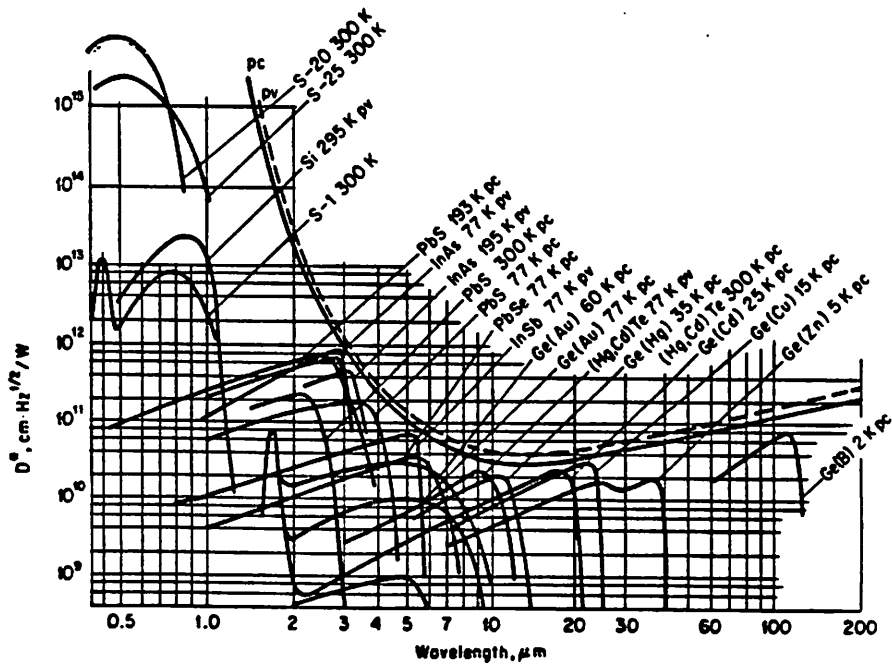
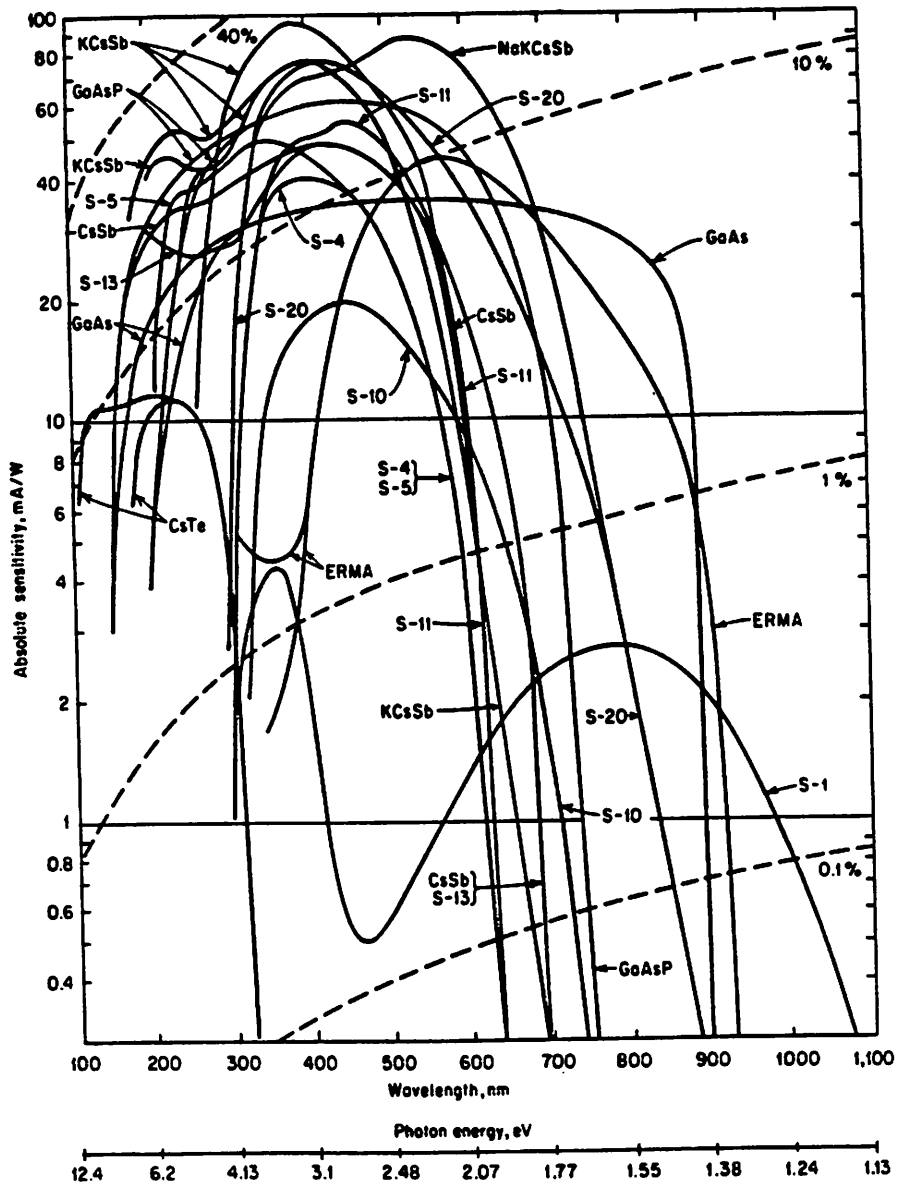


Fig. 6  $D$  vs.  $\lambda$  for selected detectors.

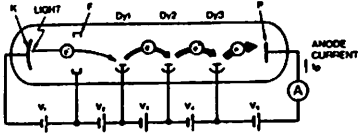
# SOCKET ASSEMBLIES

## Voltage Divider Consideration

### VOLTAGE DIVIDER CIRCUITS

To operate a photomultiplier tube, a high voltage of about 1000V is usually applied between the photocathode (K) and anode (P). In addition, a voltage gradient must be set up among the photoelectron focusing electrode (F) and secondary electron multiplier electrodes or dynodes (Dy).

Figure 1: Schematic Representation of PMT

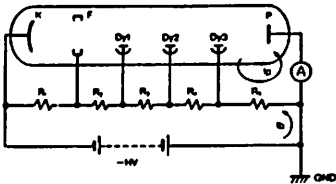


In general, the interstage voltages for the various electrodes are derived, as shown in Figure 2, by using resistors or Zener diodes across the voltage between the cathode and anode instead of using individual voltage sources. This circuit is termed a voltage divider, or bleeder circuit.

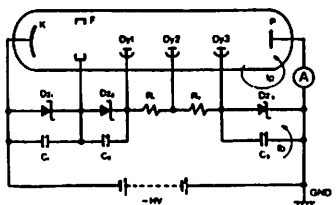
The current  $I_b$  flowing through the voltage divider circuit shown in Figures 2 (A) and (B) is known as the divider current, or bleeder current, and is highly related to the output linearity, to be described later. The capacitors  $C_1$ ,  $C_2$  and  $C_3$  connected in parallel with the Zener diodes in the circuit shown at (B) are used to

Figure 2: Voltage Divider Circuit with Anode Grounded

(A) Using Resistors Only



(B) Using Resistors and Zener Diodes



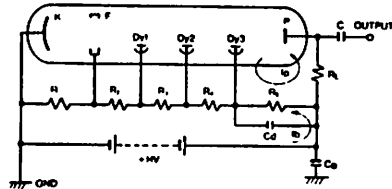
minimize noise generated by these Zener diodes. This noise becomes significant when the current flowing through the Zener diodes is of insufficient level. Thus, care is required with respect to this point, as this noise can affect the output signal-to-noise ratio of the photomultiplier tube.

### 1) Anode Grounding and Cathode Grounding

The general technique used for voltage divider circuits is to ground the anode with a high negative voltage applied to the cathode. This scheme eliminates the potential difference between the external circuit and the anode, facilitating the connection of such circuits as ammeters or current-to-voltage conversion operational amplifiers to the photomultiplier tube. However, when a grounded anode configuration is used, bringing a grounded metallic holder or magnetic shield case near the bulb of the tube can cause electrons to strike the inner bulb wall, resulting in the generation of noise. Also, for head-on type photomultiplier tubes, if the faceplate or bulb near the photocathode is grounded, the slight conductivity of the glass material causes a current to flow between the photocathode (which has a high negative potential) and ground. This may cause electrolysis of the photocathode, leading to the danger of significant deterioration. For this reason, when designing the housing for a photomultiplier tube and when using an electrostatic or magnetic shield case, extreme care is required.

In addition, when using foam rubber or similar material to mount the tube in its housing, it is essential that material having sufficiently good insulation properties be used. This problem can be solved by applying a black conductive layer around the bulb and connecting to the cathode potential (called HA Coating). However, in scintillation counting, it is often impossible to use this technique, since the grounded scintillator is in intimate contact with the photomultiplier tube. In such cases, the cathode must be grounded, as shown in Figure 3, with a high positive voltage applied to the anode. Using this scheme, a coupling capacitor C is

Figure 3: Voltage Divider Circuit with Cathode Grounded

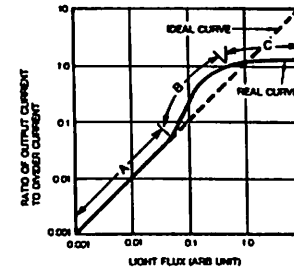


used to separate the high positive voltage applied to the anode from the signal, making it impossible to obtain a DC signal output.

### 2) Voltage Divider Circuits and Output Linearity

In either the grounded anode or grounded cathode configuration, when the incident light on the photocathode is increased in level to increase the anode current  $I_b$ , as shown in Figure 4, at above some current level, the relationship between the incident light level and the anode current deviates from the ideal linear relationship and the photomultiplier tube goes into saturation.

Figure 4: Output Linearity of PMT



### 2-1) DC Operation Output Linearity

If we consider the case of deriving DC output using the circuit configuration shown in Figure 2 (A), when the incident light level is increased, the current  $I_b$  flowing in the loop  $Dy_3$ - $R_3$ - $P$ - $Dy_3$  increases, cancelling out the current  $I_b$  which flows in the reverse direction through  $R_3$ . This effect results in a decrease in the voltage across  $Dy_3$  and P. The same effect is observed between the other electrodes, but the earlier the dynode stage, the smaller the current flowing in the dynode, so that this effect lessens. Thus the voltage to be applied to latter stages is distributed to the previous stages so that there will be an increase in dynode voltage. The result is an apparent increase in current amplification, the phenomena shown in Figure 4 at B.

If the incident light level is increased further, so that the anode current equals the voltage divider current, for the above described reason, the voltage between the last stage and the anode approaches zero. This decreases electron collection efficiency of the anode and the anode output becomes saturated, as shown in Figure 4 at C.

While there are differences depending upon the type of photomultiplier tube and voltage divider circuit used, when a DC output is derived, the maximum

practical anode current is determined by the voltage divider current calculated from the supply voltage and the total value of the voltage divider resistances. It is suggested that the anode current be smaller than 1/20 of the voltage divider current. The technique of increasing the maximum output current is to lower the voltage divider resistance values or use a Zener diode between the last dynode and the anode as shown in Figure 2 at (B), and, if necessary, the previous stages as well.

However, using the former technique, the power which must be dissipated within the voltage divider circuit increases. This may raise the photomultiplier tube temperature, and subsequently results in an increase in dark current and possible variations in output. Using the latter described technique, also, if the current flowing in the Zener diode is insufficient, Zener diode noise can increase with the danger of reducing the output signal-to-noise ratio. To absorb possible noise capacitors should be connected across the Zener diodes. Note, also, that  $Dz_1$  and  $Dz_2$  of Figure 2 are used to establish a constant voltage on the electron focusing electrode regardless of variations in the applied voltage, and are thus not related to output linearity.

### 2-2) Pulse Operation Output Linearity

To use pulse operation with a photomultiplier tube, ceramic disk capacitors having good frequency characteristics are connected in parallel with the voltage dividing resistors of the last several stages, as shown in Figure 5 (A), those capacitors provide electric charge during the duration of the pulse and result in a significant increase in the maximum peak current.

Using this type of operation, to achieve good output linearity (better than 1%), the capacitor value connected between the last stage and the anode should be roughly selected as follows.

$$C \approx 100 \frac{Q}{V} \text{ (farads)}$$

where Q: Electric charge for one output pulse (coulombs)

V: Voltage between the last stage and the anode (volts)

When adding capacitors to the last few stages, the electric charges required by the preceding stage should be assumed to be 1/2 to 1/3.

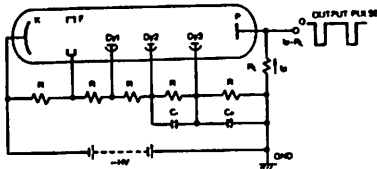
When the pulse output increases further, even using this technique, it will result in saturated output by virtue of the space charge effect in the region of the anode. In such cases, the voltage divider resistance values from the central stages to the last stages should be changed so that the voltage gradually increases towards the last stage. This scheme is known as a tapered voltage divider circuit and is effective insofar as the interstage breakdown voltages will permit. In many cases,

however, since this is accompanied by a decrease in current amplification, it is necessary to increase the applied voltage.

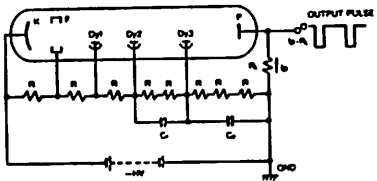
If the value of  $R_L$  in Figure 5 is made unnecessarily high, the voltage drop  $I_a \cdot R_L$  across this resistance will reduce the voltage between the last stage and the anode. And the effect of the space charge and a reduction in secondary electron collection efficiency of the anode will cause a deterioration in output linearity. In addition, care is required since mismatching of impedances with the output cable and any external circuitry can cause ringing. Techniques used to obtain linear output using parallel capacitors or tapered voltage divider circuits apply as well to the grounded cathode circuit configuration and the anode positive voltage circuits.

Figure 5: Voltage Divider Circuits for Pulse Operation

(A) Using Parallel Capacitors



(B) Tapered Divider Circuit



### TYPES OF SOCKET ASSEMBLIES

As discussed in the previous section, various cautions are required in making up the voltage divider circuit. To free the user from the necessity of designing voltage divider circuits and performing troublesome parts selection, Hamamatsu provides a variety of socket assemblies which enable sufficient performance to be derived from photomultiplier tubes by making simple connections only.

Refer to the types of socket assemblies listed on page 5.

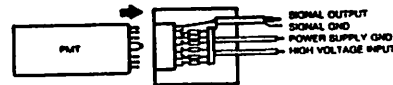
#### 1) D Type Socket Assemblies (E717 Series, E990 Series etc.)

The D type socket assemblies have a built-in voltage divider in a metallic or plastic container, as shown in Figure 6.

A selection guide is provided on page 7, enabling D type socket assemblies to be selected for individual application requirements. Note that this catalog includes only those types intended for general applications, and Hamamatsu is ready to produce special socket assemblies to individual user specifications.

Three types of D type socket assemblies are available with different circuit configurations. Figure 7 shows the general method used to make connection to an external circuit.

Figure 6: D Type Socket Assembly



#### 2) DA Type Socket Assemblies (C1053 Series, C1556 Series)

The DA type socket assemblies have a built-in voltage divider and amplifier to convert the low-level, high-impedance current output of the photomultiplier tube to a low-impedance voltage output. Since the high-impedance output of the photomultiplier tube is connected to the amplifier circuit at a minimum possible distance, the problem of external noise induced in connecting cables is eliminated.

The DA type socket assemblies are available with a bandwidth of DC to 5MHz for the C1053 series and DC to 10kHz for the C1556 series. Either series is available for 1-1/8" (28 mm) diameter side-on and head-on photomultiplier tubes as standard products. In addition, variants having a BNC connector in place of the photomultiplier socket section are also available. This type enables use of other photomultiplier tubes in combination with an appropriate D type socket assembly.

# HIGH VOLTAGE POWER SUPPLIES

## Voltage Dependence

### PHOTOMULTIPLIER TUBE VOLTAGE DEPENDENCE

Photoelectrons emitted from the photocathode of a photomultiplier tube are directed by the electron lens system and collide with the first dynode where several times this number of electrons are emitted as secondary electrons. This multiplication process of secondary electrons is repeated at latter stage dynodes, so that when electrons finally reach the anode, the number of electrons is approximately  $10^9$  times the original number emitted from the photocathode.

The relationship of the electron emission ratio  $\delta$  for each dynode stage to the applied voltage is expressed as follows.

$$\delta = A \cdot E^\alpha$$

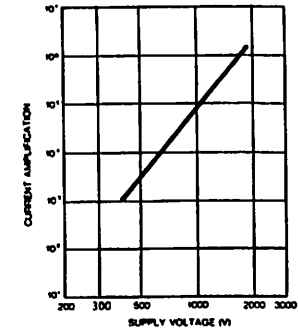
Where A is a constant, E is the interstage voltage, and  $\alpha$  is another constant determined by the dynode material and geometric structure. The value of  $\alpha$  is usually in the range 0.7 to 0.8. When a voltage V is applied between the anode and photocathode of a photomultiplier tube having n dynode stages, the overall current amplification G is given as follows.

$$G = (A \cdot E^\alpha)^n = \left[ A \cdot \left( \frac{V}{n+1} \right)^\alpha \right]^n$$

$$= \frac{A^n}{(n+1)^n} \cdot V^{\alpha n} = K \cdot V^{\alpha n} \quad (K \text{ is a constant})$$

The usual type of photomultiplier tube uses 9 to 12 stages of dynodes and, as shown in Figure 1, the current amplification is proportional to the 6th to 10th

Figure 1: Current Amplification vs. Supply Voltage



Type No.	Parameters	Features	Output Voltage	Output Polarity	Output Current	Input Voltage	Weight
Bench-top Type	C655	High Stability	-200 to -1190 V	Neg.	5 mA	100/115/220 Vdc	3.3 kg
	C3350	±C kV Output, Large Current	0 to ±3000 V	Pos./Neg.	10 mA	100/115/220 Vdc	8 kg
	C2633	Computer Compatible	±200 to ±3071 V	Pos./Neg.	5 mA	100/115/220 Vdc	8.5 kg
	C3360	-5 kV Output	0 to -5000 V	Neg.	1 mA	100/115/220 Vdc	3.5 kg
Modular Type	C1309-01	Large Current Modular Type	-400 to -800 V	Neg.	2 mA	+15 Vdc	140 g
	C1309-02	High Stability Modular Type	-200 to -1100 V		0.7 mA	+15 Vdc	120 g
	C1309-04				1 mA		
	C1309-06	-1.5 kV Output Modular Type	-400 to -1500 V		1 mA	+15 Vdc	100 g
	C2456	Small Modular Type	-190 to -1100 V		0.5 mA		

# COOLERS

## Cooling Effect on Dark Current

### FACTORS OF DARK CURRENT

The dark current of a photomultiplier tube is a slight output current which flows when a high voltage is applied to the tube and no light is entering the photocathode. Since dark current deteriorates the S/N ratio, it is a factor which establishes the minimum limit of detection when the output current is extremely low, when measuring extremely low-level light. Factors which affect dark current can be classified into the seven described below. The degree to which each of these affects dark current will depend, however, on the type of photomultiplier tube and will vary from tube to tube and with respect to operation conditions.

- 1) Thermionic emission of electrons from the photocathode and dynode surfaces.
- 2) Leakage current between electrodes and pins. This is chiefly due to impurities on the electrode supporting materials, glass stem and plastic base surfaces and on the socket surfaces.
- 3) Ion current flowing as the result of ionization of residual gases inside the bulb.
- 4) Photoelectron emission as a result of collision of internal electrons and ions with electrode supporting materials and glass.
- 5) Photoelectron emission by the glass scintillation as a result of gamma rays emitted from radioactive elements (chiefly <sup>40</sup>K) within the glass bulb.
- 6) Photoelectron emission caused by Cherenkov radiation due to cosmic rays passing through the glass.
- 7) Field emission of electron from the photocathode surface and dynode surfaces.

Figure 1: Dark Current vs. Supply Voltage

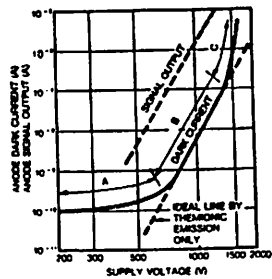
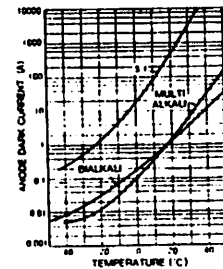


Figure 1 shows the relationship between the voltage applied between the cathode and anode of a photomultiplier tube and the anode dark current. This characteristic curve can be divided into three regions. In the low-voltage region A, the major cause of dark current is the leakage current 2) and in the high-voltage region C, 3), 4) and 7) become the governing factors which determine the dark current. In contrast to this, in the region B which approximates actual operation condition, thermal electron emission is the governing factor. From this behavior, it can be seen that cooling the photocathode surface and dynodes would be very effective in reducing dark current.

### COOLING EFFECT

Figure 2 shows a comparison of the temperature characteristics of dark current for various photocathode materials in a photomultiplier tube of the same shape and dynode structure. From this figure, it can be seen that, as the work function becomes smaller (balkali → multialkali → S-1: silver oxide cesium), the influence of temperature in determining the dark current increases. Essentially, this means that the effectiveness of refrigeration in reducing dark current and improving the S/N ratio increases. In this figure, although the cooling effect decreases in the region below -20 to -30°C, this is attributable to the fact that the contribution of factors other than thermionic emission becomes relatively large in this region. In photon counting applications since the leakage current can be ignored, it is possible to achieve greater effectiveness from cooling.

Figure 2: Dark Current vs. Temperature for Various Photocathodes



# MAGNETIC SHIELD CASES

## Influence of Magnetic Fields and Magnetic Shielding

### INFLUENCE OF MAGNETIC FIELDS

The photomultiplier tube is a type of vacuum tube in which photoelectrons emitted from the photocathode repeatedly collide with dynodes and are thus multiplied before they reach the anode. The degree of multiplication varies significantly depending upon the position of the collision on the dynode. Therefore, external magnetic fields can cause electrons to be deflected from their normal paths, causing a loss in electron multiplication factors. Essentially, the photomultiplier tube output is extremely susceptible to the effects of magnetic fields. For example, since even the terrestrial magnetic field has quite an effect, merely rotating the position of a photomultiplier tube will result in a noticeable change. Because of this phenomenon, photomultiplier tubes which must be moved and those which must operate in proximity to the leakage flux from such devices as transformers must be mounted in magnetic shields.

### MAGNETIC CHARACTERISTICS

The degree of change in output with respect to magnetic fields varies greatly depending upon the type of photomultiplier tube. Figure 1 shows the magnetic characteristics of typical photomultiplier tubes. The measurement was made by placing the photomultiplier tube and excitation coil inside a permalloy housing and degaussing the electrode before measurement. A uniform light intensity was applied to the photocathode and an output current of approximately 1μA was derived. The magnetic field direction is shown in Figure 2.

In general, photomultiplier tubes having a large distance between the photocathode and anode and, in particular, those having a large distance between the photocathode and the first dynode or a relatively small dynode opening in comparison with the photocathode area, will exhibit a large variation. Therefore, head-on types of photomultiplier tubes which usually have a long distance between the photocathode and the first dynode are more susceptible to this effect than side-on types. And of these, types which have a large photocathode area show particularly large variations.

Electrons chiefly receive the effects of a magnetic field in the region between the photocathode and the first dynode. This is because the distances between the following dynodes are relatively short and because the dynodes themselves are made of nickel or other magnetic materials which provides a shielding effect with respect to electrons travelling through the dynodes.

Figure 2: Direction of Magnetic Fields (For data shown in Figure 1)

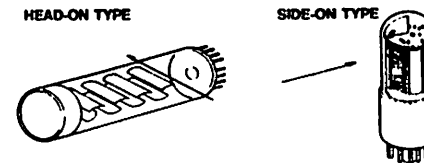
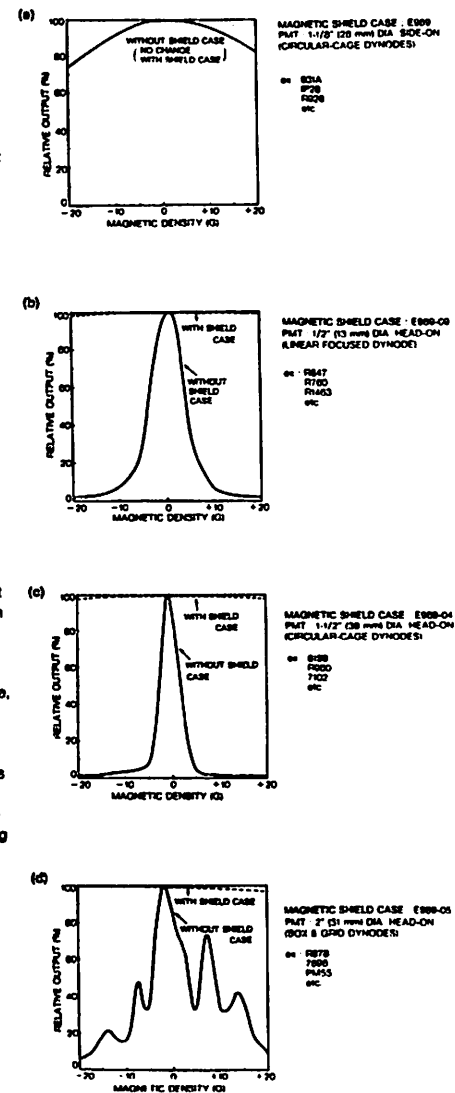


Figure 1: Examples of Magnetic Shield Effect



## SHIELDING EFFECT

Magnetic shield cases are metallic tubes fabricated from permalloy or other materials having high permeability. By positioning the photomultiplier tube within such a case, it is possible to reduce the influence of external magnetic fields on output level. To express the effect of a magnetic shield case, the magnetic shielding factor may be used. It is determined by the permeability  $\mu$ , the thickness  $t$  and inner radius  $r$  of the shield case, as shown in Figure 3.

The magnetic shielding factor for two shield cases of different radii used one within the other is the product of the two shielding factors. This scheme is usable to obtain an extremely high shielding effect.

### 1) Saturation Characteristics

The B-H curve which expresses the relationship between the external magnetic field (H) and flux density (B) within a magnetic material indicates a saturation characteristic, as shown in Figure 4. Since the permeability  $\mu$  is given by the B-H ratio, the relationship of H to  $\mu$ , as shown in Figure 5, varies depending upon the external magnetic field intensity, with subsequent change in the shielding effect. Therefore, in extremely high-intensity magnetic fields, it is recommended that a soft-iron magnetic shield case having a thickness of approximately 3 to 10  $\mu\text{m}$  be used as this material has a high saturation flux density.

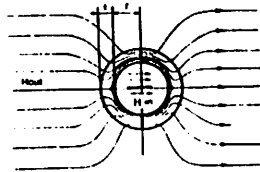
### 2) Frequency Characteristic

The above described shield case characteristics are for DC magnetic fields. In contrast to this type of field, the leakage flux from a transformer creates an AC magnetic field effect which must be considered as well. The permeability of a magnetic material decreases with increasing frequency. This is particularly noticeable for thick materials, even at low frequencies. Hamamatsu E989 Series shield cases use a material of 0.8 mm thickness, yet providing sufficient effective permeability even at normal line power frequencies of 50 or 60 Hz, shown in Figure 6. If magnetic fields of high frequencies such as 1 to 10 kHz are applied, a thin shielding material (0.05 to 0.1 mm) having good frequency characteristic should be used in combination with the normal shielding.

### 3) Edge Effect

The shielding effect given by  $3\mu t/4r$  applies in the case that the shield case is of sufficient length. Since actual shield cases have a finite length, however, there is a deterioration of the shielding effect at both ends which should be considered. For this reason, as shown in Figure 7, it is necessary to locate the photomultiplier tube so that its end is somewhat covered by the shielding tube. For head-on photomultiplier tubes, this depth should be approximately the case radius. If the magnetic field direction is parallel to that of the tube axis, however, the edge effect becomes extremely prominent, so that the photomultiplier tube should be kept to within at least the diameter depth from the end of the shield case.

Figure 3: Shielding Effect



$$\text{Shielding factor } \left( \frac{H_{out}}{H_{in}} \right) = \frac{3\mu t}{4r}$$

Figure 4:  $\beta$ -H Curve

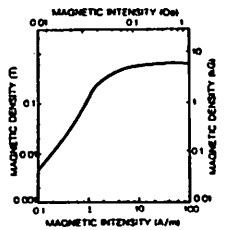


Figure 5: Permeability and Magnetic Field

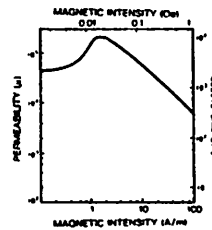


Figure 6: Frequency Characteristic

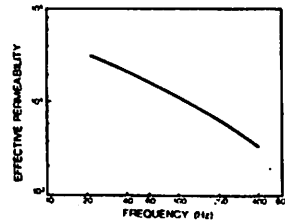
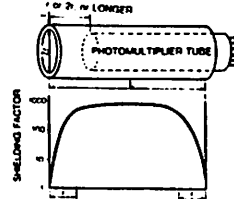


Figure 7: Edge Effect



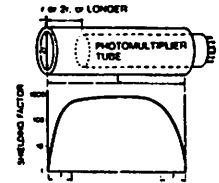
## PRECAUTIONS FOR USE

- Magnetic shield cases should not be subjected to shocks. When deformed by shocks, permeability decreases. Also whittling and drilling the case affect permeability, and therefore should be avoided.
- Some shield cases have small holes near the edge. These holes should be used to mount the shield case on the chassis and not to clamp the tube in the shield case.
- The E989-10 has a little flexibility in diameter as shown at the right. However, when the diameter exceeds the range from 14 to 17 mm, the shield case may be deformed and permeability lowered.
- The PMT tends to increase in noise when a grounded object approaches the tube. Since the shield case is generally used at the ground potential, the PMT should be positioned in the center of the shield case by using, for example, elastic foam rubber with sufficient insulation wrapped around the tube.  
\*The cathode-ground scheme and HA Coated tubes are excepted from the above.
- The magnetic shielding effect decreases towards the edge of the shield case as shown at the right. It is suggested to cover the tube with a shield case longer than the length by at least half the tube diameter. See the item "Edge Effect" on page 25.
- Shield Case Mounting Method

### ● E989-10 Flexibility (mm)



### ● Edge Effect of Magnetic Shield Case



In making precise photometric measurements, it is essential that the position of the photomultiplier tube be kept constant with respect to the other parts of the measuring system.

When using E989 Series shield cases, it is necessary to mount the photomultiplier tube securely to ensure that no looseness develops between the photomultiplier tube and the shield case or between the shield case and the other parts of the system. When a photomultiplier tube which does not have an HA coating is used in a grounded anode circuit with a high negative voltage applied to the cathode, if the shield case is grounded, there is a danger of noise being generated, as described above. This noise may be minimized by insulating the shield case from ground potential sufficiently and, even if the outside of the shield case is sufficiently insulated, by connecting the shield case to the cathode through a resistance of approximately 10 M $\Omega$ . This technique is particularly required when measuring extremely low light levels.

The following are typical shield case mounting methods.

#### E989-10: (For 1/2" Side-On Photomultiplier Tubes)

The shield case can be positioned around the photomultiplier tube using an insulating material having good insulating properties between these two components. Then tighten then using adhesive tape or thermal-shrinkable tube.

#### E989: (For 1-1/8" Side-On Photomultiplier Tubes)

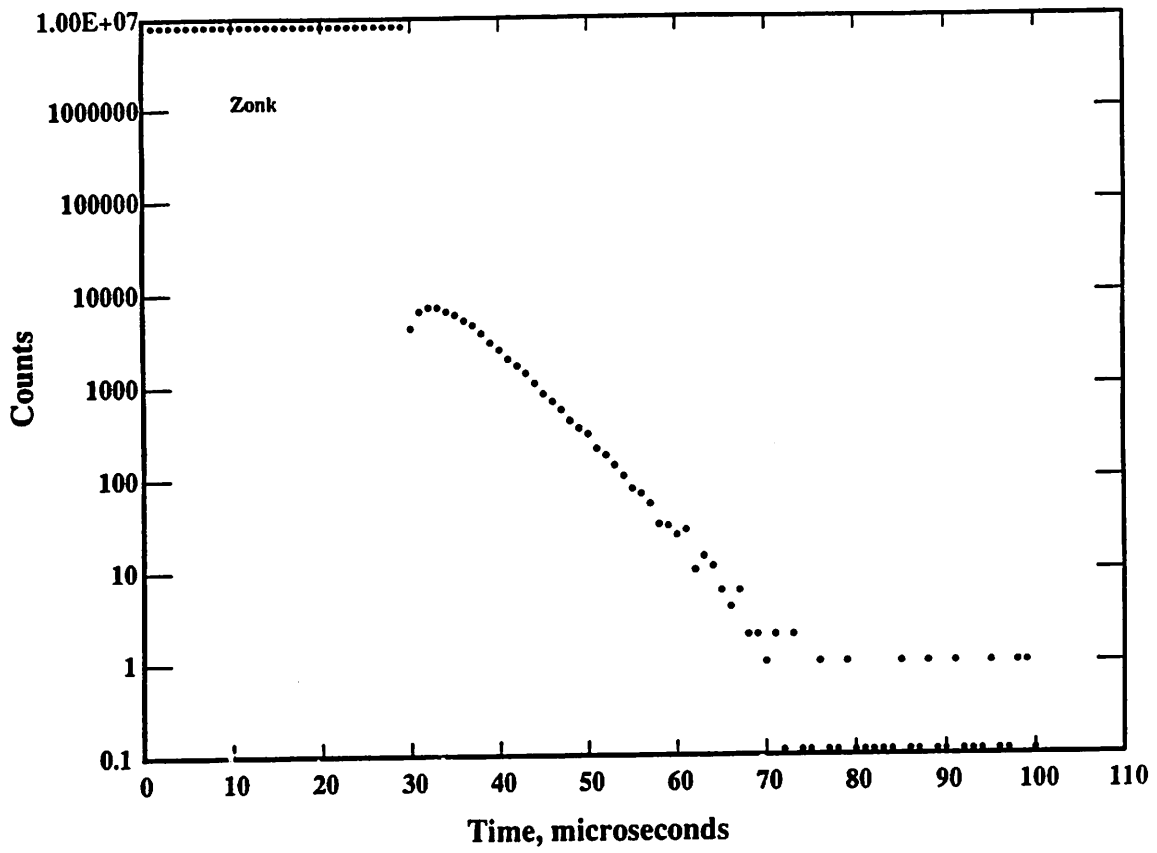
Foam rubber or a similar material having good insulating properties and elasticity can be used to hold the photomultiplier tube in the center of the shield case. By using the mounting holes in the shield case, mount the shield case to the system. When doing this, use of L clamps or other mounting fixtures are suggested.

#### Shield Cases for Head-On Photomultiplier Tubes:

Foam rubber or other similar materials having good insulating properties and elasticity can be used to securely hold the tube in the center and an appropriate holder should be used to mount the shield case to the measurement system. When tightening the shield case using bands or screws, sufficient care should be taken that force sufficient to deform the shield case is not applied.

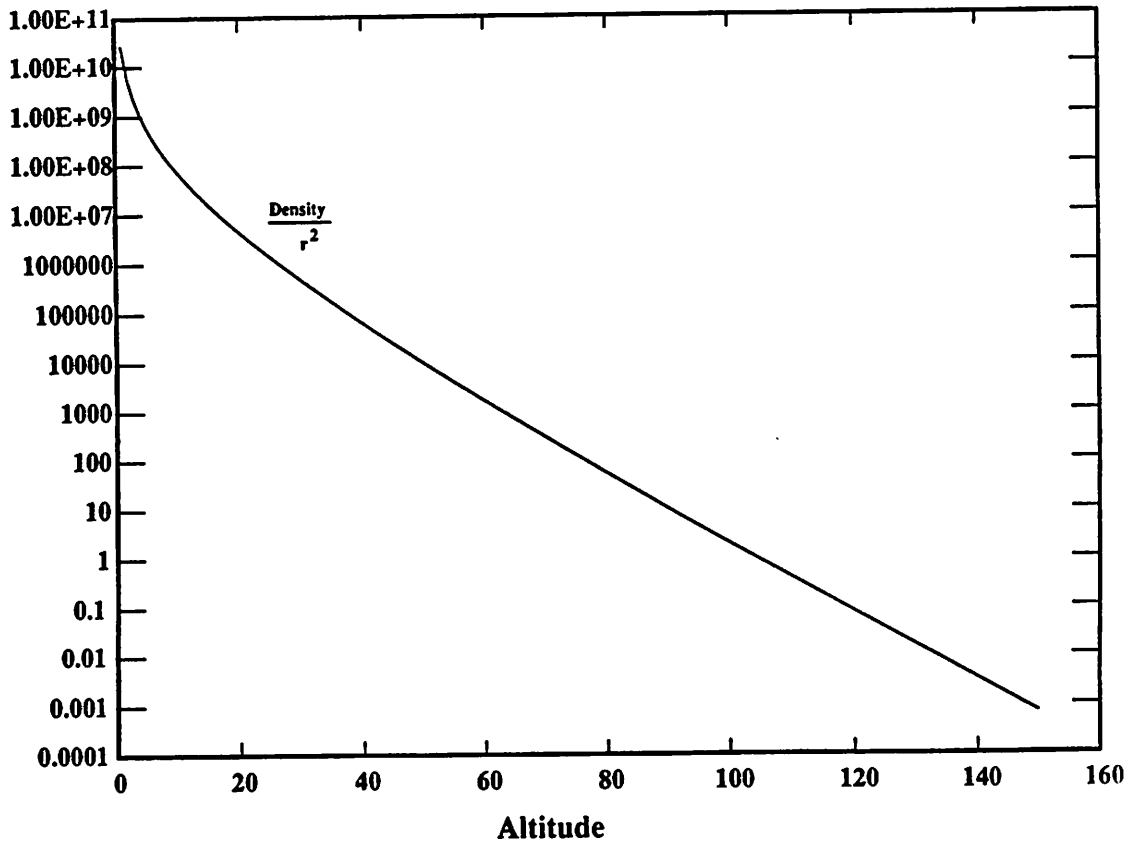
\*Some Teflon and plastic materials may cause scintillation when illuminated with UV light. Care should be taken when selecting insulators.





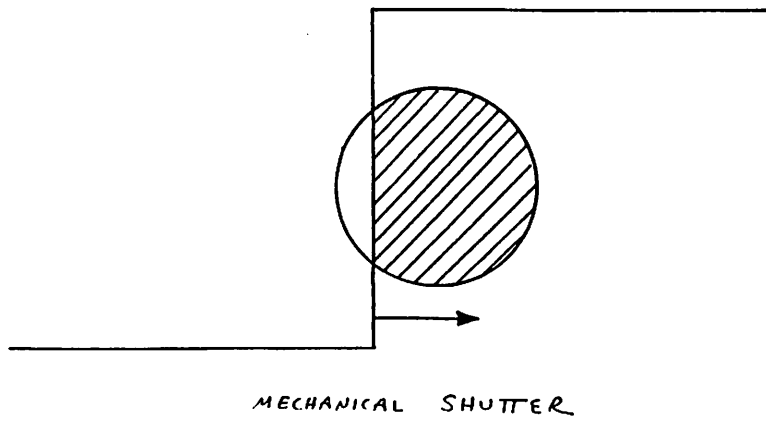
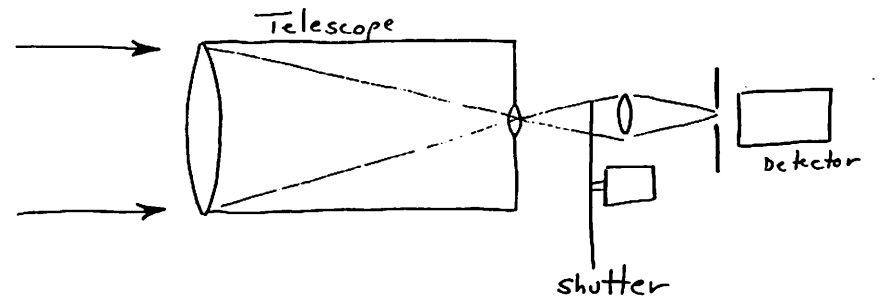
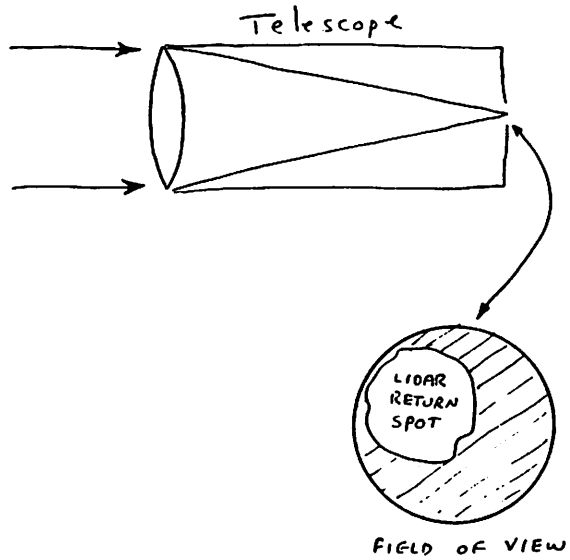
**Photomultiplier Response to being Zonked**

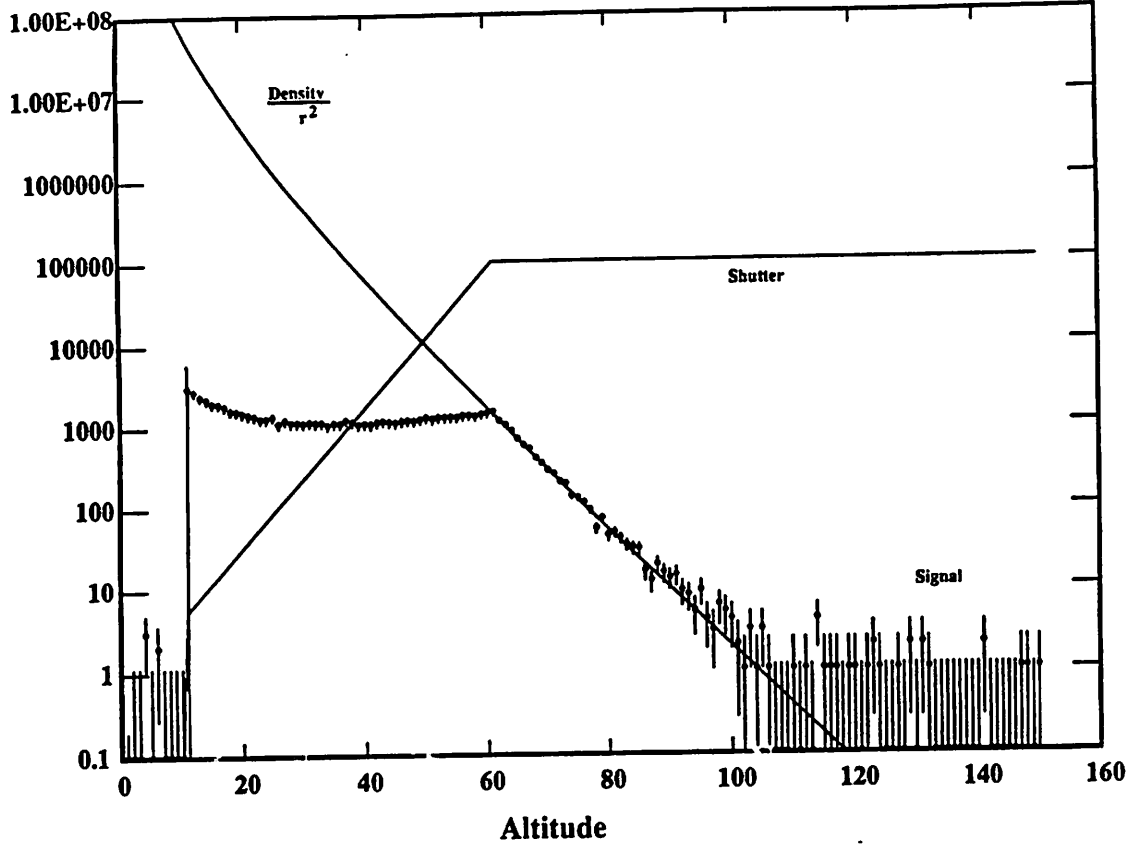
Zonk 910604/150556



**Lidar Signal**

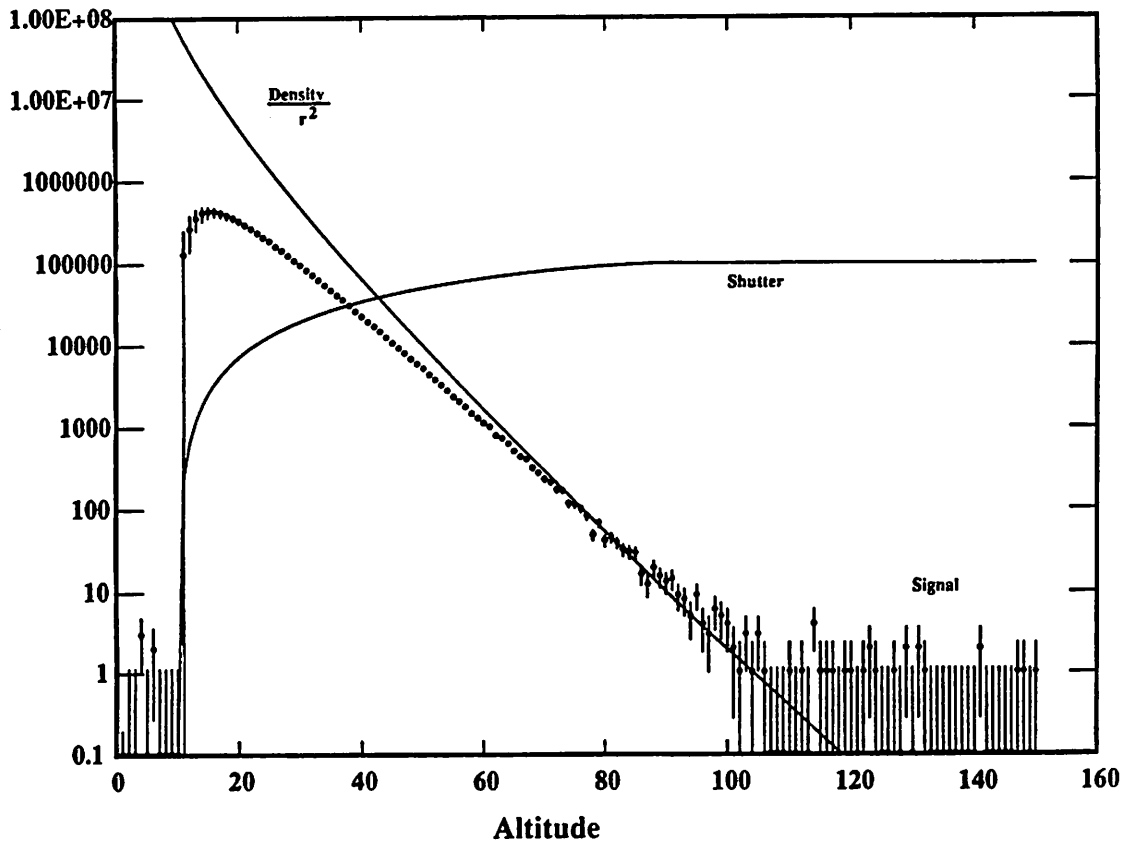
Return 910604/143149





Lidar Signal

Return 910604/145226



Lidar Signal

Return 910604/145216

**For Photon Counting  
Low Dark Counts, Wide Spectral Response, Excellent P.H.D.  
GaAs(Cs) Photocathode, 2" (51mm) Dia., Head-on Type**

Hamamatsu R943-02 is a 2" diameter, head-on type photomultiplier tube having a GaAs(Cs) photocathode and a synthetic silica window. The combination of the GaAs photocathode and the synthetic silica window allows high sensitivity over a wide spectral range from UV to IR (160 - 930nm). The R943-02 employs the linear focused dynode which is designed specifically for photon counting application. It features very low dark counts and excellent pulse height distribution (PHD) of single photoelectrons. (Fig. 2) The R943-02 is equivalent type of RCA C31034 series photomultiplier tube, but basing diagram and voltage divider are somewhat different.

**APPLICATIONS**

- Raman Spectroscopy
- Fluorescent Spectroscopy
- Astrophysical Measurement
- Laser Detection

**FEATURES**

Low Dark Counts ..... 20 cps typ. (at -20°C)  
Wide Range Spectral Response ..... 160 - 930nm  
Excellent Single Photoelectron Pulse Height Distribution  
..... Peak to Valley Ratio = 1.8 (at -20°C)  
Fast Time Response ..... Rise Time = 3.0ns (at 1500V)  
High Quantum Efficiency ..... 14% (at 632.8nm)

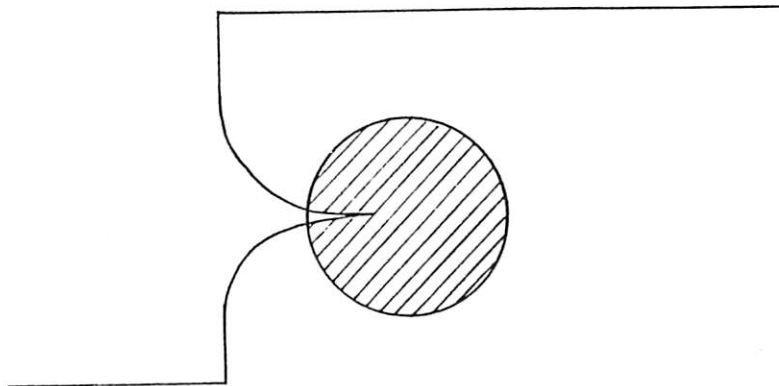
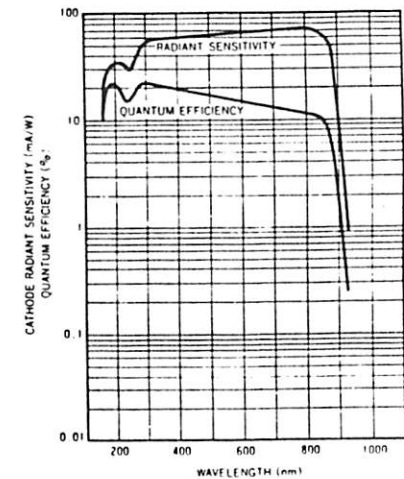
**GENERAL**

Spectral Response ..... 160 to 930nm  
Wavelength of Maximum Response ..... 300 to 800 nm  
Photocathode  
Material ..... GaAs(Cs)  
Minimum Useful Area ..... 10mm x 10mm  
Mode ..... Opaque  
Window Material ..... Synthetic Silica  
Dynode  
Secondary Emitting Surface ..... Cu-BeO  
Structure ..... Linear Focused  
Number of Stages ..... 10  
Direct Interelectrode Capacitances (Approx.)  
Anode to Last Dynode ..... 2pF  
Anode to All Other Electrodes ..... 3pF  
Base ..... 21-pin Glass Base  
Weight ..... 93g  
Suitable Socket\* ..... E678-21A (Supplied)

\* See "Note D" on page 2 and "Cautions" on page 4



Figure 1: Typical Spectral Response



## PHOTOMULTIPLIER TUBE R943-02

### MAXIMUM RATINGS (Absolute Maximum Values at 25°C)

Supply Voltage	2200Vdc
Between Anode and Cathode	250Vdc
Between Anode and Last Dynode	250Vdc
Average Anode Current <sup>A</sup>	1 $\mu$ A
Average Pulse Count Rate <sup>B</sup>	6 x 10 <sup>6</sup> cps
Average Cathode Current <sup>C</sup>	100nA
Ambient Temperature <sup>D</sup>	-80 to 50°C

### CHARACTERISTICS (at 25°C)

Cathode Sensitivity <sup>E</sup>	Min.	Typ.	Max.	Units
Quantum Efficiency				%
at 280nm	-	21	-	%
at 632.8nm (He-Ne Laser)	-	14	-	%
Luminous <sup>F</sup>	300	600	-	$\mu$ A/m
Radiant				mA/W
at 253.7nm (Hg-Line)	-	30	-	mA/W
at 632.8nm (He-Ne Laser)	-	70	-	mA/W
at 700nm	-	71	-	mA/W
at 852.1nm (Cs-Line)	-	65	-	mA/W
Red to White Ratio <sup>G</sup>	-	0.58	-	
Anode Sensitivity <sup>H</sup>				A/m
Luminous <sup>F</sup>	150	300	-	A/m
Radiant				A/W
at 253.7nm (Hg-Line)	-	1.5 x 10 <sup>4</sup>	-	A/W
at 632.8nm (He-Ne Laser)	-	3.5 x 10 <sup>4</sup>	-	A/W
at 700nm	-	3.6 x 10 <sup>4</sup>	-	A/W
at 852.1nm (Cs-Line)	-	3.3 x 10 <sup>4</sup>	-	A/W
Current Amplification <sup>I</sup>	-	5 x 10 <sup>5</sup>	-	
Equivalent Anode Dark Current <sup>J</sup>	-	1	10	nA
Anode Dark Counts <sup>K</sup>	-	20	50	cps
Time Response <sup>L</sup>				ns
Anode Pulse Rise Time <sup>L</sup>	-	30	-	ns
Electron Transit Time <sup>M</sup>	-	23	-	ns

Table 1: Voltage Distribution Ratio

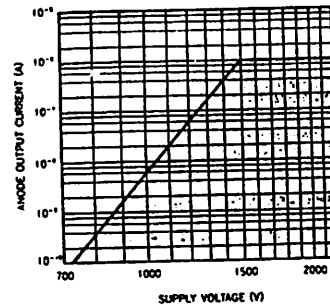
Electrode	K	Dy <sub>1</sub>	Dy <sub>2</sub>	Dy <sub>3</sub>	Dy <sub>4</sub>	Dy <sub>5</sub>	Dy <sub>6</sub>	Dy <sub>7</sub>	Dy <sub>8</sub>	Dy <sub>9</sub>	Dy <sub>10</sub>	P
Distribution Ratio	3	15	1	1	1	1	1	1	1	1	1	1

Supply Voltage: 1500Vdc

### NOTES

- Averaged over any interval of 30 seconds maximum.
- Measured at single photoelectron level. The discriminator level is set at valley point.
- In practical operation, the cathode current is desired to be lower than 0.1nA (0.001nA/mm<sup>2</sup>) to prevent life shortening of photocathode. To keep the cathode current under 0.1nA, the anode current should not get out of the region of  $\square$  in the figure below.

Recommended Anode Current vs. Supply Voltage



- At temperature of less than -50°C the tube may be damaged due to the difference in temperature coefficients between the glass stem and the socket. Don't use the socket below -50°C. However, the tube use at temperature lower than -50°C can be made possible by facilitating direct contact with the stem pin, using a socket contact (100-2520S) supplied by Winchester. For details, please contact your local HAMAMATSU representative.
- Supply voltage is 150 volts between the cathode and all other electrodes.
- The light source is a tungsten filament lamp operated at a distribution temperature of 2656K.
- The quotient of the cathode sensitivity measured with the light source same as Note E passing through a red filter (Toshiba R-68) divided by the cathode luminous sensitivity without the red filter.
- Measured with the supply voltage and voltage distribution ratio in Table 1.
- Measured with the supply voltage to provide the anode luminous sensitivity of 200 (A/m) and the voltage distribution ratio in Table 1 after 30 minute storage in the darkness.
- Measured with the supply voltage which gives 2 x 10<sup>6</sup> of current amplification and with the voltage distribution ratio shown in Table 1 after one hour storage in the cooler set at -20°C. And the discriminator is set at 1/3 of single photoelectron level.
- The rise time is the time for the output pulse to rise from 10% to 90% of the peak amplitude when the entire photocathode is illuminated by a delta function light pulse.
- The electron transit time is the interval between the arrival of a delta function light pulse at the entrance window of the tube and the time when the output pulse reaches the peak amplitude. In measurement the entire photocathode is illuminated.

**Warning—Personal Safety Hazards**  
Electrical Shock — Operating voltages applied to this device present a shock hazard

Figure 2: Typical Photoelectron Pulse Height Distribution

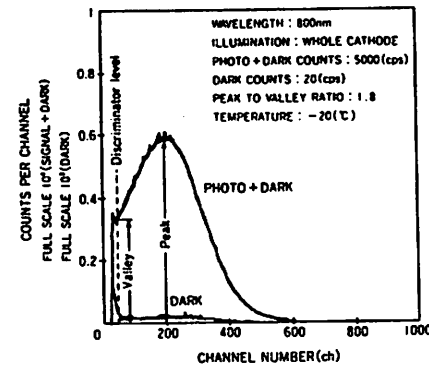


Figure 4: Typical Time Response

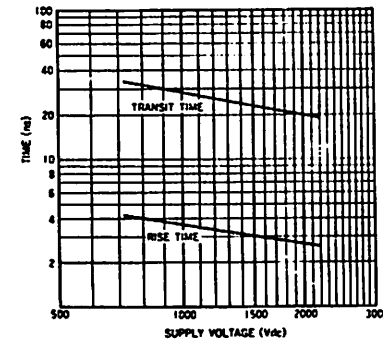


Figure 6: Typical Dark Counts vs. Temperature

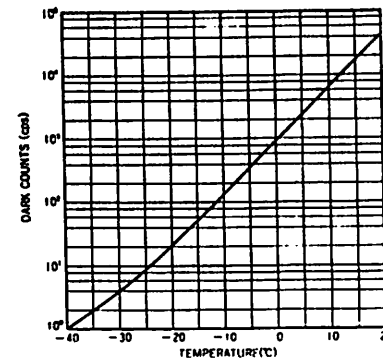


Figure 3: Typical Anode Sensitivity and Current Amplification

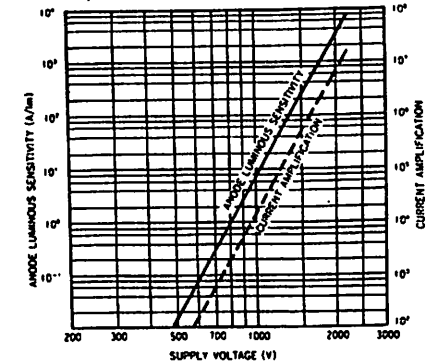
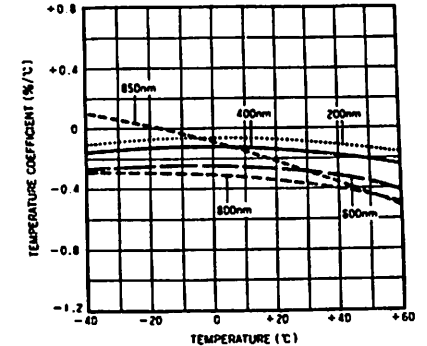


Figure 5: Typical Temperature Coefficient of Quantum Efficiency

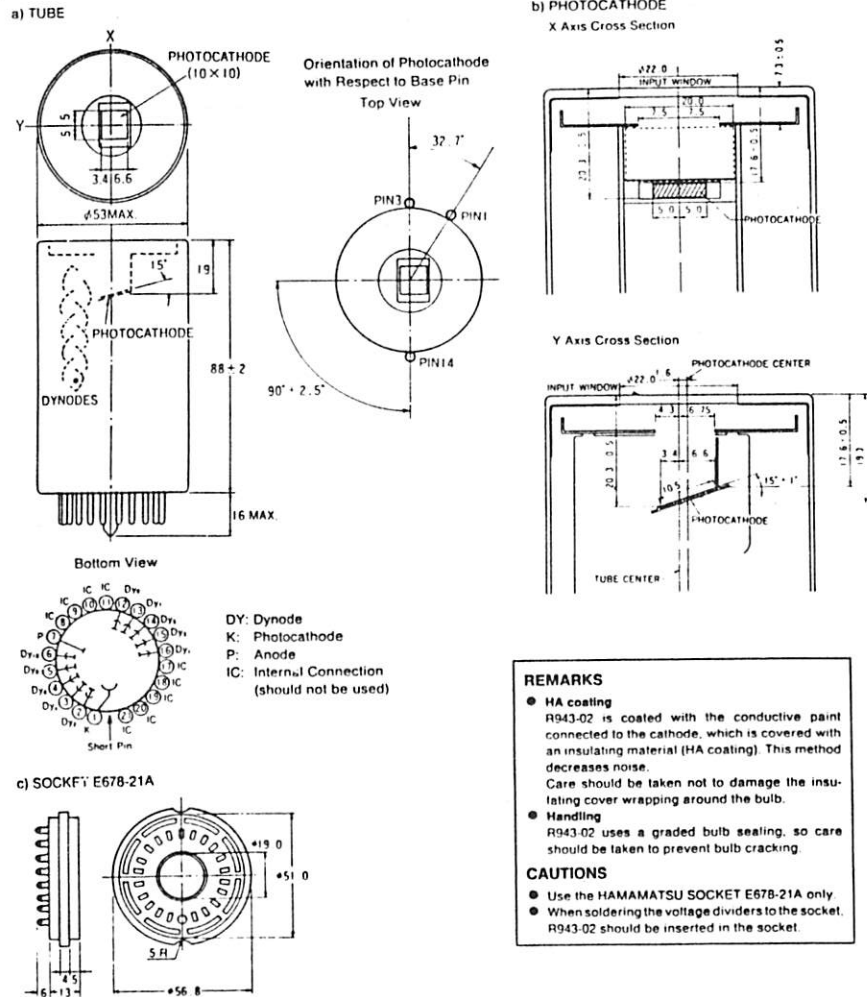


### COOLING

As Figure 6 shows, the dark counts of the R943-02 decreases by cooling the tube. Therefore, when performing photon counting, it is recommended that the tube be cooled down to about -20°C. The cooler C2761 which features temperature control from -30°C to 0°C is available from HAMAMATSU.

# PHOTOMULTIPLIER TUBE R943-02

Figure 7: Dimensional Outline and Basing Diagrams (Unit: mm)



## HAMAMATSU

HAMAMATSU PHOTONICS K.K., Electron Tube Division  
314-5, Shimokanzo, Toyooka-village, Iwata-gun, Shizuoka-ken, 438-01 Japan, Telephone: 0539625248, Fax: 0539622205, Telex: 4209-625  
U.S.A.: Hamamatsu Corporation, 360 Foothill Road, P.O. Box 6910, Bridgewater, N.J. 08807-0910, Telephone: 201-231-0960, Fax: 201-231-1539  
W.Germany: Hamamatsu Photonics Deutschland GmbH, Arzbergerstr. 10, D-8036 Herrsching am Ammersee, Telephone: 08152 375 0, Fax: 08152 2658  
France: Hamamatsu Photonics France, 49-51 Rue de la Vanne, 92120 Montrouge, Telephone: (1) 46 55 47 58, Fax: (1) 46 55 36 65

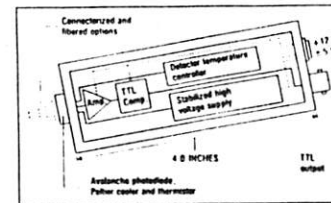
## Ultra-low light level photon counting modules

### PHOTONS IN... PULSES OUT

The SPCM-100 series of single photon counting modules, featuring a new generation of silicon avalanche photodiodes, are designed for applications such as photon correlation for particle sizing, fluorescence studies, etc.

These simple-to-use modules offer:

- Photon detection efficiencies up to 40% @ 633 nm, up to 25% @ 800 nm
- Low voltage inputs: +12, +5, -5 volts
- TTL output pulses
- Nothing to adjust



Standard modules are available with performance specifications to suit different applications. Standard optical interfaces include fiber optic connectorized and single- and multi-mode optical fibers.

If your design can benefit from simple, efficient photon counting, call and request Data Sheet SPCM-100 and pricing information. We also welcome your enquiries regarding custom and OEM applications.

Electro  
Optics

The Leader  
in Emitters  
and Detectors

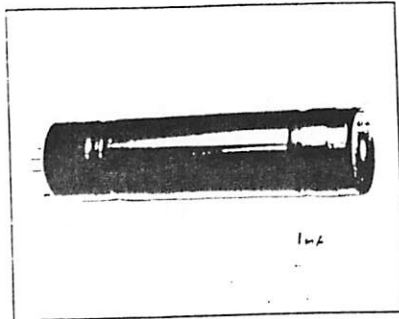
RCA Inc., Electro Optics

USA: 212-633-9122 Canada/Rest of World: 416-433-6191 Europe: 01-935-3099

## Introducing solid state photon counting modules that outperform PMTs.



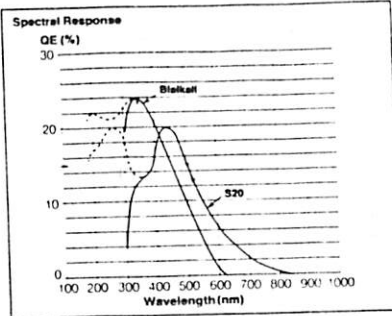
THORN EMI 14 STAGE FAST LINEAR DYNODE PHOTOMULTIPLIER



This group of tubes is primarily intended for wide bandwidth, high gain photon counting applications although most types are equally suitable for d.c. measurements.

The parent type is the S20 response 9863 which is based on the THORN EMI 14 stage fast linear focused dynode structure, with BeCu secondary emitting surfaces. However, the photocathode diameter is reduced by internal focusing to 2.5 mm in the 9863/100 and 9 mm in the 9863/350. This results in negligible cathode dark count at room temperature while still preserving the wide spectral range of the S20 photocathode.

Bialkali cathode variants are the 9893/100 and 9893/350 which are directly interchangeable with the 9863. These provide even lower dark count for applications in the visible region.



The 9883 is identical in construction to the bialkali cathode 14 stage 9813 (page 36) but has a first dynode which is specially processed to give a high secondary emission coefficient (~18 at 600 eV). This results in an improved single electron response of typically 70% l.w.h.m.

The 9884 is a 12 stage version of the 9883 for use where the higher gain is not necessary or where the slightly faster response time is an advantage.

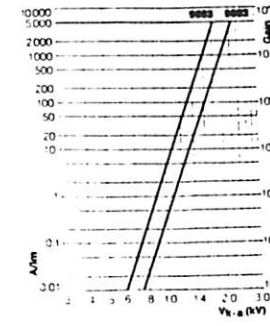
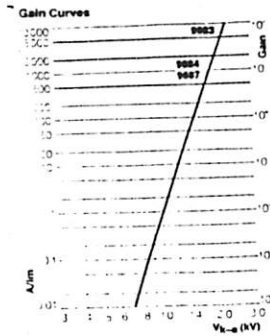
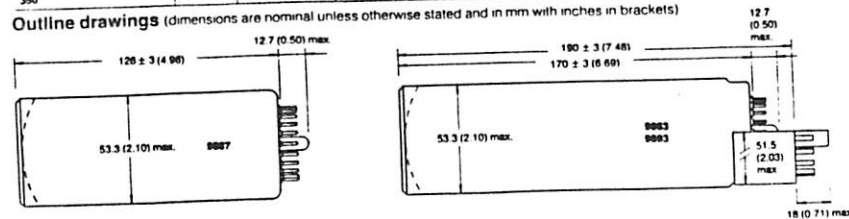
All types are available with a quartz (fused silica) window option denoted by a 'Q' suffix.

Note: These types are normally supplied graphite coated (connected to cathode pin) and black plastic sleeved to eliminate charging of the glass envelope. The sleeving is provided for insulation purposes and should not be removed without consulting THORN EMI.

Electrical Characteristics and Ratings

Tube type	Spectral response & window	No. type & material of dynodes	Effective cathode dia. mm (in)	CATHODE SENSITIVITY										ANODE SENSITIVITY						
				$\mu A/A/m$		Corning blue		Corning red		Intra red		QE% peak		QE% 700 nm		mA/V 700 nm		A/m in $V_{k-a}$		Gain (x10 <sup>6</sup> )
				nom.	min.	typ.	min.	typ.	min.	typ.	min.	typ.	min.	typ.	typ.	nom.	typ.	max.	nom.	
9863B/100	S20/B	14LF BeCu	2.5 (1)	125	185	9.5	70	2.5	20	3.9	22	5000	1950	2500	27					
9863B/350	S20/B	14LF BeCu	9 (3.5)	125	185	9.5	70	2.5	20	3.9	22	5000	1950	2500	27					
9883B	Bialk/B	14LF BeCu	48 (1.8)	75	8	11	2				27	5000	2150	2500	67					
9884B	Bialk/B	12LF BeCu	48 (1.8)	75	8	11	2				27	500	1800	2300	8.7					
9887B	Bialk/B	12LF BeCu	48 (1.8)	75	8	11	2				27	500	1700	2300	8.7					
9883B/100	Bialk/B	14LF BeCu	2.5 (1)	80	7	8.5	1				22	5000	2250	2700	83					
9893B/100	Bialk/B	14LF BeCu	9 (3.5)	80	7	8.5	1				22	5000	2250	2700	83					

Outline drawings (dimensions are nominal unless otherwise stated and in mm with inches in brackets)

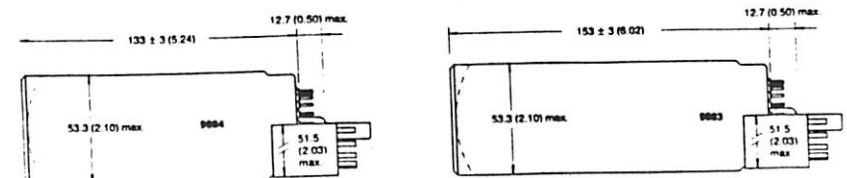


Pin Connections (viewed from below, counting clockwise from short pin or key) ic = internal connection. Socket contact not to be used

Type	1	2	3	4	5	6	7	8	9	10	11	12	13	14	15	16	17	18	19	20	21	Socket
9863	ic	d <sub>1</sub>	d <sub>2</sub>	d <sub>3</sub>	d <sub>4</sub>	d <sub>5</sub>	d <sub>6</sub>	d <sub>7</sub>	d <sub>8</sub>	d <sub>9</sub>	d <sub>10</sub>	d <sub>11</sub>	d <sub>12</sub>	d <sub>13</sub>	d <sub>14</sub>	d <sub>15</sub>	ic	ic	ic	ic	ic	B19A
9893	ic	d <sub>1</sub>	d <sub>2</sub>	d <sub>3</sub>	d <sub>4</sub>	d <sub>5</sub>	d <sub>6</sub>	d <sub>7</sub>	d <sub>8</sub>	d <sub>9</sub>	d <sub>10</sub>	d <sub>11</sub>	d <sub>12</sub>	d <sub>13</sub>	d <sub>14</sub>	d <sub>15</sub>	ic	ic	ic	ic	ic	B19A
9883K	ic	d <sub>1</sub>	d <sub>2</sub>	d <sub>3</sub>	d <sub>4</sub>	d <sub>5</sub>	d <sub>6</sub>	d <sub>7</sub>	d <sub>8</sub>	d <sub>9</sub>	d <sub>10</sub>	d <sub>11</sub>	d <sub>12</sub>	d <sub>13</sub>	d <sub>14</sub>	d <sub>15</sub>	ic	ic	ic	ic	ic	B20
9883K	ic	d <sub>1</sub>	d <sub>2</sub>	d <sub>3</sub>	d <sub>4</sub>	d <sub>5</sub>	d <sub>6</sub>	d <sub>7</sub>	d <sub>8</sub>	d <sub>9</sub>	d <sub>10</sub>	d <sub>11</sub>	d <sub>12</sub>	d <sub>13</sub>	d <sub>14</sub>	d <sub>15</sub>	ic	ic	ic	ic	ic	B19A
9883	ic	d <sub>1</sub>	d <sub>2</sub>	d <sub>3</sub>	d <sub>4</sub>	d <sub>5</sub>	d <sub>6</sub>	d <sub>7</sub>	d <sub>8</sub>	d <sub>9</sub>	d <sub>10</sub>	d <sub>11</sub>	d <sub>12</sub>	d <sub>13</sub>	d <sub>14</sub>	d <sub>15</sub>	ic	ic	ic	ic	ic	B20
9883K	ic	d <sub>1</sub>	d <sub>2</sub>	d <sub>3</sub>	d <sub>4</sub>	d <sub>5</sub>	d <sub>6</sub>	d <sub>7</sub>	d <sub>8</sub>	d <sub>9</sub>	d <sub>10</sub>	d <sub>11</sub>	d <sub>12</sub>	d <sub>13</sub>	d <sub>14</sub>	d <sub>15</sub>	ic	ic	ic	ic	ic	B19A
9884	ic	d <sub>1</sub>	d <sub>2</sub>	d <sub>3</sub>	d <sub>4</sub>	d <sub>5</sub>	d <sub>6</sub>	d <sub>7</sub>	d <sub>8</sub>	d <sub>9</sub>	d <sub>10</sub>	d <sub>11</sub>	d <sub>12</sub>	d <sub>13</sub>	d <sub>14</sub>	d <sub>15</sub>	ic	ic	ic	ic	ic	B20
9884K	ic	d <sub>1</sub>	d <sub>2</sub>	d <sub>3</sub>	d <sub>4</sub>	d <sub>5</sub>	d <sub>6</sub>	d <sub>7</sub>	d <sub>8</sub>	d <sub>9</sub>	d <sub>10</sub>	d <sub>11</sub>	d <sub>12</sub>	d <sub>13</sub>	d <sub>14</sub>	d <sub>15</sub>	ic	ic	ic	ic	ic	B20
9887	d <sub>1</sub>	d <sub>2</sub>	d <sub>3</sub>	d <sub>4</sub>	d <sub>5</sub>	d <sub>6</sub>	d <sub>7</sub>	d <sub>8</sub>	d <sub>9</sub>	d <sub>10</sub>	d <sub>11</sub>	d <sub>12</sub>	ic	ic	ic	ic	ic	ic	ic	ic	ic	B21

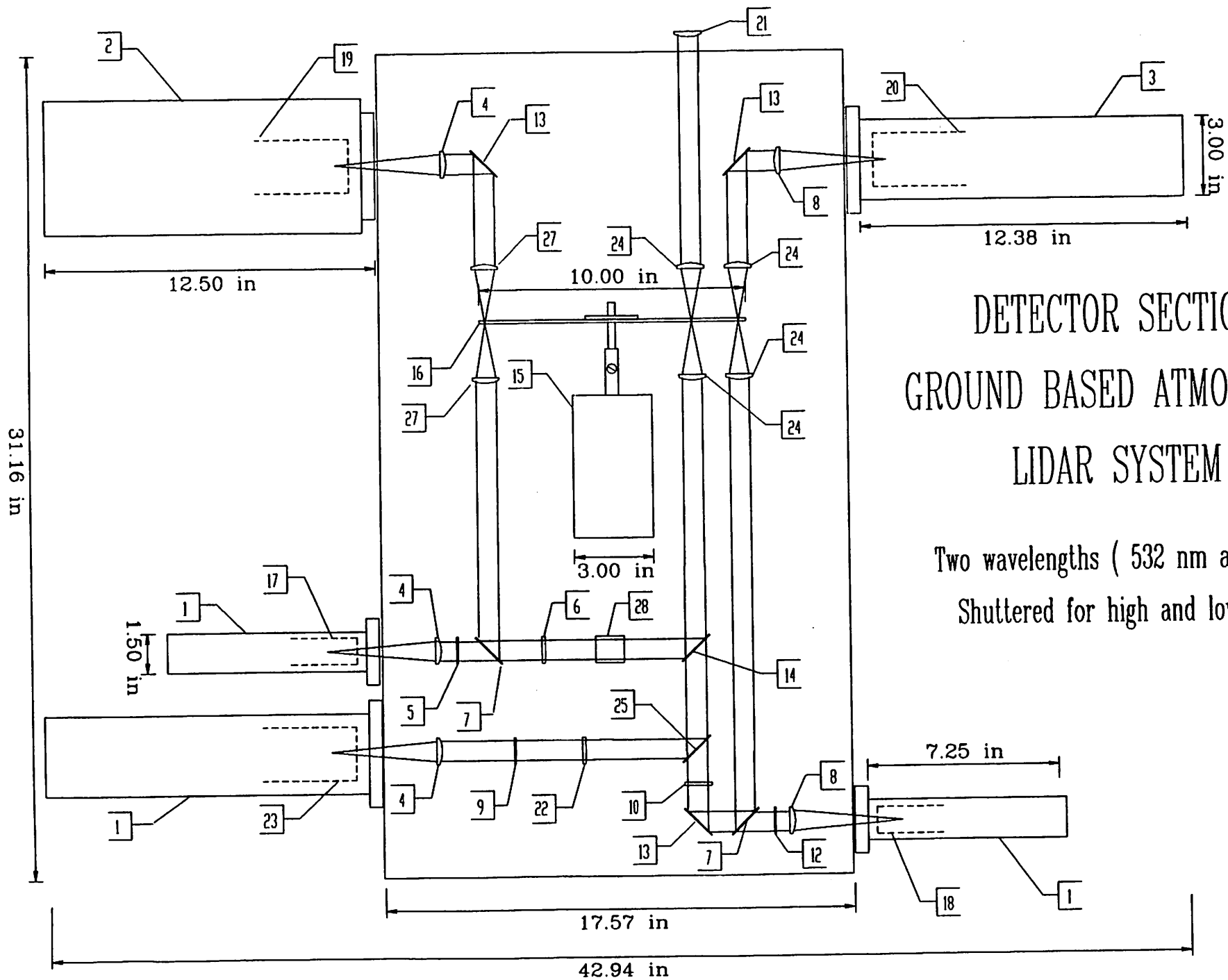
Focus should be connected to G.

Tube type	DARK EMISSION (NOM. A/m)		TIME RESPONSE (ns)				RATINGS (Subject to not exceeding max. rated A/m)						Notes		
	$I_d$ (dark) (nA)	Count (cps)	rise	transit	tail	tail	A/m	$V_{k-a}$	V	$I_a$ (ev.)	$I_c$ (ev.)	Ambient temp. (°C)			
	typ. max.	typ.	typ.	typ.	typ.	max.	max.	max.	max.	max.	max.	min.		max.	
9863B/100	0.4	4	40	2.5	45	4	10000	450	450	3000	2.5	200	-80	60	Max. dark count 500 cps
9863B/350	1	5	300	2.5	45	4	10000	450	450	3000	30	200	-80	60	Max. dark count 1200 cps
9883B	10	200	200	2.2	48	3.4	10000	650	450	3000	50	200	-30	60	
9884B	2	20	200	2	41	3	2000	650	450	2800	50	200	-30	60	Min. S.E.R. 2.1 p-v
9887B	1.5	20	200	2	41	3	2000	650	450	2800	50	200	-30	60	
9893B/100	0.1	1	20	2.5	45	4	10000	450	450	3000	0.1	200	-30	60	Max. dark count 50 cps
9893B/350	0.2	1	40	2.5	45	4	10000	450	450	3000	1.5	200	-30	60	Max. dark count 150 cps



150 - 315 911

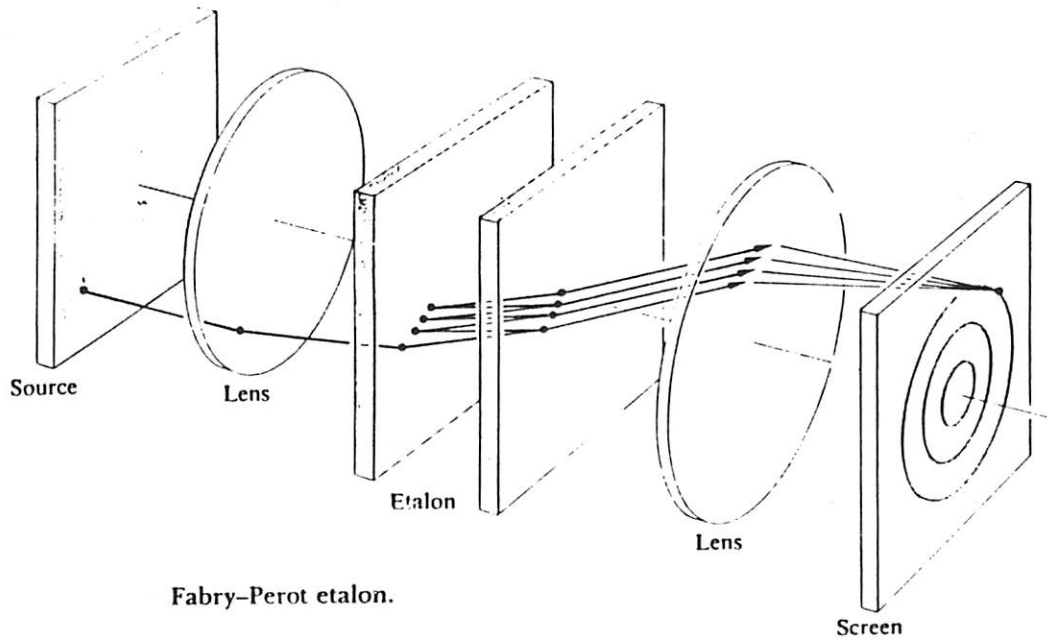
170 - 316 691



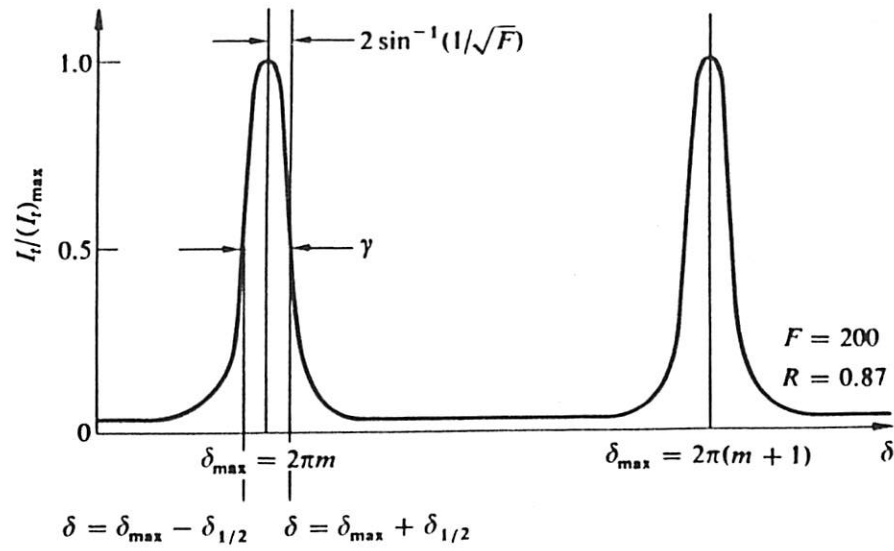
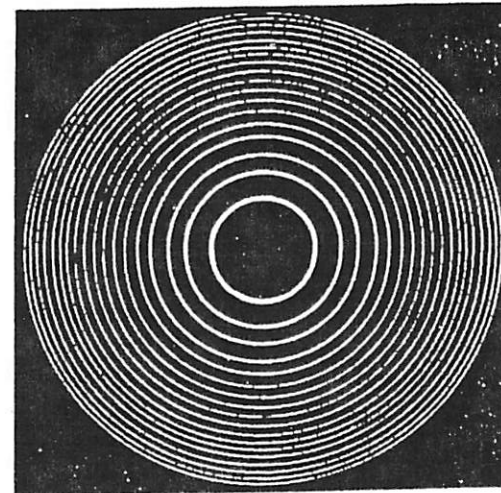
DETECTOR SECTION  
 GROUND BASED ATMOSPHERE  
 LIDAR SYSTEM

Two wavelengths ( 532 nm and 355 nm)  
 Shuttered for high and low altitudes

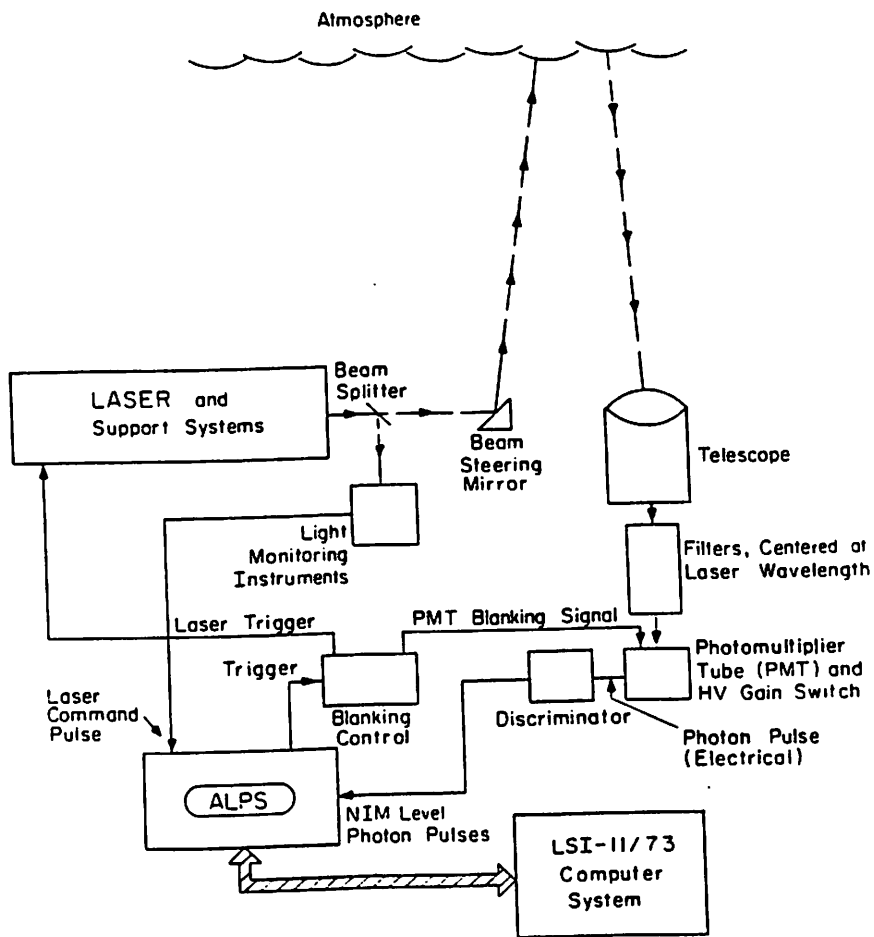




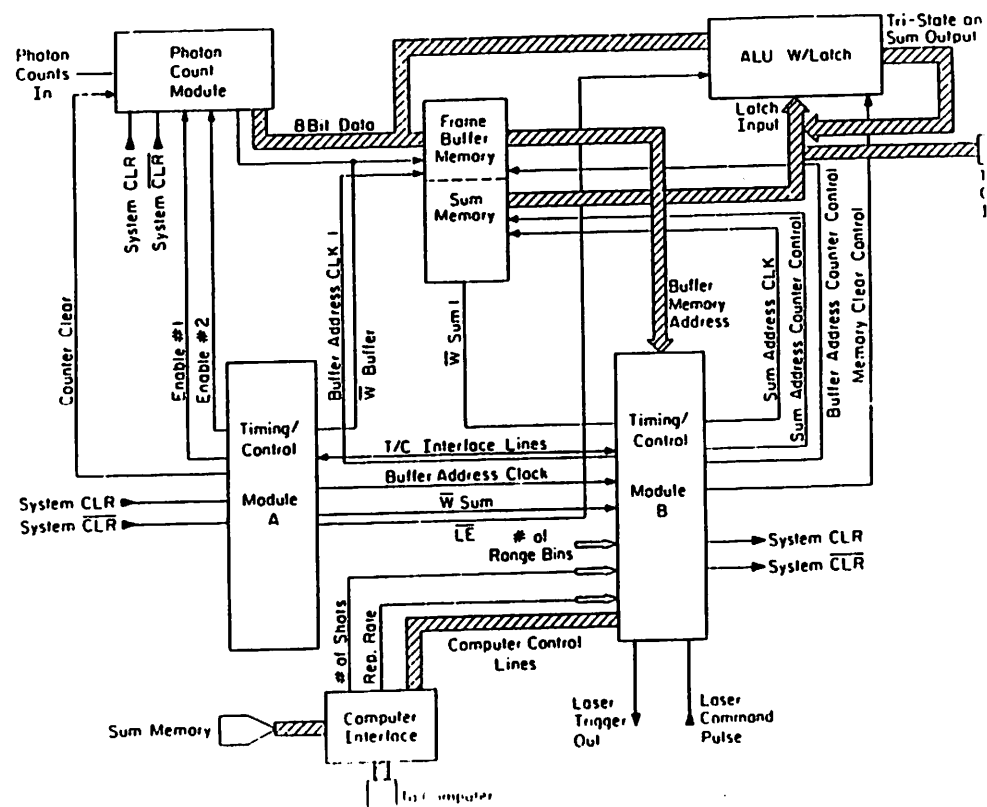
Fabry-Perot etalon.



Fabry-Perot fringes.



An Advanced Lidar Data Acquisition System



## DATA ACQUISITION

Data acquisition systems and architectures should be matched to the intended application. With the variety in standards and interlaces currently available today, the system designer can choose among variables that include capacity (size), speed, data path width, expandability, flexibility, interconnection protocol and media, in-line preprocessing and control, and ease of replacement of faulty components.

LeCroy designs instrumentation that can be incorporated into several different types of architectures ranging from small scale (single channel or data source) to large-scale (500,000 channels) data acquisition systems that support speeds from 300 bits/sec to 5 megawords/sec (32-bit words). Both conventional TTL, ECL and fiber optic interconnections can be implemented.

### GPIB

THE GPIB (IEEE Std 488-1979) Bus is the most popular instrument bus today. This byte-serial system can connect up to 15 talkers (units such as a digital voltmeter able to transmit data), listeners (units such as a programmable power supply able to receive instructions and data) or talker/listeners to a master controller. All LeCroy stand-alone instruments are equipped with GPIB interfaces for data transfer rates up to 400 kbytes per second.

The strict serial limitations of the GPIB interfacing standard can be partially bypassed by using the IEEE-488 Bus to tie CAMAC crates together and connect to the host computer.

### CAMAC

CAMAC is a modular data handling system used at every Nuclear Physics research laboratory and many industrial sites all over the world. It represents the

Committees. The CAMAC Standard (IEEE 583) is the ideal system for a high speed, medium density acquisition system. High speed means at least 1 Mbyte/second. The 1 MHz, 24-bit wide data path on both the backplane of the crates and the interconnections between crates transfers data at rates that exceed the capabilities of Direct Memory Access (DMA) channels in many minicomputers. For a more detailed discussion, see LeCroy Application Note AN-33, Introduction To CAMAC, which can be found in the Appendix.

Its primary application is data acquisition, but CAMAC may also be used for remotely programmable trigger and logic applications (LeCroy ECLine family of programmable logic units).

Most LeCroy CAMAC data acquisition modules are multi-input. They contain between 1

and 16 inputs per single-width module (23 modules per crate). A simple seven-crate system is shown in Figure 1.

The CAMAC standard covers electrical and physical specifications for the modules, instrument housings or crates, and a crate backplane. Examples of crates with 25 positions include the LeCroy Model 1434A and the high power version, Model 8025; and the Model 8013A with 13 positions.

Individual crates are controlled by slave or intelligent controllers such as the LeCroy Model 6010. The controllers are connected together with a parallel Branch Highway that ends in a Branch Driver. The Branch Driver is interfaced directly to a data acquisition computer. Alternatively, tree or parallel data acquisition architectures may be created by connecting secondary CAMAC branches via Branch Driver Modules.

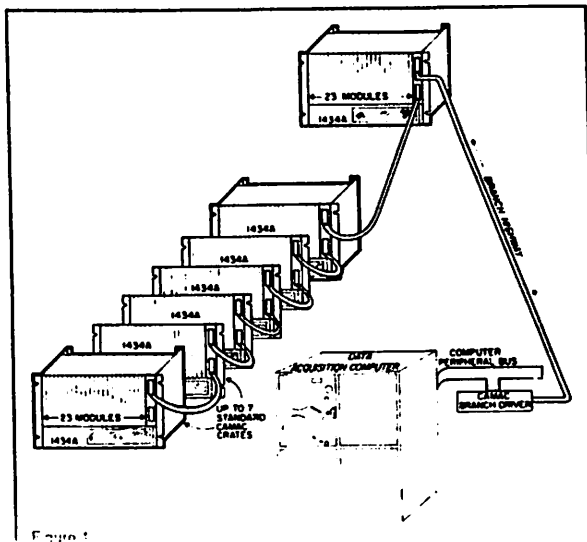


Figure 1

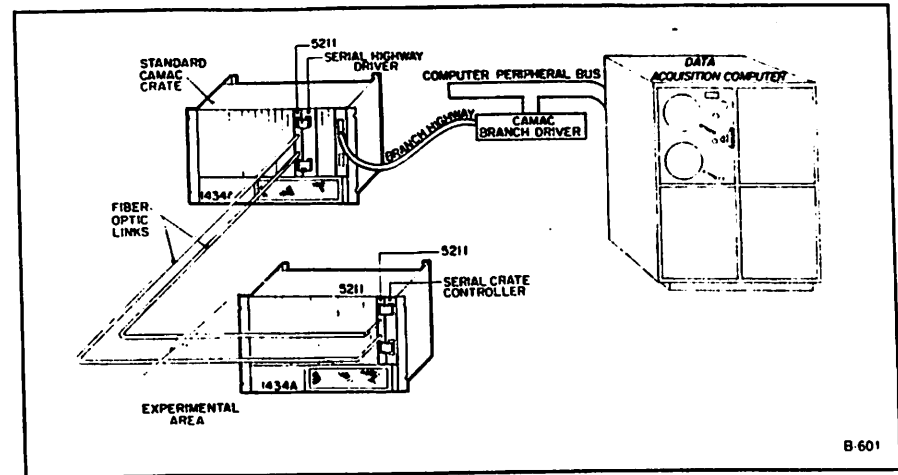


Figure 2  
CAMAC communication between CAMAC Branches via fiber optic links

CAMAC crates may also be connected in a Local Area Fiber Optic Network via the LeCroy Model 5211 Fiber Optic Serial Link and serial crate controller. Up to 62 crates separated by a maximum of 500 meters can exchange data at transmission rates of 4 to 5 megabytes/sec. (See Figure 2.)

LeCroy also offers crate controllers that interface directly with the GPIB. Therefore, the entire CAMAC crate may appear as a single instrument on this very popular laboratory instrument bus. The Model 8901A is a GPIB/CAMAC slave interface that operates as a "Talker/Listener" while the Model 6010 may be programmed to do real time computations and data compaction.

Timing and protocol specifications permit up to one million 16 or 24-bit word transfers per second for both the DATAWAY and CAMAC Branch. GPIB speeds are usually limited by the host computer, but block transfer rates of up to 300 kilobytes/sec are easily obtainable.

### THE LECROY DATABUS AND DEDICATED CAMAC SYSTEM

The LeCroy DATABUS links a family of dedicated CAMAC data acquisition systems designed to fulfill the demanding requirements of large scale Drift Chamber (4290 Timing System) and Multiwire Proportional Chamber (PCOS III Latching Systems). Information from the data acquisition modules is read via the backplane of a CAMAC crate to a dedicated "executive" controller unit. The executive controllers can handle a variety of functions including data compacting, autotrimming, system testing, and control. The executive controllers are then daisy-chained together and transfer the data via DATABUS to an interface module located in a standard CAMAC crate (See Figure 3). Due to the dedicated CAMAC architecture and the bidirectional 16-bit wide DATABUS system, transfer rates may be three times faster than standard CAMAC rates for 16-bit words.

The CAMAC Module 4299 DATABUS Interface downloads test and control commands back

to the dedicated crates. It stores data and addresses of only pertinent data acquisition channels in its 4K x 16-bit memory. Rapid and simple CAMAC block transfers can be executed under control of an internal word count register or an automatic "end-of-data" monitor (CAMAC Q-Stop Mode).

### FASTBUS

The FASTBUS Standard (ANSI/IEEE STD 960-1986) represents the fastest high density data acquisition available today. Designed for the next generation of High Energy Physics and Heavy-ion experiments, it permits almost any architecture imaginable, transferring data at speeds up to 40 Mbytes/sec (See Figure 4). LeCroy Application Note AN-26, An Introduction to FASTBUS, can be found in the Appendix.

FASTBUS was designed to keep features of older important standards while extending the capabilities of data acquisition systems. FASTBUS provides for a more densely packed system, reducing dramatically the per-input cost. This and other design goals have been achieved

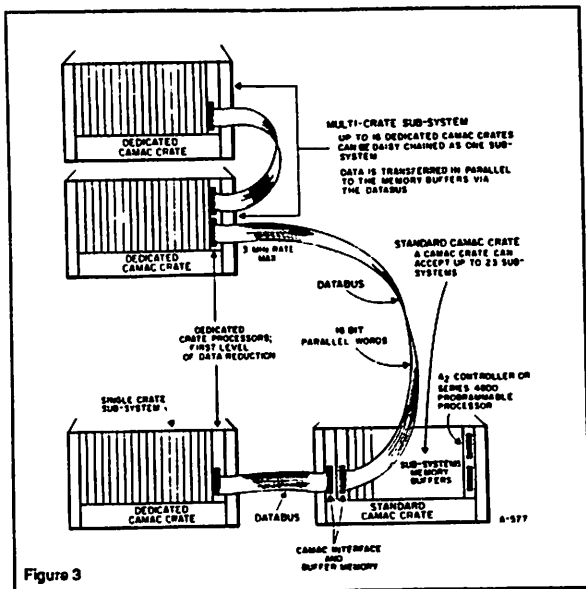


Figure 3

FASTBUS meets these requirements by incorporating several powerful features, including:

1. Modularity
2. 32-bit address and data fields
3. High speed, asynchronous ECL backplane with 32-bit wide Dataway
4. Multiple, parallel processor bus architecture with multiple bus segments that operate independently but link together for passing data
5. Asynchronous handshaking for compatibility with modules having different data transfer speeds operating on the same bus
6. Synchronous nonhandshake data transfer for maximum speed
7. Broadcast operations for initializing, clearing, etc., several modules in one operation
8. A polling structure for fast scanning of sparse data from a large number of modules

9. Easy links to computers for Host Intervention or Data Transfer

Essentially, the FASTBUS backplane is intended to be an extension of a computer backplane. By its nature, therefore, it is an expandable system. The backplane is called a "Segment". Connections between segments are made by a Segment interface, called a Segment Interconnect (SI). An SI in one segment is connected to a SI in another segment by a Cable Segment. The Segment Interconnect can be either a Master or Slave, depending on the operation it is performing. Moreover, it can be a Master on the FASTBUS Segment and simultaneously a Slave on the Cable Segment. The designations Master and Slave here are dynamic, in that the designation is defined by the role played by the SI at some given time.

FASTBUS permits Multiple Masters to have access to the segment. The standard provides a protocol for arbitration when more than one master requests control of the segment. Once mastership is granted, the Master may then proceed to establish a communications "lock" with any other device on the segment which will act as a Slave. Alternatively, the Master may Broadcast a message to all Slaves which respond to the Broadcast (e.g., Clear, Polling for Data Ready, etc.).

The integrity of communication between Master and Slave modules is insured via a handshaking scheme. This frees the standard from a speed requirement. That is, communication occurs at whatever speed the Master/Slave system will support. This, of course, is not the case with Broadcast commands where a Master talks to all Slaves in a segment, nor is it true for Hardware Block Transfers where the Master must be able to operate as fast as the fastest Slave. So while there are cautions required for use of FASTBUS, the versatility and expandability is sufficient to meet the most demanding requirements of data acquisition systems.

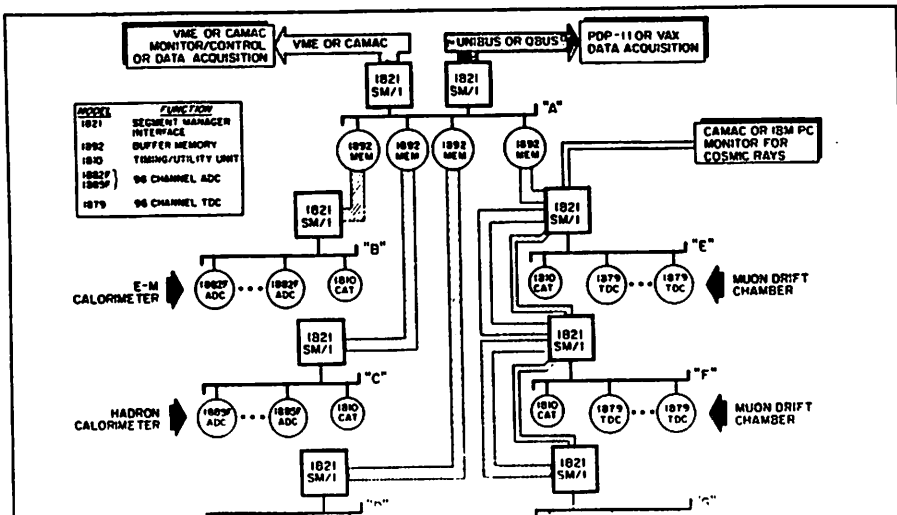
VME

The VME Bus (ANSI/IEEE Standard 1014-1987) was originally introduced to the physics research community primarily as a processing bus. Data was collected in a LeCroy DATABUS, CAMAC or FASTBUS subsystems and then ported (sometimes via the high speed, noise immune ECL Bus) to a processor farm built out of cost effective VME computational modules based on the Motorola 68000 family of CPUs. Additional data from environmental monitors was often integrated into the data stream at this point requiring some basic low performance data acquisition modules in VME.

The role of VME systems have expanded from this first architecture to include complete data acquisition systems with front end modules all in the VME standard. While never being able to reach the high densities of FASTBUS (and the subsequent cost savings), these systems have become very attractive for monitoring and control applications. LeCroy has developed a line of medium density, high performance instrumentation ideally designed for these applications. Combining 8 or 16 channels of instrumentation in a single width VME module, permits several hundred channels of high fidelity TDC, ADC or scaler to be directly integrated into a VME system.

BUS COMPARISONS

FASTBUS, VME and CAMAC are all modern, standard buses that are used in data acquisition applications. While CAMAC is the oldest, FASTBUS the most sophisticated and VME the most well known because of its commercial applications, each has a role in physics research. In the chart below, these buses are briefly compared.



	FASTBUS	VME	CAMAC
Speed	10-30 MHz transfer rate (32 bits)	10 MHz transfer rate (8, 16, or 32 bits)	1 MHz transfer rate (24 bits)
Power	Up to 75 W per module Power supply and cooling	Approximately 25 W per module	15 W per module
Master	Any slot multiple permitted	Controller Slot must be filled; Multi master	Master Controller slot only; Single master
Maximum Density	96	16	32
Convenience	Power-on installation and removal of modules (permitted by Connector type and Bus Halt.)	Power-on installation can damage modules	Power-on installation can damage modules

In order to assist with determining which data acquisition module will fulfill the experimental requirements, comparison matrices of ADCs and TDCs can be found below.

### Modular Analog-to-Digital Converters (ADCs)

Model No.	No. of Channels	No. of Bits	Package	O or V	Full Scale	Max. Resolution	Gain Width	Conversion Time	Feed Clear Time	Comments
1182	8	12	VME #1	Q	200 pC	0.05 pC	50-2000 nsec	40 $\mu$ sec <sup>†</sup>	0.0 $\mu$ sec	
1882P	06	12	FASTBUS #1	Q	200 pC	0.05 pC	50-2000 nsec	275 $\mu$ sec <sup>†</sup>	0.6 $\mu$ sec	Low range only
1882F	06	15	FASTBUS #1	Q	1600 pC	0.4 pC	50-2000 nsec	275 $\mu$ sec <sup>†</sup>	0.6 $\mu$ sec	Dual ranges
2249A	12	10	CAMAC #1	Q	-750 pC	-0.25 pC	10-200 nsec	55 $\mu$ sec	2 $\mu$ sec	Research standard
2249SG	12	10	CAMAC #2	Q	-250 pC	-0.25 pC	10-200 nsec	55 $\mu$ sec	2 $\mu$ sec	Separate gates
2249FW	12	11	CAMAC #1	Q	-512 pC	-0.25 pC	30-10000 nsec	110 $\mu$ sec	2 $\mu$ sec	
2259B	12	11	CAMAC #1	V	-2 V	-1 mV	100-5000 $\mu$ sec	110 $\mu$ sec	2 $\mu$ sec	
2262	2 or 4	10	CAMAC #1	V	2 V	1.5 mV	N/A	1.3 msec for 31A samples	N/A	Channels can be interleaved for higher rate
3512	1	13	CAMAC #2	V	$\pm$ 8 V	1 mV	N/A	5 $\mu$ sec	N/A	1 K FIFO Buffer
4300B	16	11 (10)	CAMAC #1	Q	-480 pC (-250)	-0.25 pC	50-300 nsec	4.5-8.0 $\mu$ sec	< 1 $\mu$ sec	ECL port for Fast Readout
LG8252 (1)	32	12	CAMAC #1	V	10 V	2.5 mV	N/A	2 msec all channels**	N/A	Scanning or triggered mode

\* Often readout during conversion and 8-deep event buffer options  
 \*\* Often continuous scan or triggered scan modes  
 † Faster conversion with fewer channels selected

### Modular Time-to-Digital Converters

Model No.	Package	No. of Bits	Conversion Speed	Maximum Resolution	Full Scale at Maximum Resolution	Comments
1170-501	VME #1	16	0	10 nsec	10 $\mu$ sec	Multif
1172	VME #1	12	40 $\mu$ sec <sup>†</sup>	25 psec	100 nsec	Common Stop
HTD1615/M	Hybrid	16	dependent on readout mode	8 nsec	4000 nsec	Multif
1872	FASTBUS #1	12	177 $\mu$ sec <sup>†</sup>	25 psec	100 nsec	Common Stop
1875	FASTBUS #1	15	177 $\mu$ sec <sup>†</sup>	25 psec/200 psec	100 nsec/800 nsec	ECL inputs
1879	FASTBUS #1	10	412 $\mu$ sec + 50 nsec/nf	2 nsec	1024 nsec	Multif, < 1 nsec RMS
2228A	CAMAC #1	11	100 $\mu$ sec	50 psec	102.4 nsec	NIM inputs
2229	CAMAC #1	11	100 $\mu$ sec	50 psec	102.4 nsec	ECL inputs
4204	CAMAC #2	24	< 1 $\mu$ sec	150 psec	2.62 msec	Multisource (any 1 of 16 inputs)
4205	CAMAC #1	23 + Sign	0	1 nsec	16.77 msec	Multif, Real Time

### Amplifiers and Preamplifiers

Model No.	Package	No. of Channels	Gain	Bandwidth (MHz)	RMS Input Noise	Connector Size	Required Voltage (V)	Coupling	Input Impedance ( $\Omega$ )	Risetime (nsec)	Max Output Amplitude (V)	Integral Non-Linearity (%)
612A	NIM #1	12	10 fixed	200	<50 $\mu$ V	Lemo	+6, +12, -24 and -12 or -6	DC	50	<2.0	Note (1)	0.1
612AM	NIM #1	6	2.5-40 Variable	140	<50 $\mu$ V	Lemo	+6, +12, -24 and -12 or -6	DC	50	<3.0	Note (1)	0.2
2724	Board	24	100 mV/pC	N/A	<1.5 fC	N/A	$\pm$ 9 to $\pm$ 15	DC	60	30	4 V into 100 $\Omega$ 2 V into 50 $\Omega$	1.0
2735DC/PC	Board	16	25 mV/pA	20/10	65 nA	34-pin	$\pm$ 5, -2	AC	150	5	N/A	<0.5
HQV101	Hybrid <sup>(3)</sup>	1	100 mV/pC	N/A	1.5 fC	10-pin DIP	$\pm$ 5 to $\pm$ 12	AC	60	30	4 V into 100 $\Omega$ 2 V into 50 $\Omega$	0.5
HQV110	Hybrid <sup>(3)</sup>	1	25 to 500 mV/pC	30 MHz	0.25 fC (1500 e <sup>-</sup> )	16-pin DIP	+12 and -6	AC/DC <sup>(4)</sup>	<10	15	$\pm$ 1.5 V into 50 $\Omega$	0.2 load 50 $\Omega$
HQV202-M	Hybrid <sup>(3)</sup>	8	500 mV/pC	N/A	650 e <sup>-</sup>	24-pin DIP	$\pm$ 3 to $\pm$ 12	DC <sup>(4)</sup>	N/A	<15	+2 V	0.2
HQV810	Hybrid <sup>(3)</sup>	8	500 mV/pC	N/A	550 e <sup>-</sup>	24-pin DIP	$\pm$ 3 to $\pm$ 12	DC <sup>(4)</sup>	N/A	<15	+2 V	0.2
HQV820-M	Hybrid <sup>(3)</sup>	8	500 mV/pC	N/A	250 e <sup>-</sup>	24-pin <sup>(2)</sup> DIP	$\pm$ 3 to $\pm$ 12	DC <sup>(4)</sup>	N/A	<15	+2 V	0.2
TRA402	Monolithic <sup>(3)</sup>	4	25 mV/pA	100	65 nA	18-pin DIP	$\pm$ 5, -2.5	DC <sup>(4)</sup>	75, 125	3.0	1.5 V	0.5
TRA1000	Monolithic <sup>(3)</sup>	1	2.7 to 300 mV/pA <sup>(5)</sup>	15	120 nA	16-pin DIP	$\pm$ 12	DC	0.4	25	1 V into 50 $\Omega$	<0.5 load 50 $\Omega$
VV100B	Hybrid <sup>(3)</sup>	1	10 fixed	200 <sup>(6)</sup>	<50 $\mu$ V	18-pin DIP	$\pm$ 6, or +6, -12	DC	>1 K	<2.0	+0.25 V <sup>(1)</sup> -5 V	0.1
VV100B1B	Note <sup>(7)(3)</sup>	1	10 fixed	200 <sup>(6)</sup>	<50 $\mu$ V	Lemo	$\pm$ 6, or +6, -12	DC	50	<2.0	+0.25 V <sup>(1)</sup> -5 V	0.1

Notes: (1)  $\pm$ 0.25 V to -2.0 V with -6 V supply, or  $\pm$ 0.25 V to -6.0 V with -12 V supply  
 (2) The HQV202-M and HQV820-M are packaged in 24-pin low mass DIPs with 7-pin row spacing  
 (3) Please refer to Section Two of this catalog for further details.  
 (4) External AC-coupling recommended.  
 (5) Current and charge mode gains are determined by external feedback elements.  
 (6) 200 MHz for 3 voltage operation; 175 MHz for 2 voltage operation.  
 (7) 3" x 3" x 1.5" feet box

## Interfaces

Model No.	Package	Control Transfer Rate (Maximum)	Data Transfer Rate (Maximum)	Bus	Instruments Supported
1131	VME #1	10 MB/sec	10 MB/sec	SIB 16 bit TTL Parallel	FASTBUS - 1821 SMA/ HV - System 1440 (1445A)
1601A	PC Card	2 MB/sec	2 MB/sec	SIB 16 bit TTL Parallel	FASTBUS - 1821 SMA/ HV - System 1440 (1445A)
1892	FASTBUS #1	3 MB/sec N/A	20 MB/sec	ECLine 16 bit ECL Parallel	FASTBUS - 1821/ECL MWPC System - 2738 FERA - 4300B
2132	CAMAC #1	1200 baud	1200 baud	RS-232	HV - System 1440, HV4032A
2301	CAMAC #1	N/A	N/A	LeCroy Bus	MCA - 3001 GVT
2691A	CAMAC #1	1 MB/sec	1 MB/sec	SIB 16 bit TTL Parallel	FASTBUS - 1821 SMA/ HV - System 1440 (1445A)
4299	CAMAC #1	2 MB/sec	4 MB/sec	DATABUS	Drift Chamber System - 4298 MWPC System - 2738
4302	CAMAC #1	N/A	20 MB/sec	ECLine 16 bit ECL Parallel	FASTBUS - 1821/ECL MWPC System - 2738 FERA - 4300B
6000C	PC Card	125 KB/sec	600 KB/sec	GPB	CAMAC - 6010 CAMAC - 6011A

## Modular Scalers/Counters

Model #	Package	No. of Inputs	Input Signals	Count Rate (KHz)	Dynamic Range (BRs)	Comments
1151E	VME #1	16	ECL	100	32	Bi-directional Counting
1151N	VME #1	16	NIM	100	32	Bi-directional Counting
2561	CAMAC #1	12	NIM	100	24	Cascadable Channels
3521A	CAMAC #1	1	NIM or TTL	100	14	MLR Channel Scaler with 1MB/200A Memory
4434	CAMAC #1	32	ECL or TTL	20	24	Latching Scaler



## SIGNAL AVERAGERS

### HIGH FREQUENCY SIGNAL AVERAGERS

2102SA	8 Bit,	200 Megasamples/s	Dual Channel
2103SA	8 Bit,	200 Megasamples/s	
2101ASA	8 Bit,	100 Megasamples/s	
2130SA	8 Bit,	30 Megasamples/s	
2112SA	12 Bit,	10 Megasamples/s	
2112FSA	12 Bit,	20 Megasamples/s	

### REAL TIME SIGNAL AVERAGERS

2824SA	12 Bit,	2 Megasamples/s	Dual Channel
2860SA	12 Bit,	1 Megasamples/s	Dual Channel
2812ASA	12 Bit,	100 Kilosamples/s	Eight Channel
2814SA	14 Bit,	100 Kilosamples/s	Four Channel

### FEATURES

- Fast repetition rate high frequency signal averagers (over 3000 sweeps/second for 1024 samples/sweep) with pre-trigger recording
- Real time signal averagers at conversion rates up to 2 Msamples/s
- Multiple channel real time averagers
- Complete hardware signal averaging; releases host computer from time-consuming averaging
- Programmable number of samples/sweep from 1 to 32,768
- Programmable number of sweeps from 1 to 65,536
- 24 bit per sample deep averaging memory
- Addition and subtraction modes, including algebraic sums
- Built in DAC for oscilloscope display of averaged signal during and after averaging

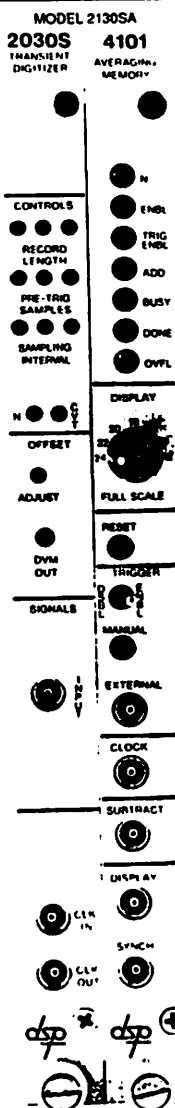
### DESCRIPTION

Signal averaging greatly improves the signal-to-noise ratio for repetitive signals with synchronized triggers. DSP Technology signal averagers use summation averaging, the arithmetic addition and/or subtraction of digitized sweeps. If the associated noise is random, the summation procedure results in a signal-to-noise improvement proportional to the square root of the number of sweeps. For example, averaging 65,536 sweeps improves the signal-to-noise ratio by a factor of 256.

Many different types of signals lend themselves to signal averaging:

- 1) Signals which are inherently repeatable (for example, signals from rotating machinery scanning spectrometers).
- 2) Signals which can be repeated using an external stimulus such as kinetic reaction studies where the reaction is stimulated by an energy source such as a laser.
- 3) Repetitive signals which have no associated synchronization or trigger pulse but have an inherent dominant feature which can be used as such.

ACTUAL SIZE



## SIGNAL AVERAGERS



### HIGH FREQUENCY SIGNAL AVERAGERS

These averagers use high speed transient recorder front ends to digitize and store one sweep of waveform data at a time. This data is then transferred over a dedicated bus to a companion Model 4101 signal averaging memory which adds each new waveform to those previously summed in its 24 bit, 32k sample memory. Data is summed and stored in 280 nsec per sample. Up to 65,536 sweeps can be programmed. Averaging can be interrupted at any time to read data and sweep counter contents. The number of samples/sweep determines the maximum sweep rate. For 8,192 samples/sweep, averaging takes 2.3 msec per sweep; for 1024 samples/sweep the time needed decreases to 0.3 msec/sweep. Averaging is automatically halted when the programmed number of sweeps has been completed or when any summed data sample reaches a count of 16,777,215 (24bits).

Sampling rates are programmable or switch selectable through an internal crystal controlled clock. An external clock source of any frequency from dc to maximum sampling rate may be used. The sweep can be divided into pre- and post- trigger segments to record information prior to the trigger point.

### REAL TIME SIGNAL AVERAGERS:

These units use DSP TRAQ™ P ADC system modules to implement multi-channel, real time averaging. An external clock (not included) commands the analog to digital converters to sample, convert, and transfer data to the Model 4101. Up to 8 channels can be controlled by one Model 4101 with a maximum conversion and transfer rate of 500 nsec/sample. Record lengths are programmable from 1 to 32,768 samples/sweep in increments of one. Sweeps can be initiated each time a trigger is received or programmed such that the first trigger initiates all sweeps. All samples in these real time averagers are post-trigger.

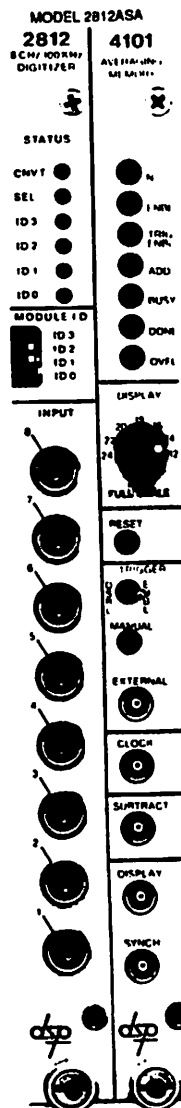
### GENERAL

Both addition and subtraction averaging modes are selectable via either a front panel input connector or by computer command. The mode can be changed from addition to subtraction, or visa-versa, without disturbing the sum already accumulated. This feature might be used, for example, to subtract a bias or background waveform from an experimental apparatus setup. The internal arithmetic is programmable as either offset binary (0 to 16,777,215) or 2's complement ( $\pm 8,388,607$ ). Averaging can be automatically disabled on overflow or underflow.

The averaged waveform can be observed with a standard laboratory oscilloscope while the data is accumulating. The display from the internal 12 bit digital-to-analog converter can be adjusted via a front panel switch to scale over any 12 of the 24 bit data range. This display is generally useful only with single channel averager configurations.

TRAQ is a Trademark of DSP Technology Inc

ACTUAL SIZE



# MODELS 2012 & 2012F

## 10 & 20 MEGASAMPLES/S, 12 BIT, 8 KSAMPLE TRANSIENT RECORDERS



### FEATURES

- ◆ 12 Bit Dynamic Range at up to 20 Megasamples/s Sampling Rate
- ◆ Switch Selectable, and Computer Readable Controls (digitizing rate, pre/post trigger samples, record length)

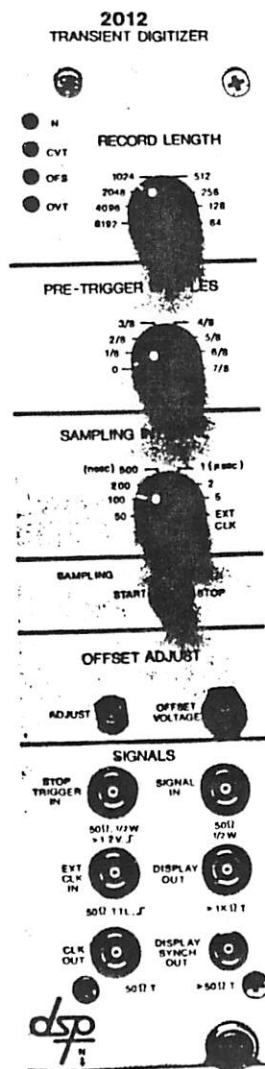
### DESCRIPTION

The Models 2012 and 2012F combine the wide dynamic range (12 bits) needed to capture signals whose baselines are either dynamically changing or are unknown with high speed digitizing rates. Both models are single module transient recorders with ADC, control and storage functions self-contained.

The digitizers can be entirely controlled from the front panel of the instrument much like a normal scope. All switch positions are readable by the computer. Access by the computer and run status are indicated by front panel LED's.

Data conversion and storage can be initiated by front panel toggle switch or computer command. An external signal (TTL level), toggle switch or computer command stops the conversion after the programmed number of post-trigger samples have been recorded. An external clock can be used to accommodate any sampling rate from D.C. to full sampling speed or variable rate importance sampling.

Digitized data can be viewed by attaching a standard laboratory oscilloscope to the DAC display out connector and triggering with the sweep trigger generated by the unit. Computer driven display of multiple waveforms is especially suitable for multichannel data acquisition systems.



### TECHNICAL SPECIFICATIONS - MODELS 2012 & 2012F



#### SIGNAL INPUTS

Impedance: 50  $\Omega$  (1K  $\Omega$  optional), 30 pF  
Voltage Range: 2.0 V full scale  $\pm$  1% full scale per 10° C.

Overvoltage Recovery: 50 ns from 2X overdrive

Overvoltage Protection: 7 V dc, 50 V for 1 ms, LED indicates input over full scale.

#### Bandwidth (3dB):

Full scale:	10 MHz
x0.1 full scale:	15 MHz
$\pm$ 0.2 dB:	DC - 5 MHz

Offset:  $\pm$  full scale. Continuous adjustment by potentiometer. Front panel test point for DVM. Drift 1 count / 10° C.

#### STOP TRIGGER

External: TTL level, positive edge sensitive, 50  $\mu$ s min. width 1 K $\Omega$  input impedance. Input protection 25 V dc, 250 V for 1 ms.

Manual: Front panel switch

Computer: F(25)A(0) command

#### ANALOG TO DIGITAL CONVERTER

Resolution: 12 bits (one part in 4096)

#### Dynamic Distribution:

- 70 dB down at 1 MHz input frequency
- 65 dB down at 2.5 MHz input frequency

Aperture Uncertainty: 24 ps

DC Linearity:  $\pm$  1/2 LSB,  $\pm$  0.05 %

Continuity: Monotonic

#### SAMPLING CLOCK

Internal: Crystal controlled clock:  
20, 10, 5, 2, 1, 0.5, 0.2 MHz

CLK IN: Edge triggered, TTL input, 20 MHz max for 2012F; 10 MHz max for 2012. No restrictions on frequency changes.

CLK OUT: TTL output, drives 50  $\Omega$  load. Regenerated internal or external sampling clock.

#### MEMORY

Type: Static ram

Size: 8192 samples

Organization: Reduction of record size is selectable by computer control for efficient matching to application. Cyclical data recording allows division of memory into pre- post-trigger periods by computer control.

#### DISPLAY

Digital to analog reconstruction of memory contents drives 1 K $\Omega$  to  $\pm$  5.0 V. Scope trigger of TTL level is also provided at the beginning of each display sweep

#### DIGITAL OUTPUT

Data Format: 16 bit 2's complement encoding (Offset binary encoding, strap selectable).

Readout Protocol: IEEE #583 CAMAC. Full NAF decoding, LAM implementation and Q = 1 is returned for every executable NAF command. After the last memory word has been read, Q = 0 is returned.

#### COMPUTER COMMANDS

F(0)A(0): Reads pre-trigger samples, record size, sampling period.

F(2)A(0): Read waveform data. Q = 0 returned after last data word.

F(3)A(0): Read module I.D. ('2012' or '2012F').

F(8)A(0): Test LAM, Q = 1 returned if LAM is on.

F(9)A(0): Initialize module and start sampling.

F(10)A(0): Reset LAM.

F(11)A(0): Computer single sample.

F(16)A(0): Write pre-trigger samples, record size, sampling period.

F(24)A(0): Disable LAM

F(25)A(0): Computer stop trigger.

F(26)A(0): Enable LAM and computer readout.

F(27)A(0): Enable offset measurement. To read, issue F(25), wait for post-trigger samples, and read offset data with F(2).

#### POWER REQUIREMENTS

$\pm$ 6 V	3 A
$\pm$ 24 V	300 mA

#### PACKAGING

#3 width CAMAC module  
221 mm H, 50 mm W, 292 mm D\* (8.7" x 2" x 11.5")  
\*Depth from front to rear panel. Rear connector is 13 mm (0.5").

In conformance with the CAMAC standard for RF shielded instrumentation modules (IEEE standard 583, European Esone Report #EUR4100e).

#### TEMPERATURE RANGE

0° to 40° C (32° F to 104° F) ambient to operate within specifications (when installed in crate with enough air flow to hold maximum air exit temperature to 55° C (131° F)).

#### MATING CONNECTORS

Cable assemblies LCOB (LEMO-BNC) and LCOL (LEMO-LEMO) are compatible with all input and output connectors. Not included.



## for the safe use of lasers

AMERICAN NATIONAL STANDARD Z136.1-1986

**Table 5**  
MPE for Direct Ocular Exposure,  
Intrabeam Viewing, to a Laser Beam

Wavelength, $\lambda$ ( $\mu\text{m}$ )	Exposure Duration $t^*$ (s)	Maximum Permissible Exposure (MPE)	Notes for Calculation and Measurement
Ultraviolet			
0.200 to 0.302	$10^{-9}$ to $3 \times 10^4$	$3 \times 10^{-1} \text{ J} \cdot \text{cm}^{-2}$	or $0.56 t^{1/4} \text{ J} \cdot \text{cm}^{-2}$ , whichever is lower.  1-mm limiting aperture  See Figs. 5 and 6 for graphical representation.
0.303	$10^{-9}$ to $3 \times 10^4$	$4 \times 10^{-1} \text{ J} \cdot \text{cm}^{-2}$	
0.304	$10^{-9}$ to $3 \times 10^4$	$6 \times 10^{-1} \text{ J} \cdot \text{cm}^{-2}$	
0.305	$10^{-9}$ to $3 \times 10^4$	$1.0 \times 10^{-2} \text{ J} \cdot \text{cm}^{-2}$	
0.306	$10^{-9}$ to $3 \times 10^4$	$1.6 \times 10^{-2} \text{ J} \cdot \text{cm}^{-2}$	
0.307	$10^{-9}$ to $3 \times 10^4$	$2.5 \times 10^{-2} \text{ J} \cdot \text{cm}^{-2}$	
0.308	$10^{-9}$ to $3 \times 10^4$	$4.0 \times 10^{-2} \text{ J} \cdot \text{cm}^{-2}$	
0.309	$10^{-9}$ to $3 \times 10^4$	$6.3 \times 10^{-2} \text{ J} \cdot \text{cm}^{-2}$	
0.310	$10^{-9}$ to $3 \times 10^4$	$1.0 \times 10^{-1} \text{ J} \cdot \text{cm}^{-2}$	
0.311	$10^{-9}$ to $3 \times 10^4$	$1.6 \times 10^{-1} \text{ J} \cdot \text{cm}^{-2}$	
0.312	$10^{-9}$ to $3 \times 10^4$	$2.5 \times 10^{-1} \text{ J} \cdot \text{cm}^{-2}$	
0.313	$10^{-9}$ to $3 \times 10^4$	$4.0 \times 10^{-1} \text{ J} \cdot \text{cm}^{-2}$	
0.314	$10^{-9}$ to $3 \times 10^4$	$6.3 \times 10^{-1} \text{ J} \cdot \text{cm}^{-2}$	
0.315 to 0.400	$10^{-9}$ to 10	$0.56 t^{1/4} \text{ J} \cdot \text{cm}^{-2}$	
0.315 to 0.400	10 to $3 \times 10^4$	$1 \text{ J} \cdot \text{cm}^{-2}$	
Visible and Near Infrared**			7-mm limiting aperture. See 8.2 for multiple pulse limitations. See Figs. 4 and 11 for graphic representation. See 8.2 and Figs. 8.9, and 12 for correction factors.
0.400 to 0.700	$10^{-9}$ to $1.8 \times 10^{-3}$	$5 \times 10^{-7} \text{ J} \cdot \text{cm}^{-2}$	
0.400 to 0.700	$1.8 \times 10^{-3}$ to 10	$1.8 t^{1/4} \times 10^{-3} \text{ J} \cdot \text{cm}^{-2}$	
0.400 to 0.550	10 to $10^4$	$10 \times 10^{-3} \text{ J} \cdot \text{cm}^{-2}$	
0.550 to 0.700	10 to $T_1$	$1.8 t^{1/4} \times 10^{-3} \text{ J} \cdot \text{cm}^{-2}$	
0.550 to 0.700	$T_1$ to $10^4$	$10 C_B \times 10^{-3} \text{ J} \cdot \text{cm}^{-2}$	
0.400 to 0.700	$10^4$ to $3 \times 10^4$	$C_B \times 10^{-6} \text{ W} \cdot \text{cm}^{-2}$	
0.700 to 1.050	$10^{-9}$ to $1.8 \times 10^{-3}$	$5 C_A \times 10^{-7} \text{ J} \cdot \text{cm}^{-2}$	
0.700 to 1.050	$1.8 \times 10^{-3}$ to $10^1$	$1.8 C_A t^{1/4} \times 10^{-3} \text{ J} \cdot \text{cm}^{-2}$	
1.051 to 1.400	$10^{-9}$ to $5 \times 10^{-3}$	$5 \times 10^{-6} \text{ J} \cdot \text{cm}^{-2}$	
1.051 to 1.400	$5 \times 10^{-3}$ to $10^1$	$9 t^{1/4} \times 10^{-3} \text{ J} \cdot \text{cm}^{-2}$	
0.700 to 1.400	$10^1$ to $3 \times 10^4$	$320 C_A \times 10^{-6} \text{ W} \cdot \text{cm}^{-2}$	
Far Infrared			See Table 9 for apertures. See 8.5 for correction factors at 1.54 $\mu\text{m}$ . See Fig. 6 for graphic representation.
1.4 to $10^1$	$10^{-9}$ to $10^7$	$10^{-2} \text{ J} \cdot \text{cm}^{-2}$	
	$10^7$ to 10	$0.56 t^{1/4} \text{ J} \cdot \text{cm}^{-2}$	
	>10	$0.1 \text{ W} \cdot \text{cm}^{-2}$	
1.54 only	$10^{-9}$ to $10^{-6}$	$1.0 \text{ J} \cdot \text{cm}^{-2}$	

\* See Note in Section 8 for pulsewidths less than 1 ns.

\*\*See Figs. 4.5, and 6 for graphic representation.

NOTES:  $C_A = 1$  for  $\lambda = 0.400$  to  $0.700 \mu\text{m}$ .

$C_A = 10^{2(0.4 - \lambda)}$  for  $\lambda = 0.700$  to  $1.051 \mu\text{m}$  (see Fig. 8).

$C_A = 5$  for  $\lambda = 1.051$  to  $1.400 \mu\text{m}$ .

$C_B = 1$  for  $\lambda = 0.400$  to  $0.550 \mu\text{m}$ .

$C_B = 10^{2(\lambda - 0.550)}$  for  $\lambda = 0.550$  to  $0.700 \mu\text{m}$  (see Fig. 9).

$T_1 = 10 \times 10^{2(\lambda - 0.550)}$  for  $\lambda = 0.550$  to  $0.700 \mu\text{m}$  (see Fig. 9).

AMERICAN NATIONAL STANDARD Z136.1-1986

**Table 6**  
MPE for Viewing a Diffuse Reflection  
of a Laser Beam or an Extended-Source Laser

Wavelength, $\lambda$ ( $\mu\text{m}$ )	Exposure Duration $t^*$ (s)	Maximum Permissible Exposure (MPE)	Notes for Calculation and Measurement
Ultraviolet			
0.200 to 0.302	$10^{-9}$ to $3 \times 10^4$	$3 \times 10^{-1} \text{ J} \cdot \text{cm}^{-2}$	or $0.56 t^{1/4} \text{ J} \cdot \text{cm}^{-2}$ , whichever is lower.  1-mm limiting aperture  See Figs. 5 and 6 for graphical representation.
0.303	$10^{-9}$ to $3 \times 10^4$	$4 \times 10^{-1} \text{ J} \cdot \text{cm}^{-2}$	
0.304	$10^{-9}$ to $3 \times 10^4$	$6 \times 10^{-1} \text{ J} \cdot \text{cm}^{-2}$	
0.305	$10^{-9}$ to $3 \times 10^4$	$1.0 \times 10^{-2} \text{ J} \cdot \text{cm}^{-2}$	
0.306	$10^{-9}$ to $3 \times 10^4$	$1.6 \times 10^{-2} \text{ J} \cdot \text{cm}^{-2}$	
0.307	$10^{-9}$ to $3 \times 10^4$	$2.5 \times 10^{-2} \text{ J} \cdot \text{cm}^{-2}$	
0.308	$10^{-9}$ to $3 \times 10^4$	$4.0 \times 10^{-2} \text{ J} \cdot \text{cm}^{-2}$	
0.309	$10^{-9}$ to $3 \times 10^4$	$6.3 \times 10^{-2} \text{ J} \cdot \text{cm}^{-2}$	
0.310	$10^{-9}$ to $3 \times 10^4$	$1.0 \times 10^{-1} \text{ J} \cdot \text{cm}^{-2}$	
0.311	$10^{-9}$ to $3 \times 10^4$	$1.6 \times 10^{-1} \text{ J} \cdot \text{cm}^{-2}$	
0.312	$10^{-9}$ to $3 \times 10^4$	$2.5 \times 10^{-1} \text{ J} \cdot \text{cm}^{-2}$	
0.313	$10^{-9}$ to $3 \times 10^4$	$4.0 \times 10^{-1} \text{ J} \cdot \text{cm}^{-2}$	
0.314	$10^{-9}$ to $3 \times 10^4$	$6.3 \times 10^{-1} \text{ J} \cdot \text{cm}^{-2}$	
0.315 to 0.400	$10^{-9}$ to 10	$0.56 t^{1/4} \text{ J} \cdot \text{cm}^{-2}$	
0.315 to 0.400	10 to $3 \times 10^4$	$1 \text{ J} \cdot \text{cm}^{-2}$	
Visible**			1-mm limiting aperture or $\alpha_{\text{lim}}$ , whichever is greater See 8.2 and Figs. 7.8, 9, 11, and 12 for graphic representation and multiple pulse limitations
0.400 to 0.700	$10^{-9}$ to 10	$10 t^{1/3} \text{ J} \cdot \text{cm}^{-2} \cdot \text{sr}^{-1}$	
0.400 to 0.550	10 to $10^4$	$21 \text{ J} \cdot \text{cm}^{-2} \cdot \text{sr}^{-1}$	
0.550 to 0.700	10 to $T_1$	$3.83 t^{1/4} \text{ J} \cdot \text{cm}^{-2} \cdot \text{sr}^{-1}$	
0.550 to 0.700	$T_1$ to $10^4$	$21 C_B \text{ J} \cdot \text{cm}^{-2} \cdot \text{sr}^{-1}$	
0.400 to 0.700	$10^4$ to $3 \times 10^4$	$2.1 C_B 10^{-3} \text{ W} \cdot \text{cm}^{-2} \cdot \text{sr}^{-1}$	
Near Infrared*			See Table 9 for apertures. See 8.5 and Fig. 6 for correction factors
0.700 to 1.400	$10^{-9}$ to 10	$10 C_A t^{1/3} \text{ J} \cdot \text{cm}^{-2} \cdot \text{sr}^{-1}$	
0.700 to 1.400	10 to $10^1$	$3.83 C_A t^{1/4} \text{ J} \cdot \text{cm}^{-2} \cdot \text{sr}^{-1}$	
0.700 to 1.400	$10^1$ to $3 \times 10^4$	$0.64 C_A \text{ W} \cdot \text{cm}^{-2} \cdot \text{sr}^{-1}$	
Far Infrared			See Table 9 for apertures. See 8.5 and Fig. 6 for correction factors
1.4 to $10^1$	$10^{-9}$ to $10^7$	$10^{-2} \text{ J} \cdot \text{cm}^{-2}$	
	$10^7$ to 10	$0.56 t^{1/4} \text{ J} \cdot \text{cm}^{-2}$	
	>10	$0.1 \text{ W} \cdot \text{cm}^{-2}$	
1.54 only	$10^{-9}$ to $10^{-6}$	$1.0 \text{ J} \cdot \text{cm}^{-2}$	

\* See Note in Section 8 for pulsewidths less than 1 ns.

\*\*See Fig. 7 and Fig. B.3 of Appendix B for graphic representation.

NOTES:  $C_A = 1$  for  $\lambda = 0.400$  to  $0.700 \mu\text{m}$ .

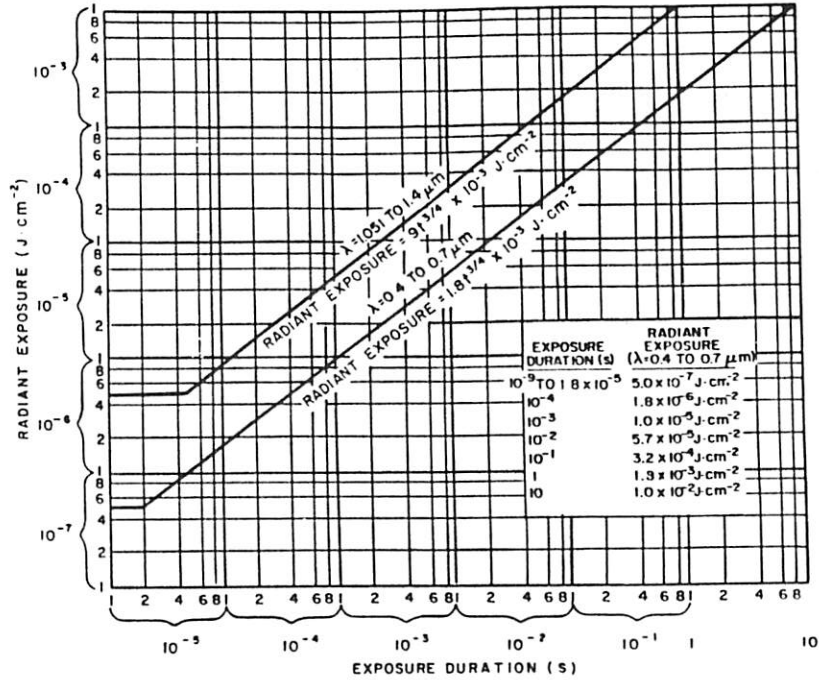
$C_A = 10^{2(0.4 - \lambda)}$  for  $\lambda = 0.700$  to  $1.051 \mu\text{m}$  (see Fig. 8).

$C_A = 5$  for  $\lambda = 1.051$  to  $1.400 \mu\text{m}$ .

$C_B = 1$  for  $\lambda = 0.400$  to  $0.550 \mu\text{m}$ .

$C_B = 10^{2(\lambda - 0.550)}$  for  $\lambda = 0.550$  to  $0.700 \mu\text{m}$  (see Fig. 9).

$T_1 = 10 \times 10^{2(\lambda - 0.550)}$  for  $\lambda = 0.550$  to  $0.700 \mu\text{m}$  (see Fig. 9).



NOTE: For correction factor information at wavelengths between 0.7  $\mu\text{m}$  and 1.4  $\mu\text{m}$ , see Table 5

Fig. 4  
MPE for Direct Ocular Exposure to Visible and Near Infrared Radiation ( $\lambda = 0.4$  to  $1.4 \mu\text{m}$ ) Intrabeam Viewing (Angular Subtense  $< \alpha_{\text{min}}$  in Fig. 3).  
for Single Pulses or Exposures

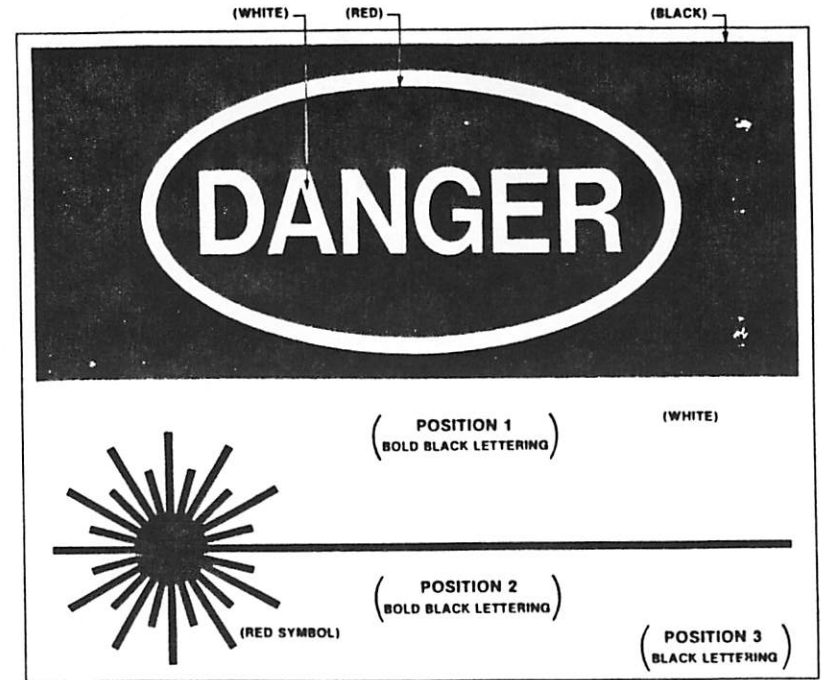


Fig. 1b  
Sample Warning Sign for Certain Class 3a Lasers and for Class 3b and Class 4 Lasers

**Table 7**  
**MPE for Skin Exposure to a Laser Beam**

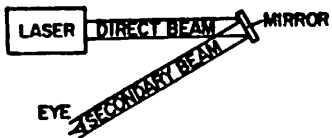
Wavelength, $\lambda$ ( $\mu\text{m}$ )	Exposure Duration $t$ (s)	Maximum Permissible Exposure (MPE)	Notes for Calculation and Measurement
<b>Ultraviolet</b>			
0.200 to 0.302	$10^{-8}$ to $3 \times 10^3$	$3 \times 10^{-3} \text{ J} \cdot \text{cm}^{-2}$	or $0.56 t^{1/2} \text{ J} \cdot \text{cm}^{-2}$ , whichever is lower.  1 mm limiting aperture.  See Figs. 5 and 6 for graphic representation
0.303	$10^{-8}$ to $3 \times 10^3$	$4 \times 10^{-3} \text{ J} \cdot \text{cm}^{-2}$	
0.304	$10^{-8}$ to $3 \times 10^3$	$6 \times 10^{-3} \text{ J} \cdot \text{cm}^{-2}$	
0.305	$10^{-8}$ to $3 \times 10^3$	$1.0 \times 10^{-2} \text{ J} \cdot \text{cm}^{-2}$	
0.306	$10^{-8}$ to $3 \times 10^3$	$1.6 \times 10^{-2} \text{ J} \cdot \text{cm}^{-2}$	
0.307	$10^{-8}$ to $3 \times 10^3$	$2.5 \times 10^{-2} \text{ J} \cdot \text{cm}^{-2}$	
0.308	$10^{-8}$ to $3 \times 10^3$	$4.0 \times 10^{-2} \text{ J} \cdot \text{cm}^{-2}$	
0.309	$10^{-8}$ to $3 \times 10^3$	$6.3 \times 10^{-2} \text{ J} \cdot \text{cm}^{-2}$	
0.310	$10^{-8}$ to $3 \times 10^3$	$1.0 \times 10^{-1} \text{ J} \cdot \text{cm}^{-2}$	
0.311	$10^{-8}$ to $3 \times 10^3$	$1.6 \times 10^{-1} \text{ J} \cdot \text{cm}^{-2}$	
0.312	$10^{-8}$ to $3 \times 10^3$	$2.5 \times 10^{-1} \text{ J} \cdot \text{cm}^{-2}$	
0.313	$10^{-8}$ to $3 \times 10^3$	$4.0 \times 10^{-1} \text{ J} \cdot \text{cm}^{-2}$	
0.314	$10^{-8}$ to $3 \times 10^3$	$6.3 \times 10^{-1} \text{ J} \cdot \text{cm}^{-2}$	
0.315 to 0.400	$10^{-8}$ to 10	$0.56 t^{1/2} \text{ J} \cdot \text{cm}^{-2}$	
0.315 to 0.400	10 to $10^3$	$1 \text{ J} \cdot \text{cm}^{-2}$	
0.315 to 0.400	$10^3$ to $3 \times 10^4$	$1 \times 10^{-3} \text{ W} \cdot \text{cm}^{-2}$	
<b>Visible and Near Infrared</b>			
0.400 to 1.400	$10^{-8}$ to $10^{-7}$	$2 C_A \times 10^{-2} \text{ J} \cdot \text{cm}^{-2}$	1 mm limiting aperture See Figs. 6 and 8
	$10^{-7}$ to 10	$1.1 C_A t^{1/2} \text{ J} \cdot \text{cm}^{-2}$	
	10 to $3 \times 10^4$	$0.2 C_A \text{ W} \cdot \text{cm}^{-2}$	
<b>Far Infrared*</b>			
1.4 to $10^3$	$10^{-8}$ to $10^{-7}$	$10^{-2} \text{ J} \cdot \text{cm}^{-2}$	1 mm limiting aperture for 1.4 to 100 $\mu\text{m}$ 11-mm limiting aperture for 0.1 to 1 mm
	$10^{-7}$ to 10	$0.56 t^{1/2} \text{ J} \cdot \text{cm}^{-2}$	
	> 10	$0.1 \text{ W} \cdot \text{cm}^{-2}$	
1.54 only	$10^{-8}$ to $10^4$	$1.0 \text{ J} \cdot \text{cm}^{-2}$	

\*See 8.4.2 for large beam cross-sections.

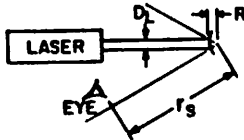


Fig. B1  
Intrabeam Viewing - Direct (Primary) Beam.

FLAT SURFACE REFLECTION



CURVED SURFACE REFLECTION



NOTE:  
r = TOTAL BEAM DISTANCE FROM LASER TO EYE  
(DIRECT PLUS SECONDARY)

Fig. B2  
Intrabeam viewing - Specularly Reflected  
(Secondary) Beam.

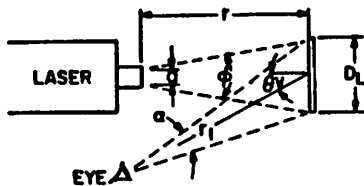
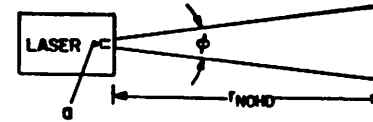
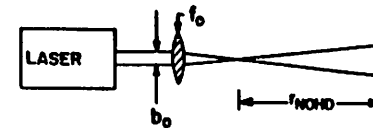


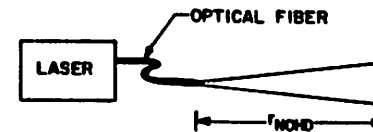
Fig. B3  
Extended Source Viewing - Normally Diffuse Reflection.



$$r_{NOHD} = \frac{1}{\phi} \left[ \left( \frac{4\phi}{\pi \cdot MPE} \right)^{1/2} - \phi \right]$$

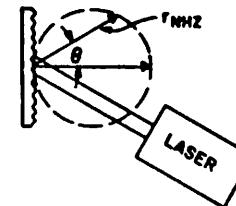


$$r_{NOHD} = \left( \frac{f_0}{b_0} \right) \left( \frac{4\phi}{\pi \cdot MPE} \right)^{1/2}$$



$$r_{NOHD} = \begin{cases} \frac{1.7}{NA} \left[ \frac{\phi}{\pi \cdot MPE} \right]^{1/2} & \text{(MULTIMODE)} \\ \frac{\omega_0}{\lambda} \left[ \frac{\phi}{MPE} \right]^{1/2} & \text{(SINGLEMODE)} \end{cases}$$

Fig. B4  
Examples of Use of Laser Range Equation for  
Determining Nominal Hazard Distances.



$$r_{NHZ} = \left( \frac{\phi \cos \theta}{\pi \cdot MPE} \right)^{1/2}$$

Fig. B5  
Nominal Hazard Zone for a Diffuse Reflection.

## Reference Guide

Cleaning of any precision optic risks degrading the surface. The need for cleaning should be minimized by returning optics to their case or covering the optic and mount with a protective bag when not in use. If cleaning is required, we recommend one of the following procedures:

### Cleaning Materials

**Polyethylene lab gloves.** Please wear them. Solvents are harsh to the skin.

**Dust free tissue.** Lens tissue or equivalent.

**Dust free blower.** Filtered dry nitrogen blown through an antistatic nozzle (Simco Inc., Hatfield, PA) is best. Bulb type blowers and brushes must be very clean to prevent redistribution of dirt.

**Mild, neutral soap, 1% in water.** Avoid perfumed, alkali or colored products. Several drops of green soap (available in any pharmacy) per 100 cc of distilled water is acceptable.

**Spectroscopic grade isopropyl alcohol and acetone.**

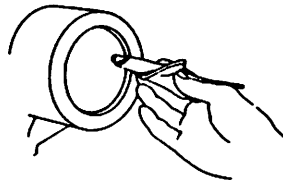
**Cotton swabs.** Avoid plastic stems which can dissolve in alcohol or acetone.

### Cleaning Procedures

Dust on optics can be very tightly bound by static electricity. Blowing removes some dirt; the remainder can be collected by the surface tension of a wet alcohol swab. Acetone promotes rapid drying of the optic to eliminate streaks.

1) Blow off dust.

2) If any dust remains, twist tissue around a swab, soak in alcohol and wipe the optic in one direction with a gentle figure-eight motion. Repeat.

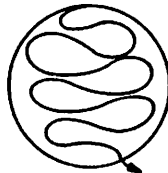


3) Repeat Step (2) with acetone soaked swabs.

**Fingerprints.** Oil or water spots should be cleaned immediately. Skin acids attack coatings and glass. Cleaning with solvents alone tends to redistribute grime. These contaminants must be lifted from an optical surface with soap or other wetting agent. The part is then rinsed in water and the water removed with alcohol. Acetone speeds drying and eliminates streaks.

1) Blow off dust.

2) Using a snap saturated lens tissue around a swab, wipe the optic gently in the same figure 8 motion. Repeat.



3) Repeat (2) with distilled water only.

4) Repeat (2) with alcohol.

5) Repeat (2) with acetone.

**Delicate optics** such as UV aluminum mirrors are most safely cleaned by immersion. Do not immerse cemented optics. Washing solutions should be used only once to prevent recontamination.

1) Blow off dust.

2) Prepare petri dishes filled with soap solution, distilled water, alcohol, and acetone. Line the bottom of each with tissue to prevent blemishing an optic.

3) Immerse the optic in soap solution. Agitate gently.

4) Immerse in distilled water. Agitate.

5) Immerse in alcohol. Agitate.

6) Immerse in acetone. Agitate.

7) Blow dry.

**Military specifications** are used by Newport to communicate the durability of optical coatings in an industry consistent manner. The primary MILSPECS used are:

**MIL-C-675** specifies that the coating will not show degradation to the naked eye after 20 strokes with a rubber pumice eraser. Coatings meeting MIL-C-675 can be cleaned repeatedly and survive moderate to severe handling.

**MIL-M-13830** sets durability standards for metallic coatings. Coatings will not peel away from the substrate when pulled with cellophane tape. Further, no damage visible to the naked eye will appear after 50 strokes with a dry cheese-cloth pad. Gentle, nonabrasive cleaning is advised.

**MIL-C-14806** specifies durability of surfaces under environmental stress. Coatings are tested at high humidity, or in brine solutions to determine resistance to chemical attack. These coatings can survive in humid or vapor filled areas.

**Surface quality** of an optical element ultimately determines the performance of a system. Even the highest quality material, if finished poorly, will cause distortion, loss or at elevated power levels, failure of the optic. In order to communicate optical surface quality, Newport has adopted the following standards.

**A clear aperture** is specified for all Newport optical components. It indicates a minimum area over which specifications are guaranteed. Although typical optics will meet or exceed their ratings to the edge of the component, a clear aperture specification allows sufficient area for safe handling of the optic during manufacture.

**Scratch-dig ratings** measure the visibility of large surface defects as defined by U.S. military standard MIL-D-13830. Ratings consist of two numbers, the first denoting the visibility of scratches, the second, of digs (small pits). A 0/0 scratch-dig number indicates a surface free of visible defects. Numbers increase as the visibility of blemishes increases. Scratch numbers are linear with a #10 scratch appearing identical to a 1 micron wide standard scratch on glass. Similarly, a #1 dig appears identical to a 0.01 mm diameter standard pit. Please note that no absolute measurement of defect size is made or implied by the scratch-dig standard.

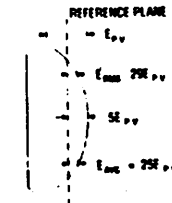
Components with small scratch-dig numbers will have increased damage thresholds, reduced scatter, and will eliminate unwanted diffraction effects. Newport recommends the following guidelines in selecting surface finish:

Scr-Dig	Applications
> 60-40	Non-laser optics
60-40	Low-power, unfocused beams
40-20	Collimated laser beams
< 40-20	High-energy, focused beams

Figure is a measure of how closely the surface of an optical element matches a reference plane. Since geometrical errors will cause

distortion of a transmitted or reflected wave, deviations from the ideal are measured in terms of wavelengths of light.

**Spherical Error** comprises the majority of figure deviations. (Optical polishing relies on circular strokes to finish a surface. For this reason, deviations from the ideal are usually spherical, either concave or convex. Newport computes spherical error as the maximum peak-to-valley deviation from a best fittings reference surface. Mathematically, the ideal surface is halfway between the points of maximum deviation. Practically, this represents the point of best alignment. Figure errors are represented by  $E$ , with  $E_{max}$  corresponding to the maximum peak-to-valley deviation from the reference surface. Although less frequently used, the root mean square error,  $E_{RMS}$ , and the average error,  $E_{AVE}$ , may also be defined.



**Irregularity**, denoted by  $\delta$ , refers to figure deviations that are not spherical in nature. It is usually caused by warpage due to internal material stress or mishandling. By means of careful processing of the highest quality optical materials, this error is negligible in magnitude.

**The wavelength** used in testing all Newport optics is 632.8 nm, consistent with modern laser interferometers. When used at longer wavelengths than 632.8, an optic will have a smaller relative error. Similarly shorter wavelengths will accentuate

$$E = E_{max} \times \frac{632.8 \text{ (nm)}}{\text{wavelength of use (nm)}}$$

the relative error. The following may be used to convert figure errors:

### Laser Damage

**Certified Damage Threshold** optics are available from Newport. Testing on a lot basis enables Newport to certify damage resistance to the rated fluence. Please see the Certified Damage Threshold optics section on page M-77 for more information.

**Safe Energy Levels** are listed for a majority of Newport optical components. Although these carry no certification, the levels published are conservative and derived from laboratory use tests.

Orders are shipped from our main plant in Fountain Valley, California. Unless otherwise noted, all optics are in stock and ready for delivery.

Items whose prices appear in brackets [XXXX] are high accuracy, material intensive products. They are offered on a limited stock basis. Please contact Newport for exact delivery times.

Unlisted (\*) prices or starred (\*) part numbers indicate high accuracy optics with very specific applications. They are stocked as uncoated substrates and coated as needed. Please contact Newport for price and delivery.

# The Discrete Prolate Spheroidal Filter as a Digital Signal Processing Tool

JOHN D. MATHEWS, SENIOR MEMBER, IEEE, J. K. BREAKALL, AND GEORG K. KARAWAS

## II. MATHEMATICAL DERIVATIONS

### A General Nonrecursive FIR Filter

In keeping with the tutorial nature of this paper we start with the simplest of statements concerning the FIR approach to filtering. Using the time and frequency domains, a tapped delay line representation of a nonrecursive FIR filter acting on analog signal  $x(t)$  is shown schematically in Fig. 1. The resultant output signal has the form

$$y(t) = \sum_{n=-K}^K a_n x(t - n\tau) \quad (1)$$

where the coefficients  $a_n$  are real and where the time reference is, for later convenience, at the center of the delay line. Assuming that the Fourier transform of  $x(t) \Rightarrow X(\omega)$  exists we Fourier transform (1) and find

$$Y(\omega) = H(\omega) \cdot X(\omega) \quad (2)$$

where

$$H(\omega) = \sum_{n=-K}^K a_n e^{-jn\omega\tau} \quad (3)$$

is the "voltage" transfer function and  $j = \sqrt{-1}$ . The corresponding "power" transfer function is

$$S(\omega) = H(\omega) \cdot H^*(\omega) = \sum_{n,m=-K}^K a_n a_m e^{-j(n-m)\omega\tau} \quad (4a)$$

$$= \sum_{n=-K}^K \left| a_n + 2 \sum_{m=-K}^{n-1} a_m a_n \cos(n-m)\omega\tau \right| \quad (4b)$$

while the inverse Fourier transform of (3) is

$$h(t) = \sum_{n=-K}^K a_n \delta(t - n\tau) \quad (5)$$

the filter impulse response with  $\delta(t')$  the unit impulse. Note that  $h(t)$  convolved with  $x(t)$  yields (1).

The filter described by (3) or (5) becomes a digital filter if we uniformly and instantaneously sample  $y(t)$  at intervals of  $\tau$  time. Then (1) becomes

$$y_l = \sum_{n=-K}^K a_n x_{l-n} \quad (6)$$

where the index  $l$  refers to consecutive members of the set of sampled signals. If we restrict  $x(t)$  to be band limited to the Nyquist frequency ( $2\pi/2\tau$ ) or less, then the sampling filtering process occurs without aliasing.

### Choice of Coefficients

Equations (3) or (5) describe the effects of the filter on an input signal given a particular set of coefficients  $\{a_n\}$ . These coefficients are often chosen such that the digital filter characteristics are similar to one of various common analog filters (e.g., the "ideal" filter). The process of synthesizing these filter characteristics often involves smoothing (windowing) of the resultant coefficient sequence to suppress ringing [14], [15].

As mentioned in the introduction, we propose to choose

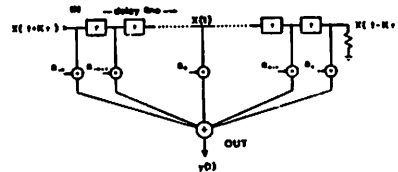


Fig. 1. Block diagram of the nonrecursive FIR filter described by (1). This schematic form of the filter is valuable because of its visual simplicity.

These "traditional" filters are all based on various windowing (weighting) functions applied to the coefficients of the infinite Fourier series representation of the ideal low-pass filter. The coefficients of this series are

$$C_n = \frac{\sin n\pi\epsilon}{n\pi} \quad (7)$$

$$n = 0, \pm 1, \pm 2, \dots$$

$$\epsilon = \omega_c/\omega_N \quad (17)$$

and the windowing function  $W(n)$  is such that  $W(n) = 0$  for  $|n| \geq K$ , thus truncating the series so that the resultant transfer function becomes

$$H_w(\omega) = \sum_{n=-K}^K W(n) C_n e^{-jn\omega\tau} \quad (18)$$

The  $W(n)$  ( $-K \leq n \leq K$ ) are chosen to minimize in some sense the ringing (Gibb's phenomena) which results from truncation of the series representation of the ideal low-pass filter [15, chap. 5], [16, chap. 3].

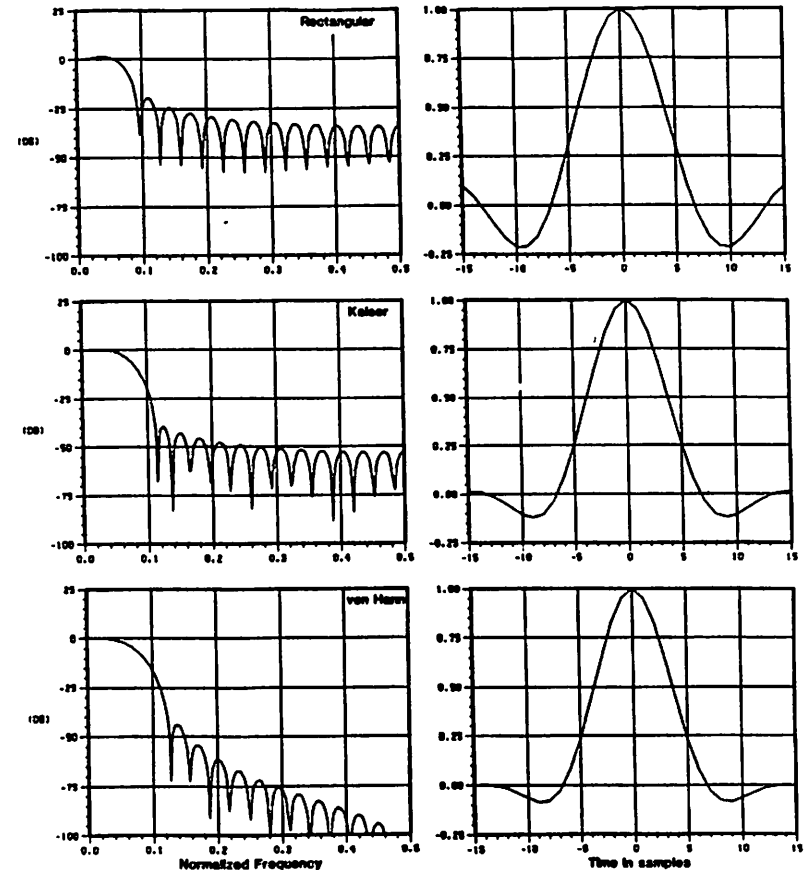


Fig. 2. Filter frequency response (dB) plotted versus normalized frequency (Nyquist frequency  $f_N = 0.5$ ) and corresponding impulse response envelope plotted versus time in samples for rectangular, Kaiser, and Von Hann windows of length 31 [see (18) and Table I]. In all cases the normalized 3 dB frequency is approximately 0.05.

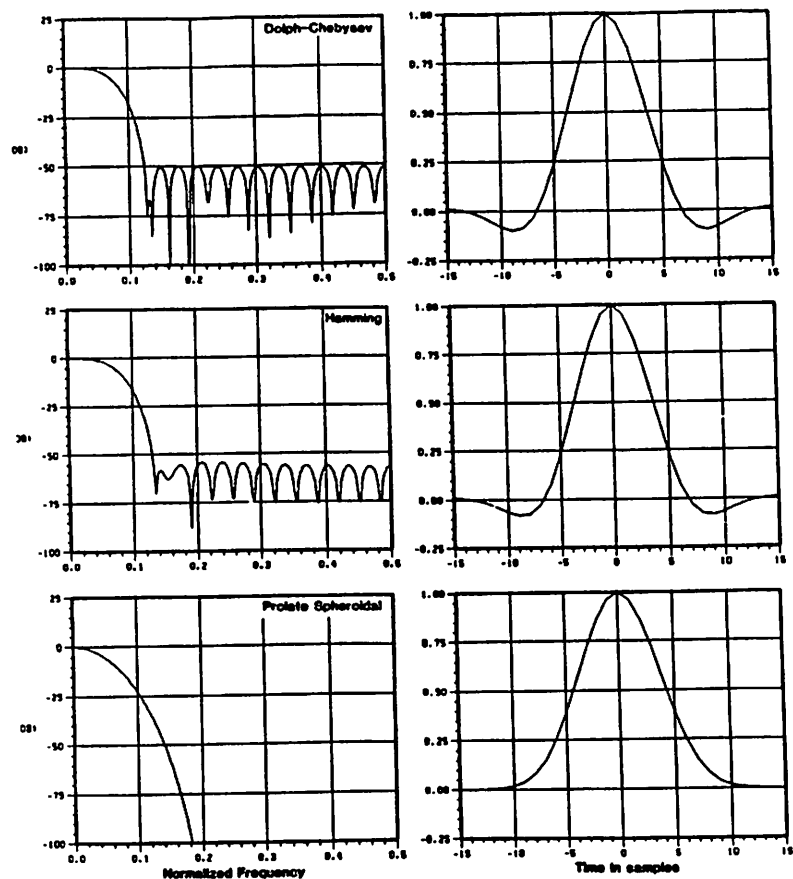


Fig. 3. Similar to Fig. 2, but for Dolph-Chebyshev and Hamming windows, and the prolate spheroidal filter. The normalized cutoff frequency of the prolate spheroidal filter is 0.2. The filters in Figs. 2 and 3 are ordered according to overall quality with, in our opinion, the rectangular window filter worst and prolate spheroidal filter best.

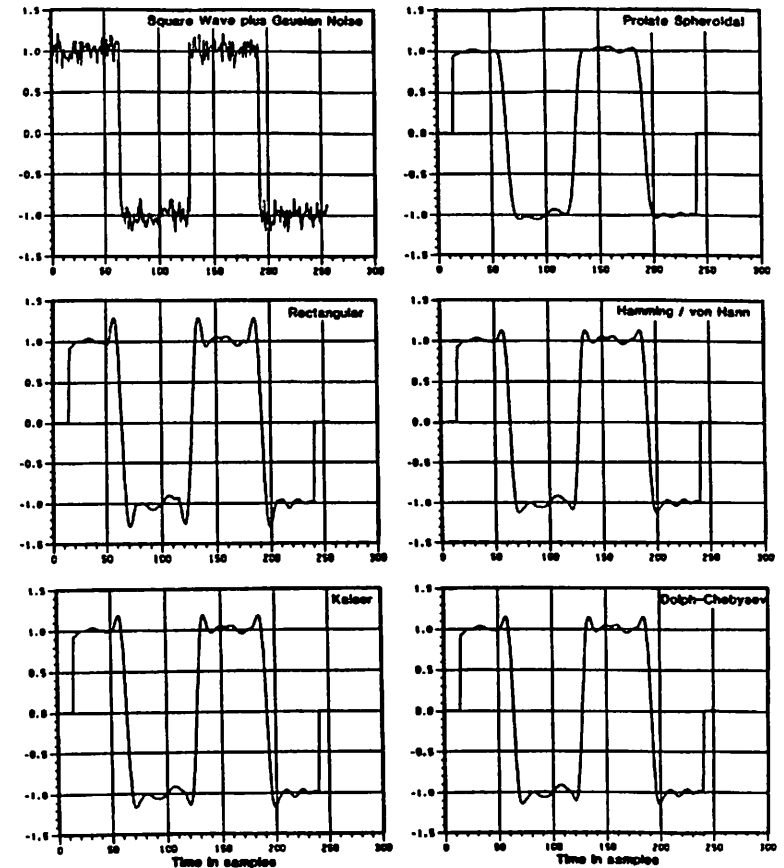
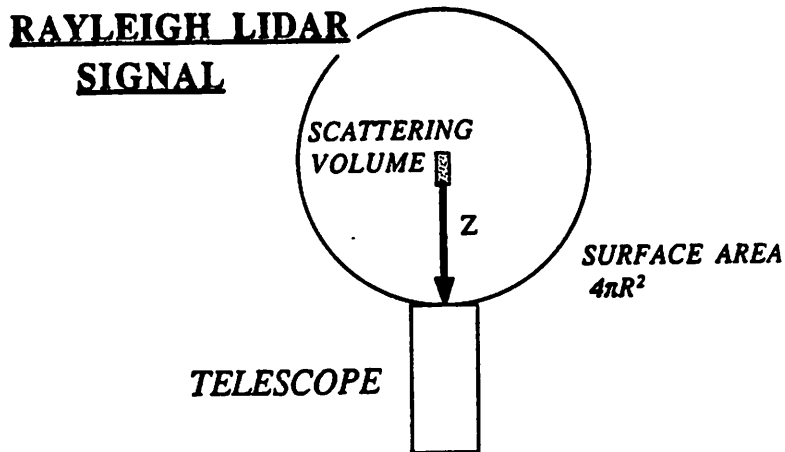


Fig. 4. We compare the time domain effects of the various filters on a square wave plus Gaussian distributed noise. Note that all filters except the prolate spheroidal filter "ring" and that the rectangular window filter rings most with the Kaiser window next while the Dolph-Chebyshev, Hamming, and Von Hann windows are similar in this case.



$$N(Z) = \eta_{\text{eff}} T_A \times \frac{P_L}{hc/\lambda} \times \sigma_R n(Z) \Delta Z \times \frac{A_R}{4\pi Z^2}$$

$$\text{PHOTOCOUNT} = \frac{\text{SYSTEM EFFICIENCY}}{\text{EFFICIENCY}} \times \frac{\text{PHOTONS TRANSMITTED}}{\text{TRANSMITTED}} \times \frac{\text{SCATTERING PROBABILITY}}{\text{PROBABILITY}} \times \frac{\text{RECEIVER PROBABILITY}}{\text{PROBABILITY}}$$

=> Special care should be taken to maximize the efficiency of the lidar's optical design by;

- 1) Maximizing transmission through lenses and filters.
- 2) Maximizing reflection off mirrored surfaces.
- 3) Minimizing the total number of surfaces in the system.



Facility	Laser	$\lambda$ (nm)	Laser Power $P_L$ (w)	Telescope Area $A_R$ (m <sup>2</sup> )	Performance Factor* $A_R P_L$ (m <sup>2</sup> w)
AFGL (mobile)	Nd:YAG	532	3	0.07	0.2
Haute Provence	Nd:YAG	532	4	0.5	2
Kyushu Univ.	Excimer	351	16	0.2	4.2
CEDAR	Dye	589	5	1.2	4
CEDAR+	Excimer	351	30	1.2	50

\*Equivalent performance at 532 nm

+Not yet tested

### DETECTOR

- 24) Fused silica plano-convex lens (1" dia. x 1" FL)  
AR coated, 99.7% trans. @ 532,355,607nm
- 14) Dichroic beamsplitter: reflects 99.5% @ 532nm  
transmits 82% @ 355nm  
transmits 86% @ 607nm
- 6) Narrow-band filter, BW = .29nm @ 532nm  
55% transmission
- 7) Beamsplitter, transmits .5%, reflects 99.5%
- 27) Glass plano-convex lens (1" dia. x 1" FL)  
AR coated, 99.7% transmission @ 532nm.
- 13) highly reflective mirror @ 532nm,355nm  
reflects 99.8%
- 4) Glass plano-convex lens (1" dia. x 2" FL.)  
AR coated, 99.7% transmission.
- 19) Photon counting PMT, 20% quantum efficiency  
@ 532nm.
- 25) Dichroic beamsplitter: reflects 99.5% @ 607nm  
transmits 82% @ 355nm
- 22) Narrow-band filter, BW = 3.5nm @ 607nm  
83% transmission.
- 23) Photon counting PMT, 7% quantum efficiency  
@ 607nm.
- 10) Narrow band filter, BW = 3.2nm @ 355.1nm.  
24% transmission.
- 8) fused silica plano-convex lens (1"dia. x 2" FL)  
AR coated, 99.7 transmission.
- 20) Photon counting PMT, 24% quantum efficiency  
@ 355nm.

$$D_{e,f} = 10.71\% @ 532nm$$

$$4.93\% @ 607nm$$

$$3.78\% @ 355nm$$

**SYSTEM EFFICIENCY**

$\eta_{\text{eff}} = T_{\text{eff}} \times R_{\text{eff}} \times D_{\text{eff}}$

	532	355	607nm
LAMP	.0718	.0251	.0324
GLINT	.0481	.0218	---

**LASER POWER**

$P_L$  = laser power in joules.

	532	355nm
LAMP	.7J	.4J
GLINT	.5J	.18J

**NUMBER DENSITY**

$n(z)$  is read from table II in the U.S. Standard Atm. 76

Alt.	$n(Z)$
30Km	3.745E23 /m <sup>2</sup>
50Km	2.135E22 /m <sup>2</sup>
60Km	5.995e21 /m <sup>2</sup>

**TELESCOPE AREA**

$A_R = \pi R^2$  where R is the radius of the primary mirror.

	$A_R$
LAMP	.13 m <sup>2</sup>
GLINT	.0804 m <sup>2</sup>

**RAYLEIGH BACKSCATTER CROSS SECTION**

$\sigma_R = 5.45 [550/\lambda(\text{nm})]^4 \times 10^{-32} \text{ m}^2 \text{sr}^{-1}$

	532	355nm
$\sigma_R =$	62.26E-33	313.6E-33 m <sup>2</sup>

**ATMOSPHERIC TRANSMISSION**

$T_A = T_{U_p} \times T_{B_{\text{Back}}}$

$T_U$  and  $T_B$  are calculated from LOWTRAN 7

Alt.	$T_U(532)$	$T_U(355)$	$T_B(607)$
30Km	.6249	.3337	.6768
50Km	.6215	.3313	.671
60Km	.6214	.3312	.6709

**PHOTON ENERGY**

$E = hc/\lambda$

	532	355	607nm
	373.9E-21	560.1E-21	327.5E-21J

**INTEGRATION HEIGHT**

$\Delta Z = c\tau_d/2$  where  $\tau_d$  = integration time

$\tau_d = 2\mu\text{s}$

$\Delta Z = 300 \text{ m}$

**ATMOSPHERIC HEIGHT**

Z = height of scattering volume

$\sigma_{\text{Raman}} = 56.12\text{E-}36 \text{ m}^2$

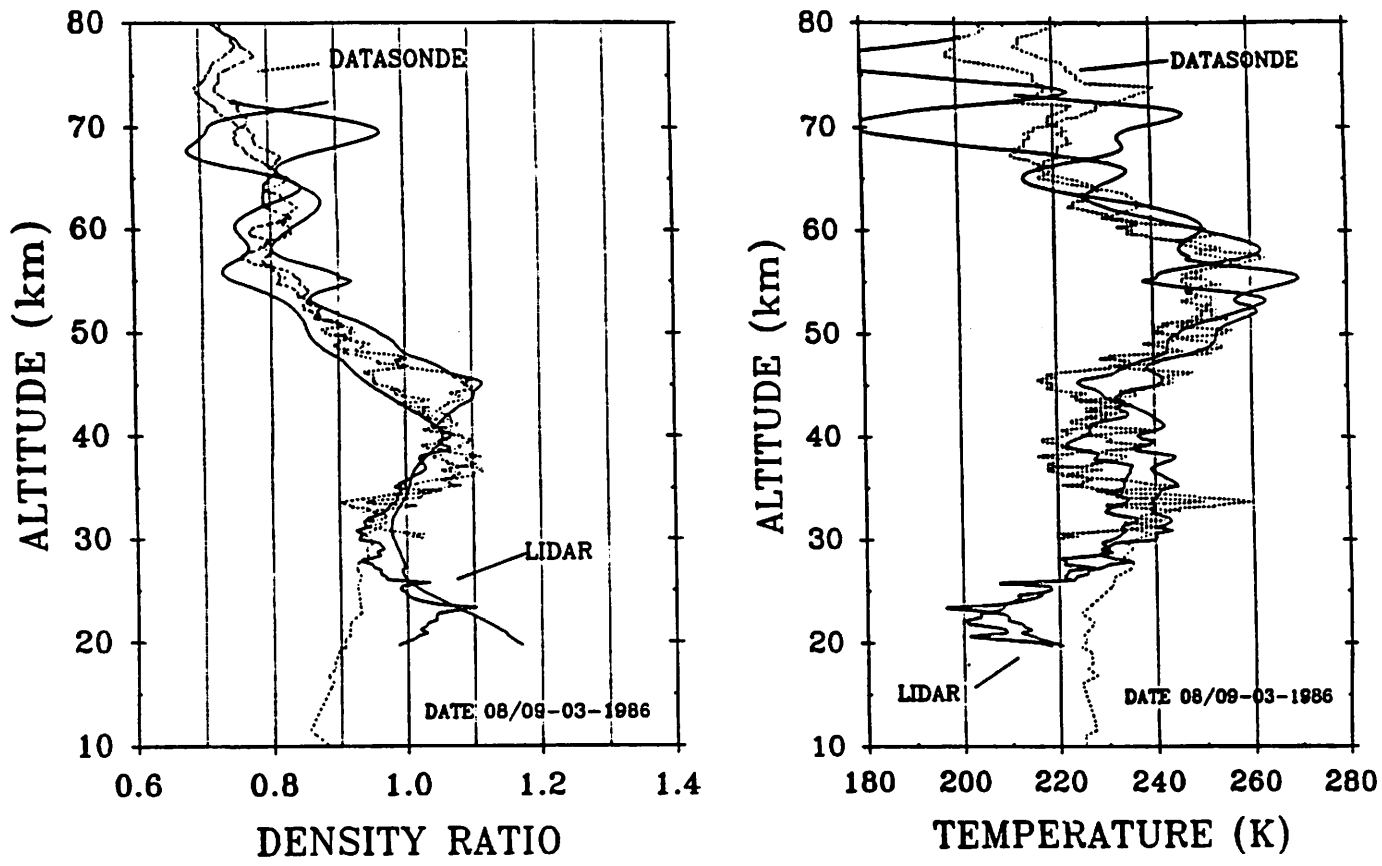


Fig. 5. The density and temperature results obtained on 8 and 9 March 1986 at the same time by rocket instrument and lidar.

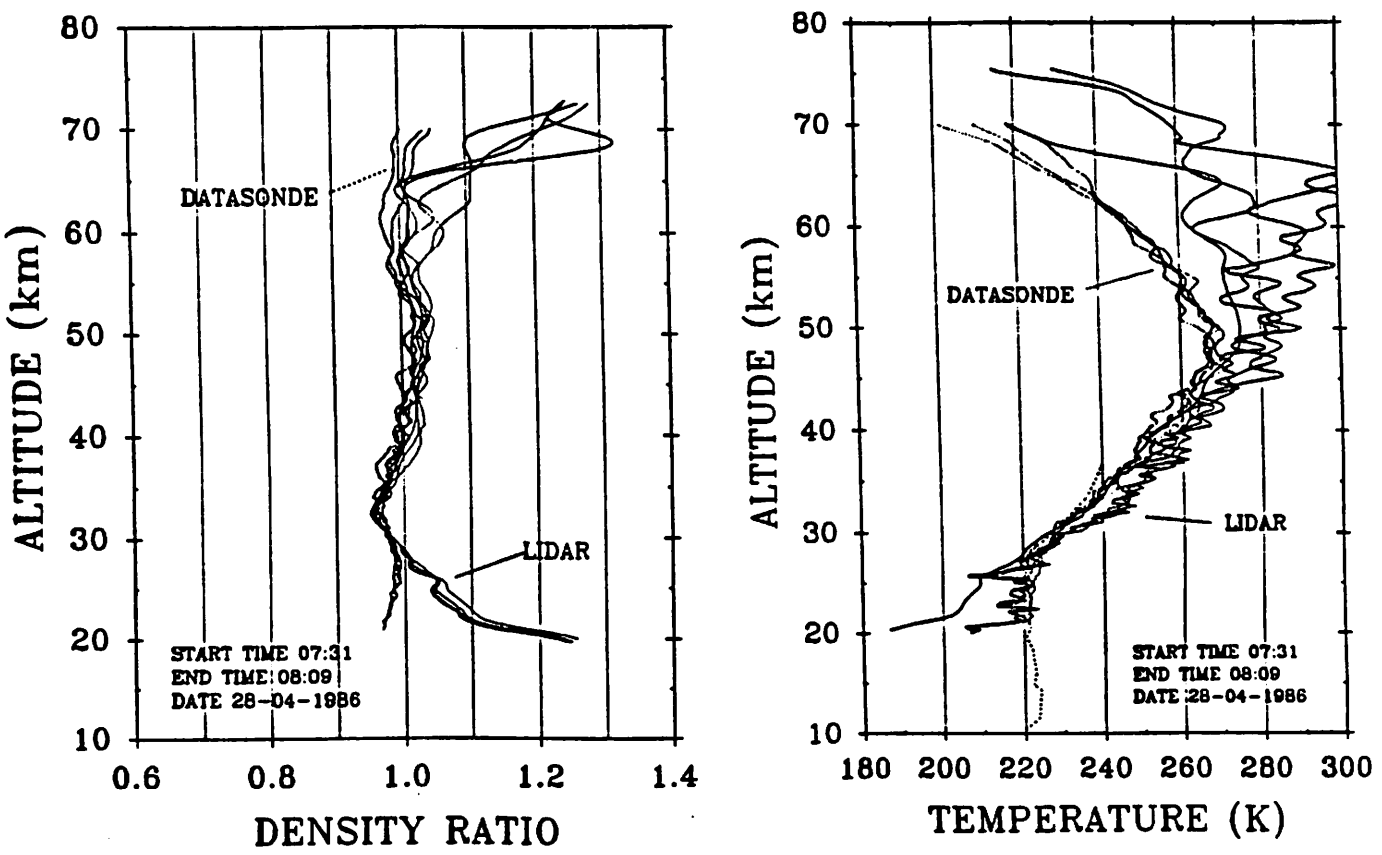


Fig 4. The four datasonde rocket flights and the corresponding lidar results are shown for the density ratio to the USSA76 model and for the temperature.

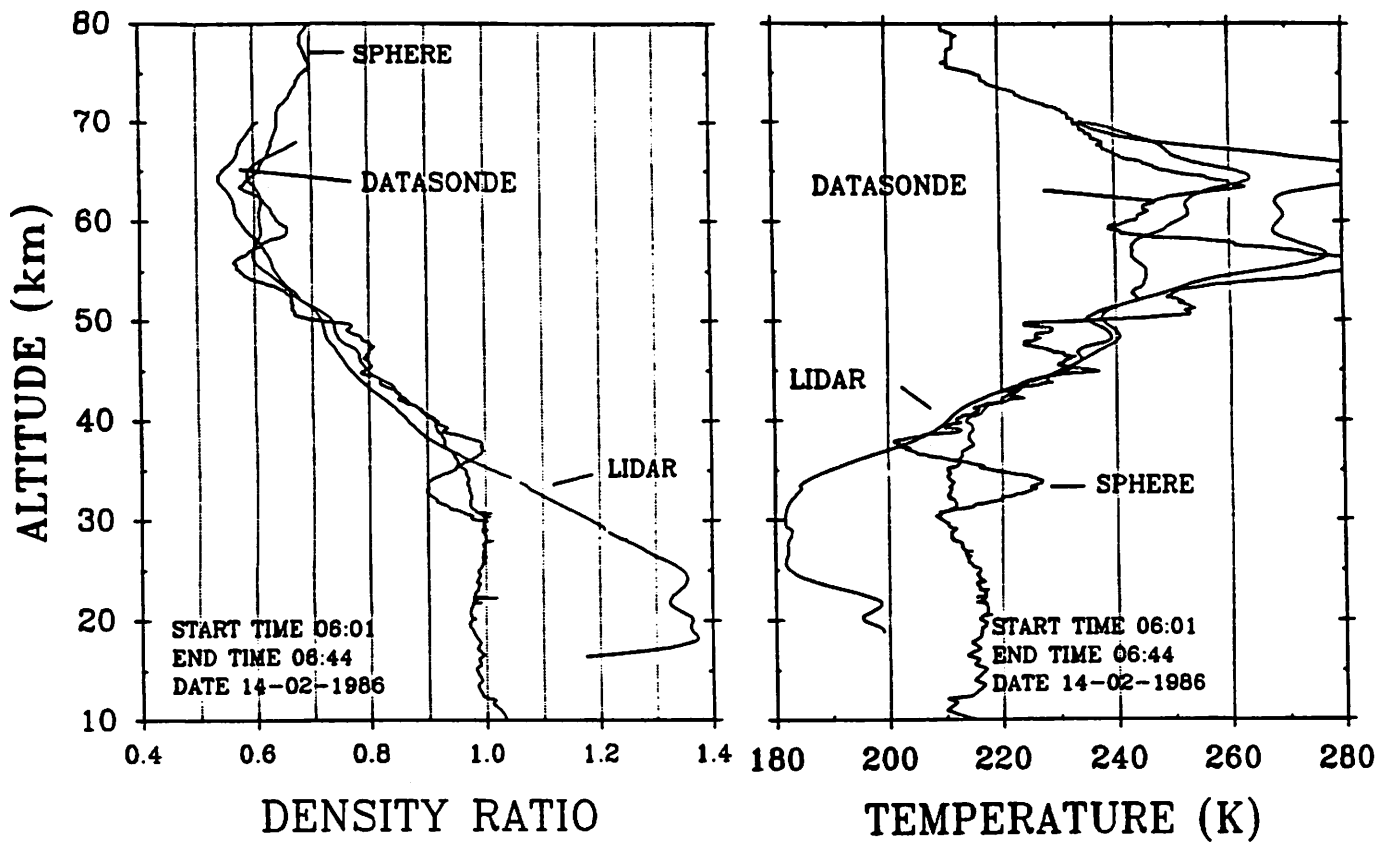


Fig. 6. The data obtained on 14 February 1986 exhibits significant departures between the lidar and rocket data. Two major difference are observed in this data set, the large wave response associated with the strong wind field during during this period and the additional optical scattering between 25 and 35 km.

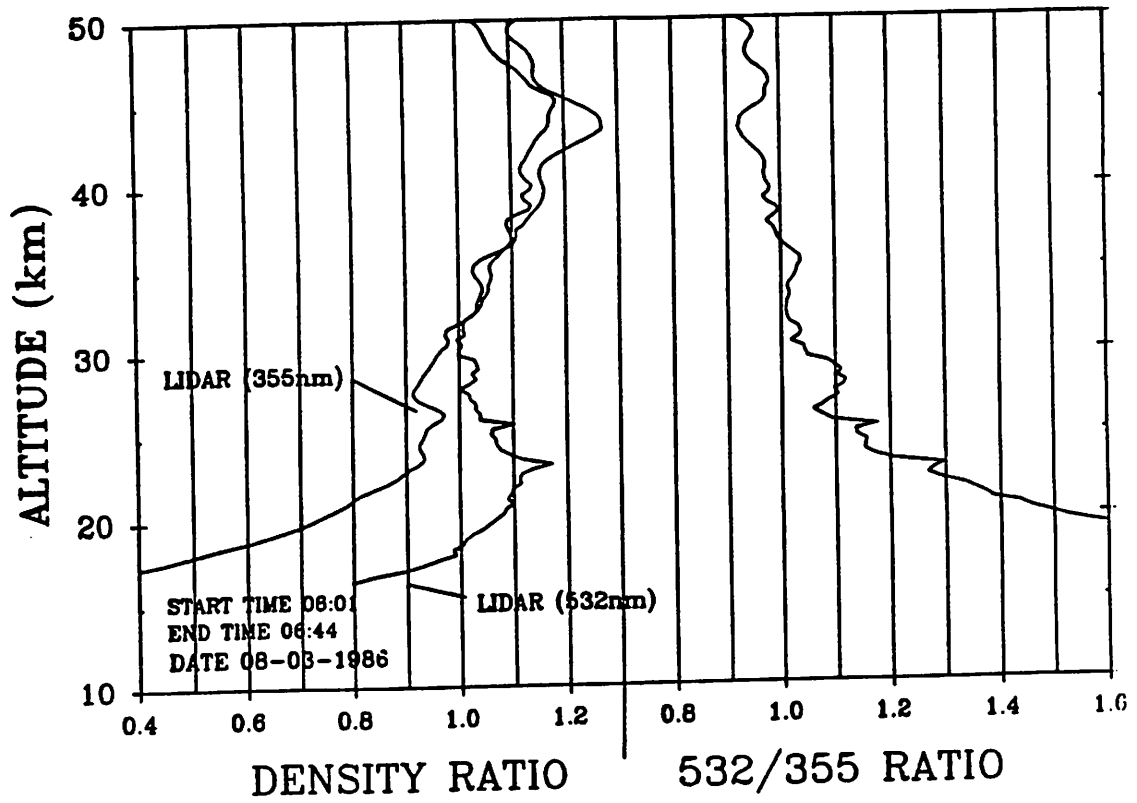


Fig. 7. The simultaneous measurement of the UV (355 nm) and the visible (532 nm) backscatter clearly shows the aerosol signal because of the relative difference in backscatter cross-section at the two wavelengths.

## Hydrostatic Equation

$$dP = -\rho g dz$$

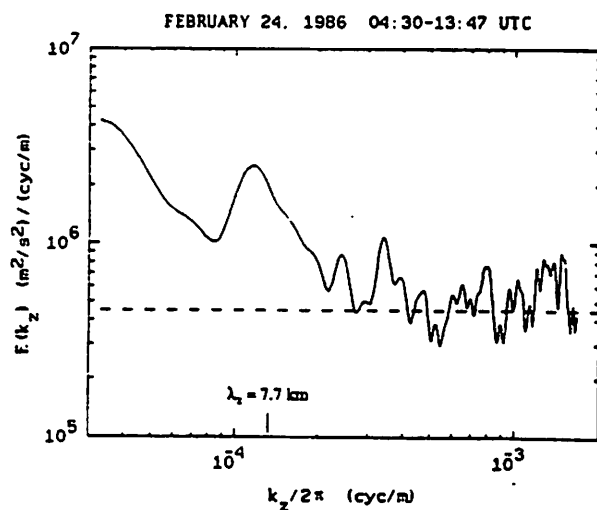
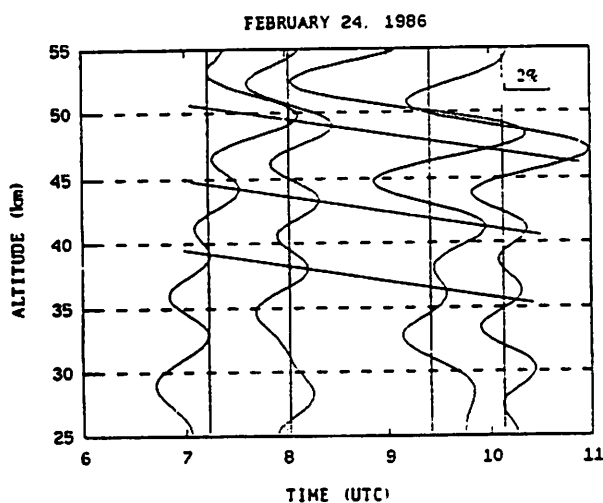
## Ideal Gas Law

$$P = \rho RT/M$$

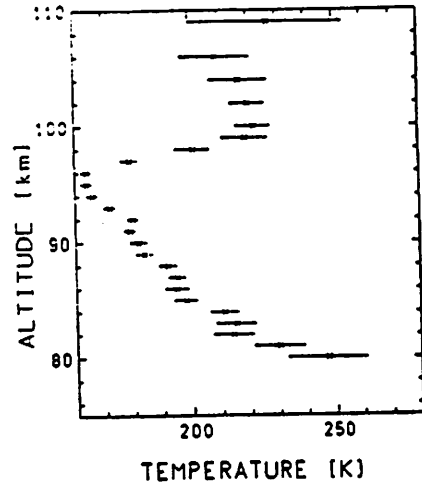
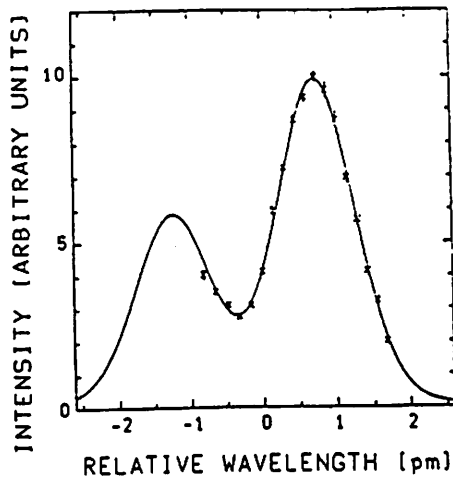
By combining these two equations and integrating downward from a starting altitude  $z_0$  and upper level temperature  $T(z_0)$  we obtain

$$T(z) = \frac{T(z_0)\rho(z_0)}{\rho(z)} + \frac{M}{R} \int_z^{z_0} \frac{g(r)\rho(r)}{\rho(z)} dr$$

- $P(z)$  = atmospheric pressure profile
- $\rho(z)$  = atmospheric density profile
- $T(z)$  = atmospheric temperature profile
- $g(z)$  = gravitational acceleration
- $M$  = mean molecular weight of atmosphere
- $R$  = universal gas constant

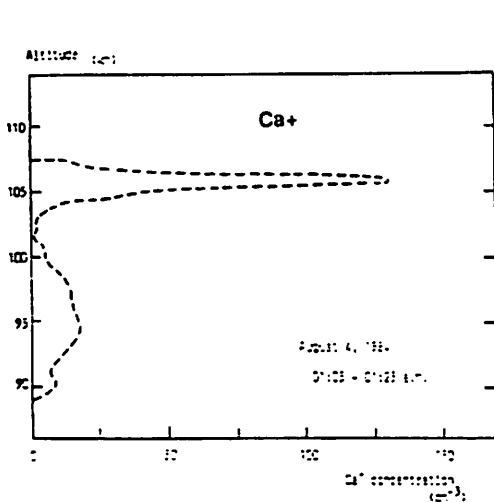


Density perturbation profiles and power spectrum measured on February 24, 1986 using the AFGL Rayleigh lidar at Poker Flat, AK. The diagonal lines indicate the 0.3 m/s phase progression of the 7.7 km wave [Miller et al., 1987].

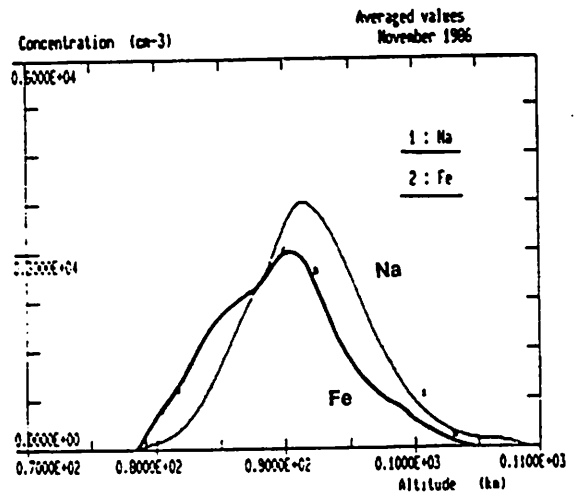


Temperature profiles obtained at Andoya, Norway on March 13, 1986 with the University of Bonn Na lidar. Integration period is 5 min. and vertical resolution is 500 m [von Zahn and Neuber, 1987].

Na temperature can be measured by scanning a narrowband laser through the D<sub>2</sub> resonance line. Technique was first demonstrated by Thomas and co-workers [Gibson et al., 1979; Thomas and Bhattacharyya, 1980].



[Granier et al., 1986]



[Granier et al., 1987]

Resonance-fluorescence lidars are used to study metallic species in the mesosphere and thermosphere. Systems have been developed to measure Na, Li, K, Fe, Ca and Ca<sup>+</sup>.

## BOOKS

- Measures, R.E., Laser Remote Sensing, Fundamentals and Applications, John Wiley & Sons.
- Hecht, E., Optics, Addison-Wesley Publishing Co.
- Hecht, J., The Laser Guidebook, McGraw-Hill Book Co.
- Meyers, R.A., Editor, Encyclopedia of Lasers and Optical Technology, Academic Press, Inc.
- Driscoll, W.G. and W. Vaughan, Editors, Handbook of Optics, McGraw-Hill Book Co.
- Born, M. and E. Wolf, Principles of Optics, Pergamon Press.
- Hernandez, G., Fabry-Perot Interferometers, Cambridge University Press, 1986.
- Seippel, R.G., Optoelectronics for Technicians and Engineering, Prentice Hall.
- Schroeder, D.J., Astronomical Optics, Academic Press, Inc.
- Cheo, P.K., Fiber Optics and Optoelectronics, Prentice Hall.
- Allard, F.C., Editor, Fiber Optics Handbook for Engineers and Scientists, McGraw-Hill Publishing Co.
- van de Hulst, H.C., Light Scattering by Small Particles, Dover Publications, Inc.
- Brevington, P.R., Data Reduction and Analysis for the Physical Sciences, McGraw-Hill Book Co.
- Kurucz, R.L., L. Testerman, I. Furenlid, and J. Brault, Solar Flux Atlas from 296 to 1300 nm, National Solar Observatory Atlas No. 1.
- Laser Institute of America, ANSI Z136.1-1986, American National Standards Institute, Inc., N.Y.
- Jursa, A.S., Editor, Handbook of Geophysics and the Space Environment, A.F.G.L., A.F.S.C., U.S.A.F., 1985.
- Rutten, H. and M. van Venrooij, Telescope Optics, Willmann-Bell, Inc., 1988.
- Meyer-Arendt, J.R., Introduction to Classical & Modern Optics, Prentice-Hall, Inc., 1989.
- Guenther, R., Modern Optics, John Wiley & Sons, Inc., 1990.

Sliney, D. and M. Wolbarsht, Safety with Lasers and Other Optical Sources, Plenum Press, N.Y., 1980.

Milonni, P.W. and J.H. Eberly, Lasers, John Wiley & Sons, N.Y., 1988.

Bohren, C.F., Editor, Selected Papers on Scattering in the Atmosphere, SPIE Milestone Series, Vol. MS 7, 1989.

Siegman, A.E., Lasers, University Science Books, 1986.

NASA, U.S. Standard Atmosphere Supplements, 1966, U.S. Government Printing Office, Washington, D.C., 1966.

## ARTICLES

Chanin, M. and A. Hauchecorne, "Lidar Observation of Gravity and Tidal Waves in the Stratosphere and Mesosphere," J. Geophys. Res., **86**, 9715-9721, 1981.

Elterman, L.B., "The Measurement of Stratospheric Density Distribution with the Search Light Technique," J. Geophys. Res., **56**, 509-520, 1951.

Elterman, L.B., "A Series of Stratospheric Temperature Profiles Obtained with the Search Light Technique," J. Geophys. Res., **58**, 519-530, 1953.

Elterman, L.B., "Seasonal Trends of Temperature, Density and Pressure to 67.6 km Obtained with the Searchlight Probing Technique," J. Geophys. Res., **59**, 351-358, 1954.

Gardner, C.S., M.S. Miller and C.H. Liu, "Rayleigh Lidar Observations of Gravity Wave Activity in the Upper Stratosphere at Urbana, Illinois," J. Atmos. Sci., **46**, 1838-1854, 1989.

Gardner, C.S. and J.D. Shelton, "Density Response of Neutral Atmospheric Layers to Gravity Wave Perturbations," J. Geophys. Res., **90**, 1745-1754, 1985.

Gardner, C.S., D.C. Senft, T.J. Beatty, R.E. Bills and C. A. Hostetler, "Rayleigh and Sodium Lidar Techniques for Measuring Middle Atmosphere Density, Temperature, and Wind Perturbations and Their Spectra," WITS Handbook, Vol 2, 148-187, SCOSTEP Secretariat, 1989.

Gibson, A., T. and S. Bhattachacharyya, "Lidar Observations of the Ground-State Hyperfine Structure of Sodium and of Temperatures in the Upper Atmosphere," Nature, **281**, 131-132,

1979.

Iwasaka, Y., T. Ono, and A. Nomura, "Changes in Aerosol Content and Temperature in the Antarctic Spring Stratosphere; Lidar Measurement at Syowa Station (69°00'S, 39°35'E) in 1983, 1984, and 1985," Geophys. Res. Lett., 13, 1407-1410, 1986.

Kwon, K.H., C.S. Gardner, D.C. Senft, F.L. Roesler, and J. Harlander, "Daytime Lidar Measurements of Tidal Winds in the Mesospheric Sodium Layer at Urbana, Illinois," J. Geophys. Res., 92, 8781-8786, 1987.

McCormick, M.P., T.J. Swisler, W.H. Fuller, W.H. Hunt, and M.T. Osborn, "Airborne and Groundbased Lidar Measurements of the El Chichon Stratospheric Aerosol from 90°N to 56°S," Geof. Inst., 23, 198-221, 1984.

McDermid, S., S.M. Godin, and L.O. Lindqvist, "Ground-based Laser DIAL System for Long-term Measurements of Stratospheric Ozone," Appl. Optics, 29, 3603-3612, 1990.

Melfi, S.H., "Remote Measurements of the Atmosphere Using Raman Scattering," Appl. Optics, 11, 1605-1610, 1972.

Philbrick, C.R., "Lidar Profiles of Atmospheric Structure Properties," SPIE Proceedings 1991.

Philbrick, C.R., D.P. Sipler, B.E. Dix, G. Davidson, W.P. Moskowitz, R. Sluder, F.J. Schmidlin, L.D. Mendenhall, K.H. Bhavnani, and K.J. Hahn, "Measurements of the High Latitude Middle Atmosphere Dynamic Structure Using Lidar," AFGL-TR-887-0053 Environmental Research Papers, No. 967, Geophysics Laboratory Report, 1987.

Philbrick, C.R., D.P. Sipler, G. Davidson, and W.P. Moskowitz, "Remote Sensing of Structure Properties in the Middle Atmosphere Using Lidar," Proceedings of Topical Meeting on Laser and Optical Remote Sensing: Instrumentation and Techniques, 1987.

She, C.Y., R.E. Bills, H. Latifi, J.R. Yu, B.J. Alvarez II and C.S. Gardner, "Two-Frequency Lidar Technique for Mesospheric Na Temperature Measurements," Geophys. Res. Lett., in press, 1989.

Tepley, C.A., S.I. Sargoytchev, and C.O. Hines, "Initial Doppler Rayleigh Lidar Results from Arecibo," Geophys. Res. Lett., 18, 167-170, 1991.

vonZahn, U. and T.L. Hansen, "Sudden Neutral Sodium Layers: A Link to Sporadic E Layers," JATP 50, 93-104, 1988.

## COMPANIES

### LASERS

Spectra-Physics  
1250 W. Middlefield Road  
P.O. Box 7013  
Mountain View, CA 94039-7013  
Phone (415) 961-2550  
FAX (415) 969-4084 TLX 348-488

Coherent Laser Group  
3210 Porter Drive  
P.O. Box 10042  
Palo Alto, CA 94303  
Phone (800) 527-3786  
(415) 858-7582  
Telex 34-8304  
FAX (415) 858-7631  
United Kingdom (0223) 420501  
Germany (06074) 9140  
Japan (03) 3648-8115

### Continuum

1. 3150 Central Expressway  
Santa Clara, CA 95051  
Phone (408) 727-3240  
FAX (408) 727-3550
2. 152 Dartmouth Street  
Marlboro, MA 01752  
Phone (508) 624-4454  
FAX (508) 624-4453
3. 4643 Spring Ridge Drive  
Flowery Branch, GA 30542  
Phone (404) 967-2129  
FZX (404) 967-2522
4. 4 Rolling Springs Court  
Carmen, IN 46043  
Phone (317) 727-3240  
FAX (317) 574-0057
5. Star Route Box 120  
Placitas, NM 87043  
Phone (505) 867-9414  
FAX (505) 867-9415

Lumonics, Inc.  
105 Schneider Road  
Kanata, Ontario  
Canada K2K 1Y3  
Phone (613) 592-1460  
FAX (613) 592-5706  
U.S.A. Phones: New England (508) 460-9871  
Mid Atlantic (703) 528-2954  
Southeast (407) 645-4708



Midwest (708) 961-5444  
Northwest/Northern CA (415) 829-9292  
Southwest/Southern CA (415) 426-0639

Lambda Physik Inc.  
289 Great Road  
Acton, MA 01720  
Phone (800) 262-1100  
(508) 263-1100  
FAX (508) 263-4296

#### PHOTOMULTIPLIERS

THORN EMI Gencom Inc.  
23 Madison Road  
Fairfield, NJ 07006  
Phone (201) 575-5586  
Telex 221236

Hamamatsu Corporation  
Main Office: 360 Foothill Road  
P.O. Box 6910  
Bridgewater, N.J. 08807-0910  
Phone (908) 231-0960  
FAX (908) 231-1539

Western U.S.A. Office:  
2444 Moorpark Avenue, Suite 312  
San Jose, CA 95128  
Phone (408) 292-8603  
FAX (408) 279-1886

Burle Industries, Inc.  
Tube Products Division  
1000 New Holland Avenue  
Lancaster, PA 17601-5688  
Phone (717) 295-6000  
Marketing and Sales:  
Phone (800) 366-2875  
FAX (717) 295-6096  
Telex 272543

EG&G JUDSON  
221 Commerce Drive  
Montgomeryville, PA 18936  
Phone (215) 368-6900  
Telex 846120  
FAX (215) 362-6107

U.S. Sales Offices: East - Salem, MA (617) 745-7400  
Central - Elk Grove, IL (708) 640-7785  
West - Sunnyvale, CA (408) 245-2060  
S. CA - El Toro, CA (714) 583-2250

EMR PHOTOELECTRIC

Box 44  
Princeton, NJ 08542-0044  
Phone (609) 799-1000  
Telex 5106015604  
FAX (609) 799-2247

Products for Research, Inc.  
Photomultiplier Tubes  
88 Holten Street  
Danvers, MA 01923  
Phone (617) 774-3250

#### OPTICAL COMPONENTS

Oriel Corporation  
250 Long Beach Blvd.  
P.O. Box 872  
Stratford, CT 06497  
Phone (203) 377-8282  
Telex 4750361  
FAX (203) 378-2457

Ealing Electro-Optics, Inc.  
New Englander Industrial Park  
Holliston, MA 01746  
Phone (800) 343-4912  
(508) 429-8370  
Telex 240041  
Facsimile (508) 875-5616

Newport Corporation  
P.O. Box 8020  
18235 Mt. Baldy Circle  
Fountain Valley, CA 92728-8020  
Phone (714) 963-9811  
Facsimile (714) 963-2015

Edmund Scientific Co.  
101 E. Gloucester Pike  
Barrington, NJ 08007-1380  
Ordering Number: (609) 573-6250  
(609) 547-3488

DSP Technology Inc.  
48500 Kato Road  
Fremont, CA 94538-7338  
Phone (415) 657-7555  
Facsimile (415) 657-7576  
Telex 283608

LeCroy Corporation  
700 Chestnut Ridge Road - Dept. H  
Chestnut Ridge, NY 10977-6499

Laser Focus World, The Buyer's Guide, A PennWell Publication

**OPTICAL COATINGS**

O C A LAMBDA/TEN OPTICS  
One Liberty Way  
Westford, MA 01886  
Phone (508) 692-8140  
FAX (508) 692-9416

SORL, Space Optics Research Labs  
7 Stuart Road  
Chelmsford, MA 010824  
Phone (508) 256-4511  
Telex 94-7443  
FAX (508) 256-1872

C VI LASER CORPORATION  
200 Dorado Place  
SE/P.O. Box 11308  
Albuquerque, NM 87192  
Phone (505) 296-9541  
FAX (505) 298-9908

C VI East - 111 Highland Drive  
Putnam, CT 06260  
Phone (203) 928-1928  
FAX (203) 928-1515

C VI West - 470 Lindbergh Avenue  
Livermore, CA 94550  
Phone (415) 449-1064  
FAX (415) 449-1150

EMF, Evaporated Metal Films Corp.  
701 Spencer Road  
Ithaca, NY 14850  
Phone (800) 456-7070  
Facsimile (800) 456-FACS  
Outside U.S.: Phone (607) 272-3320  
Facsimile (607) 272-3369

Corion Corporation  
73 Jeffrey Avenue  
Holliston, MA 01746  
Phone (508) 429-5065  
TWX 710-346-6544  
FAX (508) 429-8983

MicroCoatings  
(a division of Optical Corporation of America)  
1 Lyberty Way  
Westford, MA 10886

Phone (508) 692-8140  
(800) MICROCO (642-7626)  
FAX (508) 692-9416

OCLI  
Commercial Products Division  
2789 Northpoint Parkway  
Santa Rosa, CA 95407-7397  
Phone (707) 545-6440  
Teles II 510-744-2083  
FAX (707) 525-7410

Reynard Enterprises, Inc.  
26098 Getty Drive  
Laguna Niguel, CA 92677  
Phone (714) 831-6026  
Telex #361519 REYNARD ENT.  
FAX (714) 498-9528